University of Silesia
Faculty of Science and Technology
August Chełkowski Institute of Physics

Krzysztof Grzanka

Precise Theoretical Calculations For Future Lepton Colliders

PhD Thesis

PhD Supervisor:
prof. dr hab. Janusz Gluza
co-Supervisor:
dr Ievgen Dubovyk

UNIVERSITY OF SILESIA
IN KATOWICE

Katowice 2025

Abstract

The post-LEP e^+e^- colliders proposed for the precise high-energy physics will provide a set of ground-breaking measurements of a large number of new-physics sensitive electroweak pseudo-observables (EWPOs), with improvement by one to two orders of magnitude in experimental precision. The full exploitation of the significantly increased experimental precision at the Z boson resonance region for EWPOs (effective weak mixing angles, the Z-boson partial and total decay widths, the branching ratios, the hadronic cross section), necessitates Standard Model (SM) predictions accurate at a level commensurate with this precision, demanding leap-jumps in the precision of higher-order perturbation calculation represented by multi-scale multi-loop Feynman integrals. We discuss different techniques used for the evaluation of these Feynman integrals beyond the one-loop level, focusing on Mellin-Barnes representations, sector decomposition and differential equations. In this respect, we developed auxiliary programs and procedures to automate calculations with sector decomposition and differential equation methods. These methods have been used further to calculate SM three-loop W and Z boson self-energies and the $W\bar{\ell}\nu_\ell$ vertex of the order $\mathcal{O}(\alpha^2\alpha_s)$. These corrections are missed so far and are needed for a full exploration of EWPOs, in particular for the determination of the ρ parameter and the muon decay Δr parameter. We also show that with present tools and methods, it is possible to calculate numerically with sufficient precision the most difficult vertex integrals in Minkowskian kinematics, required by future collider physics analysis and needed for the evaluation of three-loop SM corrections to the Z boson decays.

Streszczenie

Proponowane nowe zderzacze e^+e^- po erze LEP-u w ramach precyzyjnej fizyki wysokich energii dostarczą szeregu przełomowych pomiarów dla dużej liczby czułych na nową fizykę elektrosłabych pseudoobserwabli (EWPOs), gdzie spodziewana poprawa eksperymentalnej precyzji będzie od jednego do dwóch rzędów wielkości. Pełne wykorzystanie znacznie zwiększonej precyzji eksperymentalnej w obszarze rezonansu bozonu Z dla EWPOs (efektywne kąty słabego mieszania, całkowite i częściowe szerokości rozpadu bozonu Z, stosunki rozgałęzień i hadronowy przekrój czynny) będzie wymagać dokładności przewidywań Modelu Standardowego (SM) na poziomie odpowiadającym tej precyzji, w konsekwencji potrzebna będzie skokowa poprawa w precyzji obliczeń perturbacyjnych wyższych rzędów reprezentowanych przez wieloskalowe, wielopętlowe całki Feynmana. Omawiamy różne techniki stosowane do obliczeń tych całek, koncentrując się na reprezentacjach Mellina-Barnesa, rozkładzie sektorowym i równaniach różniczkowych. W tym zakresie opracowaliśmy programy pomocnicze i procedury automatyzujące obliczenia z wykorzystaniem rozkładu na sektory i metody równań różniczkowych. Metody te zostały następnie wykorzystane do obliczenia energii własnych bozonów W i Z oraz wierzchołka $W\bar{\ell}\nu_\ell$ w trzech pętlach dla Modelu Standardowego rzędu $\mathcal{O}(\alpha^2\alpha_s)$. Poprawki te są jak dotąd zaniedbywane, jednak są potrzebne do pełnej eksploracji dla EWPOs, w szczególności do określenia parametru ρ i parametru rozpadu mionu Δr. Pokazujemy również, że przy użyciu obecnych narzędzi i metod możliwe jest numeryczne obliczenie najtrudniejszych całek wierzchołkowych w kinematyce Minkowskiego, całek wymaganych w planowanych analizach fizyki zderzaczy i potrzebnych do wyznaczenia poprawek SM w trzech pętlach dla rozpadów bozonu Z.

List of papers

The thesis is based on

[PhD1] I. Dubovyk, A. Freitas, J. Gluza, K. Grzanka, M. Hidding, J. Usovitsch, Evaluation of multiloop multiscale Feynman integrals for precision physics, Phys. Rev. D 106 (11) (2022) L111301. arXiv:2201.02576, doi:10.1103/PhysRevD.106.L111301.

[PhD2] I. Dubovyk, J. Usovitsch, K. Grzanka, Toward Three-Loop Feynman Massive Diagram Calculations, Symmetry 13 (6) (2021) 975. doi:10.3390/sym13060975.

[PhD3] I. Dubovyk, A. Freitas, J. Gluza, K. Grzanka, T. Riemann, J. Usovitsch, Electroweak precision pseudo-observables at the e^+e^- Z-resonance peak, PoS ICHEP2020 (2021) 663. arXiv:2012.06598, doi:10.22323/1.390.0663.

[PhD4] I. Dubovyk, A. Freitas, J. Gluza, K. Grzanka, S. Jadach, T. Riemann, J. Usovitsch, Theory status of Z-boson physics (Chapter B), in: Mini Workshop on Precision EW and QCD Calculations for the FCC Studies : Methods and Techniques, Vol. 3/2019 of CERN Yellow Reports: Monographs, CERN, Geneva, 2018. arXiv:1809.01830, doi:10.23731/CYRM-2019-003.

Contents

1 Introduction

1.1 Importance of precision in the past

Increasing precision of measurements and theoretical calculations allows us to change paradigms and lead to discoveries of the fundamental laws of physics.

The first example comes with Tycho de Brahe's data, obtained with the naked eye, which was accurate down to the Moon's $1/30^{th}$ angular size [1]. The data gathered and preserved in the form of the Rudolphine tables led Johannes Kepler to derive laws of planetary motion, and later, Sir Isaac Newton deduced the law of gravity. So experimental data were instrumental in getting new concepts. Experimental data were also crucial for the interpretation of the Albert Michelson and Edward Morley study [2] in which it was established by precise measurements using an interferometer that the speed of light is constant, independent of the reference frame [3]. It is said to be the most famous failed experiment [4] whose aim was to validate the existence of *ether*. Whether this experimental result influenced or even was known to Einstein and triggered him towards the theory of special relativity is not clear [4]. The opposite happened in 1919 when the experimental results of eclipse measurements by Sir Arthur Eddington proved that the General Theory of Relativity was the right model. Speaking about huge steps in the history of physics, the accurate measurement of black-body radiation led Max Planck to introduce quantum fields.

Finally, from the 21^{st} century precision physics perspective, several breakthroughs should be noticed:

(i) **1998-2002.** Discovery of the neutrino masses by Super-Kamiokande and SNO Collaborations [5, 6].

(ii) **2012.** The Higgs boson discovery at the LHC [7–9].

(iii) **2016.** Detection of gravitational waves [10] where, putting it pictorially, precision is such that the shortening of the 4-kilometre interferometer arm reaches dimensions of single atoms [11].

(iv) **2018.** Watt balance measurement of the Planck constant and new quantum definition of the kilogram [12]. Now the Planck constant is defined as exact and kilogram is determined with 8-digit accuracy [13].

(v) **2020.** Low energy electromagnetic fine-structure constant measurement which, after 22 years of measurements, is $\alpha^{-1} = 137.035\ 999\ 139(31)$ (81 parts per

trillion) [14]. The experiment is still developing. To improve the accuracy of δa_e (electron anomalous magnetic moment) by an order of magnitude in the coming years, it will be at the sensitivity level of $(g-2)_\mu$ (muon anomalous magnetic moment). Measurement of $(g-2)_e$ or $(g-2)_\mu$ is a window into the exotic Beyond Standard Models (BSM) with light and weakly coupled particles, below the TeV scale, as estimated in [14] for compositeness models. The systems with muons can already be sensitive to the TeV BSM physics.

(vi) **2021.** 'Frequency Ratio Measurements with 18-digit Accuracy Using a Network of Optical Clocks' [15], which means that the present error of one-second measurement is at the scale of the age of the Universe (14 billion years is about $4 \cdot 10^{17}$ s). Such precision can have many consequences, e.g. for communication and navigation. Amazingly, it can help detect low-frequency gravitational waves by measuring Doppler effects from satellites sent to Uranus and Neptune [16].

In passing, two remarks are in order. The history and examples above show that theories can trigger breakthroughs in experiments and vice versa. Furthermore, let us also note that new steps in accurate measurements of physical units and observables were decisive in the past and will remain crucial for developments of new technologies (e.g. GPS and time measurement) and affect civilization progress, influencing trade, business, economy, law, social life and politics [17]. *Every leap in precision generally leads to new scientific and technological advances.* Needless to say, the high-energy particle physics studies also have socioeconomic impacts [18, 19].

This thesis is devoted to some aspects of theoretical precision studies required by accurate measurements at future colliders, aiming to discover new effects by finding new particles or interactions.

1.2 Importance of precision in particle physics

For a while, particle physics was a part of the quest for an understanding of atoms and nuclei and their quantum nature. After several decades, it emerged as a well-defined subfield of physics. The way from the beginnings of particle physics in the 1890s (Perrin - observation that cathode rays are the flow of negatively charged particles; Röntgen - discovery of X-rays; Becquerel - evidence for spontaneous radioactivity effect; Thomson - discovery of the electron, the first elementary particle) to the precise confirmation of the Standard Model in the 1990s (LEP and SLAC experiments) is a fantastic illustration of how science advances with new experimental tools and hard-won data, wrong

turns and conservative dogma transformed into brilliant insights.

From a perspective of precision experiments, maybe the first worth mentioning experimental result is by Frisch and Stern, who discovered in 1933 the anomalous magnetic moment of the proton [20]. Only after more than three decades this phenomenon could be explained by finding the short-distance structure of nucleons as quark and gluon partons by the MIT-SLAC experiments [21, 22], which fitted to already introduced at this time theoretical concepts. But the first real push in development of precision theoretical calculations which are the main interest of this thesis was triggered by the issue of infinities and radiative corrections in the 1930s which appeared in electromagnetic studies of the Dirac's hole theory and vacuum polarization (mostly self-energy (SE) problem and works by Jordan, Dirac, Heisenberg, Weisskopf, Furry and others [23]). Yet in 1946 the problem of (logarithmic type) infinities seemed to be not surpassable[1]. For the first time, the role of radiative corrections in precise measurements was evident in nonrelativistic calculation by Bethe of the self-energy of a bound electron [24]. The calculation agreed with the fine-structure measurement of hydrogen by Lamb and Retherford [25] (the $2s-2p$ shift in the hydrogen energy level). A breakthrough came during the Shelter Island and Pocono conferences in 1948 [23] and new calculations by Schwinger and ideas by Feynman (formalized by Dyson) for what we call now the calculation of Feynman diagrams and integrals.

The idea was systematically treated by Dyson in his two seminal papers [26, 27] followed by Feynman himself [28, 29] (that is why initially it was called the Feynman-Dyson approach to QED) [30]. Quantum electrodynamics was achieved as a renormalizable theory in which infinities were systematically treated. Feynman, Schwinger and Tomonaga shared the Nobel Prize in 1965 for "their fundamental work in quantum electrodynamics, with deep-ploughing consequences for the physics of elementary particles".

That quantum perturbative QED effects are significant was further confirmed with a determination of the magnetic moment of charged leptons $\vec{\mu} = g\frac{e}{2m}\vec{S}$, which, as predicted by the Dirac relativistic equation, gives the g-factor $g = 2$ while the measured value differed by a small amount ($a \equiv \frac{g-2}{2} = 0.00116$). Due to this deviation from the theoretical prediction by Dirac, from now on, we are talking about the anomalous magnetic moments of electrons and muons.

Due to the photonic quantum one-loop vertex correction, the anomalous magnetic

[1] As noticed in [23], the pessimistic point of view on the theory was reflected in Cambridge concerence talks titled "Problems of Elementary-Particle Physics" (Bohr), "Difficulties of Field Theories and of Field Quantization" (Pauli), "Difficulties in Quantum Electrodynamics" (Dirac).

moment of the electron is $g = 2(1 + \frac{\alpha}{2\pi})$ [31].

Till today, the anomalous magnetic moment of the muon (a_μ) is one of the best measured physical quantity, the present worldwide value is (average of FNAL and BNL results [32])

$$a_\mu(\text{EXP}) = 116\,592\,059(22) \times 10^{-11}\ (0.19\ \text{ppm}). \tag{1.1}$$

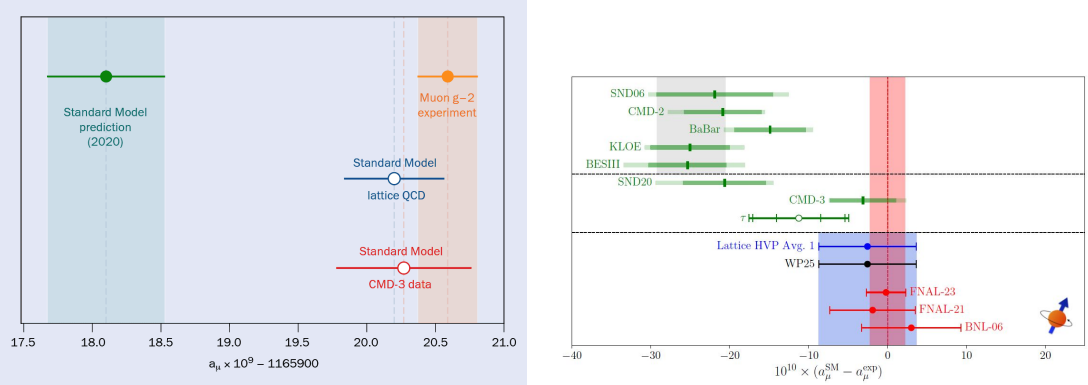

Figure 1: The Muon (g-2) theoretical predictions for the Standard Model and values from different experiments. Figures taken from [33] and [34], with copyright agreement from Alex Keshavarzi.

Until recently, theoretical prediction within the Standard Model differed from (1.1) and defined a longstanding problem [35]. The difference, $a_\mu(\text{EXP}) - a_\mu(\text{SM}) = (251 \pm 59) \times 10^{-11}$, had a significance of 4.2 σ, see Standard Model prediction (2020) in Fig. 1. This discrepancy could represent a potential hint of new physics in particle physics and it was calling for improving the theoretical prediction given planned further improvements for the Fermilab measurement [32]. Lately, there has been great progress in lattice QCD calculations, bringing the theoretical prediction, blue highlight in Fig. 1, into agreement with the experimental average marked with the red highlight on the right plot of Fig. 1.

While a_μ is sensitive to quantum corrections, it must be computed precisely, which is a highly nontrivial exercise [35]. The evaluation involves QED contributions, currently known up to $\mathcal{O}(\alpha^5)$, which corresponds to a precision of 0.001 ppm. Then there are electroweak contributions, currently known with an accuracy of 0.01 ppm. The dominant uncertainties originate from non-perturbative contributions, namely the hadronic vacuum polarisation and the hadronic light-by-light, with a precision of 0.34 ppm and 0.15 ppm, respectively.

Another important quantum effect in precision studies of particle physics, which finally took its place within SM, is due to Veltman [36] who found the quadratic mass effects of fermion doublets in the 1-loop electro-weak self-energy radiative corrections, for obvious reasons especially sensitive to the top quark mass, $\Delta\rho \sim M_t^2/M_W^2$, where $\Delta\rho$ is connected with W and Z boson self-energy corrections at zero momentum transfer as in (1.4), see also section 5.4. This effect, when confronted with other precise theoretical predictions for SM particles (notable gauge bosons), made it possible to indirectly determine the top quark mass at Tevatron (CDF and D0 collaborations) [37,38]. Milder, logarithmic in mass relation $\Delta\rho \sim \ln M_H^2/M_W^2$ was also identified by Veltman (the so-called screening effect) [39]). Beyond self-energy corrections, the first non-trivial study of electroweak (EW) loop effects was the calculation of the complete one-loop corrections to the Z decay parameters (vertex corrections) in [40–43]. Through the years of LEP and SLC studies, the effects of EW corrections became visible in global fits of the SM parameters [44–47]. Global fits to EW precision measurements allowed to predict the mass of the top quark and the Higgs boson prior to their discoveries at Tevatron in 1995 [38] and at the LHC in 2012 [7], leading to the upper limits on the Higgs boson mass.

Today, radiative corrections have become essential in precise renormalizable Standard Model tests. We will give now simple arguments for their necessity, see also section 2.3.

To show the importance of the radiative corrections, let us consider the following example of W and Z boson mass determination, discussion according to [48]. Expressions and notation below will appear in the next chapters (first, see section 2.2), though they represent the student's level of knowledge on particle physics, see e.g. [49].

The W and Z boson mass in terms of $\alpha(M_Z)$, G_μ and $\sin^2\theta_{\rm l,eff}$ are derived from

$$\sin^2\theta_W = 1 - M_W^2/M_Z^2, \qquad G_\mu = \frac{\pi\alpha}{\sqrt{2}\sin^2\theta_W M_W^2}(1+\Delta r) \tag{1.2}$$

$$\sin^2\theta_{\rm l,eff}(M_Z) = \left(1 + \frac{\cos^2\theta_W}{\sin^2\theta_W}\,\Delta\rho\right)\,\sin^2\theta_W, \tag{1.3}$$

$$\Delta\rho = \frac{\Sigma_T^{ZZ}(0)}{M_Z^2} - \frac{\Sigma_T^{WW}(0)}{M_W^2}\;; \quad \Delta\rho = \frac{3\,M_t^2\,\sqrt{2}G_\mu}{16\,\pi^2}\;; \quad M_t = 173 \pm 0.4\ \text{GeV}, \tag{1.4}$$

where $\Sigma_T^{WW(ZZ)}(0)$ denotes the transverse part of the $W(Z)$ boson self-energy defined in section 3.1.2, see also Appendix A.1. For basic definitions of the Weinberg angle θ_W, see discussion in section 2.3. The Fermi constant G_μ, Δr and $\Delta\rho$ are important parts of the muon decay parametrization. The iterative solution with experimental input

$\sin^2\theta_{\rm l,eff}(M_Z) \equiv (1 - v_l/a_l)/4 = 0.23148$ is

$$\sin^2\theta_W = 0.22426, \tag{1.5}$$

which results in W and Z boson masses

$$M_W^{\rm exp} = 80.379 \pm 0.012 \text{ GeV}, \tag{1.6}$$

$$M_Z^{\rm exp} = 91.1876 \pm 0.0021 \text{ GeV}, \tag{1.7}$$

$$1 - \frac{M_W^2}{M_Z^2} = 0.22263. \tag{1.8}$$

Using basic relations

$$M_W = \frac{A_0}{\sin^2\theta_W}\ ;\ \ A_0 = \sqrt{\frac{\pi\alpha}{\sqrt{2}G_\mu}}\ ;\ \ M_Z = \frac{M_W}{\cos\theta_W}, \tag{1.9}$$

and including photon vacuum polarization correction $\alpha^{-1}(M_Z) = 128.953 \pm 0.016$, for the W, Z mass we then get

$$M_W^{\rm the} = 81.1636 \pm 0.0346 \text{ GeV};\ \ M_Z^{\rm the} = 92.1484 \pm 0.0264 \text{ GeV}.$$

This means the deviation between the experimental and theoretical results for W and Z boson masses, while their errors are added in quadrature, is

$$W : 23\sigma \ \text{ and } \ \text{Z} : 36\sigma. \tag{1.10}$$

While the result is scheme dependent, this example very well illustrates the sensitivity of the observables to the radiative corrections and the need for the subleading SM corrections, including vertex and box diagrams in the first place, without which EWPOs would not fit experimental data, in general.

1.3 Needs for precision at future colliders: The Tera-Z case

With the discovery of the Higgs boson, the set of particles and interactions described by the SM of particle physics is complete. So far, we see no compelling deviations from this theory. Yet, the Higgs interactions are largely unknown or not precisely known. Additionally, several fundamental experimental facts remain completely unexplained, such as the matter-antimatter asymmetry, the evidence for dark matter, and the non-zero neutrino masses. Quite a few theoretical issues also point towards BSM physics. The list starts with gravity, which at the moment is outside of the SM – we have no theory of unification of all four basic interactions. Furthermore, we have no

understanding of the observed small neutrino masses, which may be described, but not explained by the so-called seesaw models. Further issues are the hierarchy problem (maybe explainable by a supersymmetric extension of the SM), parity restoration (maybe explainable by a so-called left-right symmetric extension of the SM), or the notion of extra space-time dimensions and supergravity. For a deepened understanding, we need a better experimental basis. Besides astrophysics with several recent publicly visible progresses, there are very good prospects coming from the planned new generation of particle accelerators.

The European particle physics community met in Granada, Spain in May 2019 for an open discussion on the roadmap for the future of the discipline. Though formal decisions by the CERN Council will only be taken after the next ESPPU symposium, which took place in Venice in June 2025 [50], a consensus is emerging that (see talks by F. Gianotti, M. Benedikt and others at [50])

- The next machine ought to be an e^+e^- collider;
- Europe should proceed with a flagship collider programme at CERN;
- A vigorous R&D programme must continue to pave the way towards the highest possible centre-of-mass energy with high luminosities.

Regarding the lepton colliders, a few plans are considered. First, there are circular e^+e^- colliders, LEP3 [51], FCC-ee [52], both planned location at CERN, and CEPC [53, 54] in China. Apart from that, two linear lepton colliders are also considered: Compact Linear Collider (CLIC) [55] and International Linear Collider (ILC) [56]. CLIC would be built at CERN near Geneva and could reach an energy of up to 3 TeV. ILC would operate in Japan with energies up to 1 TeV, though recently proponents of the linear collider option advocate for a linear collider at CERN, see talk by S. Stapnes [50]. The comparison of capabilities of the future lepton colliders is presented in Fig. 2. The colliders would work at a few stages with different energies corresponding to the masses of the desired particles. Integrated luminosity would depend strongly on energies and activity time, but generally, it will reach the level of ab^{-1}. Luminosity goals for future e^+e^- colliders are summarized in Fig. 3.

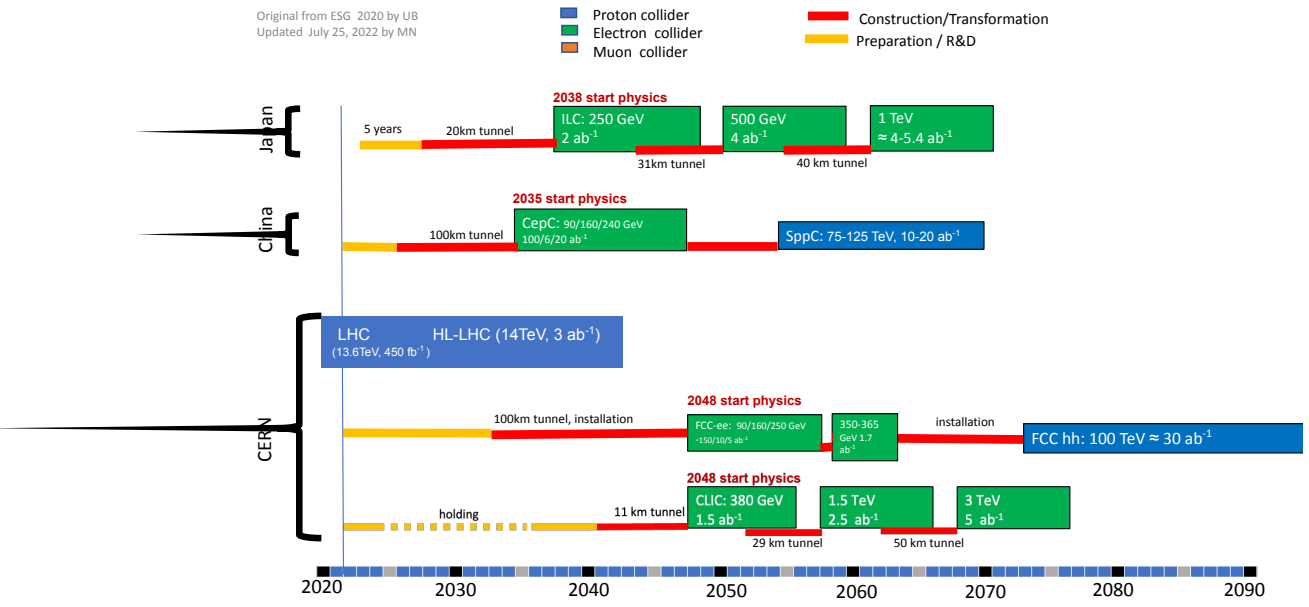

Figure 2: Summary of prospected timelines of the R&D and physics operations for the proposed future colliders. Taken from [57]. More options are discussed within the text.

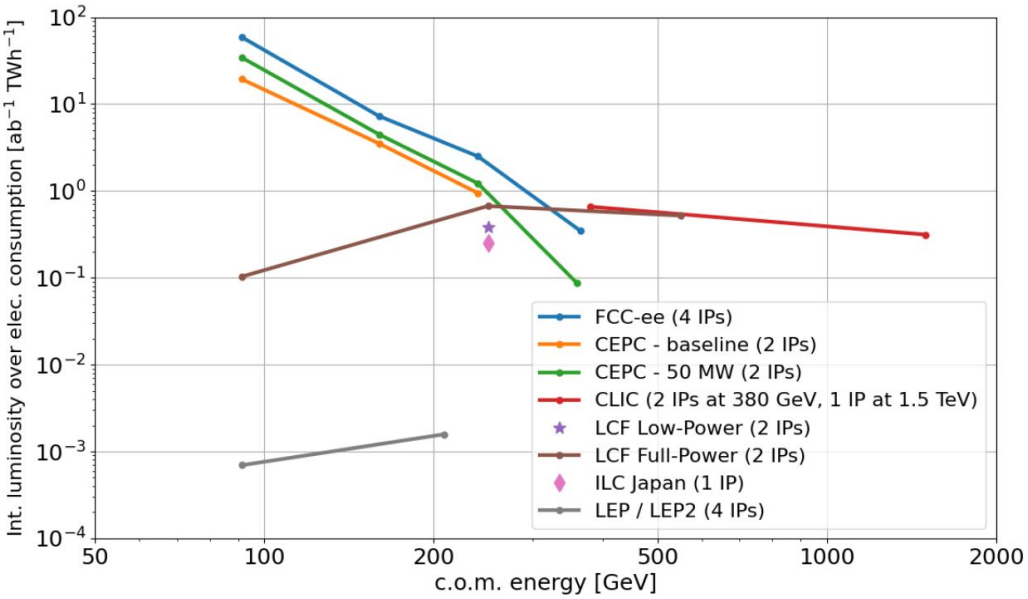

Figure 3: Expected luminosities at the future lepton colliders as a function of centre-of-mass energy $\sqrt{s}$. Plot taken from [58].

Matching the experimental precision with theoretical predictions is one of the prior-

ities for a CERN FCC-ee program, and this requirement has been listed as a strategic, high-priority item in the FCC-ee CDR [52]. The huge envisaged statistics of $5 \times \mathbf{10^{12}}$ Z decays at the **Tera-Z** FCC-ee stage - which is about 6 orders of magnitude better than in the wealthy LEP era - allows to study rare decays and processes with a precision which goes even beyond that considered in dedicated low-energy projects like B factories [59]. The broad potential FCC-ee physics programme is shown in Fig. 4. All the proposed future lepton colliders set stringent demands on the theory predictions. However, the FCC-ee project is the most ambitious, broad-reaching and demanding project for ground tests of the SM and for searches for feebly new effects in the Z resonance region [52, 60, 61].

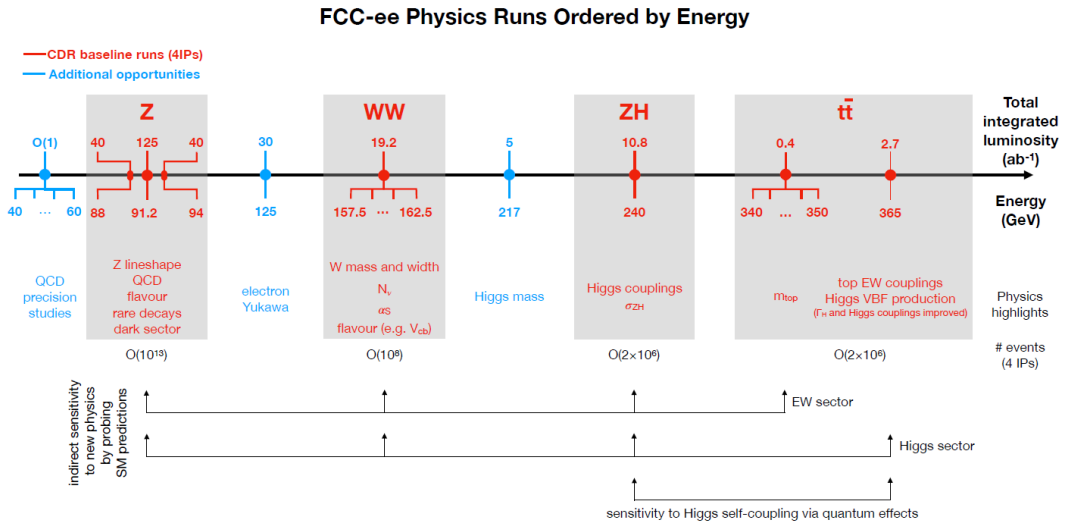

Figure 4: The outline of the potential physics programme for FCC in its e^+e^- stage. The sequence is ordered by increasing centre-of-mass energy, not chronologically. The parts marked with red belong to the minimal, 15-year running programme, whereas blue indicates other considered stages. Figure taken from [62].

Lepton-flavour violating (LFV) Z decays, rare and LFV τ decays, searches for heavy neutral leptons, and rare b-hadron decays have all been explored in [63] as benchmark or flagship searches, illustrative of the unique potential of a high-luminosity Z factory.

Observable	Theoretical error	EXP now	FCC-ee	CEPC	GigaZ
Γ_Z [MeV]	0.4	2.3	0.1	0.5	0.8
$\sin^2\theta^l_{\rm eff} \times 10^6$	43	160	6	23	10

Table 1: Two representative EWPOs, Z boson width Γ_Z and effective weak mixing angle $\sin^2\theta^l_{\rm eff}$. The prospective precision measurements at the future lepton colliders (statistical errors) are presented. The values of theoretical errors are taken from [64]. The entry "EXP now" gives the present experimental precision, as known since LEP-1 [45]. The CLIC project is omitted here because no Z resonance program is foreseen.

The present discrepancy between the foreseen experimental and the actual theoretical capabilities is a serious problem, because it is bigger than the accuracy of the planned experimental setups. The fact that theory is at the moment much behind the experimental expectations for the FCC-ee can be seen clearly from Tab. 1 where two representative Γ_Z and $\sin^2\theta^l_{\rm eff}$ electroweak pseudo-observables (EWPOs) are given. The estimated theoretical uncertainties from missing higher orders QCD and EW corrections in Tab. 1 have been discussed originally in [64]. The prospects of precision electroweak measurements at the FCC-ee are at the level of 100 keV for both the Z boson mass and width, and 6×10^{-6} for $sin^2\theta^l_{\rm eff}$. These are some flagship SM observables, sensitive also to the BSM physics. The Z boson decay width was calculated for LEP within the SM with 0.5 MeV accuracy. This was good enough because the final LEP experimental precision was 2.3 MeV. Compared to that, the FCC-ee project demands that the theoretical accuracy be five times better, namely 0.1 MeV. At the FCC Week 2018, it was announced that Γ_Z can be measured even with four times better accuracy, namely 0.025 MeV = 25 keV. So, on the experimental side, the expectations can still get even sharper. To be able to fully leverage the potential of such an intensity frontier lepton collider, a leap-jump in the precision and accuracy of theoretical computations in the Standard Model is indispensable.

The theoretical calculations in the thesis are intended to bring us closer to satisfying the experimental requirements, in particular for the Tera-Z physics.

At LEP, it was a standard analysis procedure that QED effects were extracted such that only the first and higher-order EW effects remained in the electroweak pseudo-observables [65]. The next mandatory corrections needed for EWPOs at FCC-ee are given in Tab. 2. Into the list of EWPOs go partial decay widths and coupling constants of Z boson and W boson, forward-backward and polarization asymmetries, peak cross

Observable	$\alpha\alpha_s^2$	$\alpha\alpha_s^3$	$\alpha^2\alpha_s$	α^3	Total
$\Gamma_{e,\mu,\tau}$ [MeV]	0.008	0.001	0.010	0.013	0.018
Γ_{ν} [MeV]	0.008	0.001	0.008	0.011	0.016
$\Gamma_{u,c}$ [MeV]	0.025	0.004	0.08	0.07	0.11
$\Gamma_{d,s}$ [MeV]	0.016	0.003	0.06	0.05	0.08
Γ_{b} [MeV]	0.11	0.02	0.13	0.06	0.18
Γ_{Z} [MeV]	0.23	0.035	0.21	0.20	0.4
R_{ℓ} [10^{-3}]	2.5	0.4	3.6	3.9	6
R_{c} [10^{-5}]	1.6	0.3	3.4	3.0	5
R_{b} [10^{-5}]	5.5	0.9	6.4	3.7	10
σ^0_{had} [pb]	0.2	0.03	4.2	3.7	6
$\sin^2\theta^l_{\text{eff}}$ [10^{-5}]	—	0.3	3.0	3.1	4.3
$\sin^2\theta^b_{\text{eff}}$ [10^{-5}]	0.7	0.4	4.3	3.2	5.3

Table 2: Estimated values of the leading unknown higher-order corrections for various EWPOs. Table taken from [64].

sections at the Z resonance position, effective electroweak mixing angles [45], and additional EWPOs in the WW, ZH and $t\bar{t}$ production processes. As EWPOs encapsulate experimental data after the extraction of intricate QED and QCD effects, they provide a convenient bridge between real data and the theoretical predictions of the Standard Model and beyond. This is why EWPOs were and remain key objects in precision tests of the SM, in a quest for unveiling new physics phenomena in particle physics.

One of the main aims of the thesis is the calculation of the $\mathcal{O}(\alpha^2\alpha_s)$ order contributions needed for the muon Δr parameter (G_μ/M_W) and Z decay EWPOs observables. As you can see from the Tab. 2, this contribution for many observables is the biggest of the unknown, and certainly simpler than the α^3 corrections (pure EW). Physically, $\mathcal{O}(\alpha^2\alpha_s)$ accounts for the 3-loop mixed QCD-EW contributions with one gluon and massive SM particles: EW bosons and top quark (remaining quarks and leptons are treated as massless).

As one can see in Tab. 1, the estimated present-day theory errors for unknown higher-order corrections for future colliders, apart from FCC-ee, are already at the

level of the experimental expectations. However, also here, the situation is not too comfortable because the theoretical uncertainties can differ substantially from these educated guesses after real calculations are completed. As rough estimates, educated guesses are no robust quantitative predictions, and must be treated with a grain of salt. For instance, after completion of the two-loop SM corrections to Γ_Z in [66], it turned out that the bosonic 2-loop SM corrections are 3 to 5 times larger (depending on the renormalization scheme and on input parameters) than expected before. To be on the safe side, certainly also for ILC/GigaZ and CEPC, there is a need for more precise theoretical calculations, probably by a factor of 3 to 5.

Today's state-of-the-art accuracy is at the accuracy level of complete electroweak two-loop corrections, and the needs of a future collider are at the next order, three-loop level. The difference in numbers in Tab. 1 seems to be harmless, but in fact, lowering theoretical uncertainties from 0.4 MeV to 0.1 MeV for Γ_Z, for instance, makes us explore a different world. To get this level of accuracy, not only do we have to perform higher-order loop calculations – for EWPOs at the Z resonance, we have to go to the 3-loop electroweak and 4-loop QCD levels – but also we have to understand several unexplored issues connected with Z boson resonance physics and with the interplay of QED/QCD effects. Both for the correct Laurent series expansion around the Z-peak with background resonances and for the QED deconvolution (see section 2.3), much more refined conceptual work must be done. Moreover, the determination of input parameters like running QED and QCD coupling constants must improve considerably [48, 67, 68]. Still, there are also some remaining calculations which should be done at the 2-loop level. For instance, apart from computing all the higher-order QCD and EW corrections included for the Z boson in [64], also calculations of the same order are needed for the W boson case.

The very broad program of the FCC will improve the precision of the SM parameters' determination significantly. The example of error shrinking can be seen in Fig 5, taken from [69]. The improvements for EWPOs are typically at the level of one or two orders of magnitude [70]. This allows for very precise tests of SM and studies of indirect BSM effects in various SM extensions or effective theories [64, 71].

One of the crucial measurements for the FCC-ee project with centre-of-mass energy $\sqrt{s} = 125$ GeV, showing the ultimate sensitivity of the project, is a measurement of the Higgs boson coupling modifier to electrons κ_e, see Fig. 6. Its value is predicted by the Higgs mechanism to be smaller than the Higgs boson to muon coupling by a factor of the electron to muon mass ratio.

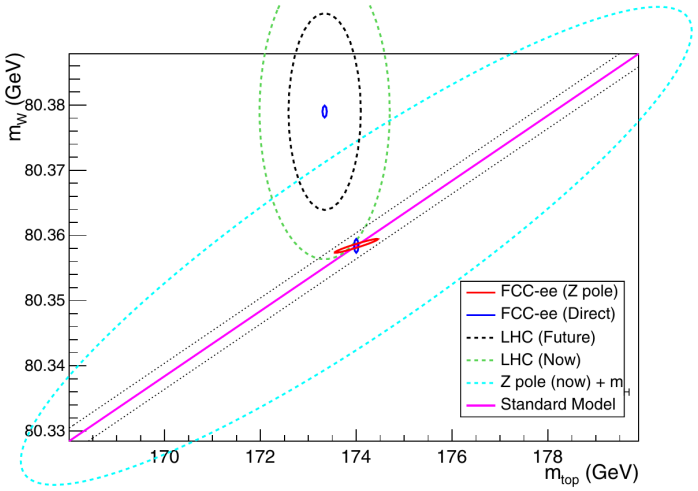

Figure 5: A 1-σ confidence level contours of the SM fits to the electroweak precision measurements, the FCC-ee in comparison to direct measurements of M_W and M_t. Plot taken from [69].

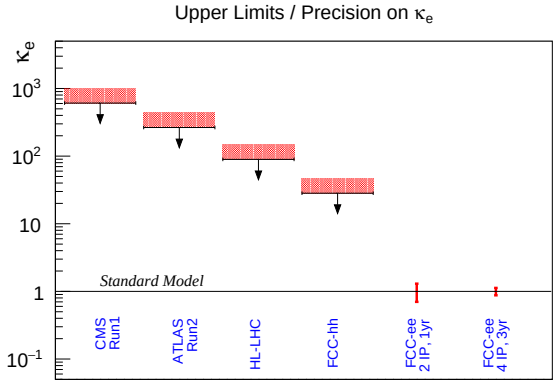

Figure 6: Current and future LHC and FCC experimental precision of the Higgs boson coupling modifier to electrons κ_e demonstrates how much the precision of $H - e^+ - e^-$ coupling will improve. Plot taken from [72].

There are also other projects beyond e^+e^- of future colliders, such as the muon collider (see a talk by D. Schulte at [50]), photon collider [73] or very promising for the extremely high energies - Wakefield plasma colliders [74]. All of these machines can lead to direct or indirect signals of BSM physics, and both cases rely heavily on the precision of SM calculations and predictions, the subject of the thesis.

2 The Standard Model and electroweak observables

The Standard Model (SM) of elementary particles is a fundamental theory in particle physics. It comprises three of the four fundamental forces, i.e. electromagnetic, weak and strong interactions; only gravity cannot yet be included in the model. It is based on the $SU(3)\times SU(2)\times U(1)$ gauge group, where $SU(3)$ represents the strong interactions, whereas $SU(2)\times U(1)$ corresponds to the unified electromagnetic and weak interactions, so-called electroweak (EW) interactions. The unification of these two basic forces was proposed in the 1960s, and it is largely attributed to Sheldon Glashow, Abdus Salam, and Steven Weinberg, for which they received the Nobel Prize in 1979 [75–78]. The Standard Model formulation was completed in the 1970s by the description of the strong forces within so-called Quantum Chromodynamics (QCD) [79–81].

Besides the interactions, SM also categorises and describes elementary particles, the basic building blocks of matter and the force carriers mediating the interactions. Historically, the development of the SM started with the discovery of the electron by J.J. Thomson in 1897 and still continues, with the latest elementary particle discovery of the Higgs boson in 2012, which was the final missing piece confirming the mechanism through which particles acquire mass. The discovery was a result of the comparison of the very precise SM predictions and experimental data gathered within the Large Hadron Collider detectors ATLAS and CMS [82, 83].

The Standard Model is a framework that allows us to predict and precisely describe phenomena observed in all known experiments. Yet, with all its success, SM is not a complete theory. It leaves some unexplained phenomena; therefore, many theoretical and experimental groups conduct searches for the so-called New Physics, i.e. physics beyond the description of the SM. Some of the phenomena beyond the description of SM are listed below, starting with six selected in [62], followed by questions of my choice.

- What is the origin of the Higgs boson?
- What is the origin of the presence of matter in the Universe?
- What is the origin of mass and flavour?
- What is the nature of dark matter?
- What lies beyond the Standard Model?
- Why is the electroweak interaction so much stronger than gravity?

- Are there charge-parity violating Higgs decays?
- Are there multiple Higgs sectors?
- What is the origin of the early Universe inflation?

Further, we summarise the SM, which will be followed by the basic ingredients and formalism needed to make precision tests of the model, i.e. we will describe radiative corrections and calculational background.

2.1 SM particles and interactions

The fundamental constituents of matter are fermions of spin 1/2, i.e. leptons and quarks. Whereas the SM interactions are mediated by gauge bosons of spin 1. Let us focus on some basic properties of these particles.

There are three (known) families/generations of leptons and quarks, each of them characterised by quantum numbers. For each of them, an antiparticle of the opposite inner quantum number and the same mass exists.

Leptons are fundamental particles that do not interact strongly; each of their three families consists of a pair of charged and neutral particles, which are characterised by a conserved quantum number, so-called lepton number. The three generations are (ν_e, e), (ν_μ, μ), (ν_τ, τ), electron, muon and tau with corresponding electron, muon and tau neutrinos, characterized by electron number $L_e = 1$, muon number $L_\mu = 1$, tau number $L_\tau = 1$, respectively. All leptons interact weakly, and the charged ones also interact electromagnetically.

The main difference between quarks and leptons is that they also interact strongly. We have not observed quarks as free particles; they are constituents of the so-called hadrons, for example, the proton and neutron of atomic nuclei. The quantum numbers characterising hadrons are the flavour quantum numbers - their isospin, strangeness, charm, bottomness, topness, and they all carry a baryon number of 1/3. The first generation of quarks consists of up and down (u, d) pair, the second of charm and strange (c, s) and the third, top-bottom doublet (t, b). Their electric charge determines the electromagnetic interaction couplings, whereas the doublet structure is important for the weak interactions. The strong interactions are described by QCD. For this, we need to mention another quantity, the colour quantum number, which has three possible values: red, green and blue (r, g, b). Each of the quarks exists in each of the three colours. The colour state of quarks cannot be observed directly, as all hadrons - the physical, directly observed particles - are all colourless bound states of quarks.

The gauge bosons are responsible for the interactions between the particles. For the electromagnetic interactions, there is a massless photon, weak interactions are mediated by the heavy neutral Z boson and charged $W^{\pm}$ bosons, and gluons are responsible for the strong interactions.

All fields and interactions of the SM are described via its Lagrangian. It can be divided into three individually gauge-invariant parts

$$\mathcal{L}_{SM} = \mathcal{L}_{Gauge} + \mathcal{L}_S + \mathcal{L}_F. \tag{2.1}$$

The gauge part reads

$$\mathcal{L}_{Gauge} = -\frac{1}{4}\left(G^i_{\mu\nu}G^{\mu\nu i} + W^a_{\mu\nu}W^{\mu\nu a} + B_{\mu\nu}B^{\mu\nu}\right), \tag{2.2}$$

The field strength tensors are the following

$$SU(3) \ : \quad G^i_{\mu\nu} = \partial_\mu G^i_\nu - \partial_\nu G^i_\mu + g_s f^{ijk} G^j_\mu G^k_\nu \tag{2.3}$$

$$SU(2) \ : \quad W^a_{\mu\nu} = \partial_\mu W^a_\nu - \partial_\nu W^a_\mu + g\varepsilon^{abc} W^b_\mu W^c_\nu \tag{2.4}$$

$$U(1) \ : \quad B_{\mu\nu} = \partial_\mu B_\nu - \partial_\mu B_\nu, \tag{2.5}$$

where f^{ijk} and ε^{abc} are the complex 3×3 matrices of Yukawa couplings of gauge groups $SU(3)$ and $SU(2)$ respectively.

Let us first focus on the electroweak part of the SM. The following relation between the hypercharge Y_W, third component of the weak-isospin T_3, and electric charge Q has to be fulfilled to ensure that U(1) stays unbroken after the electroweak symmetry breaking (EWSB)

$$Q = T_3 + \frac{Y_W}{2} \tag{2.6}$$

and $T_3 = \sigma_3/2$, where σ_3 is the Pauli matrix. The total and third component of the isospin, as well as the electric charge for all SM particles, are summarised in Tab. 3.

The next part $\mathcal{L}_S$ of the full SM Lagrangian describes the Higgs sector with a complex scalar-doublet Φ that has a non-vanishing vacuum expectation value (VEV), the doublet takes the form

$$\Phi(x) = \frac{1}{\sqrt{2}}\begin{pmatrix}\phi_3 + i\phi_4 \\ \phi_1 + i\phi_2\end{pmatrix} \equiv \begin{pmatrix}\phi^+(x) \\ \phi^0(x)\end{pmatrix}. \tag{2.7}$$

The first component of the scalar is charged and the other is neutral, by demanding Y_W to be 1

	Particles			T	T_3	Q
Leptons	$\begin{pmatrix} \nu_{\mathrm{e}} \\ \mathrm{e} \end{pmatrix}_L$	$\begin{pmatrix} \nu_{\mu} \\ \mu \end{pmatrix}_L$	$\begin{pmatrix} \nu_{\tau} \\ \tau \end{pmatrix}_L$	$1/2$	$+1/2$	0
					$-1/2$	-1
	$\nu_{\mathrm{e}R}$	$\nu_{\mu R}$	$\nu_{\tau R}$	0	0	0
	e_R	μ_R	τ_R	0	0	-1
Quarks	$\begin{pmatrix} \mathrm{u} \\ \mathrm{d} \end{pmatrix}_L$	$\begin{pmatrix} \mathrm{c} \\ \mathrm{s} \end{pmatrix}_L$	$\begin{pmatrix} \mathrm{t} \\ \mathrm{b} \end{pmatrix}_L$	$1/2$	$+1/2$	$+2/3$
					$-1/2$	$-1/3$
	u_R	c_R	t_R	0	0	$+2/3$
	d_R	s_R	b_R	0	0	$-1/3$
Bosons	$W^{\pm}$			1	±1	±1
	Z^0, γ^0, g			0	0	0
	H^0			$\frac{1}{2}$	$-\frac{1}{2}$	0

Table 3: The weak-isospin structure of the particles in the SM. L and R stand for left-handed and right-handed fermions, T and T_3 are the total weak-isospin and its third component, and Q is the electric charge.

$$Q\Phi(x) = \left(T_3 + \frac{Y_W}{2}\right)\Phi(x) = \begin{pmatrix} 1 & 0 \\ 0 & 0 \end{pmatrix}\Phi(x), \tag{2.8}$$

The interaction of the Higgs doublet with the gauge fields is through the covariant derivative and the corresponding Lagrangian reads

$$\mathcal{L}_S = (D_\mu\Phi)^\dagger(D^\mu\Phi) - V(\Phi, \Phi^\dagger), \tag{2.9}$$

where the potential V is

$$V(\Phi, \Phi^\dagger) = -\mu^2\Phi^\dagger\Phi + \frac{\lambda^2}{4}(\Phi^\dagger\Phi)^2 \tag{2.10}$$

which remains non-zero after the EWSB.

By the requirement of the left-handed fermions forming a $SU(2)$ doublet and right-handed fermions forming singlets, we construct the parity-violating interaction between gauge and matter fields

$$L_j^L = \omega_- L_j = \begin{pmatrix} l_j^L \\ \nu_j^L \end{pmatrix}, \quad Q_j^L = \omega_- Q_j = \begin{pmatrix} u_j^L \\ d_j^L \end{pmatrix} \tag{2.11}$$

$$l_j^R = \omega_+ l_j, \quad u_j^R = \omega_+ u_j, \quad d_j^R = \omega_+ d_j, \tag{2.12}$$

where $\omega_\pm = \frac{1\pm\gamma_5}{2}$ are the projectors and j index indicates the lepton and quark family. The right-handed neutrinos could easily be added in (2.12), yet neutrinos are treated as massless, as their contributions are negligible in the SM calculations. The last part of the SM Lagrangian $\mathcal{L}_F$ can be written as

$$\begin{aligned} \mathcal{L}_F &= \sum_i \left(i\overline{L}_i^L \not{D} L_i^L \right) + \sum_i \left(i\overline{l}_i^R \not{D} l_i^R + \overline{u}_i^R \not{D} u_i^R + i\overline{d}_i^R \not{D} d_i^R \right) - & (2.13) \\ & \sum_i \left(\overline{L}_i^L Y_{ij}^l l_j^R \Phi + \overline{Q}_i^L Y_{ij}^u u_j^R \tilde{\Phi} + \overline{Q}_i^L Y_{ij}^d d_j^R \Phi + h.c. \right), & (2.14) \end{aligned}$$

where $Y_{ij}^{l,u,d}$ are the Yukawa coupling matrices corresponding to fermion masses and $\tilde{\Phi}$ is a charge conjugated scalar field

$$\tilde{\Phi} = i\tau^2 \Phi^* = (\phi^{0*}(x), -\phi^-)^T. \tag{2.15}$$

Let us now focus on the strong, interactions described by the first term in (2.2). Collecting all terms connected with QCD, we can write the corresponding Lagrangian

$$-\frac{1}{4} G_{\mu\nu}^i G^{\mu\nu i} + \sum_{flavours} \overline{q}_i (i\not{D} - m)_{ij} q_j, \tag{2.16}$$

with the covariant derivative defined as in (2.17).

$$(D_\mu)_{ij} = \partial_\mu \delta_{ij} + i g_s \left(T^k A_\mu^k \right)_{ij} \tag{2.17}$$

The covariant derivative for QCD also includes colour and couples quarks and gluons. Similarly, we also need to introduce the covariant derivative for electroweak interactions as in (2.18)

$$D_\mu = \partial_\mu - i g T_a W_\mu^a + i g' \frac{Y_W}{2} B_\mu, \tag{2.18}$$

where g' is the U(1) coupling constant.

Colour is an internal degree of freedom of particles, we expect that the theory is invariant under rotations in this colour space. The colour charge of a gluon is

represented by a matrix in the colour space. These 8 matrices T^i, $i = 1, \ldots, 8$ can be related to Hermitian Gell-Mann matrices λ^i, the extension of Pauli matrices [84].

$$T^i = \frac{1}{2}\lambda^i \tag{2.19}$$

The following relations are fulfilled

$$\mathrm{Tr}(\lambda^i \lambda^j) = 2\delta^{ij}, \qquad [\lambda^i, \lambda^j] = 2if^{ijk}\lambda^k. \tag{2.20}$$

Translating back to the colour matrices

$$[T^i, T^j] = if^{ijk}T^k, \qquad \mathrm{Tr}(T^i T^j) = T_R\delta^{ij}, \tag{2.21}$$

where $T_R = 1/2$. Matrices T^i are the generators of the SU(3) group, and the antisymmetric f^{ijk} contains the SU(3) structure constants. The group structure is characterized by

$$\sum_{k,l} f^{ikl} f^{jkl} = C_A\delta^{ij}, \qquad \sum_i T^i T^i = C_F\mathbf{1}, \tag{2.22}$$

where $C_A = N_c = 3$ and $C_F = \frac{N_c^2-1}{2N_c} = \frac{4}{3}$. N_c is a number of colours and $C_{A,F}$ are Casimir operators and $\mathbf{1}$ is the identity matrix. We use these relations directly in chapter 5.

In the SM, the transitions between different quark flavours are parametrized by the unitary Cabibbo-Kobayashi-Masakawa (CKM) matrix V. The four mixing parameters left after the quark field redefinition are contained in the matrix which relates quark weak and mass eigenstates. There are different parametrisations of the CKM matrix, for instance

$$V = \begin{pmatrix} V_{ud} & V_{us} & V_{ub} \\ V_{cd} & V_{cs} & V_{cb} \\ V_{td} & V_{ts} & V_{tb} \end{pmatrix} = \begin{pmatrix} c_{12}c_{13} & s_{12}c_{13} & s_{13}e^{-i\delta} \\ -s_{12}c_{23} - c_{12}s_{23}s_{13}e^{i\delta} & c_{12}c_{23} - s_{12}s_{23}s_{13}e^{i\delta} & s_{23}c_{13} \\ s_{12}s_{23} - c_{12}c_{23}s_{13}e^{i\delta} & -c_{12}s_{23} - s_{12}c_{23}s_{13}e^{i\delta} & c_{23}c_{13} \end{pmatrix}, \tag{2.23}$$

where $s_{ij} = \sin\theta_{ij}$, $c_{ij} = \cos\theta_{ij}$, the angles θ_{ij} are the mixing angles between quark generations and δ is the CP-violating phase.

2.2 Muon decay and Δr

The relation between the masses of gauge bosons M_W and M_Z, the Fermi constant G_μ and the fine structure constant α is one of the most important quantities while testing the SM and its extensions. This relation can be derived from the muon decay as the Fermi constant enters the expression for the muon lifetime τ_μ [85–90]

$$\tau_\mu^{-1} = \frac{G_\mu^2 m_\mu^5}{192\pi^3} F\left(\frac{m_e^2}{m_\mu^2}\right)(1+\Delta q), \tag{2.24}$$

where $F(x) = 1 - 8x - 12x^2 ln(x) + 8x^3 - x^4$ is the kinematic factor coming from the phace space integration and $\Delta q = \frac{\alpha}{2\pi}(\frac{25}{4} - \pi^2)$ is a QED correction within the Fermi model, m_e and m_μ are electron and muon masses, respectively. To account for the SM corrections, we start from the effective matching between the Fermi and the SM theory, namely, the effective interaction amplitude in the Fermi model reads

$$\mathcal{M}^{Fermi}_{(\mu\to e\nu_e\nu_\mu)} = \frac{G_\mu}{\sqrt{2}}\left[\bar{u}_{\nu_\mu}\gamma^\sigma(1-\gamma^5)u_\mu\right]\left[\bar{u}_e\gamma_\sigma(1-\gamma^5)u_{\nu_e}\right], \tag{2.25}$$

while the SM amplitude for the muon decay is

$$\mathcal{M}^{SM}_{(\mu\to e\nu_e\nu_\mu)} = \left[\frac{g}{\sqrt{2}}\bar{u}_{\nu_\mu}\gamma^\sigma\frac{1}{2}(1-\gamma^5)u_\mu\right]\frac{1}{M_W^2 - p^2}\left[\frac{g}{\sqrt{2}}\bar{u}_e\gamma_\sigma\frac{1}{2}(1-\gamma^5)u_{\nu_e}\right], \tag{2.26}$$

where $g/\sqrt{2}$ is a weak coupling and p is W boson four momentum. By comparison, taking the case of the muon decay $p^2 \ll M_W^2$, we get a relation

$$\frac{G_\mu}{\sqrt{2}} = \frac{g^2}{8M_W^2}. \tag{2.27}$$

Let us recall that

$$\frac{g^2}{8} = \frac{\pi\alpha}{2\sin^2\theta_W} \qquad \text{and} \qquad \sin^2\theta_W = s_W^2 = 1 - \frac{M_W^2}{M_Z^2}. \tag{2.28}$$

Putting all of this together, we get

$$M_W^2\left(1 - \frac{M_W^2}{M_Z^2}\right) = \frac{\pi\alpha}{\sqrt{2}G_\mu}(1+\Delta r) \tag{2.29}$$

where $\Delta r = \Delta r(\alpha, G_F, M_W, M_Z, M_H; m_f)$ collects in addition symbolically all possible SM radiative corrections. Over the years, a great effort has been devoted to computations at various orders in both the EW theory [91–96] and QCD [97–101]. Currently, the full two-loop contributions are known [102–117] as well as partial three-loop and four-loop results [118–123].

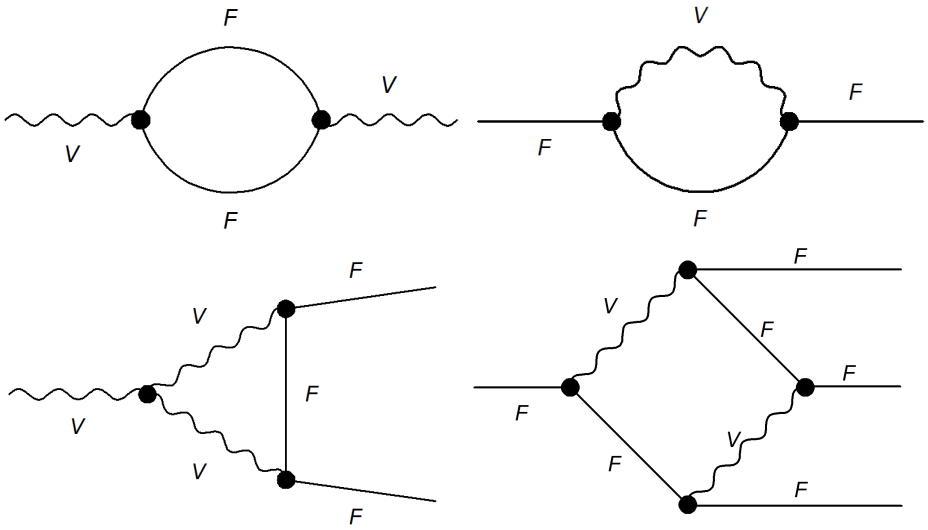

Figure 7: Types of Feynman diagrams contributing to Δr at the one-loop level, **V** denotes the vector boson and **F** are fermions. From top-left to bottom-right, there are vector boson SE, fermions SE, vertex and box diagrams.

At the one-loop order, the Fermi constant matched with the SM corrections can be written as [88–90]

$$\begin{aligned} G_\mu &= \frac{\pi\alpha}{\sqrt{2}s_W^2 M_W^2}\left(1+2\frac{\delta e}{e}-\frac{\delta s_W^2}{s_W^2}-\frac{\delta M_W^2}{M_W^2}+\frac{\Sigma_T^{WW}(0)}{M_W^2}+\delta_{vert+box}\right) \\ &= \frac{\pi\alpha}{\sqrt{2}s_W^2 M_W^2}(1+\Delta r), \end{aligned} \tag{2.30}$$

where $\Sigma_T^{WW}(0)$ denotes the transverse part of the W boson self-energy. Δr is a finite combination of one-loop diagrams and counterterms; the same concept follows for higher loop orders. The contributing types of Feynman diagrams that need to be included are presented in Fig. 7.

The $\delta_{vert+box}$ contribution contains corrections coming from vertex and box diagrams and is given by [89]

$$\delta_{vert+box} = \frac{\alpha}{\pi s_W^2}\left(\Delta - \log\frac{M_W^2}{\mu^2}\right) + \frac{\alpha}{4\pi s_W^2}\left(6+\frac{7-4s_W^2}{2s_W^2}\log\frac{M_W^2}{M_Z^2}\right), \tag{2.31}$$

where

$$\Delta = \varepsilon^{-1} - \gamma\log(4\pi), \tag{2.32}$$

ε is a dimensional regularization parameter and γ is the Euler constant.

The first term in (2.31), which is a UV-divergent part can be expressed in terms of the transverse part of photon and Z boson mixing $\Sigma_T^{AZ}(p^2)$ at $p^2 = 0$ which is also a wave renormalization constant δZ_{ZA} as described later in section 3.2

$$\frac{\alpha}{\pi s_W^2}\left(\Delta - \log\frac{M_W^2}{\mu^2}\right) = \frac{2}{s_W c_W}\frac{\Sigma_T^{AZ}(0)}{M_Z^2}. \tag{2.33}$$

Finally at the one-loop level in the on-shell scheme the Δr result is [88, 90–93]

$$\begin{aligned}\Delta r = \quad & \Pi^{AA}(0) + \frac{\Sigma_T^{WW}(0) - \mathrm{Re}\left(\Sigma_T^{WW}(M_W^2)\right)}{M_W^2} \\ & -\frac{c_W^2}{s_W^2}\mathrm{Re}\left(\frac{\Sigma_T^{ZZ}(M_Z^2)}{M_Z^2} - \frac{\Sigma_T^{WW}(M_W^2)}{M_W^2}\right) \\ & +2\frac{c_W}{s_W}\frac{\Sigma_T^{AZ}(0)}{M_Z^2} + \frac{\alpha}{4\pi s_W^2}\left(6 + \frac{7-4s_W^2}{2s_W^2}\log\frac{M_W^2}{M_Z^2}\right)\end{aligned} \tag{2.34}$$

The first term $\Pi^{AA}(0)$, which is a derivative of the photon self-energy at $p^2 = 0$, is a bit tricky, it follows from

$$\Pi^{AA}(p^2) = \frac{\Sigma_T^{AA}(p^2)}{p^2}. \tag{2.35}$$

Treatment of these derivatives is automated in our in-house methods (see next chapters). Traditionally, it is divided into three parts: one with light fermions, one with the top quark, which is the only fermion whose mass is considered non-zero in our calculations, and the bosonic part

$$\Pi^{AA}(0) = \Pi^{AA}_{light}(0) + \Pi^{AA}_{top}(0) + \Pi^{AA}_{bos}(0). \tag{2.36}$$

The light fermion contribution can be calculated as

$$\Pi^{AA}_{light}(0) = -\Re\,\Pi^{AA}_{light}(M_Z^2) + \Pi^{AA}_{light}(0) + \Re\,\Pi^{AA}_{light}(M_Z^2) \tag{2.37}$$

$$= -\Re\,\hat{\Pi}^{AA}_{light}(M_Z^2) + \Re\,\Pi^{AA}_{light}(M_Z^2). \tag{2.38}$$

The $\Re\,\hat{\Pi}^{AA}_{light}(M_Z^2)$ term is a renormalized vacuum polarization corresponding to the electromagnetic coupling

$$\alpha(M_Z^2) = \alpha(1 + \Delta\alpha) + \mathcal{O}(\alpha^3), \qquad \Delta\alpha = -\Re\,\hat{\Pi}^{AA}_{light}(M_Z^2). \tag{2.39}$$

As already mentioned, the top quark mass is not neglected in our calculations, and due to the QCD effects, it can be evaluated directly (see section 3.3.1)

$$\Pi^{AA}_{top}(0) = \frac{\alpha}{\pi}(D-2)\frac{\mathrm{A}_0(M_t)}{9M_t^2}. \tag{2.40}$$

The calculation described in the thesis aims to add another three-loop contribution to the list, namely $\mathcal{O}(\alpha^2\alpha_s)$. For the precision needed at the future colliders at least all three-loop terms should be computed and accounted, see discussion around Tab. 2 and [PhD4] in List of papers. Currently, the missing higher-order contributions lead to a theoretical uncertainty $\delta M_W = 4$ MeV using the on-shell renormalization scheme [124]. A 1σ variation of all the input parameters to Δr leads to the parametric uncertainty $\delta M_W = 5$ MeV while the predicted experimental accuracy for the W boson mass at the FCC is estimated to be of the order 0.5 MeV [60, 61].

For the three-loop calculations of the muon decay of the order $\mathcal{O}(\alpha^2\alpha_s)$, one needs to determine the W and Z boson self-energy and $W\bar{l}\nu$ vertex contributions, so we will discuss Feynman diagrams with one gluon in loops or one-loop top quark counterterm insertion (both proportional to α_s). Details of the calculations at the three-loop level can be found in chapter 5.

2.3 Z boson decay and EWPOs

Apart from the muon decay, which is relevant for precision EWPOs studies, the second important information about the Standard Model comes from the observables connected with Z-pole physics, [PhD1,PhD3,PhD4] in List of papers.

Data collected by the LEP experiment enabled the accurate determination of numerous electroweak observables by measuring the Z boson line-shape and of the cross section asymmetries along with high-precision parity-violating asymmetries at the SLC [45].

To determine the Z boson properties, measurements of fermion pair production in electron-positron collisions were conducted at the Z boson pole, i.e., for $\sqrt{s} \sim 91$ GeV. To extract the physics related to the Z boson, a typical set of EWPOs is established, including the total width Γ_Z and partial decay widths $\Gamma_{e,\mu,\tau}, \Gamma_\nu, \Gamma_{u,c,d,s,b}$, the hadronic peak cross-section σ^0_{had}, branching ratios R_l, R_c, R_b [125–127]

$$\Gamma_Z = \sum_f \Gamma[Z \to f\bar{f}], \tag{2.41}$$

$$\sigma^0_{\rm had} = \sigma[e^+e^- \to \text{hadrons}]_{s=M_Z^2}, \tag{2.42}$$

$$R_\ell = \frac{\Gamma[Z \to \text{hadrons}]}{\Gamma[Z \to \ell^+\ell^-]}, \quad \ell = e, \mu, \tau, \tag{2.43}$$

$$R_q = \frac{\Gamma[Z \to q\bar{q}]}{\Gamma[Z \to \text{hadrons}]}, \quad q = u, d, s, c, b. \tag{2.44}$$

For instance, for the Z boson decay width, the general SM formula (valid for both Z and W boson decays) is [89]

$$\Gamma_{V\to f_1\bar{f}_2} = \frac{\sqrt{2}G_\mu M_V^3}{12\pi}\frac{2|\vec{p}|}{M_V} \times N_{cf}\left[(v^2+a^2)(1-\frac{1}{2}\frac{m_1^2+m_2^2}{M_V^2}-\frac{1}{2}\frac{(m_1^2-m_2^2)^2}{M_V^4})+(v^2-a^2)3\frac{m_1m_2}{M_V^2}\right] \tag{2.45}$$

Up-to-date results for the $Z \to e^+e^-, \mu^+\mu^-, \tau^+\tau^-$ decay widths can be found at the high precision SM package `DIZET` [128], created as an electroweak and QCD library of the `ZFITTER` program [125]. The input parameters are defined in the `Dizet` benchmark file in [128], the numbers are: $\Gamma_{e^+e^-} = 83.985$ MeV, $\Gamma_{\mu^+\mu^-} = 83.985$ MeV, $\Gamma_{\tau^+\tau^-} = 83.795$ MeV. The hadronic vacuum polarization has been calculated with the flag `IHVP=5` [129], EW corrections include complete (`IAMT4=8`) NNLO corrections [64]. As already discussed, the theoretical uncertainty due to missing higher-order terms is at the level of 0.4 MeV [64], and the experimental uncertainty will decrease in future FCC-ee Tera-Z measurements to the level of 0.1 MeV or below [PhD4], [70].

The other EWPOs connected to the Z boson are the cross-section asymmetries measured at the Z pole. For example, forward-backward asymmetry, which is defined as

$$A_{\rm FB}^f = \frac{\sigma_f\left[\theta < \frac{\pi}{2}\right] - \sigma_f\left[\theta > \frac{\pi}{2}\right]}{\sigma_f\left[\theta < \frac{\pi}{2}\right] + \sigma_f\left[\theta > \frac{\pi}{2}\right]}, \tag{2.46}$$

where θ denotes the scattering angle between the incoming and outgoing fermions. This formula can also be written in an approximate form as a product of two terms [PhD4], [130]

$$A_{\rm FB}^f = \frac{3}{4}\mathcal{A}_e\mathcal{A}_f, \tag{2.47}$$

where

$$\mathcal{A}_f \;=\; \frac{2\Re e\frac{v_f}{a_f}}{1+\left(\Re e\frac{v_f}{a_f}\right)^2} = \frac{1-4|Q_f|\sin^2\theta_W^{f,\text{eff}}}{1-4|Q_f|\sin^2\theta_W^{f,\text{eff}}+8(Q_f\sin^2\theta_W^{f,\text{eff}})^2}. \tag{2.48}$$

Note that the factorization to $\mathcal{A}e$ and $\mathcal{A}_f$ in (2.47) is an approximation. In reality, we must account for non-factorizable effects like box diagrams or initial-final interference, see Fig. 8

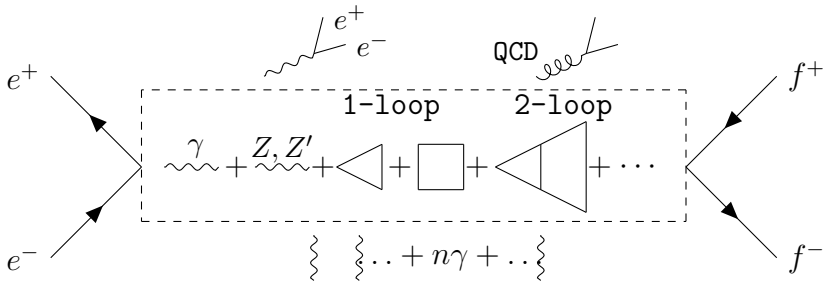

Figure 8: Schematic representation of the $e^+e^- \to f\bar{f}$ process including typical real radiation effects, represented outside of the dashed box, as well as exemplary virtual effects of different perturbative order (including BSM effects) inside the dashed frame.

The correct extraction of vertex form factors from the scattering process is complicated and was defined based on the so-called S-matrix approach. The S-matrix ansatz in the complex energy plane can be written in the following way

$$\mathcal{A}^{e^+e^-\to b\bar{b}} = \underbrace{\frac{R_Z}{s-s_Z}+\overbrace{\frac{R_\gamma}{s}+S+(s-s_Z)S'+\ldots,}^{Background}}_{\gamma-Z\ interference} \quad s_Z = \overline{M}_Z^2 - i\overline{M}_Z\overline{\Gamma}_Z, \tag{2.49}$$

where $R, S, S', \ldots$ are individually gauge-invariant and UV-finite due to the unitarity and analyticity of the S-matrix and IR-finite, when soft and collinear real photon emission is added [131–138].

$\overline{M}_\text{Z}$ and $\overline{\Gamma}_\text{Z}$ are the on-shell mass and width of the Z boson, respectively. According to (2.49), the approximate line shape of the cross-section near the Z pole is given by $\sigma \propto [(s-\overline{M}_\text{Z}^2)^2+\overline{M}_\text{Z}^2\overline{\Gamma}_\text{Z}^2]^{-1}$. It is important to note that this differs from the line shape used in experimental analyses, which is of the form $\sigma \propto [(s-M_\text{Z}^2)^2+s^2\Gamma_\text{Z}^2/M_\text{Z}^2]^{-1}$. As a result, the parameters in (2.49) differ from the experimental mass M_Z and width Γ_Z

from LEP by a fixed factor, as found for the first time in a seminal work [139]:

$$\overline{M}_{\rm Z} = M_{\rm Z}\Big/\sqrt{1+\Gamma_{\rm Z}^2/M_{\rm Z}^2}\,,$$
$$\overline{\Gamma}_{\rm Z} = \Gamma_{\rm Z}\Big/\sqrt{1+\Gamma_{\rm Z}^2/M_{\rm Z}^2}\,. \qquad (2.50)$$

Numerically, this leads to a substantial shift in the resonance point: $\overline{M}_{\rm Z} \approx M_{\rm Z} - 34\,\text{MeV}$, and $\overline{\Gamma}_{\rm Z} \approx \Gamma_{\rm Z} - 0.9\,\text{MeV}$. Visible effect of the Z boson resonance shape is given in Fig. 9. [45]

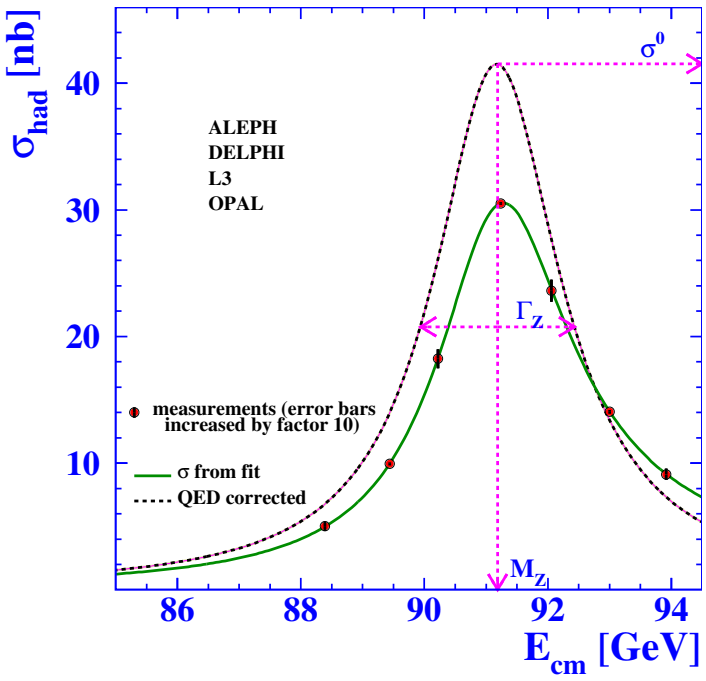

Figure 9: The hadronic cross-section as a function of centre-of-mass energy, averaged over measurements by the four LEP ADLO experiments (Aleph, Delphi, L3 and Opal). The full line represents the results of model-independent fits to the measurements. Correcting for QED photonic effects yields the dashed curves, see [45] from where the plot has been taken.

Physically, note that $\mathcal{A}$ has two poles, at $s = 0$ and $s_0 = s_Z$ for the photon and Z boson exchange, respectively. Thus for proper Laurent series expansion around the Z boson pole, the photon $s = 0$ exchange is shifted to the background. This process can be written in the following way, where only the Z resonance is present [140]

$$
\begin{aligned}
\frac{R_\gamma(s)}{s} &= \frac{\sum_{n=0}^{\infty} R_n (s-s_0)^n}{s} \\
&= \frac{\sum_{n=0}^{\infty} R_n (s-s_0)^n}{s_0-(s_0-s)} \\
&= \sum_{n=0}^{\infty} R_n (s-s_0)^n \, \frac{1}{s_0} \, \frac{1}{1-\frac{s_0-s}{s_0}} \\
&= \sum_{n=0}^{\infty} R_n (s-s_0)^n \, \frac{1}{s_0} \left[1+\frac{s_0-s}{s_0}+\left(\frac{s_0-s}{s_0}\right)^2 \cdots\right].
\end{aligned} \tag{2.51}
$$

Even after accounting for QED photons in the background (the procedure of the QED radiation effect extraction is also called a deconvolution [65]), defining SM parameters is challenging, and multiple solutions exist, depending on the precision of calculations [65]. A common example is the effective weak mixing angle, denoted as $\sin^2\theta_W^{f,\text{eff}}$, which incorporates the radiative corrections to the Weinberg angle. First, it can be defined using the ratio of vector and axial-vector couplings of an on-shell Z boson interacting with fermions:

$$
\frac{v_f}{a_f} = 1 - 4|Q_f| \sin^2\theta_W^{f,\text{eff}}, \tag{2.52}
$$

where v_f and a_f are vector and axial-vector couplings respectively and Q_f is a fermion charge.

Secondly, it can be defined using the ratio of the two gauge couplings:

$$
\frac{g'}{g} = \frac{\cos\theta_W}{\sin\theta_W}, \tag{2.53}
$$

where g and g' are the SU(2) and U(1) couplings respectively.

Lastly, it can be represented as the ratio of the masses of two gauge bosons (on-shell):

$$
\sin^2\theta_W = 1 - \frac{M_W^2}{M_Z^2}. \tag{2.54}
$$

These definitions correspond to different renormalization schemes and chosen input parameters [48]. The up to date discussion at the NNLO level can be found in [64,141].

To calculate the EWPOs outlined in equations (2.41)-(2.44), vector and axial-vector couplings v_f and a_f need to be known separately. These couplings are built up from the terms of the perturbative Z boson decay amplitude and taken as an effective form factor. This can be illustrated as shown in Fig. 10.

$$V_\mu^{Zf\bar{f}} = \gamma_\mu[v_f(s) + \ a_f(s)\gamma_5] = \cdots + \overbrace{\underbrace{\quad + \quad}_{\text{planar,non}-\text{planar}}}^{\text{fermionic,bosonic}} + \cdots \tag{2.55}$$

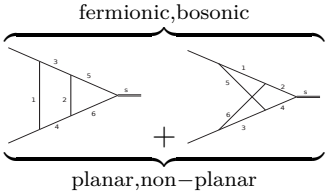

Figure 10: The general formula for the effective Z-boson form factor. Here, fermionic indicates diagrams with only fermionic loops, while bosonic signifies the remaining. Planar diagrams can be constructed such that no lines cross, whereas non-planar diagrams cannot. These calculations proceed in an order-by-order manner, incorporating leading terms, next-to-leading (1-loop) terms and so forth.

$V_\mu^{Zf\bar{f}}$ is the effective Z boson form factor.

Vector and axial couplings for the charged current can be found in section 2.2. For completeness, vector and axial couplings in the neutral sector in the SM for the Z boson are

$$v_f = -Q_f \sin^2\theta_W + \frac{T_3}{2}, \tag{2.56}$$

$$a_f = \frac{T_3}{2}. \tag{2.57}$$

Today's state of the art is that all corrections to the Z boson vertex are computed up to the 2-loop order [64, 66, 141], see Fig. 11. The demand for computations at higher order(s) was justified in section 1.3.

In the next chapter basic definitions, notations and examples are discussed needed for the SM renormalization and calculation of the 3-loop corrections given in chapter 5.

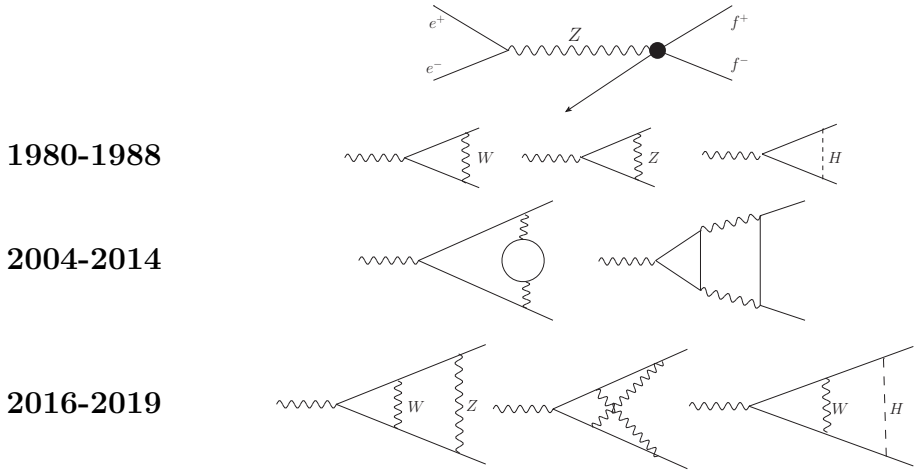

Figure 11: The past and current state of the art for the Z boson SM vertex corrections. For works connected with 1-loop corrections, see [40–43, 92, 142–144], for 2-loop corrections which include fermionic closed loops, see [138, 145–152] and for remaining (bosonic) 2-loop corrections see [64, 66, 141].

3 Radiative corrections

The problem of radiative corrections, which include infinite integrals, appeared within QED in the 1930s [23], so let us first illustrate the main concepts for this theory, which will be further extended to the SM framework.

We start with a bare Lagrangian, which means that we introduce a priori unphysical fields connected with a charged fermion ψ and electromagnetic field A_0^μ (photon)

$$\mathcal{L} = -\tfrac{1}{4} F_{0,\mu\nu} F_0^{\mu\nu} + \overline{\psi}_0 \Big(i\partial\!\!\!/ + e_0 A\!\!\!/_0 - m_0 \Big) \psi_0, \qquad F_{0,\mu\nu} = \partial_\mu A_{0,\nu} - \partial_\nu A_{0,\mu}. \tag{3.1}$$

This expression contains two free parameters: e_0 and m_0, the charge and mass of the fermion ψ_0, respectively.

When including radiative corrections, these parameters will, in general, differ from the observable charge and mass of the fermion. Denoting the latter as e and m, the relation can be written as

$$e_0 = Z_e\, e = (1 + \delta Z_e) e, \qquad\qquad m_0 = m + \delta m \tag{3.2}$$

The quantities δX are called *counterterms*. Here and in the following, the index "0" is used for Lagrangian "bare" quantities, whereas the corresponding symbols without a subscript denote physical renormalized quantities.

To determine the counterterms, one needs to specify a set of *renormalization conditions* that define what we mean by "physical quantities." For the charge and mass, we can find a set of conditions that formally reflect how these quantities are typically measured in an experiment. We proceed to the SM renormalization now.

3.1 Renormalization

The Standard Model involves a number of free parameters that need to be determined experimentally. These parameters often have intuitive physical meaning at the tree level, like masses or couplings so they are directly related to the experimental observables. Although when calculating the higher-order corrections, this direct connection is broken. In the thesis, we focus on the UV-divergences for which EWPOs can be determined. In renormalizable theories, such as SM [79], the UV-divergent parts cancel in relation to physical quantities, allowing meaningful predictions.

There are several schemes used for renormalization. For the purpose of the thesis we will focus on the so-called on-shell renormalization scheme following the notations

and definitions in [153, 154]. First, we need to choose the set of independent parameters, e.g. charge, masses and mixings $\{e, M_W, M_Z, M_H, m_{f,i}, V_{ij}\}$ for the SM. Secondly, we need to separate the bare parameters into two parts - renormalized parameters and renormalization constants, similarly for the fields. Then, we need to choose the renormalization conditions to fix the counterterms. Having the counterterms fixed, we can express the physical quantities in terms of the renormalized parameters. Next, we choose the input data to get the values of the renormalized parameters. At last, we can evaluate predictions for physical quantities in terms of input data. The renormalization conditions can be chosen such that the finite renormalized parameters correspond to physical parameters in all orders of perturbation theory. The advantage of this scheme is that all parameters have a clear physical meaning and can be directly measured in experiments (with the exception of the quark mass). This approach is most commonly used in the electroweak calculations. Yet, depending on the studies, different renormalization schemes can become advantageous. One of them is the Minimal Subtraction (MS) scheme, used together with dimensional regularization (see Appendix B). The principle of this method is to renormalize the integrals by subtracting only the divergent parts of the loop integrals, i.e. poles in powers of $1/\varepsilon$, without subtracting any finite parts. The renormalization constants Z_{MS} are of the form

$$Z_{\mathrm{MS}} = 1 + \sum_{n=1}^{\infty} \frac{a_n(g)}{\varepsilon^n} \,, \tag{3.3}$$

where $a_n(g)$ is a function of the renormalized coupling g. More commonly used is a so-called modified minimal subtraction ($\overline{\mathrm{MS}}$) scheme. The difference between these two renormalization methods is that in $\overline{\mathrm{MS}}$ scheme, besides the $1/\varepsilon$ poles, we also subtract a specific universal constant, $\ln(4\pi) - \gamma_E$, where γ_E is the Euler gamma constant, that appears naturally in the dimensional regularization. These schemes are quite simple and widely used in QCD, but the physical interpretation of the results is not as easy as in the on-shell renormalization scheme, as the subtracted quantities are not directly connected to physical observables.

It is sufficient to renormalize the parameters in order to get the finite elements of the S-matrix, but the Green functions are left divergent. To get finite vertex functions and propagators, we need to renormalize fields as well. Another problem is that radiative corrections introduce non-diagonal terms to the mass matrices, and so the bare fields are no longer mass eigenstates. These matrices can be rediagonalized by introducing matrix-valued field renormalization constants. As a result, we can define the renormalized fields such that they are the correct physical mass eigenstates in all

orders of perturbation theory. The choice of field renormalization does not influence the results for the physical S-matrix. The on-shell approach is presented in detail in the next sections.

3.1.1 Renormalization constants and counterterms

Let us consider the on-shell renormalization scheme for the electroweak Standard Model, with a set of independent parameters as mentioned before. Renormalization constants and the renormalized quantities are defined as follows for all orders of perturbation theory

$$\begin{aligned} e_0 &= Z_e e = (1+\delta Z_e)e, \\ M^2_{W,0} &= M^2_W + \delta M^2_W, \\ M^2_{Z,0} &= M^2_Z + \delta M^2_Z, \\ M^2_{H,0} &= M^2_H + \delta M^2_H, \\ m_{f,i,0} &= m_{f,i} + \delta m_{f,i}, \\ V_{ij,0} = (U_1 V U_2^\dagger)_{ij} &= V_{ij} + \delta V_{ij}. \end{aligned} \tag{3.4}$$

The U_1 and U_2 matrices are unitary, since $V_{ij,0}$ and V_{ij} are both unitary. We assume CKM and lepton mixing matrices V_{ij} to be diagonal, as it gives enough accuracy for our needs (considered already at the two-loop order [64, 66, 141]). All quarks other than top are assumed to be massless, all leptons are treated as massless as well. Thus, from now on, we assume $V_{ij} = \delta_{ij}$. The minimum of the Higgs potential is shifted due to the radiative corrections. To compensate for the shift, one needs to introduce a counterterm to the vacuum expectation value (VEV) of the Higgs field in such a way that the renormalized VEV is given by the actual minimum of the effective Higgs potential. To have all of S-matrix elements finite, the counterterms defined in (3.4) are enough. Yet, renormalization of the fields is needed to get finite Green functions as well. The relevance of Green functions is mentioned in more detail in section A.2, where the charge renormalization constant is considered up to the three-loop order. Field renormalization matrices are necessary to define renormalized fields, which are mass eigenstates, thus

$$
\begin{aligned}
W_0^{\pm} &= Z_W^{1/2} W^{\pm} = (1 + \tfrac{1}{2}\delta Z_W) W^{\pm}, \\
\begin{pmatrix} Z_0 \\ A_0 \end{pmatrix} &= \begin{pmatrix} Z_{ZZ}^{1/2} & Z_{ZA}^{1/2} \\ Z_{AZ}^{1/2} & Z_{AA}^{1/2} \end{pmatrix} \begin{pmatrix} Z \\ A \end{pmatrix} = \begin{pmatrix} 1 + \frac{1}{2}\delta Z_{ZZ} & \frac{1}{2}\delta Z_{ZA} \\ \frac{1}{2}\delta Z_{AZ} & 1 + \frac{1}{2}\delta Z_{AA} \end{pmatrix} \begin{pmatrix} Z \\ A \end{pmatrix}, \\
H_0 &= Z_H^{1/2} H = (1 + \tfrac{1}{2}\delta Z_H) H, \\
f_{i,0}^L &= Z_{ij}^{1/2,f,L} f_j^L = (\delta_{ij} + \tfrac{1}{2}\delta Z_{ij}^{f,L}) f_j^L, \\
f_{i,0}^R &= Z_{ij}^{1/2,f,R} f_j^R = (\delta_{ij} + \tfrac{1}{2}\delta Z_{ij}^{f,R}) f_j^R.
\end{aligned}
\tag{3.5}
$$

In the (3.5) the renormalization constants are expanded up to 1-loop level. Going beyond, more general expansions are needed, as exemplified in section 3.3.2 for vertex counterterms including $Z - A$ mixing, and in Appendix A.2 for the case of charge renormalization constant expansion up to the three-loop level.

3.1.2 Renormalization conditions

The renormalization constants are set by specifying renormalization conditions, which can be divided into two parts. First, the conditions which define the renormalized parameters, their choice affects the physical predictions in the finite orders of perturbation theory. Second, the conditions defined for renormalized fields, which are only relevant for Green functions. We can take advantage of the freedom in the choice of the latter. By the convenient choice we can remove the explicit wave function renormalization of the external particles and also significantly simplify the form of the renormalization conditions for the physical parameters.

In the on-shell renormalization scheme, all renormalization conditions are defined for the external fields on the mass shell. The standard definition of the on-shell mass is the location of the lowest energy pole of the two-point Green's function. The mass and field renormalization constants as well as the renormalization constant of the quark mixing matrix are fixed by the one-particle irreducible two-point functions. One three-point function fixes the charge renormalization, we can choose the $ee\gamma$ vertex function for this purpose. Below, to stress the physical fields, the renormalized quantities are denoted by the same symbols as unrenormalized quantities, but with a hat (a convention in Dittmaier and Denner works [153, 154]).

Moving on, the first renormalization condition involves the tadpole T, the one-point,

amputated renormalized Green function for the Higgs field

$$\hat{T} = \quad , \tag{3.6}$$

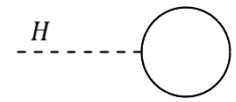

which translates into

$$\hat{T} = T + \delta T = 0. \tag{3.7}$$

The consequence of this condition is that we do not have to consider tadpoles in the actual calculations. This is valid at any loop order. However, δT is sometimes needed, for example, in vertex counterterms (for a complete list, see the Appendix in [154]) or as a part of the three-loop contribution to W boson mass renormalization constant (dTH2 term in (5.40)).

The next step involves the renormalized one-particle irreducible two-point functions defined in the 't Hooft-Feynman gauge as follows:

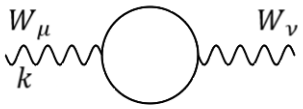

$$= \hat{\Gamma}^{W}_{\mu\nu}(k) =$$

$$-ig_{\mu\nu}(k^2 - M_W^2) - i\left(g_{\mu\nu} - \frac{k_\mu k_\nu}{k^2}\right)\hat{\Sigma}^{W}_{T}(k^2) - i\frac{k_\mu k_\nu}{k^2}\hat{\Sigma}^{W}_{L}(k^2), \tag{3.8}$$

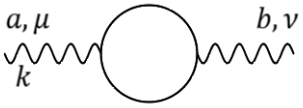

$$= \hat{\Gamma}^{ab}_{\mu\nu}(k) =$$

$$-ig_{\mu\nu}(k^2 - M_\alpha^2)\delta_{ab} - i\left(g_{\mu\nu} - \frac{k_\mu k_\nu}{k^2}\right)\hat{\Sigma}^{ab}_{T}(k^2) - i\frac{k_\mu k_\nu}{k^2}\hat{\Sigma}^{ab}_{L}(k^2), \tag{3.9}$$

where $a, b \in A, Z$ and $M_A^2 = 0$,

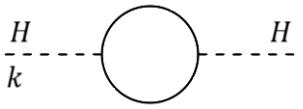

$$= \hat{\Gamma}^{H}(k) = i(k^2 - M_H^2) + i\hat{\Sigma}^{H}(k^2), \tag{3.10}$$

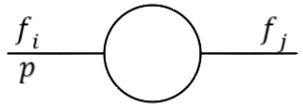

$$= \hat{\Gamma}^{f}_{ij}(p) =$$

$$i\delta_{ij}(\not{p} - m_i) + i\left[\not{p}\omega_- \hat{\Sigma}^{f,L}_{ij}(p^2) + \not{p}\omega_+ \hat{\Sigma}^{f,R}_{ij}(p^2) + (m_{f,i}\omega_- + m_{f,j}\omega_+)\hat{\Sigma}^{f,S}_{ij}(p^2)\right]. \tag{3.11}$$

One can obtain the corresponding propagators by inverting the two-point functions. In (3.8) and (3.9), longitudinal and transverse parts are separated, as the transverse part will be directly connected with gauge boson mass renormalization, see (3.18). In (3.11), the fermionic self-energy is divided conveniently into chiral and scalar parts.

The renormalization conditions for the two-point functions for on-shell external physical fields are the following

$$
\begin{aligned}
&\Re\left(\hat{\Gamma}^{W}_{\mu\nu}(k)\varepsilon^{\nu}(k)\Big|_{k^2=M_W^2}\right)=0,\\
&\Re\left(\hat{\Gamma}^{ZZ}_{\mu\nu}(k)\varepsilon^{\nu}(k)\Big|_{k^2=M_Z^2}\right)=0, \qquad \Re\left(\hat{\Gamma}^{AZ}_{\mu\nu}(k)\varepsilon^{\nu}(k)\Big|_{k^2=M_Z^2}\right)=0,\\
&\hat{\Gamma}^{AZ}_{\mu\nu}(k)\varepsilon^{\nu}(k)\Big|_{k^2=0}=0, \qquad \hat{\Gamma}^{AA}_{\mu\nu}(k)\varepsilon^{\nu}(k)\Big|_{k^2=0}=0,\\
&\frac{1}{k^2-M_W^2}\Re\left(\hat{\Gamma}^{W}_{\mu\nu}(k)\varepsilon^{\nu}(k)\right)\Big|_{k^2=M_W^2}=-i\varepsilon_{\mu}(k),\\
&\frac{1}{k^2-M_Z^2}\Re\left(\hat{\Gamma}^{ZZ}_{\mu\nu}(k)\varepsilon^{\nu}(k)\right)\Big|_{k^2=M_Z^2}=-i\varepsilon_{\mu}(k),\\
&\frac{1}{k^2}\Re\left(\hat{\Gamma}^{AA}_{\mu\nu}(k)\varepsilon^{\nu}(k)\right)\Big|_{k^2=0}=-i\varepsilon_{\mu}(k),\\
&\hat{\Gamma}^{H}(k)\Big|_{k^2=M_H^2}=0, \qquad \frac{1}{k^2-M_H^2}\Re(\hat{\Gamma}^{H}(k))\Big|_{k^2=M_H^2}=-i\varepsilon_{\mu}(k),\\
&\Re\left(\hat{\Gamma}^{f}_{ij}(p)u_j(p)\right)\Big|_{p^2=m_{f,j}^2}=0, \qquad \Re\left(\bar{u}_j(p')\hat{\Gamma}^{f}_{ij}(p')\right)\Big|_{p'^2=m_{f,j}^2}=0,\\
&\frac{\not{p}+m_{f,i}}{p^2-m_{f,i}}\Re\left(\hat{\Gamma}^{f}_{ii}(p)u_i(p)\right)\Big|_{p^2=m_{f,i}^2}=iu_i(p),\\
&\frac{\not{p}'+m_{f,i}}{p'^2-m_{f,i}}\Re\left(\bar{u}_i(p')\hat{\Gamma}^{f}_{ii}(p')\right)\Big|_{p'^2=m_{f,i}^2}=i u_i(p'),
\end{aligned}
\tag{3.12}
$$

where $\varepsilon(k), u(p), \bar{u}(p')$ are the polarization vectors and spinors of the external fields.

From (3.12) one gets the following renormalization conditions for the self-energy functions

$$
\begin{aligned}
&\Re\left(\hat{\Sigma}_T^W(M_W^2)\right) = 0, \\
&\Re\left(\hat{\Sigma}_T^{ZZ}(M_Z^2)\right) = 0, && \Re\left(\hat{\Sigma}_T^{AZ}(M_Z^2)\right) = 0, \\
&\hat{\Sigma}_T^{AZ}(0) = 0, && \hat{\Sigma}_T^{AA}(0) = 0, \\
&\Re\left(\frac{\partial\hat{\Sigma}_T^W(k^2)}{\partial k^2}\right)\Bigg|_{k^2=M_W^2} = 0, \\
&\Re\left(\frac{\partial\hat{\Sigma}_T^{ZZ}(k^2)}{\partial k^2}\right)\Bigg|_{k^2=M_Z^2} = 0, && \Re\left(\frac{\partial\hat{\Sigma}_T^{AA}(k^2)}{\partial k^2}\right)\Bigg|_{k^2=0} = 0, \\
&\Re\left(\hat{\Sigma}^H(M_H^2)\right) = 0, && \Re\left(\frac{\partial\hat{\Sigma}_T^H(k^2)}{\partial k^2}\right)\Bigg|_{k^2=M_H^2} = 0,
\end{aligned} \tag{3.13}
$$

$$
\begin{aligned}
&m_{f,j}\Re\left(\hat{\Sigma}_{i,j}^{f,L}(m_{f,j}^2)\right) + m_{f,j}\Re\left(\hat{\Sigma}_{i,j}^{f,S}(m_{f,j}^2)\right) = 0, \\
&m_{f,j}\Re\left(\hat{\Sigma}_{i,j}^{f,R}(m_{f,j}^2)\right) + m_{f,j}\Re\left(\hat{\Sigma}_{i,j}^{f,S}(m_{f,j}^2)\right) = 0, \\
&\Re\left(\hat{\Sigma}_{tt}^{f,R}(m_{f,i}^2)\right) + \Re\left(\hat{\Sigma}_{tt}^{f,L}(m_{f,i}^2)\right) \\
&+2m_{f,i}^2\frac{\partial}{\partial p^2}\left(\Re\left(\hat{\Sigma}_{tt}^{f,R}(p^2)\right) + \Re\left(\hat{\Sigma}_{tt}^{f,L}(p^2)\right) + \Re\left(\hat{\Sigma}_{tt}^{f,S}(p^2)\right)\right)\Big|_{p^2=m_{f,i}^2} = 0.
\end{aligned} \tag{3.14}
$$

It is important to note that for the gauge boson self energies, the longitudinal (unphysical) part drops out for the on-shell external gauge bosons, as can be seen in detail in Appendix A.1.

At last, the electric charge is defined as the full $ee\gamma$-coupling for on-shell external particles in the Thomson limit, which means that for on-shell external particles and for the zero momentum transfer, all corrections to this vertex vanish

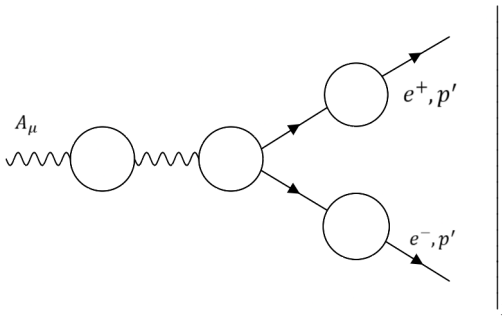

$$= ie\bar{u}(p)\gamma_\mu u(p). \tag{3.15}$$

The self-energy corrections in the external legs contribute to the S-matrix elements with a factor of 1/2, due to the wave function renormalization, see (3.5).

The field renormalization is chosen such that the corrections in the external legs vanish, leading to the following condition

$$\bar{u}(p)\Gamma^{ee\gamma}_{\mu}(p,p)u(p)|_{p^2=m_e^2} = ie\bar{u}(p)\gamma_\mu u(p), \tag{3.16}$$

for the (amputated) vertex function:

$$\hat{\Gamma}^{ee\gamma}_{\mu}(p,p') = \tag{3.17}$$

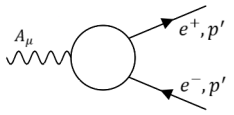

All of the Feynman diagrams in this section were generated using an online Feynman diagram maker [155].

3.2 Explicit form of renormalization constants

In subsection 3.1.1, the renormalized quantities were defined and they consist of the unrenormalized part and the counterterms. Counterterms can be expressed by the unrenormalized self-energies at specific external momenta with the use of the renormalization conditions e.g. as defined in subsection 3.1.2.

From the conditions (3.7) and (3.13) we get the Higgs and gauge boson sector counterterms

$$\begin{aligned}
&\delta t = -T, \\
&\delta M_W^2 = \Re\left(\Sigma_T^W(M_W^2)\right), && \delta Z_W = -\Re\left(\frac{\partial\Sigma_T^W(k^2)}{\partial k^2}\right)\Big|_{k^2=M_W^2}, \\
&\delta M_Z^2 = \Re\left(\Sigma_T^{ZZ}(M_Z^2)\right), && \delta Z_{ZZ} = -\Re\left(\frac{\partial\Sigma_T^{ZZ}(k^2)}{\partial k^2}\right)\Big|_{k^2=M_Z^2}, \\
&\delta Z_{AZ} = -2\Re\left(\frac{\Sigma_T^{AZ}(M_Z^2)}{M_Z^2}\right), && \delta Z_{ZA} = 2\frac{\Sigma_T^{AZ}(0)}{M_Z^2}, \\
&\delta Z_{AA} = -\frac{\partial\Sigma_T^{AA}(k^2)}{\partial k^2}\Big|_{k^2=0}, \\
&\delta M_H^2 = \Re\Sigma^H(M_H^2), && \delta Z_H = -\Re\left(\frac{\partial\Sigma^H(k^2)}{\partial k^2}\right)\Big|_{k^2=M_H^2}.
\end{aligned} \tag{3.18}$$

An example for the W boson case is given in Appendix A.1. In the fermion sector from conditions in (3.14) we get

$$
\begin{aligned}
\delta m_{f,i} &= \frac{m_{f,i}}{2}\Re\left[\Sigma^{f,L}_{ii}(m^2_{f,i}) + \Sigma^{f,R}_{ii}(m^2_{f,i}) + 2\Sigma^{f,S}_{ii}(m^2_{f,i})\right], \\
\delta Z^{f,L}_{ij} &= \frac{2}{m^2_{f,i} - m^2_{f,j}}\Re\left[m^2_{f,j}\Sigma^{f,L}_{ij}(m^2_{f,j}) + m_{f,i}m^2_{f,j}\Sigma^{f,R}_{ij}(m^2_{f,j}) + \right. \\
&\qquad \left. + (m^2_{f,i} + m^2_{f,j})\Sigma^{f,S}_{ij}(m^2_{f,j})\right], \qquad i \neq j, \\
\delta Z^{f,R}_{ij} &= \frac{2}{m^2_{f,i} - m^2_{f,j}}\Re\left[m^2_{f,j}\Sigma^{f,R}_{ij}(m^2_{f,j}) + m_{f,i}m^2_{f,j}\Sigma^{f,L}_{ij}(m^2_{f,j}) + \right. \\
&\qquad \left. + 2m_{f,i}m_{f,j}\Sigma^{f,S}_{ij}(m^2_{f,j})\right], \qquad i \neq j, \\
\delta Z^{f,L}_{ii} &= -\Re\left(\Sigma^{f,L}_{ii}(m^2_{f,i})\right) - m^2_{f,i}\frac{\partial}{\partial p^2}\Re\left[\Sigma^{f,L}_{ii}(p^2) + \Sigma^{f,R}_{ii}(p^2) + 2\Sigma^{f,S}_{ii}(p^2)\right]\Big|_{p^2=m^2_{f,i}}, \\
\delta Z^{f,R}_{ii} &= -\Re\left(\Sigma^{f,R}_{ii}(m^2_{f,i})\right) - m^2_{f,i}\frac{\partial}{\partial p^2}\Re\left[\Sigma^{f,L}_{ii}(p^2) + \Sigma^{f,R}_{ii}(p^2) + 2\Sigma^{f,S}_{ii}(p^2)\right]\Big|_{p^2=m^2_{f,i}}.
\end{aligned}
\tag{3.19}
$$

The charge renormalization constant is determined from the $ee\gamma$ vertex. Its renormalized function is

$$
\hat{\Gamma}^{\gamma ee}_{ij,\mu}(p,p') = -ieQ_f\delta_{ij}\gamma_\mu + ie\hat{\Lambda}^{\gamma ee}_{ij,\mu}(p,p'). \tag{3.20}
$$

which can be brought into the following form (using (3.18)).

$$
\delta Z_e = -\frac{1}{2}\delta Z_{AA} - \frac{s_W}{2c_W}\delta Z_{ZA} = \frac{1}{2}\frac{\partial\Sigma^{AA}_T(k^2)}{\partial k^2}\bigg|_{k^2=0} - \frac{s_W}{c_W}\frac{\Sigma^{AZ}_T(0)}{M^2_Z}. \tag{3.21}
$$

The equation (3.21) for δZ_e up to the 3-loop level is derived in Appendix A.2.

Finally, let us consider the weak mixing angle on-shell

$$
\sin^2\theta_W = s^2_W = 1 - \frac{M^2_W}{M^2_Z}. \tag{3.22}
$$

As the s_W and c_W are often in use, it is reasonable to introduce the following counterterms

$$
c_{W,0} = c_W + \delta c_W, \qquad s_{W,0} = s_W + \delta s_W. \tag{3.23}
$$

Since these are straightforwardly related to the gauge boson masses via (3.22), at the one-loop order, we arrive at

$$\frac{\delta c_W}{c_W} = \frac{1}{2}\left(\frac{\delta M_W^2}{M_W^2} - \frac{\delta M_Z^2}{M_Z^2}\right) = \frac{1}{2}\Re\left(\frac{\Sigma_T^W(M_W^2)}{M_W^2} - \frac{\Sigma_T^{ZZ}(M_Z^2)}{M_Z^2}\right), \tag{3.24}$$

$$\frac{\delta s_W}{s_W} = -\frac{c_W^2}{s_W^2}\frac{\delta c_W}{c_W} = -\frac{c_W^2}{2s_W^2}\Re\left(\frac{\Sigma_T^W(M_W^2)}{M_W^2} - \frac{\Sigma_T^{ZZ}(M_Z^2)}{M_Z^2}\right). \tag{3.25}$$

With this, we have all renormalization constants at hand (besides the quark mixing matrix V_{ij} which is irrelevant for the purpose of the thesis).

In the next section, we will show the examples of how to compute the renormalization constants using modern tools.

3.3 Examples of renormalization constants computation

In this subsection, we will describe and show examples of how to compute the renormalization constants using Mathematica packages `FeynArts, FeynCalc` and `FormCalc` [156–158]. There are no general tools for these calculations beyond one-loop order. We will review this situation in chapter 4, as our aim is the calculation of 3-loop amplitudes, in general.

3.3.1 One loop renormalization and counterterms

Both `FeynCalc` and `FormCalc` are used together with `FeynArts`, which is needed for the creation of diagrams and initial expressions associated with them. Let's start with `FormCalc` as it is more straightforward. `FormCalc` has an automatic way of computing renormalization constants, as long as they are well defined in the model file. Most of the `FeynArts` models provide files with renormalization constants definitions up to the one-loop level. In this thesis, we focus on the SM calculations, so we describe them below.

First, we need to load the packages

```
In[1]:= << "FeynArts.m";
In[2]:= << "FormCalc.m";
```

Then we need to specify the model which we want to work with

```
In[3]:= SetOptions[InsertFields, Model -> {SM}];
```

By default, it will be the **SM** model file, but we can choose to work with other models provided with the packages or our own modified model. For the latter case, the easiest way is to use `FeynRules` [159], which allows for quite simple model extensions. In this case, all we need to do is replace **SM** with the name of another model file. There is no universal tool for full renormalization even at the 1-loop level for BSM. To our knowledge, probably the most advanced in this regard is `FeynMaster` [160].

Having the model selected, we can now use the **CalcRenConst**[ ] function of `FormCalc` to compute any of the renormalization constants, for example Z boson mass squared renormalization constant, i.e. dMZsq1 in `FeynArts` notation.

```
In[4]:= CalcRenConst[dMZsq1] // Simplify;
```

The command outputs relevant options used for the generation of the self-energy diagrams and the corresponding expressions needed for the renormalization constant computation. At the end, it prints out the result in the form of a list of replacement rules in terms of Passarino-Veltman integrals

```
{RenConstList[RenConst][dMZsq1 → 1/(48 CW2^2 π SW2)
  Alfa (-8 CW2^3 Finite MZ2 + 3 CW2 (Re[A0[MH2]] + Re[A0[MZ2]]) + 12 MW2 Re[B0i[bb0, MZ2, MH2, MZ2]] -
     3 CW2 (4 CW2^2 (2 MW2 + 5 MZ2) - 8 MW2 SW2^2) Re[B0i[bb0, MZ2, MW2, MW2]] +
     36 CW2 Re[B0i[bb00, MZ2, 0, 0]] - 12 CW2 Re[B0i[bb00, MZ2, MH2, MZ2]] +
     6 CW2 (9 CW2^2 - 2 CW2 SW2 + SW2^2) (Re[A0[MW2]] - 2 Re[B0i[bb00, MZ2, MW2, MW2]]) -
     18 CW2 MZ2 Re[B0i[bb1, MZ2, 0, 0]] - 24 CW2^3 MZ2 Re[B0i[bb1, MZ2, MW2, MW2]] +
     2 CW2 (-((9 - 24 SW2 + 32 SW2^2) Re[A0[Mf2[3, Gen3]]]) - (9 - 12 SW2 + 8 SW2^2)
         Re[A0[Mf2[4, Gen3]]] - 3 Mf2[2, Gen3] Re[B0i[bb0, MZ2, Mf2[2, Gen3], Mf2[2, Gen3]]] -
        9 (Mf2[3, Gen3] Re[B0i[bb0, MZ2, Mf2[3, Gen3], Mf2[3, Gen3]]] +
           Mf2[4, Gen3] Re[B0i[bb0, MZ2, Mf2[4, Gen3], Mf2[4, Gen3]]]) - 3 × (1 - 4 SW2 + 8 SW2^2)
         (Re[A0[Mf2[2, Gen3]]] - 2 Re[B0i[bb00, MZ2, Mf2[2, Gen3], Mf2[2, Gen3]]]) +
        2 × (9 - 24 SW2 + 32 SW2^2) Re[B0i[bb00, MZ2, Mf2[3, Gen3], Mf2[3, Gen3]]] +
        2 × (9 - 12 SW2 + 8 SW2^2) Re[B0i[bb00, MZ2, Mf2[4, Gen3], Mf2[4, Gen3]]] -
        3 MZ2 (1 - 4 SW2 + 8 SW2^2) Re[B0i[bb1, MZ2, Mf2[2, Gen3], Mf2[2, Gen3]]] -
        MZ2 (9 - 24 SW2 + 32 SW2^2) Re[B0i[bb1, MZ2, Mf2[3, Gen3], Mf2[3, Gen3]]] -
        MZ2 (9 - 12 SW2 + 8 SW2^2) Re[B0i[bb1, MZ2, Mf2[4, Gen3], Mf2[4, Gen3]]]) SumOver[Gen3, 3])]}
```

(3.26)

Here, `Alfa` is the fine structure constant α, `CW2` and `SW2` are cosine squared and sine squared of the Weinberg angle, `MW2`, `MZ2` and `MH2` are the squared masses of W, Z and Higgs bosons, respectively. `Finite` is a symbol to indicate terms that can be omitted when calculating terms of order $\varepsilon^{-1}, \varepsilon^{-2}$, where ε is a dimensional regularization parameter. `Mf2[i,Gen3]`, where $i \in \{2, 3, 4\}$ denotes masses of fermions, charged

leptons, up and down quarks. Then, in the end `SumOver[Gen3,3]` denotes the summation of the expression over all possible combinations of flavours and quark generations to take into account the mixing of quarks in the particle interactions.

In this case, there is only one replacement rule, but in other cases, e.g. for the sine of the Weinberg angle, dSW1 in `FeynArts` notation, it computes all the needed contributions, i.e. W and Z bosons mass renormalization constants and they are all listed at the end of the commands output.

One can use the `ExpandSums` function to get an explicit form of the integral, with all of the fermion contributions and without the leftover summation. At this point, it can be useful to simplify the expression by neglecting the small masses. In our calculations, for the level of accuracy needed at the 2- and 3-loop radiative corrections, we neglect all masses but the mass of W, Z, H bosons and top quark. For further simplification, in the following result, the cosine and sine of the Weinberg angle are expressed in terms of M_W and M_Z.

```
{RenConstList[RenConst][dMZsq1 → 1/(48 MW2 (MW2 - MZ2) π)
  Alfa (8 Finite MW2^2 MZ2 - 3 MZ2^2 Re[A0[MH2]] + (64 MW2^2 - 80 MW2 MZ2 + 34 MZ2^2) Re[A0[MT2]] -
     72 MW2^2 Re[A0[MW2]] + 24 MW2 MZ2 Re[A0[MW2]] - 6 MZ2^2 Re[A0[MW2]] -
     3 MZ2^2 Re[A0[MZ2]] - 12 MZ2^3 Re[B0i[bb0, MZ2, MH2, MZ2]] +
     18 MT2 MZ2^2 Re[B0i[bb0, MZ2, MT2, MT2]] + 108 MW2^2 MZ2 Re[B0i[bb0, MZ2, MW2, MW2]] -
     24 MW2 MZ2^2 Re[B0i[bb0, MZ2, MW2, MW2]] - 640 MW2^2 Re[B0i[bb00, MZ2, 0, 0]] +
     800 MW2 MZ2 Re[B0i[bb00, MZ2, 0, 0]] - 412 MZ2^2 Re[B0i[bb00, MZ2, 0, 0]] +
     12 MZ2^2 Re[B0i[bb00, MZ2, MH2, MZ2]] - 128 MW2^2 Re[B0i[bb00, MZ2, MT2, MT2]] +
     160 MW2 MZ2 Re[B0i[bb00, MZ2, MT2, MT2]] - 68 MZ2^2 Re[B0i[bb00, MZ2, MT2, MT2]] +
     144 MW2^2 Re[B0i[bb00, MZ2, MW2, MW2]] - 48 MW2 MZ2 Re[B0i[bb00, MZ2, MW2, MW2]] +
     12 MZ2^2 Re[B0i[bb00, MZ2, MW2, MW2]] + 320 MW2^2 MZ2 Re[B0i[bb1, MZ2, 0, 0]] -
     400 MW2 MZ2^2 Re[B0i[bb1, MZ2, 0, 0]] + 206 MZ2^3 Re[B0i[bb1, MZ2, 0, 0]] +
     64 MW2^2 MZ2 Re[B0i[bb1, MZ2, MT2, MT2]] - 80 MW2 MZ2^2 Re[B0i[bb1, MZ2, MT2, MT2]] +
     34 MZ2^3 Re[B0i[bb1, MZ2, MT2, MT2]] + 24 MW2^2 MZ2 Re[B0i[bb1, MZ2, MW2, MW2]])]}
```

(3.27)

This expression can be plugged into one of numerous analytic/numerical tools such as `LoopTools` [158], `Xpackage` [161, 162], `QCDloop` [163] and `OneLOop` [164] to compute the Passarino-Veltman integrals and get the final result. This procedure, using `FormCalc` is rather simple and it can be repeated for any defined in the model renormalization constant.

As for the `FeynCalc`, its usage is more complex but also gives a better control over the whole process. To start with, we again need to load packages, now `FeynArts` is loaded as an addon of `FeynCalc`.

```
In[1]:= << $LoadAddOns={"FeynArts"};
In[2]:= << "FeynCalc.m";
```

Here, we have to specify the exact process we are interested in, incoming and outgoing particles and the number of loops. For the Z boson mass renormalization constant at the one-loop level:

```
In[3]:= diagsdMZsq1 = InsertFields[CreateTopologies[1, 1 -> 1,
↪  ExcludeTopologies -> {Tadpoles}], {V[2]} -> {V[2]}, InsertionLevel ->
↪  {Particles}];
```

Process generation is handled by `FeynArts`. The {V[2]}→{V[2]} part defines the incoming and outgoing particle, in this case, V[2] represents the Z boson. Then to convert the amplitude to the `FeynCalc` notation, we use the function `FCFAConvert` and specify the naive dimensional regularization (NDR) γ_5 treatment, as described in more detail in Appendix B.

```
In[4]:= ampdMZsq1[0] =
  FCFAConvert[CreateFeynAmp[diagsdMZsq1, Truncated -> True],
   IncomingMomenta -> {p}, OutgoingMomenta -> {p}, LoopMomenta -> {q},
    LorentzIndexNames -> {mu, nu}, UndoChiralSplittings -> True,
   ChangeDimension -> D, List -> True, SMP -> True, Contract -> True];
```

```
In[5]:= FCSetDiracGammaScheme["NDR-Discard"];
In[6]:= ampdMZsq1[1] = DiracSimplify[#] & /@ ampdMZsq1[0];
```

Then we have to apply the suitable projector to separate the transverse part of the process in (3.8). The properly normalized gauge boson projectors has the following form

$$\Sigma_T(p^2) = \frac{1}{D-1}\left[-g^{\mu\nu} + \frac{p^\mu p^\nu}{p^2}\right]\Sigma_{\mu\nu}(p), \qquad (p^2 \neq 0), \tag{3.28}$$

$$\Sigma_T(0) = -\frac{1}{D} g^{\mu\nu}\Sigma_{\mu\nu}(p=0). \tag{3.29}$$

Thus, for the Z boson

```
In[7]:= ampdMZsq1[2] =
  Plus @@ FCReplaceAll[Contract[(-MTD[mu, nu] + FVD[p, mu] FVD[p,
  ↪  nu]/Pair[Momentum[p, D], Momentum[p, D]])*ampdMZsq1[1]/(D - 1)] //
  ↪  Expand, SumOver[_, _] -> 3];
```

Finally, the simplifications are done with 1-loop tensor integral decomposition (TID function), neglecting the masses and expressing the Weinberg angle in terms of M_W and M_Z.

```
In[8]:= ampdMZsq1[3] = TID[ampdMZsq1[2], q, ToPaVe -> True];
```

```
In[9]:= ampdMZsq1[4] = FCReplaceAll[ampdMZsq1[3],
  Pair[Momentum[p, D], Momentum[p, D]] -> SMP["m_Z"]^2,
  SMP["m_e"] -> 0, SMP["m_mu"] -> 0, SMP["m_tau"] -> 0,
  SMP["m_u"] -> 0, SMP["m_d"] -> 0, SMP["m_c"] -> 0, SMP["m_s"] -> 0,
  SMP["m_b"] -> 0];
```

```
In[10]:= ampdMZsq1[5] =
 FCReplaceAll[ampdMZsq1[4], SMP["cos_W"] -> SMP["m_W"]/SMP["m_Z"],
  SMP["sin_W"] -> Sqrt[(SMP["m_Z"]^2 - SMP["m_W"]^2)/SMP["m_Z"]^2]]
```

```
In[11]:= finresdMZsq1 = SMPToSymbol[ampdMZsq1[5]] // Simplify
```

The output result agrees with (3.27).

A similar approach can be used for the wave function renormalization constant. Let us consider Higgs boson wave function renormalization. We know from (3.18) that δZ_H is given by the real part of the derivative of the Higgs boson self-energy at $p^2 = M_H^2$.

First, the difference is in the incoming and outgoing particle; for the Higgs boson, it should be S[1] (in SM). Next, in the input line `In[7]`, we do not need the projector for the transverse part. Then we simply take the derivative of the amplitude with respect to the squared momentum. The rest of the approach is the same as in the previously described case.

Finally, results for fermion self-energies with general decomposition

$$\Sigma^f(p) = \not{p} P_L \Sigma_L^f(p^2) + \not{p} P_R \Sigma_R^f(p^2) + m_f \Sigma_S^f(p^2), \tag{3.30}$$

at any order can be obtained using the following set of projectors

$$\Sigma_S^f(p^2) = \mathrm{Tr}[\Sigma^f \frac{1}{4}], \qquad (p^2 \neq 0), \tag{3.31}$$

$$\Sigma_L^f(p^2) = \mathrm{Tr}[P_L \not{p} \Sigma^f \frac{1}{2p^2}], \qquad (p^2 \neq 0), \tag{3.32}$$

$$\Sigma_R^f(p^2) = \mathrm{Tr}[P_R \not{p} \Sigma^f \frac{1}{2p^2}], \qquad (p^2 \neq 0). \tag{3.33}$$

For contributions with $p^2 = 0$ one needs to take the limit $p^2 \to 0$ of the above expressions.

As a side remark, some care is needed in numerical analysis and comparisons with results like in (3.26) and (3.27), as various programs may differ in the definition of Feynman integrals. This is important if we use different programs simultaneously. For instance, the default definition in the discussed later `AMFlow` or `AMBRE` packages is

$$\mathrm{A}_0(m^2) = \frac{1}{i\pi^{D/2}} \int \frac{d^D q}{q^2 - m^2}. \tag{3.34}$$

Other programs can add EulerGamma prefactors

$$\mathrm{A}_0(m^2) = \frac{e^{\varepsilon\gamma_E}}{i\pi^{D/2}} \int \frac{d^D q}{q^2 - m^2}. \tag{3.35}$$

In `LoopTools`:

$$\mathrm{A}_0(m^2) = \frac{1}{i\pi^{D/2} r_\Gamma} \int \frac{d^D q}{q^2 - m^2}, \quad r_\Gamma = \frac{\Gamma^2(1-\varepsilon)\Gamma(1+\varepsilon)}{\Gamma(1+2\varepsilon)}. \tag{3.36}$$

So for $\mathrm{A}_0(1)$ we have three different results

$$\mathrm{A}_0{}^{\mathrm{NoPrefactor}}(1) = 0.422784 + 1/\varepsilon + 1.41184\varepsilon + 0.504361\varepsilon^2 + \ldots \tag{3.37}$$

$$\mathrm{A}_0{}^{\mathrm{EulerGamma}}(1) = 1 + \frac{1}{\varepsilon} + 1 + \left(1 + \frac{\zeta_2}{2}\right)\varepsilon + \left(1 + \frac{\zeta_2}{2} - \frac{\zeta_3}{3}\right)\varepsilon^2 + \ldots \tag{3.38}$$

$$= 1 + 1/\varepsilon + 1.82247\varepsilon + 1.42178\varepsilon^2 + \ldots \tag{3.39}$$

$$\mathrm{A}_0{}^{\mathrm{LoopTools}}(1) = 1 + 1/\varepsilon + 2.64493\varepsilon + 5.04905\varepsilon^2 + \ldots \tag{3.40}$$

For more on the Feynman integrals definitions and conventions, see remarks in [165]. Throughout our calculations, we use a convention defined by (3.35) and expansion (3.38).

Similarly to the sketched above self-energy case, vertex amplitudes can be generated for which similar steps follow. They are needed both in the case of the muon decay ($W-$

$l-\nu$ electron and muon vertices) and Z boson decay (Z decay to leptons and quarks). If the electroweak charged vertex with a left-handed current, needed for instance for the muon decay amplitude, is written in the form $\mathcal{V}_\mu = C\,\bar{u}_\ell(k_1)\gamma_\mu\frac{1-\gamma^5}{2}u_\nu(k_2)$, then the C can be extracted using the following projection

$$C = \frac{1}{2D}\mathrm{Tr}\left\{\tfrac{1-\gamma^5}{2}\gamma^\mu\mathcal{V}_\mu^{\mathrm{amp}}\right\}_{k_1=k_2=0}. \tag{3.41}$$

$\mathcal{V}_\mu^{\mathrm{amp}}$ stands for the any order amplitude with external u spinors removed. Higher order results for the C form factor will be given in chapter 5.

All one-loop renormalization constants relevant for the main calculations of the thesis are gathered in the 1LCT_FAFC.nb notebook in the repository (`https://github.com/k-grzanka/PhD_res`) [166]. These renormalization constants needed, following `FeynArts` notation, and used internally throughout all the calculations, are

dMWsq1	dMZsq1	dMHsq1	
dZH1	dZW1	dZZZ1	
dZAZ1	dSW1	dCW1	(3.42)
dZAA1	dZe1	dMf1[3, 3].	

3.3.2 Beyond one-loop contributions

Going beyond the one-loop order, we sketch the needed basic manipulations by discussing vertices and corresponding counterterms. In general, the following expansions up to the third order of perturbation apply, such as inverse, square root and inverse square root of the functions

$$
\begin{aligned}
Z &\equiv 1+\varepsilon\delta Z^{(1)}+\varepsilon^2\delta Z^{(2)}+\varepsilon^3\delta Z^{(3)} && (3.43)\\
Z^{-1} &= 1-\varepsilon\delta Z^{(1)}-\varepsilon^2\delta Z^{(2)}-\varepsilon^3\delta Z^{(3)}+\varepsilon^2(\delta Z^{(1)})^2-\varepsilon^3(\delta Z^{(1)})^3+2\varepsilon^3\delta Z^{(1)}\delta Z^{(2)} && (3.44)
\end{aligned}
$$

$$
\begin{aligned}
Z^{1/2} &= 1+\frac{1}{2}\varepsilon\delta Z^{(1)}+\frac{1}{2}\varepsilon^2\delta Z^{(2)}+\frac{1}{2}\varepsilon^3\delta Z^{(3)}-\frac{1}{8}\varepsilon^2(\delta Z^{(1)})^2+\frac{1}{16}\varepsilon^3(\delta Z^{(1)})^3\\
&- \frac{1}{4}\varepsilon^3\delta Z^{(1)}\delta Z^{(2)} && (3.45)\\
Z^{-1/2} &= 1-\frac{1}{2}\varepsilon\delta Z^{(1)}-\frac{1}{2}\varepsilon^2\delta Z^{(2)}-\frac{1}{2}\varepsilon^3\delta Z^{(3)}+\frac{3}{8}\varepsilon^2(\delta Z^{(1)})^2-\frac{5}{16}\varepsilon^3(\delta Z^{(1)})^3\\
&+ \frac{3}{4}\varepsilon^3\delta Z^{(1)}\delta Z^{(2)} && (3.46)
\end{aligned}
$$

$$
Z_{ZA}^{1/2} \equiv \frac{1}{2}\varepsilon\delta Z_{ZA}^{(1)}+\frac{1}{2}\varepsilon^2\delta Z_{ZA}^{(2)}+\frac{1}{2}\varepsilon^3\delta Z_{ZA}^{(3)} \qquad (3.47)
$$

$$
\begin{aligned}
s &\equiv s+\varepsilon\delta s^{(1)}+\varepsilon^2\delta s^{(2)}+\varepsilon^3\delta s^{(3)}, && (3.48)\\
&\text{analogous for c and } \delta c^{(i)}=-\frac{s}{c}\delta s^{(i)}\\
s^{-1} &= s^{-1}-\varepsilon s^{-2}\delta s^{(1)}-\varepsilon^2 s^{-2}\delta s^{(2)}-\varepsilon^3 s^{-2}\delta s^{(3)}+2\varepsilon^3 s^{-3}\delta s^{(2)}\delta s^{(1)}+\varepsilon^2 s^{-3}(\delta s^{(1)})^2-\varepsilon^3 s^{-2}(\delta s^{(1)})^3\\
&\text{(analogous for c)} && (3.49)\\
s^{-2} &= s^{-2}-2\varepsilon s^{-3}\delta s^{(1)}-2\varepsilon^2 s^{-3}\delta s^{(2)}-2\varepsilon^3 s^{-3}\delta s^{(3)}+3\varepsilon^2 s^{-4}(\delta s^{(1)})^2\\
&+ 6\varepsilon^3 s^{-3}\delta s^{(2)}\delta s^{(1)}-4\varepsilon^3 s^{-5}(\delta s^{(1)})^3 && (3.50)\\
&\text{(analogous for c).}
\end{aligned}
$$

Here, ε^i flag denotes the order of expansion, s and c are the sine and cosine of the Weinberg angle. These relations help to find the vertex counterterms beyond the one-loop level.

Let us consider a four-point vertex in SM, defined as in [154].

$VVVV$ vertex:

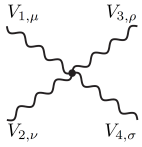

$$
= ie^2C\Big[2g_{\mu\nu}g_{\rho\sigma}-g_{\mu\sigma}g_{\nu\rho}-g_{\mu\rho}g_{\nu\sigma}\Big]. \qquad (3.51)
$$

At the tree level, coefficients C of the $VVVV$ vertices are

$V_1V_2V_3V_4$	C
$W^+W^+W^-W^-$	$\frac{1}{s^2}$
W^+W^-ZZ	$-\frac{c^2}{s^2}$
W^+W^-AZ	$\frac{c}{s}$
W^+W^-AA	-1

(3.52)

All SM vertices with 1-loop counterterms are encoded in the `SM.mod` in the `FeynArts` package. Here we show the verbatim form of the $W^-W^-W^+W^+$ vertex

```
  C[-V[3], -V[3], V[3], V[3]] ==
{{((2*I)*EL^2)/SW^2, ((-4*I)*EL^2*(dSW1 - (dZe1 + dZW1)*SW))/SW^3,
  ((2*I)*EL^2*(3*dSW1^2 - 4*dSW1*(dZe1 + dZW1)*SW +
     SW*(-2*dSW2 + (dZe1^2 + 2*dZe2 + 4*dZe1*dZW1 + dZW1^2 + 2*dZW2)*SW)))/
   SW^4}, {((-I)*EL^2)/SW^2, ((2*I)*EL^2*(dSW1 - (dZe1 + dZW1)*SW))/SW^3,
  ((-I)*EL^2*(3*dSW1^2 - 4*dSW1*(dZe1 + dZW1)*SW +
     SW*(-2*dSW2 + (dZe1^2 + 2*dZe2 + 4*dZe1*dZW1 + dZW1^2 + 2*dZW2)*SW)))/
   SW^4}, {((-I)*EL^2)/SW^2, ((2*I)*EL^2*(dSW1 - (dZe1 + dZW1)*SW))/SW^3,
  ((-I)*EL^2*(3*dSW1^2 - 4*dSW1*(dZe1 + dZW1)*SW +
     SW*(-2*dSW2 + (dZe1^2 + 2*dZe2 + 4*dZe1*dZW1 + dZW1^2 + 2*dZW2)*SW)))/
   SW^4}},
```

According to (3.51), on the right side, there is a list with three entries corresponding to the three entries in the kinematic vector. Each component is again a list where the first element is the usual (counter-term order 0, or tree-level) coupling, the second, the counterterm order 1 coupling, and so on.

These relations can be obtained using relations (3.43)-(3.50), expanding all four fields in a given vertex to the desired order in ε together with expansion of the e^2 factor and C coefficients. We get, here up to the third order in ε

$$
\begin{aligned}
C^{\text{Tree}}_{WWWW} &= \frac{1}{s^2}, && (3.53)\\
C^{(1)}_{WWWW} &= \frac{1}{s^2}\left(2\delta Z_e^{(1)} - 2\frac{\delta s^{(1)}}{s} + 2\delta Z_W^{(1)}\right), && (3.54)\\
C^{(2)}_{WWWW} &= \frac{1}{s^2}\Bigg[\left(\delta Z_e^{(1)}\right)^2 + 2\delta Z_e^{(2)} + 4\delta Z_e^{(1)}\delta Z_W^{(1)} + \left(\delta Z_W^{(1)}\right)^2 + 2\delta Z_W^{(2)}\\
&+ \frac{1}{s}\left(\frac{3\left(\delta s^{(1)}\right)^2}{s} - 2\delta s^{(2)} - 4\delta s^{(1)}\delta Z_e^{(1)} - 4\delta s^{(1)}\delta Z_W^{(1)}\right)\Bigg], && (3.55)\\
C^{(3)}_{WWWW} &= \frac{1}{s^2}\Bigg[2\delta Z_e^{(1)}\delta Z_e^{(2)} + 2\delta Z_e^{(3)} + 2\left(\delta Z_e^{(1)}\right)^2\delta Z_W^{(1)} + 4\delta Z_e^{(2)}\delta Z_W^{(1)}\\
&+ 2\delta Z_e^{(1)}\left(\delta Z_W^{(1)}\right)^2 + 4\delta Z_e^{(1)}\delta Z_W^{(2)} + 2\delta Z_W^{(1)}\delta Z_W^{(2)} + 2\delta Z_W^{(3)}\\
&+ \frac{1}{s}\Big(-\frac{4\left(\delta s^{(1)}\right)^3}{s^2} + \frac{6\delta s^{(1)}\delta s^{(2)}}{s} + \frac{6\left(\delta s^{(1)}\right)^2\delta Z_e^{(1)}}{s}\\
&+ \frac{6\left(\delta s^{(1)}\right)^2\delta Z_W^{(1)}}{s} - 2\delta s^{(3)} - 4\delta s^{(2)}\delta Z_e^{(1)} - 2\delta s^{(1)}\left(\delta Z_e^{(1)}\right)^2\\
&- 4\delta s^{(1)}\delta Z_e^{(2)} - 4\delta s^{(2)}\delta Z_W^{(1)} - 8\delta s^{(1)}\delta Z_e^{(1)}\delta Z_W^{(1)}\\
&- 2\delta s^{(1)}\left(\delta Z_W^{(1)}\right)^2 - 4\delta s^{(1)}\delta Z_W^{(2)}\Big)\Bigg], && (3.56)
\end{aligned}
$$

where the number in superscript brackets indicates the order of correction. In this case, the procedure is rather simple; we expand the functions in the ε flag, denoting the order of the expansion. It gets a little bit trickier when we consider fields mixing, as in the $A - Z$ case, for instance, considering the W^+W^-AZ vertex. In this case, one needs to actually consider three different scenarios: the initial $WWAZ$ vertex and $WWAA$ and $WWZZ$ vertices, as the photon and the Z boson can be transformed into each other. In the end, we need to sum up the results as follows

$$
C^{(i)}_{WWAZ} + 1/2\left(C^{(i)}_{WWAA} + C^{(i)}_{WWZZ}\right) \tag{3.57}
$$

Taking all of the terms into account, the final results are

$$C^{\text{Tree}}_{WWAZ} = \frac{c}{s}, \tag{3.58}$$

$$C^{(1)}_{WWAZ} = \frac{c}{s}\left[2\delta Z^{(1)}_e - \frac{1}{c^2}\frac{\delta s^{(1)}}{s} + \delta Z^{(1)}_W + \frac{1}{2}\delta Z^{(1)}_Z + \frac{1}{2}\delta Z^{(1)}_A\right] - \frac{1}{2}\delta Z^{(1)}_{AZ} - \frac{1}{2}\frac{c^2}{s^2}\delta Z^{(1)}_{ZA}\,, \tag{3.59}$$

$$\begin{aligned} C^{(2)}_{WWAZ} = \frac{c}{s}\Bigg[& -\frac{3\left(\delta s^{(1)}\right)^2}{2c^4} - \frac{\left(\delta Z^{(1)}_A\right)^2}{8} + \frac{\delta Z^{(2)}_A}{2} + \delta Z^{(1)}_A \delta Z^{(1)}_e + \left(\delta Z^{(1)}_e\right)^2 \\ & + 2\delta Z^{(2)}_e + \frac{\delta Z^{(1)}_A \delta Z^{(1)}_W}{2} + 2\delta Z^{(1)}_e \delta Z^{(1)}_W + \delta Z^{(2)}_W \\ & + \frac{\delta Z^{(1)}_{AZ}\delta Z^{(1)}_{ZA} + \delta Z^{(1)}_A \delta Z^{(1)}_Z}{4} + \delta Z^{(1)}_e \delta Z^{(1)}_Z + \frac{\delta Z^{(1)}_W \delta Z^{(1)}_Z}{2} \\ & - \frac{\left(\delta Z^{(1)}_Z\right)^2}{8} + \frac{\delta Z^{(2)}_Z}{2} + \frac{\left(\delta s^{(1)}\right)^2}{c^4 s^2} + \frac{\delta s^{(1)}\delta Z^{(1)}_{ZA}}{c\,s^2} - \frac{\delta s^{(2)}}{c^2 s} \\ & - \frac{\delta s^{(1)}\delta Z^{(1)}_A}{2c^2 s} - \frac{2\delta s^{(1)}\delta Z^{(1)}_e}{c^2 s} - \frac{\delta s^{(1)}\delta Z^{(1)}_W}{c^2 s} - \frac{c\,\delta Z^{(1)}_e \delta Z^{(1)}_{ZA}}{s} \\ & - \frac{c\,\delta Z^{(1)}_W \delta Z^{(1)}_{ZA}}{2s} - \frac{c\,\delta Z^{(2)}_{ZA}}{2s} - \frac{\delta s^{(1)}\delta Z^{(1)}_Z}{2c^2 s} - \frac{c\,\delta Z^{(1)}_{ZA}\delta Z^{(1)}_Z}{4s} \\ & - \frac{s\,\delta Z^{(1)}_A \delta Z^{(1)}_{AZ}}{4c} - \frac{s\,\delta Z^{(2)}_{AZ}}{2c} - \frac{s\,\delta Z^{(1)}_{AZ}\delta Z^{(1)}_e}{c} - \frac{s\,\delta Z^{(1)}_{AZ}\delta Z^{(1)}_W}{2c}\Bigg]. \end{aligned} \tag{3.60}$$

The three-loop result is not presented here due to its size.

The complete derivation with detailed steps for the discussed vertices can be found in a file Vertices_CT.nb in repository [166]. For our purposes, we have extended `FeynArts` 1-loop SM.mod model file with necessary higher order counterterms. Altogether, there are 118 2- 3- and 4-point vertex counterterms for all SM particles, including Faddeev-Popov ghost and Goldstone fields.

As an example of higher order counterterms relevant for the chapter 5 calculation, we present the W boson propagator as well as the charged current vertex at the two-loop order

$$= \delta Z^{(2)}_W (k^2 - M^2_W) - \delta M^{2,(2)}_W - \delta Z^{(1)}_W \delta M^{2,(1)}_W \tag{3.61}$$

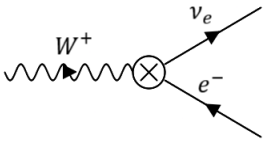

$$= \frac{ie}{\sqrt{2}s_W}\gamma_\mu\omega_- \left[\delta Z_e^{(2)} - \frac{\delta s_W^{(2)}}{s_W} + \frac{1}{2}(\delta Z_e^{(2)} + \delta Z_W^{(2)} + \delta Z_{\nu_e}^{(2)}) + 1LRC\right]. \tag{3.62}$$

Here $1LRC$ stands for 1-loop renormalization constants, numbers in parentheses indicate the loop order and the index T indicates the transverse part of the propagator.

For the higher-order calculations, we also need to include mixed contributions of loop integrals with counterterms. These can be treated similarly to the 1-loop procedure outlined in section 3.3.1. Consider a three-loop contribution from W boson self-energy integrals composed of one-loop integral with two 1-loop counterterms, see Fig. 12.

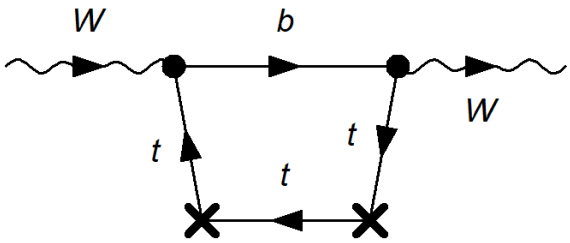

Figure 12: Exemplary one-loop diagram with two one-loop counterterms insertions generated with `FeynArts`.

In our calculations, we are finally interested in contributions of the $\mathcal{O}(\alpha^2\alpha_s)$ order. In the case of this diagram, the strong coupling comes from one of the top quark mass counterterm insertion dMf1[3,3]. This counterterm is the only one-loop counterterm that contains a term of the order $\mathcal{O}(\alpha_s)$, it comes from the following diagram

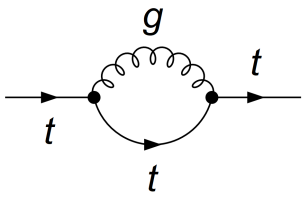

$$= \mathrm{dMf1}[3,3] = -\frac{C_F * g_s^2 * (2 - 3D + D^2) * \mathrm{A}_0[M_t^2]}{(32 * M_t * \pi^2 * (-3 + D))}. \tag{3.63}$$

Of course, for mixed EW-QCD effects, we must also consider electroweak contributions to dMf1[3,3] of the $\mathcal{O}(\alpha)$ order.

`FeynArts` treats the diagram in Fig. 12 as a box diagram with four propagators. The corresponding integral is the following

$$I = \frac{1}{k_1^2 * ((k_1 - p_1)^2 - M_t^2)^3}. \tag{3.64}$$

The `TID` `FeynCalc` function can translate it to a form of the D_0 Passarino-Veltman integral. This we can express back in terms of A_0 and B_0 integrals, using Integration by parts (IBP) reduction. The integral can also be computed analytically or numerically using tools described in section 3.3.1. Going beyond the 1-loop level, we use IBP reductions directly.

Using the same approach, we can generate and simplify expressions for the integrals composed of a two-loop integral with a one-loop counterterm, see Fig. 13.

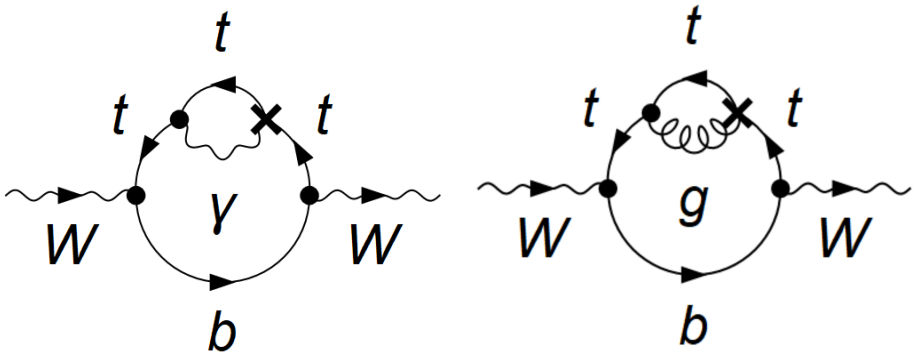

Figure 13: Exemplary two-loop diagrams with one-loop counterterm insertions generated with `FeynArts` needed for $\mathcal{O}(\alpha^2\alpha_s)$

Notice that the diagram on the left in Fig. 13 and similar diagrams with 1-loop vertex counterterms do not contribute at the $\mathcal{O}(\alpha^2\alpha_s)$ order. As just discussed in the case of the diagram in Fig. 12, there are no nonzero 1-loop vertex counterterms proportional to the strong coupling at this order. The other diagram, on the right side of Fig. 13, in contrast, has a gluon explicitly and thus contributes at the $\mathcal{O}(\alpha^2\alpha_s)$ order. In the 2-loop case, though, we cannot express the integrals in terms of 1-loop Passarino-Veltman integrals and one of the existing 1-loop numerical packages. To compute integrals beyond 1-loop level, e.g. corresponding to diagrams in Fig. 13, we can use methods described in the next chapter, such as sector decomposition, Mellin-Barnes method or `AMFlow`. Similarly, we proceed to calculate pure three-loop contributions.

The approach outlined in the present chapter for creation and evaluation of Feynman amplitudes using `FeynArts` with `FeynCalc` can be used for calculations at any loop order. The automated procedure for numerical calculation of multiloop integrals extracted from investigated amplitudes using both `pySecDec` and `AMFlow` will be de-

scribed in sections 5.1.1 and 5.1.4, respectively. However, before giving details of the concrete calculations in chapter 5, in the next chapter, we discuss the status of the main methods and tools developed in recent years for the calculation of multiloop Feynman integrals. Results analogous to (3.42) at the two-loop level necessary for the full three-loop calculation can be found in 2LCT.txt in repository [166]. In our calculations, we have excluded the contributions that have already been computed, i.e. diagrams with a gluon exchange and two closed fermionic loops as well as diagrams with three closed fermionic loops [167, 168] to avoid the double counting in the final merging of all the available results that will be included in phenomenological studies.

4 Multiloop calculation methods

Analytic computation of Feynman integrals can be rather difficult beyond the one-loop level, especially when corresponding diagrams include many massive propagators and external legs (many kinematical variables) [169]. As we discuss SM multiloop calculations up to the NNNLO (3-loop) order, we rely on numerical techniques. Thankfully, many numerical/approximate methods of evaluation have been developed and implemented in publicly available programs. To begin with, we can list the following

- Sector decomposition (SD)
  - `pySecDec` [170, 171]
  - `FIESTA` [172]
- Numerical Mellin-Barnes (MB) method
  - `MB` [173]
  - `MBnumerics` [174] (with automatic generation of MB representations: `AMBRE` [175, 176], `MBcreate` [177], method of brackets [178])
- Differential equations (DEqs)
  - `DiffExp` [179]
  - `Seasyde` [180]
  - `AMFlow` [181]
  - `Numerical Differential Equations with Euclidean Boundary Transport (DEqsEBT) [PhD1]`
  - `LINE` [182]
- Integration By Parts (IBP), used with DEqs
  - `Kira` [183–185]
  - `Fire` [186–188]
  - `LiteRed` [189]
  - `Reduze` [190, 191]

The above are the main methods used nowadays, see discussion in [165]. However, there are more exploratory ideas on numerical calculations. The pace is for fast and stable numerical implementations. Here we list some of the ideas developed in recent years

- Numerical Loop-Tree Duality
  - `cLTD` [192]
  - `Lotty` [193]
- Tropical sampling - `Feyntrop` [194]
- Taylor expansion in Feynman Parameters - `TayInt` [195]
- Multi-Dimensional Integration with Quantum Adaptive Importance Sampling

We cited only a few examples of exploratory directions with public packages. There are also new ideas and techniques like direct numerical evaluation of multi-loop integrals without contour deformation [196] or a quantum algorithm for multi-dimensional integration with quantum adaptive importance sampling [197].

Now we will shortly introduce the main methods which are used in getting numerical results in the next chapter.

4.1 Sector Decomposition (SD)

The method can be shown on an example of the simple two-dimensional parameter integral

$$I \;=\; \int_0^1 dx \int_0^1 dy\, x^{-1-a\varepsilon}\, y^{-b\varepsilon} \Big(x + (1-x)\, y\Big)^{-1} . \tag{4.1}$$

Such integrals appear in Feynman parametrization of virtual amplitudes as well as in real phase space integration [169]. Before settling the problem, let us first briefly review the general parametrization of Feynman amplitudes, which include such integration regions. For simplicity we focus on multillop scalar integrals $G_L[1]$, for general tensor integrals see e.g constructions in [175]

$$G_L[1] = \frac{1}{(i\pi^{d/2})^L} \int \frac{d^d k_1 \dots d^d k_L}{(q_1^2 - m_1^2)^{n_1} \dots (q_i^2 - m_i^2)^{n_j} \dots (q_N^2 - m_N^2)^{n_N}}. \tag{4.2}$$

A single Feynman propagator D_i is of the form

$$D_i = q_i^2 - m_i^2 = \left[\sum_{l=1}^{L} c_i^l k_l + \sum_{e=1}^{E} d_i^e p_e\right]^2 - m_i^2, \tag{4.3}$$

where k_l and p_e are internal and external momenta, respectively. The c_i^l, $d_i^e \in [-1, 1]$ are integer coefficients and depend on a particular topology.

To proceed further, we introduce a generalized Feynman parameter representation

$$\begin{aligned} \frac{1}{D_1^{n_1} D_2^{n_2} \dots D_N^{n_N}} &= \frac{\Gamma(n_1 + \dots + n_N)}{\Gamma(n_1) \dots \Gamma(n_N)} \\ &\int_0^1 dx_1 \dots \int_0^1 dx_N \frac{x_1^{n_1 - 1} \dots x_N^{n_N - 1} \delta(1 - x_1 - \dots - x_m)}{(x_1 D_1 + \dots + x_N D_N)^{N_\nu}}, \end{aligned} \tag{4.4}$$

with $N_\nu = n_1 + \dots + n_N$.

Let us now consider the momentum dependent function

$$m^2(\vec{x}) = x_1 D_1 + \dots + x_i D_i + \dots + x_N D_N = k_i M_{ij} k_j - 2 Q_j k_j + J, \tag{4.5}$$

where M is an $(L \times L)$-matrix, $Q = Q(x_i, p_e)$ – an L-vector and $J = J(x_i x_j, m_i^2, p_{e_i} \cdot p_{e_j})$.

Before integration over loop momenta, one has to perform several preparatory steps:

- Shift momenta in order to remove linear terms in k,

$$k \to k + M^{-1} Q \Rightarrow m^2 = kMk - QM^{-1}Q + J. \tag{4.6}$$

  Shifts over internal momenta leave the integrals unchanged.

- Wick rotations – transform Minkowskian space into the Euclidean for all loop momenta:

$$k_0 \to i k_0; \;\; k_j \to k_j (1 \leqslant j \leqslant d-1) \Rightarrow k^2 \to -k^2; \;\; d^d k \to i d^d k.$$

- Diagonalization of the matrix M:

$$k^\dagger M k = (V(x)k)^\dagger V(x) M V(x)^{-1} V(x) k, \;\; k(x) = V(x) k$$

$$V M V^{-1} = M_{\text{diag}}\,, \;\; (V^\dagger = V^{-1}),$$

$$kMk \Rightarrow k(x) M_{\text{diag}} k(x) = \sum_{i=1}^{L} \alpha_i k_i^2(x).$$

  The operation leaves integrals unchanged. After such manipulations, the function m^2 has the following form:

$$m^2 = -\sum_{i=1}^{L} \alpha_i k_i^2 - QM^{-1}Q + J.$$

- Rescale k_i:

$$k_i \to \sqrt{\alpha_i} k_i \Rightarrow d^d k_i \to (\alpha_i)^{-d/2} d^d k_i \quad \text{and} \quad \prod_{i=1}^{L} \alpha_i = \det M.$$

Finally, we obtain

$$G_L[1] = (-1)^{N_\nu} (i)^L (\det M)^{-d/2} \frac{\Gamma(N_\nu)}{\prod\limits_{i=1}^{N} \Gamma(n_i)} \int dx_1 \dots dx_N \int \frac{Dk_1 \dots Dk_L}{\left(\sum\limits_{i=1}^{L} k_i^2 + QM^{-1}Q - J \right)^{N_\nu}}, \tag{4.7}$$

with $Dk = \dfrac{d^d k}{i\pi^{d/2}}$.

Now the integration over loop momenta can be done in a simple way

$$i^L \int \frac{Dk_1 \dots Dk_L}{\left(\sum\limits_{i=1}^{L} k_i^2 + \mu^2(x) \right)^{N_\nu}} = \frac{\Gamma\left(N_\nu - \frac{d}{2}L\right)}{\Gamma(N_\nu)} \frac{1}{(\mu^2(x))^{N_\nu - \frac{dL}{2}}}, \tag{4.8}$$

$$\int Dk_1 \dots Dk_L e^{-i\left(\sum\limits_{i=1}^{L} k_i^2 + \mu^2(\alpha) \right)} = (-i)^{-Ld/2} e^{-i\mu^2(\alpha)}, \tag{4.9}$$

with $\mu^2(x) = QM^{-1}Q - J$. The final result (Feynman parametrization) is

$$G_L[1] = \frac{(-1)^{N_\nu} \Gamma\left(N_\nu - \frac{d}{2}L\right)}{\prod\limits_{i=1}^{N} \Gamma(n_i)} \int \prod_{j=1}^{N} dx_j \; x_j^{n_j - 1} \delta(1 - \sum_{i=1}^{N} x_i) \frac{U(\vec{x})^{N_\nu - d(L+1)/2}}{F(\vec{x})^{N_\nu - dL/2}}, \tag{4.10}$$

where we introduced two Feynman graph polynomials U and F

$$m^2 = kMk - 2Qk + J \Leftrightarrow \; U = \det M, \tag{4.11}$$

$$F = -\det M \; J + QM^T Q. \tag{4.12}$$

An example of how F and U polynomials can be obtained is given in Appendix C.

Coming back to the integral in (4.1), it contains a singular region where the singularities in x and y are overlapping. The aim of this method is to divide the integration range into two (or more) sectors, in which the singularities for $x \to 0$ and $y \to 0$ are factorised (see Fig. 14).

$$I \;=\; \int_0^1 dx \int_0^1 dy \, x^{-1-a\varepsilon} \, y^{-b\varepsilon} \Big(x + (1-x)\, y \Big)^{-1} \Big[\underbrace{\Theta(x-y)}_{(1)} + \underbrace{\Theta(y-x)}_{(2)} \Big] .$$

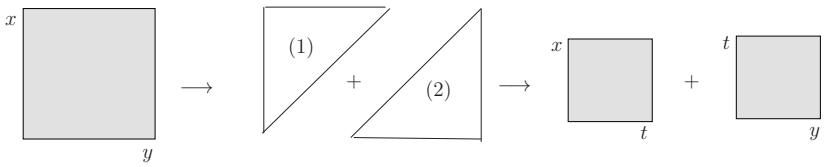

Figure 14: Sector decomposition schematically.

The following substitutions can be made $y = x\,t$ in sector (1) and $x = y\,t$ in sector (2) to remap the range of the integration into the unit square and get:

$$\begin{aligned} I &= \int_0^1 dx\, x^{-1-(a+b)\varepsilon} \int_0^1 dt\, t^{-b\varepsilon} \Big(1 + (1-x)\,t\Big)^{-1} \\ &+ \int_0^1 dy\, y^{-1-(a+b)\varepsilon} \int_0^1 dt\, t^{-1-a\varepsilon} \Big(1 + (1-y)\,t\Big)^{-1} . \end{aligned} \tag{4.13}$$

In this form, we can see that the singularities are factorized in a way that they can be read off from the powers of monomials in the integration variable, while the denominator goes to a constant when the integration variables approach zero.

In order to get complete factorization of the singularities, iteratively, the same concept can be applied to N-dimensional parameter integrals over polynomials raised to powers. Such more complicated integrals appear in the case of multiloop Feynman integrals.

The automatic `SD` approach to the three-loop self-energy integrals considered in the thesis is discussed in detail in section 5.1.

4.2 Mellin-Barnes (MB) Method

The method is based on the following relation

$$\frac{1}{(A+B)^\lambda} = \frac{1}{\Gamma(\lambda)} \frac{1}{2\pi i} \int_{c-i\infty}^{c+i\infty} dz \Gamma(\lambda+z)\Gamma(-z) \frac{B^z}{A^{\lambda+z}}, \tag{4.14}$$

where the poles of Gamma functions $\Gamma(-z)$ and $\Gamma(\lambda+z)$ are separated by the integration contour in the complex plane. A and B are complex numbers that fulfill the $|arg(A) - arg(B)| < \pi$ condition, for details see [165].

This relation can be applied to physical problems, for example we can rewrite the massive propagator as discussed originally in works by A. Davydychev, B. Arbuzov, E. Boos, V. Smirnov, see e.g. [198–200]

$$\frac{1}{(p^2-m^2)^a} = \frac{1}{\Gamma(a)} \frac{1}{2\pi i} \int_{-i\infty}^{+i\infty} dz \Gamma(a+z)\Gamma(-z) \frac{(-m^2)^z}{(p^2)^{a+z}}. \tag{4.15}$$

However, a real breakthrough in the application of the MB method to Feynman integrals came with works by Smirnov and Tausk, who applied the MB formula (4.14) to Symanzik polynomials in (4.10), which results in analytic evaluation of two-loop planar and non-planar box diagrams [201, 202].

In general, MB applications cover basic research areas:

- Real (soft, collinear) and virtual corrections
- Analytical and numerical solutions.

All these issues have been extensively discussed in the textbook [165]. *One of the key features of the MB approach (similarly to the SD approach) is its focus on an individual Feynman integral, which can become advantageous.* In the context of this thesis and multiloop calculations, MB was crucial for the completion of 2-loop Z decay EWPOs (8-digit accuracy was demanded for numerical evaluation of MB integrals in Minkowskian region) in conjunction with the SD method [64, 66, 141].

As a simple example of how the method can be applied in real calculations, let's consider first real radiation and typical phase space integration for the following massless integral with kinematics $p_1^2 = p_2^2 = p_3^2 = 0$ [203]

$$\int d\phi_3(p_1, p_2, p_3, Q) \frac{1}{(p_1 \cdot p_2)(p_1 \cdot p_2 + p_1 \cdot p_3)}. \tag{4.16}$$

It can be shown [204] that in $d = 4 - 2\varepsilon$ dimensions the integral is proportional to

$$\int_0^1 dx \int_0^{1-x} dy \; x^{-\varepsilon} y^{-\varepsilon} (1 - x - y)^{-\varepsilon} \frac{1}{x(x + y)}, \tag{4.17}$$

which, by change of the variables $y \to (1 - x)y$, can be brought into the form

$$\int_0^1 dx \int_0^1 dy \; x^{-1-\varepsilon} (1 - x)^{1-2\varepsilon} y^{-\varepsilon} (1 - y)^{-\varepsilon} \frac{1}{x + (1 - x)y}. \tag{4.18}$$

Now we can use the Mellin-Barnes formula (4.14) to get the MB representation

$$\int_{-i\infty}^{+i\infty} dz \frac{\Gamma(1 - \varepsilon)\Gamma(-z_1)\Gamma(z_1 + 1)\Gamma(-\varepsilon - z_1)\Gamma(z_1 - \varepsilon)}{\Gamma(1 - 3\varepsilon)}. \tag{4.19}$$

This 1-dim integral is obtained by applying in addition the following (first) Barnes lemma (1BL)

$$\int_{z_0 - i\infty}^{z_0 + i\infty} dz \, \Gamma(a+z)\Gamma(b+z)\Gamma(c-z)\Gamma(d-z) = \frac{\Gamma(a + c)\Gamma(a + d)\Gamma(b + c)\Gamma(b + d)}{\Gamma(a + b + c + d)}, \tag{4.20}$$

where $a + b + c + d < 1, \quad a, b, c, d \in \mathbb{R}$.

In this form, the integral (4.19) can either be expanded in ε or evaluated either numerically or analytically, as discussed in [165].

Knowing the general idea behind the MB representation, we can proceed to more complex examples connected with multiloop problems. The level of complexity, at a given loop order, depends on the number of virtual massive particles in the Feynman integrals. Let us discuss an example for the 3-loop studies of the fermionic class of diagrams. In Fig. 15 (left) a single-scale six propagator two-loop integral is shown, which has been discussed in section 2.1 in [141]. This is one of the difficult cases for sector decomposition. Its MB representation is 3-dimensional and it can be treated accurately with the integration package `Cuhre` [205,206]. Typically, for a 3-dimensional integral to get an absolute accuracy of 10^{-8}, with a sample of 10^7 points, `Cuhre` needs a few minutes on a medium-sized 1-core notebook. Roughly, we may assume that 10^2 points are needed per dimension. Consequently, to take into account about 10^8 points will already take hours. Inserting a top-quark loop to the Z propagator in the left diagram of Fig. 15 results in the 3-loop fermionic diagram shown in the right part of the figure. Fermionic insertions increase the dimensionality of the `MB` representation by one, and the corresponding result generated by the *Mathematica* package `AMBRE v.2.1.1.m` for the scalar integral corresponding to Fig. 15 is

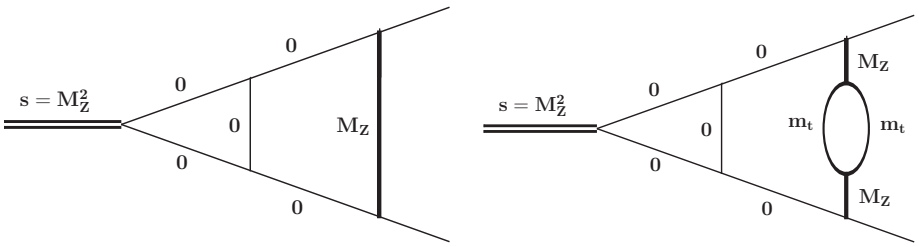

Figure 15: An example of a 3-loop fermionic Feynman diagram with a self-energy insertion derived of the two-loop diagram on the left.

$$\texttt{MB}_{\texttt{Fig. 15}} = -\int dz_1 \int dz_2 \int dz_3 \int dz_4 (-s)^{-3\varepsilon-3} \left(-M_t^2/s\right)^{z_3} \left(-M_Z^2/s\right)^{z_4} \tag{4.21}$$

$$\times \frac{\Gamma(-z_1)\Gamma(-z_2)\Gamma(-z_3)\Gamma(-z_4)\Gamma(2\varepsilon - z_1 - z_2 + z_3 + z_4 + 2)}{\Gamma(1-2\varepsilon)\Gamma(1-z_1)\Gamma(1-z_2)\Gamma(-2\varepsilon - 2z_3 + 2)\Gamma(-3\varepsilon + z_1 + z_2 - z_3 - z_4)}$$

$$\times \Gamma(z_4+2)\Gamma(-\varepsilon - z_1)\Gamma(-\varepsilon - z_2)\Gamma^2(-\varepsilon - z_3 + 1)\Gamma(\varepsilon + z_3)\Gamma(z_1 + z_2 + 1)$$

$$\times \Gamma(\varepsilon + z_1 + z_2 + 1)\Gamma(-2\varepsilon + z_1 - z_3 - z_4 - 1)\Gamma(-2\varepsilon + z_2 - z_3 - z_4 - 1).$$

As expected, such MB integrals are quite unstable in the physical region, e.g., $s = M_Z^2$. One of the reasons is the kinematical factor in the first line of (4.21). There are several methods to make the integral stable (shift and deformation of integration contours, transformation of variables). The *Mathematica* package `MBnumerics.m` can be used for that, as discussed in [176, 207–209]. The result for the point $s = M_Z^2 + i\varepsilon$ is

$$\texttt{MB}(s = M_Z^2) = \frac{3.548726835333682\ (4.7 \cdot 10^{-11}) - 4.630478414501253i\ (6.1 \cdot 10^{-11})}{\varepsilon}$$
$$- 7.5448035410152805\ (2.4 \cdot 10^{-7}) - 31.14924308603089i\ (2.4 \cdot 10^{-7}). \tag{4.22}$$

In brackets, the absolute error of the calculation is given. The maximum number of sampling points for `Cuhre` was set to 10^7.

It is interesting to note that for some cases the standard integration (without any manipulation of the integrations paths) with `MB.m` can work also in Minkowskian regions using transformation or mapping of the infinite integration region $(-\infty, \infty)$ into a finite one, $[0, 1]$ with trigonometric functions, $t_i = \tan\left(\pi(x_i - \frac{1}{2})\right)$; instead of logarithms, $t_i = \ln\left(\frac{x_i}{1-x_i}\right)$, as implemented in `MB.m` [173]. This changes the asymptotic behavior of the integrand and makes the numerical integrations more stable.

Typically, if we would like to get an accuracy of 10^{-10} for 3-dimensional integrals with the deterministic integrator `Cuhre` of the package CUBA [206], about 10^9 points are needed, and the numerical evaluation will take days. For the same accuracy and 4-dimensional integrals, it would take months on a 1-core computer. These are some rough estimates of the present boundaries of calculations. Some other interesting MB representations which were explored for the purpose of the 3-loop SM self-energy calculations in the present thesis can be found in [PhD2] in List of papers.

4.3 MB versus SD

In general, MB works well for hard threshold, on-shell cases, not many internal masses. On the other hand, SD is more useful for integrals with many internal masses (no need for a larger number of sector decompositions). Before we proceed to the presently most robust method of multiloop calculations by differential equations, let us compare MB and SD approaches taking an example of the 2-loop non-planar integral in Fig. 16 with one internal mass only, which in addition equals the square of the external four momenta.

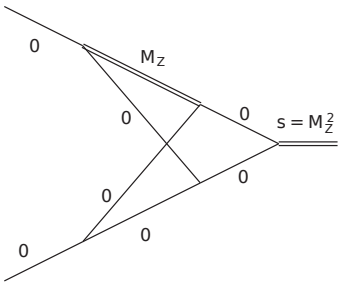

Figure 16: Nonplanar two-loop vertex V6l1m with one massive propagator which mass M_Z coincides with external invariant energy.

The numerical result for the constant part ε^0 of this integral is

- Euclidean results (constant part in ε)

$$\begin{array}{ll} \text{Analytical}: & -0.4966198306057021 \\ \text{MB(Vegas)}: & -0.4969417442183914 \\ \text{MB(Cuhre)}: & -0.4966198313219404 \\ \text{FIESTA}: & -0.4966184488196595 \\ \text{SecDec}: & -0.4966192150541896 \end{array} \tag{4.23}$$

- Minkowskian results (constant part in ε)

$$\begin{array}{ll} \text{Analytical}: & -0.778599608979684 - 4.123512593396311 \cdot i \\ \text{MBnumerics}: & -0.778599608324769 - 4.123512600516016 \cdot i \\ \text{MB + thresholds}: & -0.7785242512636401 - 4.123512600516016 \cdot i \\ \text{SecDec}: & \text{big error [\textbf{2016}]}, -0.77 - \text{i} \cdot 4.1 \text{ [\textbf{2017}]}, \\ \text{SecDec}: & -0.778 - i \cdot 4.123 \text{ [\textbf{2019}]} \\ \text{pySecDec + rescaling}: & -0.778598 - i \cdot 4.123512 \text{ [\textbf{2020}]} \end{array} \tag{4.24}$$

Numbers in blue denote the accuracy of the result. The integral was evaluated at $s = M_Z^2 \equiv 1 + i\delta'$ where δ' is a small parameter, here $\delta' = i \cdot 10^{-7}$. To get the correct sign of the imaginary part of Feynman integrals in calculations, the same $i\delta'$ prescription is assumed everywhere. The analytical result can be found in [210]. The `MB` running file `MB_V6l1m.sh` for `MBnumerics.m` and configuration files `SD_V6l1m_generate.py` and `SD_V6l1m_integrate.py` for the `pySecDec` evaluation are for the scalar integral which corresponds to Fig. 16 available at [211].

The `MB+thresholds` method for which the result is given in (4.24) relies on an appropriate grouping of the F polynomial terms (see Appendix C) for the `MB` transformation, namely, the F polynomial for a given Feynman diagram can be written as a sum of two parts

$$F = F_0 + U \sum_{i=1}^{n} x_i m_i^2. \tag{4.25}$$

$F_0(x)$ corresponds to a diagram with all massless propagators. It depends on kinematic invariants. The second term $U(x) \sum_i m_i^2 x_i$ depends on the masses of internal particles. We can construct the `MB` representation *by not expanding the second (in blue colour) term*

$$G(X) \sim \frac{U(x)^{N_\nu - d(L+1)/2}}{\left(F_0(x) + U(x) \sum_{\mathbf{i}} \mathbf{m_i^2 x_i}\right)^{N_\nu - dL/2}} \sim \prod_{\mathbf{i}} \left(\mathbf{m_i^2 x_i}\right)^{\mathbf{z_i}} \frac{U(x)^{N_\nu - d(L+1)/2 + \sum_i z_i}}{F_0(x)^{N_\nu - dL/2 + \sum_i z_i}}. \tag{4.26}$$

This approach gives optimal dimensionality, but at a price: we lose information about physical and pseudo-thresholds. By a physical threshold, we consider a kinematic point where the F polynomial starts to be negative. For the pseudo-threshold, one of the terms in F becomes negative. Typically, we can separate and collect $x_l x_n x_k$ terms with a common $\sum (m_i^2 - s)$ dependency in F. There is a physical threshold at $s = 0$ and pseudo-thresholds at points $s = \sum m_i^2$. For $m^2 = s$, this term vanishes, and the F polynomial with non-negative terms can be resolved numerically without contour deformations like in the Euclidean case directly with `MB.m`.

The discussion of the integral by the `pySecDec` team (2017) can be found in [170]. Rescaling for the 2020 `SD` result in (4.24), with additional investigations for the purpose of precision studies done in this thesis, will be discussed in chapter 5.

Finally, we should note a remarkable progress by the `pySecDec` team described recently in [212]. The point is that knowledge of Landau poles and expansions by regions makes it possible to avoid contour deformations. The new result is[2]

[2] S. Jones, private communication

$$
\begin{aligned}
I_{\text{V6l1m}} &= \varepsilon^{-3}(+0.000000000000000 + i \cdot 0.0000000000000000) \\
&\pm \varepsilon^{-3}(+0.0000000000000000 + i \cdot 0.0000000000000000) \\
&+ \varepsilon^{-2}(+1.2337005501361702 + i \cdot 0.000000000000000e) \\
&\pm \varepsilon^{-2} * (+7.0283541660394319 \cdot 10^{-16} + i \cdot 0.0000000000000000) \\
&+ \varepsilon^{-1}(+2.8902545096590662 + i \cdot 3.8757845850374752) \\
&\pm \varepsilon^{-1}(+3.1043864641637521e-12 + 1.2989348865275077 \cdot 10^{-16}) \\
&+ (+0.77859960898646108 + i \cdot 4.1235125933366232) \\
&\pm (+3.6966843561201167 \cdot 10^{-11} + i \cdot 1.2914986997032820 \cdot 10^{-13}).
\end{aligned}
\tag{4.27}
$$

As we can see, there is a huge progress in precision for the used method as well as at the speed of calculation (declared one to two orders of magnitude).

4.4 Integration by parts and Differential Equations (DEqs)

Integration by parts reduction is an important part of most of the multi-loop calculations nowadays. The IBP identities in D dimensional spacetime are used for the reduction of multi-loop Feynman integrals to the basis of master integrals.

Let us consider a Feynman integral with L loops

$$
\int \prod_{j=1}^{L} \frac{d^D l_j}{i\pi^{D/2}} \frac{1}{\prod_{i=1}^{n} D_i^{\alpha_i}}, \tag{4.28}
$$

where α_i are integer indices, denominators D_i are given by

$$
D_i = \sum_{j \geq k \geq 1}^{L} A_i^{jk} l_j \cdot l_k + \sum_{i=1}^{L} B_i^j \cdot l_j + E_i \,, \tag{4.29}
$$

i.e they are linear or quadratic functions of external momenta p_i and loop momenta l_i.

The well known IBP relation [213, 214] has the following form

$$
0 = \int \prod_{j=1}^{L} \frac{d^D l_j}{i\pi^{D/2}} \frac{\partial}{\partial l_m} \left(q_k \prod_{i=1}^{n} D_i^{-\alpha_i} \right), \tag{4.30}
$$

where $m = 1, ..., L$ and q_k is a linear combination of external momenta and loop momenta. Using the IBP identities, one can find a set of master integrals (MIs), which are the basis of a given integral family. It has been proved in [215] that the number of master integrals is always finite. Thus, one can rewrite a Feynman integral as a linear combination of master integrals

$$I[\alpha_i, ..., \alpha_n] = \sum_i c_i I_i, \tag{4.31}$$

where I_i are the MIs and α_i are the integer indices of denominators.

There are various algorithms for the IBP reduction, such as Laporta algorithm [216], finite-field interpolation [217–220], direct solutions IBP recursive relations [221], intersection theory [222], module intersection [223], the algebraic structures of IBP relations [224–226], η expansion [227]. There is also plenty of public codes for the IBP reduction, such as `KIRA, REDUZE, LiteRed, FIRE, AIR` [183–191, 228–230].

The idea of solving Feynman Integrals using differential equations appeared in the 1990s in papers by Kotikov and Remiddi [231–234]. The basic idea behind the use of differential equations in connection to IBP reduction in loop calculations is the following. Having a basis of master integrals of a given integral family, one can notice that their derivatives can be expressed as a combination of Feynman integrals within the same family with different exponents of propagators. These can, again, be IBP reduced back to the original set of master integrals, and thus we obtain the derivatives of master integrals as a linear system of differential equations.

Consider a Feynman integrals family with m master integrals put into a vector $\vec{f} = (f_1, ..., f_m)$. Let the Feynman integrals depend on a set S, which consists of squares of internal masses and kinematic invariants, thus, squares of the sums of external momenta. The related system of differential equations can be written as

$$d\vec{f} = \left(\sum_{s \in S} \mathbf{A}_s ds\right) \vec{f}, \tag{4.32}$$

where $\mathbf{A}_s$ are the so-called partial derivative matrices. Knowing that the total differential should vanish, $d^2 = 0$, we obtain the integrability condition

$$\partial_{s_1} \mathbf{A}_{s_2} - \partial_{s_2} \mathbf{A}_{s_1} + [\mathbf{A}_{s_1}, \mathbf{A}_{s_2}] = 0 \text{ for all } s_1, s_2 \in S. \tag{4.33}$$

The choice of the so-called canonical basis can significantly simplify the differential equations. The concept was first introduced in [235]. Considering a general shift of basis $\vec{B} = \mathbf{T}^{-1}\vec{f}$, where matrix $\mathbf{T}$ can depend on internal masses, ε and kinematic invariants, the partial derivative with respect to variable s takes the following form

$$\frac{\partial}{\partial s}\vec{B} = [(\partial s \mathbf{T}^{-1})\mathbf{T} + \mathbf{T}^{-1}\mathbf{A}_s\mathbf{T}]\vec{B}. \tag{4.34}$$

In [235] it was observed that if $\mathbf{T}$ fulfills

$$(\partial s \mathbf{T}^{-1})\mathbf{T} + \mathbf{T}^{-1}\mathbf{A}_s\mathbf{T} = \varepsilon\tilde{\mathbf{A}}_s, \tag{4.35}$$

for all internal masses and kinematic invariants $s \in S$ and $\tilde{\mathbf{A}}_s$ does not depend on ε, the differential equations are considerably simplified. It is supposed that such a choice of $\mathbf{T}$ matrix is always possible.

The canonical basis for the integrals, that can be expressed in terms of multiple polylogarithms, can be written in the form

$$d\vec{B} = \varepsilon d\tilde{\mathbf{A}}\vec{B}, \qquad \tilde{\mathbf{A}} = \sum_{l\in\mathcal{A}} \tilde{\mathbf{A}}_l log(l). \tag{4.36}$$

In general, finding a canonical basis is a key step in constructing solvable differential equations (both numerically and analytically). One of the features of this construction is that solutions constitute uniform weights for HPLs (harmonic polylogarithms) solutions (if they exist). This is especially important when a system of differential equations includes more coupled MIs, e.g. in [236] DEqs with up to 6 MIs appeared (two-loop Bhabha scattering in massive QED). These systems have been solved only after the canonical basis was implemented for planar Feynman diagrams [237]. There are many public programs for such construction like `Libra` [238, 239], `epsilon` [240], `Fuchsia` [241], `Canonica` [242], `Initial` [243]. Nowadays, the solutions go beyond HPLs (harmonic polylogarithms) and include elliptic functions and possible generalizations. For some latest reviews, see [244–246].

4.5 Numerical Differential Equations with Euclidean Boundary Transport (DEqsEBT)

As will be discussed in the next chapter with numerical results, our aim is to go one step above the present status of EWPOs calculations presented in section 1.3 and tables Tab. 1 and Tab. 2, i.e. we aim at the calculation of $\mathcal{O}(\alpha^2\alpha_s)$ contributions needed for the muon Δr parameter and Z decay observables.

The methods described earlier of sector decomposition and Mellin-Barnes representation were used for the calculation of the complete SM 2-loop corrections to Z boson production and decay [64, 66, 141]. However, these methods require large amounts of computing resources and do not always converge to the required level of accuracy (or have failed completely in many cases), so that a straightforward extension to more loops and/or legs is practically not possible at the current state of the methods, see further discussion in section 5.1.2. As for the three-loop calculations, we aim for at least

3 digits of accuracy for the final result for any practical application. This, based on the experience gathered in [66] is expected to translate to at least 8-10 digits accuracy for individual loop integrals[3].

Thus, in [PhD1] we evaluated for the first time the most difficult three-loop tensor self-energy and vertex integrals in the SM framework at the precision level required by future collider physics analysis.

As I spent a considerable amount of time during the PhD studies for a thorough investigation of the DEqs method, I describe this issue and the worked-out approach with basic results in more detail.

As already discussed, for many families of Feynman integrals, one can choose a particularly simple "canonical" form of master integrals [235]. These, in turn, in many cases, can be solved in terms of multiple polylogarithms straightforwardly. In general, not all Feynman integrals are of polylogarithmic type and finding a closed set of analytic functions in terms of which DEqs can be solved may become more difficult. To avoid this problem and tackle a wider class of integrals, one can evaluate a set of master integrals by numerically solving a system of differential equations either in terms of kinematic parameters [247–249] or in by introducing an auxiliary mass flow variable [227, 250, 251].

The numerical method we used in [PhD1] relies on the iterated series expansion approach [252, 253] extended to be fully automated. To do this, `DiffExp` [179] was used, which needs a basis of master integrals resulting in a finite system of differential equations as an input. The basis is constructed in an automatic way.

To introduce the method, let us consider a basis of master integrals (MIs), $\vec{F}(x,\varepsilon)$, depending on the scale x in dimensional regularization, with $D = 4 - 2\varepsilon$ space-time dimensions. Differential equations of the following form can be derived:

$$\frac{d}{dx}\vec{F}(x,\varepsilon) = \hat{M}(x,\varepsilon)\vec{F}(x,\varepsilon)\,, \tag{4.37}$$

where $\hat{M}(x,\varepsilon)$ is a block-triangular matrix and each of the blocks is connected with a sector of integrals. With these sectors denoted by $\vec{f}_i(x,\varepsilon)$, the following decomposition of DEqs can be done:

$$\frac{d}{dx}\vec{f}_i(x,\varepsilon) = M_i(x,\varepsilon)\vec{f}_i(x,\varepsilon) + B_i(x,\varepsilon)\vec{g}_i(x,\varepsilon)\,, \tag{4.38}$$

[3]The estimate takes into account the number of diagrams at the level of 10^5 and higher number of corresponding scalar and tensor Feynman integrals. Also, the loss of digit precision is expected due to numerical cancellations between individual loop integrals. For a way how to estimate higher orders uncertainties, see [PhD4] in List of papers and tables Tab. 9, Tab. 10 in chapter 5.

where $M_i(x,\varepsilon)$ is a diagonal block of $\hat{M}(x,\varepsilon)$ corresponding to the sector i, and $B_i(x,\varepsilon)\vec{g}_i(x,\varepsilon)$ captures the off-diagonal terms. Now we can expand the integrals and matrices in ε:

$$\begin{aligned}\vec{f}_i(x,\varepsilon) &= \sum_{j=-k}^{\infty} \vec{f}_i^{(j)}(x,\varepsilon)\,\varepsilon^j\,,\\ M_i(x,\varepsilon) &= \sum_{j=0}^{\infty} M_i^{(j)}(x,\varepsilon)\,\varepsilon^j\,.\end{aligned} \tag{4.39}$$

The system can be solved order by order in ε. The system of differential equations in (4.38) settles the master integrals up to the boundary conditions. The convenient choice of the boundary terms, for our approach, are master integrals which are finite in the dimensional regulator ε. To find this MIs representation, we use the package `Reduze`. These boundary conditions can be efficiently evaluated in the Euclidean region using sector decomposition or MB methods. Since these integrals result in a small number of sectors and there is no need to avoid Minkowskian thresholds by the contour deformation, we employ `pySecDec` for the calculation. This computation can be done with high accuracy.

The system of DEqs, on the other hand, is derived using `Kira`. Having boundary conditions evaluated numerically and the system of DEqs derived analytically, we transport the result from Euclidean point to the Minkowski point with an excellent precision using the method of series expansions of the DEqs system [247, 252, 253] and `DiffExp`. For the purpose of this thesis and the discussion which follows, we call the approach worked out in [PhD1] as Differential Equations with Euclidean Boundary Transport (`DEqsEBT`).

A scheme of the `DEqsEBT` method is presented in Fig. 17. We may choose different Euclidean points in which we compute the boundary terms numerically. To estimate the numerical error of the method, we can compute the difference between two (or more) results for the same final point in Minkowski kinematics obtained from the different boundary points. The uncertainty of the final results estimation depends on the error of the boundary conditions computation.

The most important novelty of our work is the construction of a framework for the application of the DEqs transport method to the calculation of physical processes. This method is based on two key features: (a) an algorithmic procedure for finding an integral basis for which the DEqs system is finite, and (b) a prescription for analytically continuing the series solutions across physical thresholds. With the availability of these

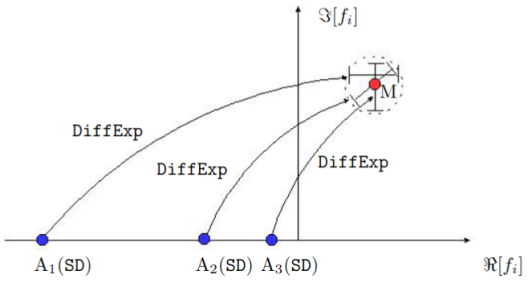

Figure 17: Illustration of the `DEqsEBT` method. The boundary conditions for the integral f_i are evaluated at one or several Euclidean points A_k, where the integral can easily be evaluated numerically with high precision using e.g. `pySecDec`. These boundary value(s) are then transported to the physical kinematic point of interest, using solutions of the DEqs system (4.38) derived with `DiffExp`, with the final result indicated in the figure by the red dot.

procedures, the feasibility of any cutting-edge calculation is only limited by the availability of the numerical boundary conditions and the integration-by-parts reductions, but no further analytic studies are needed.

Our method was developed in parallel to and independently of the papers which appeared practically at the same time [180,181]. Due to the complexity of calculations, it is desired to have several competing technical implementations, allowing cross-checks for these very complex calculations. In particular, our aim was to develop an approach that is not tailored to a particular process but that can be applied to a wide variety of problems.

To illustrate the benefits of our numerical `DEqsEBT` approach compared to the computation of each point individually, for example, with auxiliary mass flow methods, we take a scan over the kinematic phase-space of the two-loop box diagram, reproduced here in Fig. 18. A corresponding Feynman integral is a part of the $\mathcal{O}(\alpha^2)$ corrections to massive $e\mu$ scattering [254]

$$I_{\text{Fig. 18}}[D,\{a_i\},s,t,m_1^2,m_2^2] = \int \frac{\mathfrak{D}q_1\mathfrak{D}q_2}{[(q_1-p_1)^2]^{a_1}[q_1^2-m_1^2]^{a_2}} \times \frac{1}{[(q_1-p_1+p_3)^2-m_1^2]^{a_3}[(q_1-q_2)^2-m_1^2]^{a_4}} \frac{[(q_2-p_1)^2]^{-a_8}[(q_1-p_2)^2]^{-a_9}}{[(q_2-p_1+p_3)^2]^{a_5}[(q_2+p_2)^2-m_2^2]^{a_6}[q_2^2]^{a_7}} \tag{4.40}$$

where $\mathfrak{D}q_n \equiv \frac{d^Dq_n}{i\pi^{D/2}}$ and $p_1^2 = p_3^2 = m_1^2$, $p_2^2 = p_4^2 = m_2^2$, $p_1\,p_2 = (s-m_1^2-m_2^2)/2$, $p_1\,p_3 = (2m_1^2-t)/2$, $p_2\,p_3 = (s+t-m_1^2-m_2^2)/2$.

This $2 \to 2$ scattering example is more general than the main 3-loop numerical results discussed in the next chapter for up to 3-loop self-energy and vertex Feynman diagrams.

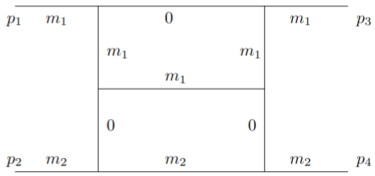

Figure 18: Two-loop box diagram with four scales: s, t, m_1, m_2.

With input parameters $s = 2$, $t = 5$, $m_1^2 = 4$ and $m_2^2 = 16$ we obtain

$$\begin{aligned} &I_{\text{Fig. 18}}[2,1,1,1,1,1,1,0,0,s,t,m_1^2,m_2^2] = \\ &+ 0.000328707579/\varepsilon^2 - (0.0014129475 - 0.0020653306\ i)/\varepsilon \\ &- (0.005702737 - 0.000485980\ i) + \mathcal{O}(\varepsilon). \end{aligned} \tag{4.41}$$

The $I_{\text{Fig. 18}}$ integral family involves 55 master integrals. Here and in all the following results, we show all significant digits, i.e. the numerical error only affects digits beyond the ones shown in the equations.

Since the `DEqsEBT` strategy deals with the thresholds in an automatic way and system of differential equations with a basis of finite master integrals, we are able to cover the full physical phase space by performing the DEqs transport along the differential variable t, as discussed originally in [179]. The result is shown in Fig. 19.

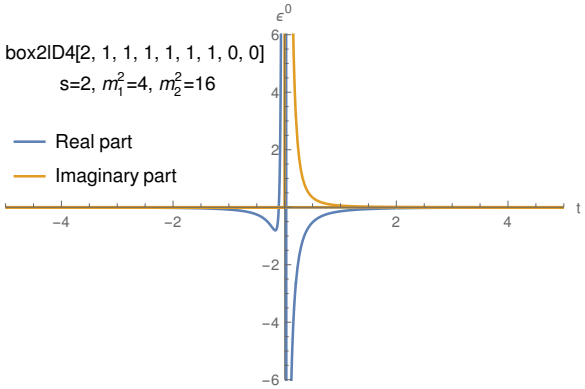

Figure 19: A plot of the finite part `box2lD4` of the integral $I_{\text{Fig. 18}}$ evaluated in $D = 4 - 2\varepsilon$. The plot range is $t \in [-5, 5]$ containing 456 points.

The integration-by-parts reduction and boundary terms need to be evaluated only once before sampling any number of phase-space points. The transport along the t axis

crosses one threshold region for this case, and it can be carried out with `DiffExp` in 30 minutes on 1 core. Subsequently, the finite basis results are transformed back to a basis in $D = 4 - 2\varepsilon$ to arrive at the desired physical result. The numerical evaluation of this result for any single phase-space point requires only a few seconds. Thus, it is possible to efficiently evaluate a large number of phase-space points. Such a strategy for fast phase-space sampling is not available for methods where the DEqs transport is performed in terms of an unphysical or complex variable, such as auxiliary mass flow [181, 227, 250, 251]. Thus, the `DEqsEBT` is worth further tests and developing in future.

The part that needs the most computing resources in the `DEqsEBT` approach is the IBP reduction with `Kira` and numerical boundary condition evaluation with `pySecDec`. The transport from Euclidean points to the Minkowski region is automated, very fast and deals with thresholds. The approach developed in [PhD1] is not uniquely tied to using `pySecDec` for the boundary conditions, but any other sector decomposition tool or other numerical method can be used. The point is that in the Euclidean region, the integral is free of singularities and thus one has robust numerical convergence. More digits of precision could be achieved by simply increasing the number of integration points (assuming that one does not reach the limit imposed by the machine precision). In our strategy, knowing the boundary conditions numerically is not a backup solution but a primary use case: it is important to stress that the capabilities of the differential equations method to reach new state-of-the-art computations are merely limited by the availability of the numerical boundary conditions and the integration-by-parts reductions, when following our strategy. No further analytic studies are involved. In practice, a set of $\pm i\delta$-prescriptions has to be given to `DiffExp` in order to cross singularities and branch-cuts. In the `DiffExp` paper [179], it is not fully specified how to obtain such prescriptions in an automated manner. For that, we consider all unitarity cuts across a diagram topology [255], and for each cut we obtain a linear polynomial of the form $s - M^2$, where s is the square of the momentum flowing across the cut, and M^2 is the square of the sum of the masses of the cut propagators. Each polynomial is assigned a $+i\delta$-prescription and given to `DiffExp`, which allows for the automated crossing of the unitarity cut. Interestingly, we do not search for anomalous thresholds [256, 257], which cannot be found by unitarity cuts. This was sufficient for our applications as we did not observe such thresholds during the transport from the Euclidean to the physical region. In general, `DiffExp` will give an error if a singularity is encountered for which a delta-prescription is not provided. This way, we manage to fully automate the question of crossing thresholds. In previous studies, it was not discussed how to

perform the basis choice and threshold crossing in an automated fashion. Let us note that recently identification of Landau poles was applied to `SD` in [212], see sections 4.3 and 5.1.3. For more on recent applications of Landau poles to the analysis of multiloop Feynman integrals, see [258].

Concerning the run time needed to evaluate MIs within `DEqsEBT`, at the moment we are focusing on self-energy and vertex integrals, thus let us discuss the vertex defined in Fig. 24 for which a numerical solution will be given in chapter 5.2. First, DEqs must be prepared for `DiffExp` and the major bottleneck is the run time of `Kira`. For the vertex in Fig. 24 we need 4 hours to construct the DEqs system on a 12-core, 2.7 GHz Intel Xenon processor cluster with 128 GB of RAM. The second part is the computation of Euclidean boundary terms,which we evaluate with the sector decomposition program `pySecDec`. Since the boundary terms are finite integrals by construction and are free of thresholds in the Euclidean region, the Monte-Carlo (MC) or quasi-Monte-Carlo (QMC) scaling rules apply straightforwardly. With QMC, we expect to require $\mathcal{O}(10^{10})$ points to reach an accuracy of 10 digits for an arbitrary Feynman integral, whereas presently unrealistic $\mathcal{O}(10^{20})$ points are expected to be needed for pure MC [259].

With 10^7 points, we ran the computation on a machine equipped with a 16-core Threadripper Pro 3955WX. Two different points in the Euclidean region were chosen, and both took approximately 3 days to complete. The convergence of the numerical integration appeared better than expected by the approximate $\mathcal{O}(1/N)$-estimate for QMC. In particular, the maximum relative accuracy estimated by `pySecDec` was $2.2 \cdot 10^{-9}$ among all the integrals in the basis.

The final part of the computation is the transport of the boundary terms to the Minkowski regions. The run time of this part of the computation highly depends on the individual application of the transported result. In our case, we are interested in the evaluation of the Feynman integral at one particular point. With `DiffExp` this is accomplished in about 3.5 hours on a single CPU core for the discussed vertex in Fig. 24. Note that once the computation with `DiffExp` is finished, the integral is available for a fast evaluation (in terms of milliseconds) at an arbitrary point along the line of the transport from Euclidean to Minkowski point.

The numerical error estimation has two main ingredients: the numerical series expansion of the differential equation system with `DiffExp` and the numerical evaluation of the boundary terms with `pySecDec`. The numerical error from the series expansion can always be rendered negligible compared to the error from the boundary terms by evaluating the expansion to sufficiently high order. On the other hand, the numerical errors of the initial boundary terms can usually be directly mapped to the final result.

However, instead of relying on the error estimate from `pySecDec`, we verify the accuracy by carrying out separate transports from two different initial boundary points to the same final Minkowski point and taking the difference as an error estimate. This cross-check was sufficient for the examples presented here. Also, if necessary, it is relatively straightforward to increase the accuracy of the boundary terms by using more Monte-Carlo integration points, since the `SD` integrand is well-behaved in the Euclidean region.

Though in [PhD1] we have proved that the `DEqsEBT` method we developed and the obtained accuracy for MIs evaluation are sufficient for the final precision needs for the Tera-Z precision physics, the results which will be discussed in the next section for $\mathcal{O}(\alpha^2\alpha_s)$ precision EWPOs will be obtained mainly with the `AMFlow` package [181]. This method gives easily higher than 10-digit accuracy. Other methods like `MB`, `SD`, or just described `DEqsEBT` serve us with additional cross-checks. For our purposes, the `AMFlow` package appeared to be the most efficient, thus it deserves special attention.

4.6 `AMFlow`

`AMFlow` [181] is a *Mathematica* package for Feynman integrals computation with the use of the auxiliary mass flow method, which is based on IBP and differential equations.

Let us follow the conventions used in [181] when describing the method. Consider a general Feynman integral within the dimensional regularization scheme:

$$I(\vec{\nu},\vec{s},\varepsilon)=\int\prod_{i=1}^{L}\frac{d^Dl_i}{i\pi^{D/2}}\frac{\mathcal{D}_{K+1}^{-\nu_{K+1}}\cdots\mathcal{D}_N^{-\nu_N}}{(\mathcal{D}_1+i0^+)^{\nu_1}\cdots(\mathcal{D}_K+i0^+)^{\nu_K}}, \tag{4.42}$$

where $\nu_1...\nu_K$ are integers and $\nu_K+1...\nu_N$ are non-positive integers, $\vec{s}$ is a list of all kinematic variables including Mandelstam variables and particle masses, $D=4-2\varepsilon$ is a spacetime dimension, l_i are loop momenta, and L is the number of loops. Now we can define an auxiliary integral family, putting auxiliary parameter η to all propagators of (4.42)

$$I(\vec{\nu},\vec{s},\varepsilon,\eta)=\int\prod_{i=1}^{L}\frac{d^Dl_i}{i\pi^{D/2}}\frac{\mathcal{D}_{K+1}^{-\nu_{K+1}}\cdots\mathcal{D}_N^{-\nu_N}}{(\mathcal{D}_1-\eta)^{\nu_1}\cdots(\mathcal{D}_K-\eta)^{\nu_K}}. \tag{4.43}$$

The physical result can be easily recovered in the following limit

$$I(\vec{\nu},\vec{s},\varepsilon)=\lim_{\eta\to i0^-}I(\vec{\nu},\vec{s},\varepsilon,\eta). \tag{4.44}$$

The auxiliary integrals family can be computed conveniently when η approaches infinity. By the region analysis [260, 261], when $|\eta|$ is very large, the only contributing

region is the one with $l_i^\mu \sim \mathcal{O}(\sqrt{\eta})$ and so, we can expand every propagator in the following way

$$\frac{1}{((l+p)^2-m^2-\eta)^\nu} = \frac{1}{(l^2-\eta)^\nu} \sum_{i=0}^{\infty} \frac{(\nu)_i}{i!} \left(-\frac{2l \cdot p + p^2 - m^2}{l^2-\eta} \right)^i , \tag{4.45}$$

where $(\nu)_i \equiv \Gamma(\nu+i)/\Gamma(\nu)$ is the Pochhammers symbol. After expanding all of the propagators this way, what we are left with are combinations of the vacuum integrals of the equal mass, which have been studied widely in the literature [262–267]. Though, auxiliary integrals $I_aux(\vec{\nu}, \vec{s}, \varepsilon, \eta)$ can easily be obtained. Then the remaining step is to recover the physical result, as a result of analytic continuation.

To perform the analytic continuation, we need to set up and then solve a set of differential equations. Auxiliary integrals can be expressed as a linear combination of master integrals, and then we only need to do the continuation for the master integrals. Let us denote the master integrals vector as $\vec{\mathcal{I}}_{aux}(\vec{s}, \varepsilon, \eta)$. By the integral reduction, we can also get the set of differential equations in the following form

$$\frac{\partial}{\partial \eta} \vec{\mathcal{I}}_{aux}(\vec{s}, \varepsilon, \eta) = A(\varepsilon, \eta) \vec{\mathcal{I}}_{aux}(\vec{s}, \varepsilon, \eta). \tag{4.46}$$

These differential equations can be numerically solved with the use of the series expansion for any generic, fixed kinematic configuration $\vec{s} \to \vec{s_0}$. Note that it is reasonable to choose $\vec{s_0}$ as some simple rational numbers if possible, as the computational time depends heavily on the choice of $\vec{s_0}$. It is similar to solving differential equations with respect to kinematic variables numerically, which can be used for the flow of parameter η from ∞ to the physical value of $i0^-$.

As for the analytic continuation, first we have to define a path connecting points $\eta = \infty$ and $\eta = i0^-$, characterized by a set of points $\{\eta_0, \eta_1, ..., \eta_l\}$. The series expansion is then performed on them in order. After the choice is made, the flow of auxiliary mass is performed in three main steps. First is to expand the integrals around $\eta = \infty$ and estimating at $\eta = \eta_0$. Then, expanding at $\eta = \eta_i$ and estimating at $\eta = \eta_{i+1}$ for $i = 0, ..., l-1$. Lastly, expanding at $\eta = 0$ and matching at $\eta = \eta_l$ to determine the unknown coefficients in the formal asymptotic series. As a result, it is possible to take the limit $\eta \to i0^-$ for the expansion at $\eta = 0$ to retrieve the physical results.

This method is efficiently implemented in the `AMFlow` package for *Mathematica*. In section 5.1.4 it is described how the package was used for the three-loop computation within the automated scripts.

5 Calculations at the three-loop order for the SM muon and Z boson decays

In this chapter, it is shown how we split and calculate the full two-loop $\mathcal{O}(\alpha\alpha_s)$ and three-loop $\mathcal{O}(\alpha^2\alpha_s)$ terms for W, Z boson self-energies and $W\bar{l}\nu$ vertex. As mentioned in subsection 3.3.2, to avoid the double counting in the final merging of all the available results that will be included in phenomenological studies, in calculations we exclude simpler, factorizable contributions that have already been computed, i.e. diagrams with a gluon exchange and two closed fermionic loops as well as diagrams with three closed fermionic loops [167, 168].

We break the genuine 3-loop contributions into parts that can be evaluated and cross-checked individually. The final results for each part are presented. The procedure for amplitudes evaluation is an extension and continuation of what was outlined at the one-loop level in section 3.3. With each loop order, the complexity and the bookkeeping of calculations grow rapidly. Our approach, based on `FeynArts` and `FeynCalc`, later connected with numerical packages, mainly `AMFlow`, is one of the three approaches developed in recent years in the working group to which I belong. These independent studies include calculations at the University of Silesia in Katowice. As mentioned before, it is based on `FeynArts` and `FeynCalc` and `AMFlow` or previously `pySecDec` and `MB` for numerics. The translation of integral notations from `FeynArts` with or without simplified algebraic manipulations of Feynman integrals for the numerical calculations by `pySecDec` and `AMFlow` is described in sections 5.1.1 and 5.1.4, respectively. Most of the suitable transformations were prepared in `FORM`, `Python` and `Mathematica` scripts by me. Examples of such studies are given in sections 5.1.1, 5.1.2, 5.1.4, 5.2 and appendices D and F. For the 3-loop order results, other automations connected with the calculation of derivatives of self-energy amplitudes over squared momenta are needed for charge and wave function renormalization, as defined in section 3.1.2 and 3.1.1. As an example, let us consider a derivative of the B_0 one-loop Passarino-Veltman integral over the external momentum p

$$\frac{\partial^2}{\partial p_\mu \partial p^\mu}\mathrm{B}_0(p^2, m_1, m_2)\bigg|_{p^2=0} = \left(\frac{\partial^2 \mathrm{B}_0}{\partial (p^2)^2}\, 4p^2 + 2D\, \frac{\partial \mathrm{B}_0}{\partial (p^2)}\right)\bigg|_{p^2=0} = 2D\, \frac{\partial \mathrm{B}_0}{\partial (p^2)}\bigg|_{p^2=0}. \quad (5.1)$$

Then

$$\begin{aligned}
\frac{\partial}{\partial(p^2)}\mathrm{B}_0(p^2,m_1,m_2)\Big|_{p^2=0} &= \frac{1}{2D}\ \frac{\partial^2}{\partial p_\mu \partial p^\mu}\left\langle \frac{1}{[q^2-m_1^2]\,[(q+p)^2-m_2^2]}\right\rangle\Big|_{p^2=0} \\
&= \frac{1}{2D}\ \frac{\partial}{\partial p_\mu}\left\langle -\frac{2(q_\mu+p_\mu)}{[q^2-m_1^2]\,[(q+p)^2-m_2^2]^2}\right\rangle\Big|_{p^2=0} \\
&= \frac{1}{2D}\left[\left\langle -\frac{2D}{[q^2-m_1^2]\,[(q+p)^2-m_2^2]^2}\right\rangle \right. \\
&\qquad \left. + \left\langle \frac{8(q+p)^2}{[q^2-m_1^2]\,[(q+p)^2-m_2^2]^3}\right\rangle\right]_{p^2=0},
\end{aligned}$$

where $\langle\cdots\rangle$ denotes a loop integral and q is a loop momentum. For 1-loop derivatives used directly with `FeynArts`, see the file 1LCT.nb in repository [166]. Beyond one-loop, we derived recursive relations for general 2- and 3-loop Feynman integrals in Mathematica.

In the treatment of topologically equivalent diagrams/amplitudes, we relied on the method developed in [268] for the identification of Feynman integrals based on Symanzik polynomials defined in Appendix C, adjusted to our needs.

The second approach is by A. Freitas, based on `FeynArts`, `FORM` [269], `TVID2` [270] and with basic algebraic amplitudes simplification, which result in the sets of `Yint` multiloop tensor integrals worked out analytically or numerically with high accuracy, see section 5.1. We should mention that `TVID2` is presently limited to the calculation of a class of planar three-loop self-energy master integrals with arbitrary masses, with 12 master integrals (no dotted propagators) and 15 MIs with dotted propagators. For the 2-loop case, there are 6 MIs, which are enough to calculate 3-loop counterterms with one and two-loop Feynman diagrams discussed below.

The last, third approach to evaluation of amplitudes is based on the `DIAGEN` C++ generator of Feynman diagrams and amplitudes by M. Czakon, developed originally for calculation of radiative corrections with Majorana fields [271, 272]. The package was improved recently by J. Usovitsch to include additional automation tools, e.g. generating higher order counterterms.

It appeared that independent cross-checks of intermediate 1- 2- and 3-loop calculations based on the just described three approaches helped to eliminate errors, starting from such trivial problems as the proper normalization of integrals in various programs, as briefly discussed in section 3.3.1, equations (3.37)-(3.40). The independent cross-checks of the results are necessary at various levels, i.e. amplitudes, semi-numerical results, with lower order renormalization constants kept symbolically and on the pure

numeric level. In this way, we can check all the intermediate results and track for possible errors while extending the calculations to the three-loop level.

In the next section, the genuine three-loop Z and W boson self-energy diagrams treatment will be described in detail.

5.1 Bookkeeping for the Z boson self-energy 3-loop diagrams

The following conventions for naming the integrals were used throughout the thesis and our in-house calculations. We keep similar conventions to those used for the complete two-loop calculations within our working group. We work on a list of YInt[{dd[mom,mass]},{dn[mom]}] with notation explained in Fig. 20.

```
1. yints. = lists of integrals in YInt form.

2. zz = Z boson self-energy

3. ta = diagrams with top quark and photon
4. th = diagrams with top quark and W/Z/H
5. lh = diagrams with light quark(s) W/Z/H
6. la = diagrams with light quark(s) and photon

7. merc = Mercedes star topologies
8. pl = planar ladder topologies
9. np = non-planar topologies
10. sl2 = topologies with two separate sub-loop bubbles
11. nsl = topologies with two nested sub-loop bubbles
12. sl1 = topologies with one sub-loop bubble
13. tlsl = topologies with a two-loop self-energy subloop



14. The integrals themselves have the header "YInt"
15. dd[pp,mm] is a propagator with momentum pp and mass mm
16. dn[pp] is the scalar production pp^2 in the numerator
```

Figure 20: Three-loop Z boson self-energy integral classes naming conventions. Blue coloured names indicate classes calculated with `pySecDec`

The list of all self-energy classes that have been calculated using `pySecDec` consists of all combinations of the topologies and particle contents marked with blue colour in Fig. 20, and it is listed below

- yints.zz.lh_merc yints.zz.lh_np yints.zz.lh_pl
- yints.zz.ta_merc yints.zz.ta_np yints.zz.ta_pl
- yints.zz.th_merc yints.zz.th_np yints.zz.th_pl

The results of all genuine three-loop W and Z boson self-energy calculations using both `pySecDec` and `AMFlow` are collected in repository [166].

The exemplary diagrams for topologies - *merc, pl* and *np* are depicted in Fig. 21

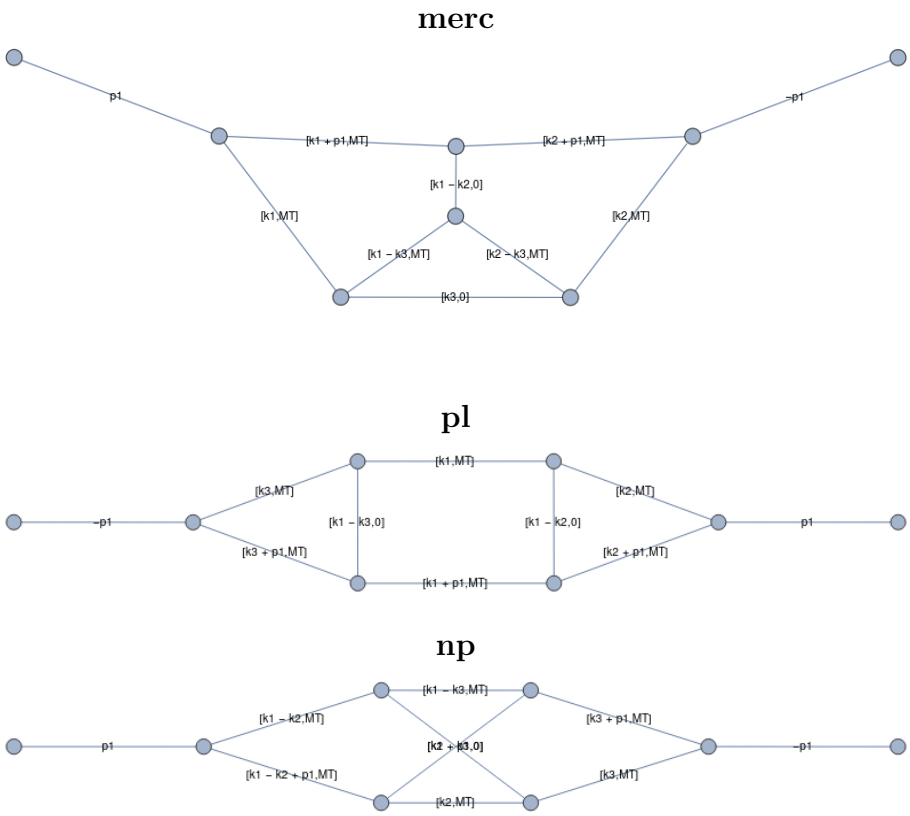

Figure 21: Exemplary diagrams representing three-loop Z boson self-energy topologies *merc, pl* and *np* respectively.

All of the bare three-loop self-energy integral classes for the W and Z bosons were computed with `AMFlow`.

Throughout the pySecDec calculations the following approximated mass values were used:

$$M_Z = 1, \quad M_W = \sqrt{0.78}, \quad M_H = \sqrt{1.88}, \quad M_t = \sqrt{3.6} \tag{5.2}$$

Other masses were neglected in our calculations. The mass approximation is a typical procedure while testing the methods.

All of the parameters used throughout the pySecDec calculations are listed in Tab. 4, see pySecDec Documentation for a detailed description of parameters. The QMC integrator was used with iterative decomposition method and contour deformation (for cases when it was necessary), no split option was necessary.

```
IntegratorOptions:

"verbosity=2,
minn=10**6,
maxeval=10**6,
epsabs=10**-8,
epsrel=10**-4,
transform='korobov3'"

IntegrationParameters:

"number_of_presamples=10**7,
deformation_parameters_maximum=0.01,
deformation_parameters_minimum=10**-7"
```

Table 4: The parameters used for the pySecDec calculations.

A short explanation of the settings and parameters for the pySecDec calculation, quoted from the pySecDec documentation

- `verbosity` - sets the amount of the output messages generated during integration.
- `minn` - minimal number of QMC latice points
- `maxeval` - the maximal number of integrand evaluation

- `epsabs` - sets the desired absoulte accuracy for the numerical evaluation
- `epsrel` - sets the desired relative accuracy for the numerical evaluation
- `transform` - the periodizing transform applied before the integration
- `numer_of_presamples` - Number of samples used for the contour optimization.
- `deformation_parameters_maximum` - maximal value the deformation parameters λ_i can obtain
- `deformation_parameters_minimum` - minimal value the deformation parameters λ_i can obtain

Although `pySecDec`, `MB`, and `AMFlow` are well suited for single integral calculation or, in the case of `AMFlow`, for a list of integrals sharing the same propagators, it is non-trivial to make the calculations in a fully automatic manner for a bigger list of integrals, as the run setup necessary for the computation becomes complex and time-consuming.

5.1.1 `pySecDec` automation

To understand the difficulties one encounters during automation of `pySecDec` calculations, it is important to know what the minimal set of information we need to provide to the program is, what the conventions are, how to run the program and finally, how to access and store the results in a convenient way.

`pySecDec` is interfaced via Python scripts, whereas internally for the algebraic part it uses Python and `FORM` and for the numerical part it is based on C++ code.

The general steps for the calculations are:

- Prepare two python scripts, following the names used in `pySecDec` examples, `generate.py` and `integrate.py`.
- Run the `generate.py` script, resulting in a subdirectory named as specified in the script.
- Call `make -C <name>` where <name> is the name of the previously created directory. It builds the code and produces a library for the numerical calculation for the integral.
- Run the `integrate.py` to perform the numerical computation of the integral.

To run the `pySecDec` calculation, first, we need to provide a definition of the integral, its internal and external lines. Internal lines can be defined in two different ways. First, by specifying the so-called *graph*. It is a list of vertices, to which the propagator is connected, for each propagator, and the propagator mass. As for the external lines, we need to specify which momenta is attached to which vertex. The other option is to provide a list of propagators in the '$momenta^2 - mass^2$' form along with the list of powers associated with each of the propagators. I decided to use the latter, as it was more convenient to construct from the integrals in the YInt form described earlier. Secondly, we need to specify loop momenta and the replacement rules to be used for our calculations. Keep in mind that it is not yet a place to provide numerical values for masses; it is to provide a set of symbolic replacements for the external momenta, defining Mandelstam variables or specifying vector replacements. Then, we need to specify the symbols for masses and Mandelstam variables, if they are real or complex, and to later associate numeric values with them. One may also specify additional prefactors, numerators, whether or not to perform contour deformation, which is needed if the F polynomial is smaller than 0, and the requested order of expansion in the ε regulator.

All of these are needed just for the preparation of the integral library and performing sector decomposition. Luckily, some settings could stay fixed for all integrals. The list of propagators, their powers, the name of the integral and whether contour deformation is needed has to be specified for each integral separately.

The next step is to prepare the *integrate.py* script. For this, we need to specify the path of the integral library, created in previous steps, choose integrator and integration options, such as number of integration points, demanded accuracy of the integration, etc., numerical values of the parameters, e.g. masses and finally, output file and formatting. Most of these settings do not have to be changed for different integrals, only the input path and output file.

The following setup was prepared to automate the whole procedure:

1. Generic `generate.py` and `integrate.py` files, that contain the structure of the files needed for `pySecDec` with placeholders, that are later substituted with the input for a given integral.

2. Generic *Mathematica* script translating YInt (YInt[{dd[mom,mass]},{dn[mom]}]) notation to `pySecDec` format of propagators and their powers (including numerators) and assigning integral names, by the integral family name and its number

in the list. It also saves the complete list of integrals of a given family in both YInt and `pySecDec` format to the output directory.

3. Control script, written in Python, passing all the chosen options for `pySecDec` calculation to *Mathematica* script described above, creating all `pySecDec` files for given classes of integrals. It also creates the structure of result files:

   - `Results/`
     - `Name_of_integral_family/` - separate directories for each integral family
       - `AllIntegrals.txt` - list of all integrals in the class, in `pySecDec` and YInt format
       - `MathScript_familyname.m` - *Mathematica* script, as described in point 2 with all the input already set for the given class of integrals
       - `Euclidean/` - directory for the results in Euclidean kinematics
       - `Minkowskian/` - directory for the results in Minkowskian kinematics
         - `results.out` - textfile containing all the numerical results for the class of integrals and kinematics
         - `numerical_results/`
           - `INT_N.in` - Definition of the N-th integral in YInt and `pySecDec` format
           - `INT_N.out` - `pySecDec` numerical result for the N-th integral
         - `pySecDec_files/`
           - Subdirectories for each integral containing all the `pySecDec` files needed for the computation as well as the output/log files for each of the commands.

4 Python script to run `pySecDec` computation for all the integrals for the given classes.

5 *Mathematica* notebooks to create the result tables.

Having prepared this setup is almost enough to run the `pySecDec` calculations smoothly, in an automated manner. The only remaining issue is the error handling. In general, errors could come up for two main reasons. One, in case of integrals with many propagators and high tensor rank, for example, 8 propagators and 3 inverse

propagators, during the `generate.py` run it could happen that the memory necessary for the sector decomposition exceeds the memory available on the machine (128GB in our case). If that happened, it would get stuck, without any error message, unless the whole automated script was killed. The other possibility was when the contour deformation option was enabled, but the deformation parameters for the calculation were not sufficient, and the code failed to find the contour and printed out the error during the `integrate.py` script run. As for the second error, the workaround is to simply try tuning the contour deformation parameters. It does not stop the whole automated script, but requires additional manual work. For the fix, one only has to rerun the last step of the whole process, i.e. the numerical integration for the integrals that were not calculated. Although the first issue is a bit more problematic in its nature, inspecting the process showed that it happens more or less after a given runtime, simply skipping the integral after this time solved as a workaround, to keep the calculations running. Yet, it does not serve as a solution to the problem. These integrals could not be solved directly in `pySecDec`, these would have to be either treated with IBP first, or reduced by hand, as described in the next section.

5.1.2 `pySecDec` benchmarks for 3-loop SE calculations

Result tables for all of the classes calculated in Minkowskian kinematics are available in repository [166] in the pySecDec_results/Tables/Complete directory.

`$Failed` means that the calculation was not handled till the end so either it exceeded 6h computation time for sector decomposition part (this was the time after which the integral got stuck anyways on our machine, so we set a time limit for this one part to avoid waiting for results that will not come anyways), or there was some issue in latter steps of calculations.
Result tables for only the scalar integrals are available in repository [166].

Result table with comparison between `pySecDec` results and MB results for lh_merc scalar integrals can be found in repository [166].

The last three integrals in the full `ta_np` class (INT33-35) mentioned above failed to calculate straightforwardly. Reducing one tensor rank by cancellation of the denominator with numerator terms appears to be helpful so that the resulting set of integrals can be calculated. For instance

$$I33 = \frac{k_1^2 * k_1^2 * (k_2 + p_1)^2}{((k_1 - k_2)^2 - M_t^2) * (k_2^2 - M_t^2) * ((k_1 - k_3)^2 - M_t^2) * (k_2 - k_3)^2} * \frac{}{(k_3^2 - M_t^2) * (k_1 + p1)^2 * ((k_1 - k_2 + p_1)^2 - M_t^2) * ((k_3 + p_1)^2 - M_t^2)} \tag{5.3}$$

can be written as

$$I33 = \frac{(\overbrace{(k_1+p_1)^2}^{1} - \overbrace{2k_1p_1}^{2} - \overbrace{p_1^2}^{3}) * k_1^2 * (k_2+p_1)^2}{((k_1-k_2)^2 - M_t^2) * (k_2^2 - M_t^2) * ((k_1-k_3)^2 - M_t^2) * (k_2-k_3)^2} * \frac{}{(k_3^2 - M_t^2) * (k_1+p1)^2 * ((k_1-k_2+p_1)^2 - M_t^2) * ((k_3+p_1)^2 - M_t^2)} \tag{5.4}$$

Three parts explicitly

$$I33_1 = \frac{(1) * k_1^2 * (k_2+p_1)^2}{((k_1-k_2)^2 - M_t^2) * (k_2^2 - M_t^2) * ((k_1-k_3)^2 - M_t^2) * (k_2-k_3)^2} * \frac{}{(k_3^2 - M_t^2) * ((k_1-k_2+p_1)^2 - M_t^2) * ((k_3+p_1)^2 - M_t^2)} \tag{5.5}$$

$$I33_2 = \frac{(-2k_1p_1) * k_1^2 * (k_2+p_1)^2}{((k_1-k_2)^2 - M_t^2) * (k_2^2 - M_t^2) * ((k_1-k_3)^2 - M_t^2) * (k_2-k_3)^2} * \frac{}{(k_3^2 - M_t^2) * (k_1+p1)^2 * ((k_1-k_2+p_1)^2 - M_t^2) * ((k_3+p_1)^2 - M_t^2)} \tag{5.6}$$

$$I33_3 = \frac{(-{p_1}^2) * k_1^2 * (k_2+p_1)^2}{((k_1-k_2)^2 - M_t^2) * (k_2^2 - M_t^2) * ((k_1-k_3)^2 - M_t^2) * (k_2-k_3)^2} * \frac{}{(k_3^2 - M_t^2) * (k_1+p1)^2 * ((k_1-k_2+p_1)^2 - M_t^2) * ((k_3+p_1)^2 - M_t^2)} \tag{5.7}$$

Having this, we can cancel the red part in one of the three 'new' integrals; the other two parts are -1 and -2 ranks, respectively, from the integral we have started with. With this simple method, it seems to be possible to go around problems with (at least) some of the tensor integrals. Below are the results for all 3 integrals arising from reducing the INT33 tensor rank calculated in the Minkowskian region

$$\begin{aligned} I33_{(1)} = \varepsilon^{-3} &: 8.00833340104159497 \pm (1.08726560064887988 * 10^{-7}) \\ \varepsilon^{-2} &: -19.9282296580690748 \pm (1.07082843736891324 * 10^{-6}) \\ \varepsilon^{-1} &: 51.9407417049247329 \pm (4.63507929766674586 * 10^{-6}) \\ \varepsilon^{0} &: -113.229130870223855 \pm (0.0000239977999079303774) \end{aligned} \tag{5.8}$$

$$\begin{aligned} I33_{(2)} = \varepsilon^{-3} &: -0.749999999523622618 \pm (1.53778428499841512 * 10^{-9}) \\ \varepsilon^{-2} &: 1.98325397728214048 \pm (1.76703999135918654 * 10^{-7}) \\ \varepsilon^{-1} &: -5.34792922577319274 \pm (5.96767220253102382 * 10^{-7}) \\ \varepsilon^{0} &: 16.1903791677231688 \pm (3.17038081118347636 * 10^{-6}) \end{aligned} \tag{5.9}$$

$$
\begin{aligned}
I33_{(3)} = \varepsilon^{-3} &: 0.500000000037367887 \pm (9.63062578009716486 * 10^{-10}) \\
\varepsilon^{-2} &: -1.34994707164775152 \pm (3.96306924219847208 * 10^{-8}) \\
\varepsilon^{-1} &: 3.28236060528419493 \pm (7.76426881841271045 * 10^{-8}) \\
\varepsilon^{0} &: -8.58702962662703762 \pm (4.18780226715803424 * 10^{-7})
\end{aligned}
\tag{5.10}
$$

Summing up the results, we get:

$$
\begin{aligned}
I33 = \varepsilon^{-3} &: 8.25833340052785 \pm (1.08741699147935 * 10^{-7}) \\
\varepsilon^{-2} &: -20.5615365637035 \pm (1.08603335002679 * 10^{-6}) \\
\varepsilon^{-1} &: 54.0063103254137 \pm (4.67398326888917 * 10^{-6}) \\
\varepsilon^{0} &: -120.83248041132 \pm (2.42099378724373 * 10^{-5})
\end{aligned}
\tag{5.11}
$$

For comparison, the results from `AMFlow`

$$
\begin{aligned}
I33_{\text{AMFlow}} = \varepsilon^{-3} &: 8.258328686139234884863703846694291348 26‘28.629706735702637 \\
\varepsilon^{-2} &: 20.561509311576615472654648384194697784 61‘28.283889658405894 \\
\varepsilon^{-1} &: 54.006239961537970106445943297940254615 96‘28.175914822351462 \\
\varepsilon^{0} &: -120.832326158703024410020832763699407992 45‘28.11234603800177
\end{aligned}
\tag{5.12}
$$

As a test of this method, the same calculation was done in the Euclidean region. The results for each part and the full result are

$$
\begin{aligned}
I33_{(1)} = \varepsilon^{-3} &: 7.59166680844217545 \pm (9.85655572039133668 * 10^{-8}) \\
\varepsilon^{-2} &: -20.7058822437051866 \pm (8.62058895228057950 * 10^{-7}) \\
\varepsilon^{-1} &: 55.2775401005482223 \pm (4.15341994614910242 * 10^{-6}) \\
\varepsilon^{0} &: -121.760015759083217 \pm (0.0000207199076949497914)
\end{aligned}
\tag{5.13}
$$

$$
\begin{aligned}
I33_{(2)} = \varepsilon^{-3} &: 0.749999999972988496 \pm (1.76033786105748168 * 10^{-9}) \\
\varepsilon^{-2} &: -2.19181726801324261 \pm (1.93793666215441322 * 10^{-7}) \\
\varepsilon^{-1} &: 5.96700462011761790 \pm (6.70983596045038024 * 10^{-7}) \\
\varepsilon^{0} &: -16.1689301802892835 \pm (3.56517086852064105 * 10^{-6})
\end{aligned}
\tag{5.14}
$$

$$
\begin{aligned}
I33_{(3)} = \varepsilon^{-3} &: 0.500000000729866834 \pm (8.92942843833251899 * 10^{-10}) \\
\varepsilon^{-2} &: -1.48898936314846209 \pm (3.00880392952002667 * 10^{-8}) \\
\varepsilon^{-1} &: 3.72341477857426462 \pm (9.76640126664948071 * 10^{-8}) \\
\varepsilon^{0} &: -8.78511422350637972 \pm (4.25952817276685563 * 10^{-7})
\end{aligned}
\tag{5.15}
$$

Summing up the results, we get

$$
\begin{aligned}
I33 = \varepsilon^{-3} &: 6.34166680773932 \pm (9.8585319410272 * 10^{-8}) \\
\varepsilon^{-2} &: -17.0250756125435 \pm (8.84085297929827 * 10^{-7}) \\
\varepsilon^{-1} &: 45.5871207018563 \pm (4.20840284366895 * 10^{-6}) \\
\varepsilon^{0} &: -96.8059713552876 \pm (2.1028705476361 * 10^{-5})
\end{aligned}
\tag{5.16}
$$

The next set of tests was to choose the best setup for our integrations in `pySecDec`, including the choice of the integrator that should be used. Looking into the Tab. 5, one can easily see that the QMC works best for the exemplary integral from the *lh_pl* family given in (5.17). The advantage is noticeable for all classes of integrals in our calculations, and the analysis is an extension of our work that was described in [PhD2] in List of papers. Not only does the integrator give the best accuracy for any number of points, but also, if we look at the error shrinking when increasing the number of points, it is much better than for other integrators.

$$
\frac{1}{(k_1^2) * (k_1 - k_2)^2 * (k_2^2) * ((k_1 - k_3)^2 - M_W^2) * (k_3^2) * (k_1 + p_1)^2 * (k_2 + p_1)^2 * (k_3 + p_1)^2}
\tag{5.17}
$$

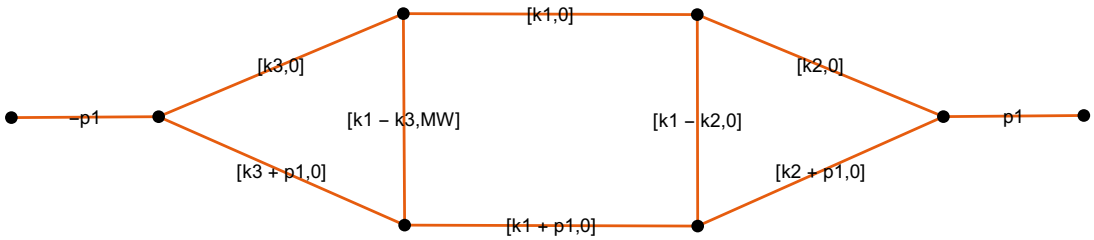

Figure 22: Feynman diagram corresponding to integral given by (5.17).

	Number of integration points				
Integrator	10^5	10^6	10^7	10^8	10^9
QMC v1.6.4	$4.047 * 10^{-6}$	$1.645 * 10^{-8}$	$8.266 * 10^{-11}$	$3.894 * 10^{-12}$	$7.678 * 10^{-13}$
QMC v1.5.2	$1.214 * 10^{-1}$	$1.629 * 10^{-4}$	$4.939 * 10^{-6}$	$7.484 * 10^{-7}$	$4.131 * 10^{-11}$
Vegas v1.5.2	$2.898 * 10^{-3}$	$6.770 * 10^{-4}$	$2.135 * 10^{-4}$	$6.746 * 10^{-5}$	$2.137 * 10^{-5}$
Divonne v1.5.2	$1.62 * 10^{-3}$	$2.697 * 10^{-4}$	$5.309 * 10^{-5}$	$1.147 * 10^{-5}$	$2.564 * 10^{-6}$

Table 5: Comparison of absolute errors given by different integrators within `pySecDec` for the integral given in (5.17).

The computations were performed within Euclidean kinematics ($s = -1$) using `pySecDec` version 1.5.2, extended by the update from the latest version 1.6.4. The huge upgrade in performance is due to the better optimisation of the integrand code and the updated, faster implementation of the old integrator library. A majority of intermediate results were obtained using the older `pySecDec` version 1.5.2, which was the most recent version available at the time of computation. Through a comparison of different integrators within the same version of the software, it was observed that the QMC integrator has better scaling with respect to the number of integration points, outperforming other integrators. Consequently, the QMC integrator was used in the `pySecDec` computations. Furthermore, an analysis of QMC accuracy in the latest `pySecDec` version reveals significant improvements over the older version.

As mentioned earlier, the desired accuracy for each individual integral is $\mathcal{O}(10^{-10})$. Using `pySecDec` version 1.5.2, computation of a single integral varied between 10 minutes and a day, with an average of a few hours per integral to get the accuracy as presented in Tab. 6, which was often not sufficient. With all the improvements of the `pySecDec` it is still not enough to compute each integral with demanded accuracy. Roughly estimating, assuming that `pySecDec` is soon capable of solving each integral with the accuracy that we need and the computation of each integral takes around 1 hour, there are $\mathcal{O}(10^3)$ self-energy integrals for W and Z bosons, which sum up to $\mathcal{O}(100)$ days of computing time just for the self-energy integrals evaluation. When considering vertices, there are in total $\mathcal{O}(10^6)$ integrals, more demanding than self-energy integrals, which makes the complete `pySecDec` computation still virtually impossible, at least using resources we have presently in our disposal.

Family Name	All	6 digits	8 digits	10 digits	<8 digits
yints.zz.lh_merc	67	6	1	1	40
yints.zz.ta_merc	18	12	5	1	13
yints.zz.th_merc	154	65	15	0	117
yints.zz.lh_np	76	5	0	0	29
yints.zz.ta_np	35	14	3	0	29
yints.zz.th_np	125	35	7	0	79
yints.zz.lh_pl	18	0	0	0	10
yints.zz.ta_pl	8	5	1	0	7
yints.zz.th_pl	45	14	5	0	28

Table 6: The table presents the number of integrals with at least 6, 8, 10 digits, as well as integrals with less than 8 digits of accuracy. The number of integrals from 8-digit and <8 digit columns may not add up to the whole number of integrals, since failed integrals are not counted here. Parameters and masses used for `pySecDec` calculations as discussed before. Explicit results can be found in repository [166].

5.1.3 Numerical results for chosen 3-loop SM Z boson decay integrals with `DEqsEBT`, `SD` and `AMFlow`

In this thesis, we developed some methods based on SD and DEqs towards the evaluation of the 3-loop SM calculations. Examples below prove that we are able nowadays to approach this level of precision towards the determination of Tera-Z EWPOs, which should be the next step after completion of the analysis for the $\mathcal{O}(\alpha^2\alpha_s)$ order, see section 5.3.

Let us consider the example of three-loop non-planar representative integrals with top quarks and W, Z internal masses shown in Fig. 23,

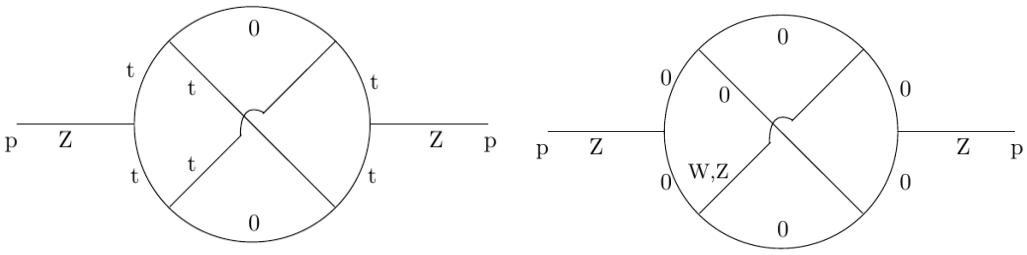

Figure 23: Three loop self-energy non-planar integral defined in (5.18). Z and t stand for the massive SM Z gauge boson and the top quark, respectively.

defined by (5.18) and (5.19), respectively,

$$I_{\text{Fig. 23}t}[D,\{a_i\},p^2,M_t^2] = \int \mathfrak{D}q_1\mathfrak{D}q_2\mathfrak{D}q_3 \frac{1}{[(q_1+p)^2]^{a_1}[(q_1-q_2)^2-M_{\rm t}^2]^{a_2}[(q_1-q_2+p)^2-M_{\rm t}^2]^{a_3}} \times \frac{1}{[q_2^2-M_{\rm t}^2]^{a_4}[(q_1-q_3)^2-M_{\rm t}^2]^{a_5}[(q_2-q_3)^2]^{a_6}} \frac{[q_1^2]^{-a_9}[(q_2+p)^2]^{-a_{10}}}{[q_3^2-M_{\rm t}^2]^{a_7}[(q_3+p)^2-M_{\rm t}^2]^{a_8}}, \quad (5.18)$$

$$I_{\text{Fig. 23}WZ}[D,\{a_i\},p^2,M_a^2 = M_W^2 \text{ or } \mathrm{M_Z^2}] = \int \frac{\mathfrak{D}\mathrm{q}_1\mathfrak{D}\mathrm{q}_2\mathfrak{D}\mathrm{q}_3}{[(\mathrm{q}_1-\mathrm{q}_2)^2]^{\mathrm{a}_1}[\mathrm{q}_2^2]^{\mathrm{a}_2}[(\mathrm{q}_1-\mathrm{q}_3)^2]^{\mathrm{a}_3}} \times \frac{[q_1^2]^{-a_9}}{[(q_2-q_3)^2-M_a^2]^{a_4}[q_3^2]^{a_5}[(q_1+p)^2]^{a_6}[(q_1-q_2+p)^2]^{a_7}[(q_3+p)^2]^{a_8}}. \quad (5.19)$$

Diagram on the left in Fig. 23 includes the top quark, which circulates through six propagators. These integrals are computed with at least ten digits of accuracy in the Minkowski point around $\varepsilon = 0$ for $D = 4 - 2\varepsilon$ with `DEqsEBT`

$$I_{\text{Fig. 23}t}[1,1,1,1,1,1,1,1,-2,-1,M_{\rm Z}^2,M_{\rm t}^2] = 8.27490485938/\varepsilon^3 - 34.9869281045/\varepsilon^2 + 102.43077689/\varepsilon - 253.5072352, \quad (5.20)$$

$$I_{\text{Fig. 23}t}[4-2\varepsilon,1,1,1,1,1,1,1,1,-1,-2,M_{\rm Z}^2,M_{\rm t}^2] = 9.47745432492/\varepsilon^3 - 40.4955852564/\varepsilon^2 + 116.63419570/\varepsilon - 273.3763275, \quad (5.21)$$

$$I_{\text{Fig. 23}t}[1,1,1,1,1,1,1,1,1,0,-3,M_{\rm Z}^2,M_{\rm t}^2] = 19.8715753165/\varepsilon^3 - 74.436608700/\varepsilon^2 + 239.02713087/\varepsilon - 540.2221570. \quad (5.22)$$

Note that the tenth propagator in (5.18) is linearly dependent and can be written in terms of the first nine propagators. We included it as an auxiliary propagator to the definition to improve the readability of the final results in (5.20)-(5.22).

The non-planar integral in (5.19) consists of eight propagators with only one massive W or Z boson internal line. The other, massless propagators come from neglecting all particle masses other than the gauge boson masses, the Higgs boson and the top quark mass.

This example, for the parameter point $p^2 = M_{\mathrm{Z}}^2$ and $M_a = M_{\mathrm{Z}}$, belongs to a group of integrals which are difficult to evaluate with SD due to threshold effects (see previous discussion in section 4.3). Using `pySecDec` with 10^7 integration points, we obtain a result with less than two digits of precision

$$I^{\texttt{pySecDec}}_{\text{Fig. 23}WZ}[4-2\varepsilon,1,1,1,1,1,1,1,1,0,M_{\mathrm{Z}}^2,M_{\mathrm{Z}}^2] = 0.460 - 19.164\,i \pm (0.298 + 0.281\,i). \tag{5.23}$$

Increasing the number of integration points does not improve the accuracy substantially. On the other hand, `pySecDec` can deliver accurate results for Euclidean parameter points, $p^2 < 0$, which are used as boundary terms for our `DEqsEBT` method described in section 4.5. We thus obtain stable and precise results at the physical point

$$\begin{aligned} &I_{\text{Fig. 23}WZ}[4-2\varepsilon,1,1,1,1,1,1,1,1,0,M_{\mathrm{Z}}^2,M_{\mathrm{Z}}^2] \\ &= -0.000000000 - 19.1262302\,i + (151.51529 - 150.40641\,i)\,\varepsilon + \mathcal{O}(\varepsilon^2), \end{aligned} \tag{5.24}$$

$$\begin{aligned} &I_{\text{Fig. 23}WZ}[4-2\varepsilon,1,1,1,1,1,1,1,1,0,M_{\mathrm{Z}}^2,M_{\mathrm{W}}^2] \\ &= (5.1112260 - 18.5692007\,i) + (194.660753 - 78.842016\,i)\,\varepsilon + \mathcal{O}(\varepsilon^2). \end{aligned} \tag{5.25}$$

For the comparison, the corresponding constant parts of the results obtained with `AMFlow` are

$$\begin{aligned} &I^{\texttt{AMFlow}}_{\text{Fig. 23}WZ}[4-2\varepsilon,1,1,1,1,1,1,1,1,0,M_{\mathrm{Z}}^2,M_{\mathrm{Z}}^2] \\ &= 0.00000000000000 - 19.12623029908009\,i + \mathcal{O}(\varepsilon), \end{aligned} \tag{5.26}$$

$$\begin{aligned} &I^{\texttt{AMFlow}}_{\text{Fig. 23}WZ}[4-2\varepsilon,1,1,1,1,1,1,1,1,0,M_{\mathrm{Z}}^2,M_{\mathrm{W}}^2] \\ &= 5.11122637142328 - 18.56920074255880\,i + \mathcal{O}(\varepsilon). \end{aligned} \tag{5.27}$$

We can see they agree with good precision.

The integral family $I_{\text{Fig. 23}WZ}$ (5.19) involves 30 master integrals and is considered simple in the context of our method.

The next example is a family of 3-loop vertex integrals with one massive top quark

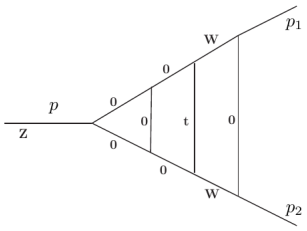

Figure 24: Three loop planar vertex diagram which corresponds to the integral in (5.28). W, Z and t stand for the W boson, Z boson and top quark, respectively.

and two massive W boson propagators, see Fig. 24, defined as

$$\begin{aligned} I_{\text{Fig. 24}}[D,\{a_i\},p^2,M_W^2,M_t^2] &= \int \frac{\mathfrak{D}q_1\mathfrak{D}q_2\mathfrak{D}q_3}{[q_3^2-M_{\text{W}}^2]^{a_1}[q_2^2]^{a_2}} \\ &\times \frac{1}{[q_1^2]^{a_3}[(q_1-p)^2]^{a_4}[(q_2-p)^2]^{a_5}[(q_3-p)^2-M_W^2]^{a_6}} \\ &\times \frac{[(q_1-q_3)^2]^{-a_{10}}[(q_1-p_2)^2]^{-a_{11}}[(q_2-p_2)^2]^{-a_{12}}}{[(q_3-p_1)^2]^{a_7}[(q_2-q_3)^2-M_t^2]^{a_8}[(q_1-q_2)^2]^{a_9}}, \end{aligned} \tag{5.28}$$

where $p = p_1 + p_2$ and $p_1^2 = p_2^2 = 0$. These integrals also appear in so far unknown $\mathcal{O}(\alpha^2\alpha_{\text{s}})$ corrections to Z-pole electroweak precision observables, constituting their most difficult parts.

With `pySecDec` we are unable to obtain a numerical result for the Minkowski point $p^2 = M_{\text{Z}}^2$. The problem already starts with the contour deformation, which is necessary for SD with Minkowski kinematics, and which fails to complete in a reasonable time. Similar to the SD method, the MB technique fails to deliver high-accuracy results for the considered integrals for $p^2 = M_{\text{Z}}^2$.

Using our `DEqsEBT` method, the calculation requires the numerical evaluation of 77 master integrals with Euclidean kinematics, $p^2 < 0$, for the boundary terms. For the purpose of the present example, they have been evaluated with `pySecDec` to 10-digit accuracy. After the transport to the physical point $p^2 = M_{\text{Z}}^2$, we get at least eight significant digits for integrals of the family (5.28) up to tensor rank-3 (i.e. $-3 \leq a_{10} + a_{11} + a_{12} \leq 0$). We here give numerical results for one rank-3 case

$$\begin{aligned} &I_{\text{Fig. 24}}[1,1,1,1,1,1,1,1,1,-1,-1,-1,M_{\text{Z}}^2,M_{\text{W}}^2,M_{\text{t}}^2] = \\ &0.0833333333/\varepsilon^3 + 0.636273147/\varepsilon^2 + (0.63462699 + 0.77044487\ i)/\varepsilon \\ &+ (5.5847828 + 6.1606031\ i) + \mathcal{O}(\varepsilon). \end{aligned} \tag{5.29}$$

The corresponding `AMFlow` result

$$
\begin{aligned}
&I^{\texttt{AMFlow}}_{\text{Fig. 24}}[1,1,1,1,1,1,1,1,1,-1,-1,-1,M_{\mathrm{Z}}^2,M_{\mathrm{W}}^2,M_{\mathrm{t}}^2] = \\
&0.08333333333333/\varepsilon^3 + 0.63627314842142/\varepsilon^2 \\
&+ (0.63462697873037 + 0.77044487418377\ i)/\varepsilon \\
&+ (5.58478329673337 + 6.16060310556605\ i) + \mathcal{O}(\varepsilon).
\end{aligned} \tag{5.30}
$$

5.1.4 Complete calculations with use of AMFlow - automation and results

In this section, we present our in-house method of automation of the AMFlow calculations using the list of integrals generated using FeynArts and further simplified with FORM. These algebraic simplifications were done to prepare the integrals for further computation with TVID2, but also for pySecDec and MB methods, and make individual integrals easier to compute. For instance, decreasing the rank of tensors by manipulation between numerators and denominators, as exemplified in section 5.1.2. Yet, the AMFlow individual integrals, in our studies, are not difficult to calculate, and to an extent, these simplifications would only slow down the overall calculations. To reverse the situation, we find integrals originating from the same Feynman diagrams and compute them together, saving up a lot of computational time, as we do not recompute the same integrals many times. Such reversed engineering for the calculation of alternative sets of simplified integrals served us as an alternative, independent check of calculations at the 3-loop level.

Analyzing the results presented in the previous subsections, one can see that the methods used for the complete two-loop calculation for the Z boson decay are not sufficient to compute each of the 3-loop self-energy integrals for the Z and W bosons. It is especially noticeable, taking into account the desired level of precision for this calculation, which is $\mathcal{O}(10^{-10})$ for each integral. For some of the integrals, one could play around and increase the precision of calculation by, for example, including more points in Monte-Carlo computation, but this would not solve the issue completely. I have prepared a script that creates a minimal set of integrals that need to be calculated for a single class (e.g. ta_np) of the SE integrals. It can be generalized, for instance, for 3-loop vertices, with small adjustments. It takes into account all possible momentum shifts and speeds up calculations significantly. It is then connected with AMFlow for the numerical evaluation.

The automation goes as follows:

- Load a list of integrals (YInt[{dd[mom,mass]},{dn[mom]}] form)

- Run the following steps in a loop (unless there are no integrals left unprepared for `AMFlow` calculation):

(1) Split the list of integrals into sublists of topologies which can possibly fit into one basis of propagators, inspecting U and F polynomials. (for now by hand, later on automated.)

(2) For each sublist, we take integrals with the largest number of propagators to create the initial *basis* constructed from these propagators. Three-loop self-energy diagrams include maximally 8 propagators in the denominator, yet for IBP reduction, we need one auxiliary propagator in the basis. This is obtained with `AMFlow` function `ToCompleteExplicit`. The resulting list of 9 propagators forms our initial *basis*.

(3) Set the family name that is needed by `AMFlow`, associated with the basis.

(4) Check if all masses for the given integral are the same as in *basis*. If yes, we proceed to the next step. Otherwise, we skip the integral and repeat step (4) for the next integral.

(5) Trying to shift momenta in propagators for the integral to the *basis*. The procedure for shifting is described individually later and depicted in Fig. F

(6) Save the list of integrals that were expressed in terms of the *basis* in `AMFlow` notation (i.e. j[familyname,powers]*coefficient, where powers is a list of powers of *basis* propagators) to a file.

(7) Remove the integrals from step (4) from the list of integrals and use the remaining integrals as a new list of integrals that we will try to resolve back in step 1. Again, it will result in a new basis, and the iteration continues this way.

- All of the bases created in the loop are also exported to the file.
- Feed the target integrals to the `AMFlow` for the numerical result with 30 digits accuracy.

The shift of momenta in propagators, mentioned in point (5) of the above loop, is done in the following way:

(1) Check if the mass configuration for the integral is the same as in the basis. If yes, proceed to step (2). Otherwise, proceed to the next integral.

(2) Check if all of the propagators of the integrals are not already in the basis, without the shifts.

(3) Create a list of replacements for all possible scalar products that can appear in the numerator, in terms of basis propagators.

(4) We set the replacements for each of the loop momenta as follows:

$$k_1 \to k_1 c_1 + k_2 c_2 + k_3 c_3 + p_1 c_4$$
$$k_2 \to k_1 c_5 + k_2 c_6 + k_3 c_7 + p_1 c_8$$
$$k_3 \to k_1 c_9 + k_2 c_{10} + k_3 c_{11} + p_1 c_{12}$$

Coefficients $c_1, \ldots, c_{12}$ may only take values from the set $\{-1, 0, 1\}$. Dismissing the combinations of coefficients resulting in the determinant of the Jacobian equal to zero.

(5) Create a list of all possible shifts.

(6) In a parallel loop, we take possible shifts, apply them to the integral propagators and check if they are all contained within the basis. If we find a shift that works (no matter if optimal by any criteria), we just break the loop and move to the next integral. It is done this way not to waste too much time searching for an optimal shift, which cannot save up a lot of time compared to any other shift, whereas searching for shifts naturally takes a relatively long time, as for each integral we have to check $\sim 2 * 10^5$ shifts.

Running the script results in creation of the following files:

- bases.m - List of bases used in the calculation
- ReplacementRulesX.m - List of replacements from YInts -> j-ints that we calculate with `AMFlow` for X-th basis in the list.
- targetintsX.m - Union of all the j-ints needed to represent each of the YInts - our target for `AMFlow` calculations for X-th basis in the list.
- jintsNumResX.m - List of the numerical replacement rules for the j-ints associated with the X-th basis in the list.
- YintsNumResX.m - List of replacements from YInts -> numbers for the X-th basis in the list.

Input used for the AMFlow calculation:

```
AMFlowInfo["Loop"] = {k1, k2, k3};
AMFlowInfo["Leg"] = {p1, p2};
AMFlowInfo["Conservation"] = {p2 -> p1};
AMFlowInfo["Replacement"] = {p1^2 -> s};
AMFlowInfo["Cut"] = {0, 0, 0, 0, 0, 0, 0, 0, 0};
AMFlowInfo["Numeric"] = {s -> 1};
AMFlowInfo["NThread"] = 6;

masses = {MZ -> 1, MW -> 401925/455938, MT -> 433000/227969,
          MH -> 312750/227969};
```

These results of automatically computed integrals with use of the AMFlow were later compared and cross-checked with pySecDec results whenever available. The results from both methods agree up to the accuracy of the pySecDec results.

Nr	The difference [AMFlow – pySecDec]	pySecDec error
1	-5.43749×10^{-9}	1.01754×10^{-8}
2	1.38627×10^{-10}	8.17054×10^{-10}
3	$9.44875\times10^{-8}-\frac{1.84686\times10^{-13}}{\text{eps}^3}+\frac{1.27918\times10^{-8}}{\text{eps}^2}+\frac{3.9239\times10^{-9}}{\text{eps}}$	$1.77638\times10^{-7}+\frac{1.75412\times10^{-13}}{\text{eps}^3}+\frac{1.26893\times10^{-8}}{\text{eps}^2}+\frac{1.18177\times10^{-8}}{\text{eps}}$
4	$-7.56094\times10^{-8}-\frac{1.5371\times10^{-13}}{\text{eps}^3}+\frac{4.64121\times10^{-9}}{\text{eps}^2}+\frac{7.06215\times10^{-9}}{\text{eps}}$	$2.24571\times10^{-7}+\frac{1.97021\times10^{-13}}{\text{eps}^3}+\frac{5.72647\times10^{-9}}{\text{eps}^2}+\frac{7.01857\times10^{-8}}{\text{eps}}$
5	$4.96074\times10^{-9}+\frac{1.76613\times10^{-8}}{\text{eps}}$	$8.45188\times10^{-8}+\frac{1.61926\times10^{-8}}{\text{eps}}$
6	$0.000017525+\frac{4.41425\times10^{-13}}{\text{eps}^3}-\frac{3.7912\times10^{-7}}{\text{eps}^2}+\frac{3.79687\times10^{-6}}{\text{eps}}$	$0.0000123162+\frac{3.34773\times10^{-12}}{\text{eps}^3}+\frac{4.32369\times10^{-7}}{\text{eps}^2}+\frac{1.96153\times10^{-6}}{\text{eps}}$
7	$-0.0000384912+\frac{9.3916\times10^{-12}}{\text{eps}^3}-\frac{9.29772\times10^{-8}}{\text{eps}^2}+\frac{8.83155\times10^{-7}}{\text{eps}}$	$0.0000211711+\frac{8.41012\times10^{-12}}{\text{eps}^3}+\frac{3.00071\times10^{-7}}{\text{eps}^2}+\frac{2.9724\times10^{-6}}{\text{eps}}$
8	$-3.73028\times10^{-7}-\frac{2.75753\times10^{-9}}{\text{eps}^3}+\frac{1.14596\times10^{-7}}{\text{eps}^2}-\frac{1.82801\times10^{-7}}{\text{eps}}$	$2.88821\times10^{-6}+\frac{1.72255\times10^{-9}}{\text{eps}^3}+\frac{1.56947\times10^{-7}}{\text{eps}^2}+\frac{3.80607\times10^{-7}}{\text{eps}}$

Table 7: Comparison between the difference of AMFlow and pySecDec results and pySecDec absolute error for the zz.ta_np class of integrals in Minkowski kinematics.

One may notice that the masses used in `pySecDec` calculations and `AMFlow` calculations do not match perfectly; this is because `AMFlow` needs rational numbers, whereas `pySecDec` can take any number format. Either way, for the comparison of the results, we choose to repeat the `AMFlow` calculations with the masses used in `pySecDec` (see (5.1)), rationalized with the use of the *Mathematica* `Rationalize[]` function, up to 10^{-12} accuracy. The comparison of the `AMFlow` and `pySecDec` results is shown in the table in Tab. 7. The comparison shows that the results obtained with both methods agree up to the `pySecDec` error. The two conclusions that can be drawn out of it are that, first of all, `pySecDec` error estimation is correct. Secondly, the system for the automated `AMFlow` calculation produces correct results.

The whole computation of nine integral classes mentioned before took less than two days on our computational server with use of the `AMFlow`, which is much shorter than `pySecDec` computation.

Later, the rest of the integral classes mentioned before in Fig. 20 were calculated. All of the results of `AMFlow` and `pySecDec` computations are available in repository [166].

The example of output in a table form for *zz.ta_merc* class is presented in Tab. 8.

zztamerc numeric results

Nr	Integral	AMFlow result
1	YInt[dd[q1, MT], dd[p1 + q1, MT], dd[q12, 0], dd[q2, MT], dd[q3, 0], dn[q13]]	0
2	YInt[dd[q1, MT], dd[p1 + q1, MT], dd[q12, MT], dd[q2, 0], dd[q3, MT], dn[q13]]	$163.573047410990696590159513888 + \frac{26.030253907516961753615552549 95}{\text{eps}^3} + \frac{23.306495739560551952819731455}{\text{eps}^2} + \frac{140.164064318762578459123683107}{\text{eps}}$
3	YInt[dd[p1 + q1, 0], dd[q12, MT], dd[q13, MT], dd[q2, MT], dd[q23, 0], dd[q3, MT]]	$-11.003957762151782725786106810 9 + \frac{2.4041138063191885070994763230 2}{\text{eps}}$
4	YInt[dd[q1, 0], dd[q12, MT], dd[q13, MT], dd[q2, MT], dd[p1 + q2, MT], dd[q3, MT], dd[p1 + q3, MT]]	$-0.60827910979390919403538613572 3$
5	YInt[dd[q1, MT], dd[p1 + q1, MT], dd[q12, MT], dd[q13, 0], dd[p1 + q2, 0], dd[q23, MT], dd[q3, MT]]	$-0.51997221068721533493577196489 7$
6	YInt[dd[p1 + q1, 0], dd[q12, MT], dd[q13, MT], dd[q2, MT], dd[q23, 0], dd[q3, MT], dn[q1]]	$58.132875588086001485252596913 + \frac{2.405098931091422403718619250 05}{\text{eps}^3} + \frac{9.337745023766037277506240308 3}{\text{eps}^2} + \frac{40.896833672126312467165973805 7}{\text{eps}}$
7	YInt[dd[q1, 0], dd[q12, MT], dd[q13, MT], dd[q2, MT], dd[p1 + q2, MT], dd[q3, MT], dd[p1 + q3, MT], dn[p1 + q1]]	$-4.601836423371124964939860400 6 + \frac{0.333333333333333333333333333 3}{\text{eps}^3} - \frac{0.324975265616082107075283301 99}{\text{eps}^2} + \frac{1.147778624599794785455899290 0}{\text{eps}}$
8	YInt[dd[q1, 0], dd[q12, MT], dd[q13, MT], dd[q2, MT], dd[p1 + q2, MT], dd[q3, MT], dd[p1 + q3, MT], dn[q23]]	$-8.782677656787380809790084150 8 + \frac{0.333333333333333333333333333 3}{\text{eps}^3} + \frac{0.341691401050584559591383364 68}{\text{eps}^2} + \frac{1.116509180589829036125512287 99}{\text{eps}}$
9	YInt[dd[q1, MT], dd[p1 + q1, MT], dd[q12, 0], dd[q13, MT], dd[q2, MT], dd[p1 + q2, MT], dd[q23, MT], dd[q3, 0]]	0.025397131986254597981696694373 8
10	YInt[dd[q1, MT], dd[p1 + q1, MT], dd[q12, MT], dd[q13, 0], dd[p1 + q2, 0], dd[q23, MT], dd[q3, MT], dn[q2]]	$-4.692352167651698751259288925 6 + \frac{0.166666666666666666666666666 67}{\text{eps}^3} + \frac{0.170845700525292279795691682339}{\text{eps}^2} + \frac{0.891587923628247851396089477 33}{\text{eps}}$
11	YInt[dd[q1, MT], dd[p1 + q1, MT], dd[q12, MT], dd[q13, 0], dd[p1 + q2, 0], dd[q23, MT], dd[q3, MT], dn[p1 + q3]]	$-4.030044338487875292937683200 6 + \frac{0.166666666666666666666666666 67}{\text{eps}^3} + \frac{0.170845700525292279795691682339}{\text{eps}^2} + \frac{0.891587923628247851396089477 33}{\text{eps}}$
12	YInt[dd[p1 + q1, 0], dd[q12, MT], dd[q13, MT], dd[q2, MT], dd[q23, 0], dd[q3, MT], dn[q1], dn[q1]]	$747.57091283083952956447577106 + \frac{30.368629558769788712551446416 0}{\text{eps}^3} + \frac{95.247036404840873895306067735}{\text{eps}^2} + \frac{419.263612142285339294420170609}{\text{eps}}$
13	YInt[dd[q1, 0], dd[q12, MT], dd[q13, MT], dd[q2, MT], dd[p1 + q2, MT], dd[q3, MT], dd[p1 + q3, MT], dn[p1 + q1], dn[p1 + q1]]	$-42.822351154790168838453214335 + \frac{5.226864528849511474103905166 77}{\text{eps}^3} - \frac{2.737184454613973284846917739 8}{\text{eps}^2} + \frac{22.638856071098197071911807034}{\text{eps}}$
14	YInt[dd[q1, 0], dd[q12, MT], dd[q13, MT], dd[q2, MT], dd[p1 + q2, MT], dd[q3, MT], dd[p1 + q3, MT], dn[p1 + q1], dn[q23]]	$-53.371687689813984986663620677 + \frac{9.620395724365689614874770002 1}{\text{eps}^3} - \frac{4.583409065086693444326797750 1}{\text{eps}^2} + \frac{19.818592969747337515734987274}{\text{eps}}$
15	YInt[dd[q1, 0], dd[q12, MT], dd[q13, MT], dd[q2, MT], dd[p1 + q2, MT], dd[q3, MT], dd[p1 + q3, MT], dn[q23], dn[q23]]	$23.438338173460835113014018121 + \frac{11.775494655457112018593096250 3}{\text{eps}^3} + \frac{22.952003843188403452467079949 8}{\text{eps}^2} + \frac{103.371391661611171922383879977}{\text{eps}}$
16	YInt[dd[q1, MT], dd[p1 + q1, MT], dd[q12, 0], dd[q13, MT], dd[q2, MT], dd[p1 + q2, MT], dd[q23, MT], dd[q3, 0], dn[p1 + q3]]	$\left\{1.205571162570276680928480662 27 - \frac{0.291874005359774980938782755569}{\text{eps}}\right\}$
17	YInt[dd[q1, MT], dd[p1 + q1, MT], dd[q12, MT], dd[q13, 0], dd[p1 + q2, 0], dd[q23, MT], dd[q3, MT], dn[q2], dn[q2]]	$10.950106744226336204591939683 + \frac{4.333923129409989206507583687 59}{\text{eps}^3} + \frac{7.044712735775344413431265568 5}{\text{eps}^2} + \frac{38.944177591080176772939734427 8}{\text{eps}}$
18	YInt[dd[q1, MT], dd[p1 + q1, MT], dd[q12, MT], dd[q13, 0], dd[p1 + q2, 0], dd[q23, MT], dd[q3, MT], dn[q2], dn[p1 + q3]]	$\left\{9.734099286725759909477481965 + \frac{4.375589796076655873174250354 26}{\text{eps}^3} + \frac{4.059014250400984776484955128 4}{\text{eps}^2} + \frac{22.613378394540114635644651645 0}{\text{eps}}\right\}$

Table 8: `AMFlow` result table for the *zz.ta_merc* class of integrals as defined in Fig. 20.

5.2 Towards complete 3-loop results for the Z decay EWPOs

After all of the W and Z boson self-energy contributions are calculated, the next step would be to add the contributions coming from the three-loop Z boson vertices. This is a much bigger and more complex task, as estimated in [PhD4]. In this section, a brief overview of the issue and some preparatory studies are presented. One of the contributing diagrams and its numerical result was already discussed in section 5.1.3.

$\mathbf{Z} \to b\ \bar{b}$		
Number of topologies	2 loops	3 loops
	14	211
Number of diagrams	2383	490387
Bosonic	2012	374296
1 Fermionic loop	371 (4)	108804 (76)
2 Fermionic loops	0	7287 (6)
QCD	185	39041
EW	2198	451346
Planar	2250 (13)	424362 (183)
Non-planar	133 (1)	66025 (28)
Number of configurations	101	721
Configurations with FL	27	352

Table 9: Classification made with respect to massive particles (H, W, Z, t), appearance and the number of fermionic loops inside. Numbers in brackets refer to the number of topologies in which those appear. QCD stands for diagrams where gluons appear, EW is the remaining part. The number of configurations with FL describes how many different internal particle configurations also contain at least one closed fermionic loop.

We have generated vertex diagrams for the $Z \to e^+e^-, ...$ and $Z \to b\bar{b}$ decay in the framework of SM using `aITALC` [273] at the two- and three-loop level. These diagrams have been split into classes, taking into account different features, such as

- topologies,
- number of closed fermionic loops,
- whether they contain gluons,
- planarity,
- couplings,
- massive internal particles.

The numbers of diagrams for all of them are collected in Tab. 9 and Tab. 10.

$\mathbf{Z} \to e^+ e^-, \ldots$		
Number of topologies	2 loops	3 loops
	14	211
Number of diagrams	2012	397690
Bosonic	1711	305293
1 Fermionic loop	301 (4)	86790 (76)
2 Fermionic loops	0	5607 (6)
QCD	1	1228
EW	2011	396462
Planar	1914 (13)	350709 (183)
Non-planar	98 (1)	46981 (28)
Number of configurations	69	449
Configurations with FL	27	313

Table 10: Classification made with respect to massive particles (H, W, Z, t) appearance and the number of fermionic loops inside. Numbers in brackets refer to the number of topologies in which those appear. QCD stands for diagrams where gluons appear, and EW is the remaining part. The number of configurations with FL describes how many different internal particle configurations also contain at least one closed fermionic loop.

The classification was done using a script written in Python, in which one needs to specify the file generated by aITALC for a given process as an input. As an output, one gets a directory containing

- List of particle configurations
- List of different coupling configurations
- List of topologies with two closed fermionic loops
- List of topologies with at least one closed fermionic loop
- List of numbers of diagrams in the input file for each particle configuration

- List of numbers of diagrams in the input file for each coupling configuration
- Analogous lists for each topology separately
- A summary file containing all above information for each topology, with the structure as shown below in Fig. 25.

These lists can be further used for the calculation of the diagrams sharing the same features.

```
Topology 191
Couplings list: ['e5gs2', 'e7gs0', 'e1gs6', 'e3gs4']
Bosonic: 9286
1 Fermionic loop: 7462
2 Fermionic loops: 1890
EW diagrams: 16795
QCD diagrams: 1843
```

Figure 25: Summary of the features of diagrams in exemplary topology for the $Z \to e^+e^-$ process.

As we can see, the total number of diagrams at 3-loops equals approximately $4 \cdot 10^5$ for leptonic Z decay and half a million for Z decay to quarks, whereas, for the self-energies, it was $\mathcal{O}(3 * 10^3)$ integrals for each of W and Z bosons. The vast majority amounts to the electroweak corrections (bosonic) and planar topologies. This explains why, usually, for any higher-order process at a given order, we start with less demanding diagrams which include fermionic subloops. At the moment, factorizable fermionic 3-loop SM contributions to the EWPOs are known [167, 168, 274]. We discussed the ability of numerical solutions for massive 3-loop SM vertex diagrams in section 5.1.3 and an explicit example for a genuine 3-loop $W\bar{l}\nu$ vertex at the $\mathcal{O}(\alpha^2\alpha_s)$ order will be given in the next section. Here, we only estimated the size of the future complete work needed for the evaluation of genuine 3-loop Feynman diagrams. We start this task in the next section with the calculation of non-factorizable 3-loop SM (mixed QCD-EW) corrections.

5.3 Results for the W and Z boson mass renormalization constants and the $W\bar{\ell}\nu_\ell$ vertex at the $\mathcal{O}(\alpha^2\alpha_s)$ order

Let us first consider the two-loop diagrams, with no counterterms, as in Fig. 26.

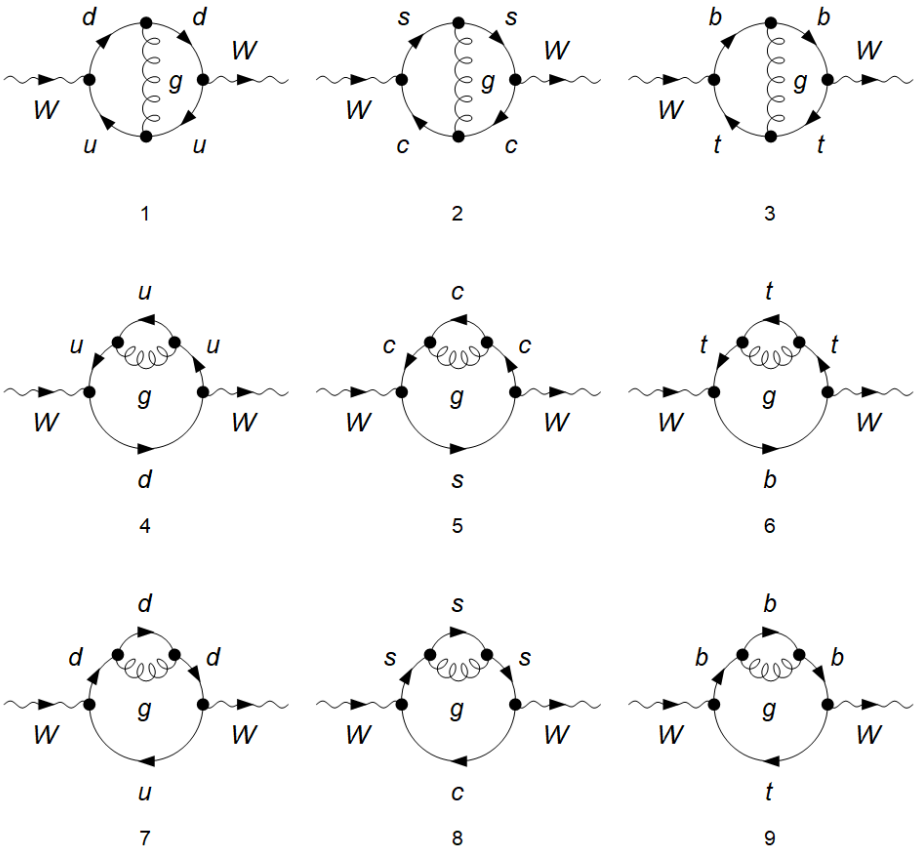

Figure 26: Diagrams for the two-loop δM_W^2, with no counterterms included.

To compute these integrals, we use `AMFlow` as it allows for quick and precise evaluation. The numerical result for these contributions can be evaluated with arbitrary precision. For the purpose of the thesis, the accuracy is shown only up to 10^{-10}

$$\delta^{(2)} M_W^2|_{p^2=M_W^2} = C_A C_F \left(-0.6744862802 + 0.4050613223/\varepsilon - 0.1537414874/\varepsilon^2\right) \alpha\alpha_s \,, \tag{5.31}$$

where α is the fine structure constant, α_s is the strong coupling constant, C_A and C_F are Casimir operators kept symbolically for convenience during expression manipulations and results comparisons.

The above and numerical results given below and in repository [166] are obtained for taking special, rationalize for the purpose of numerical evaluations, non-zero masses, scaled to the Z boson mass

$$M_Z = 1, \quad M_W = \frac{401925}{455938}, \quad M_T = \frac{433000}{227969}, \quad M_H = \frac{312750}{227969}. \tag{5.32}$$

Next, we account for the counterterms, one diagram with a two-loop counterterm and all 99 remaining diagrams are composed of a one-loop diagram with a one-loop counterterm, see Fig. 27 for exemplary diagrams.

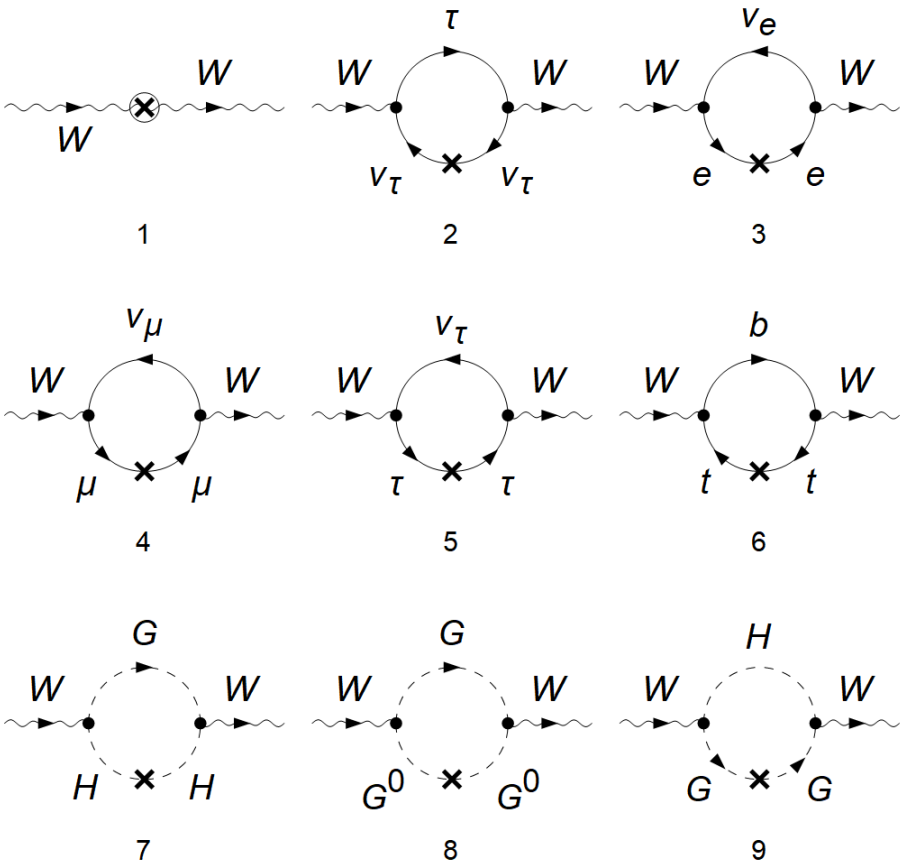

Figure 27: Two-loop diagrams for the δM_W^2 with the counterterm insertions. The complete set of 99 diagrams can be found in repository [166].

As mentioned before in section 3.3.2, these can be expressed in terms of Passarino-Veltman integrals. The result is

$$\delta^{(2)}_{CT} M_W^2|_{p^2=M_W^2} = \frac{3e^2 M_t M_Z^2 \mathrm{dMf1(3,3)} \left(((\mathrm{D}-3)\mathrm{M_W^2}+\mathrm{M_t^2})\,\Re\left(\mathrm{B_0(M_W^2,0,M_t^2)}\right)-\mathrm{A_0(M_t^2)}\right)}{16\pi^2 M_W^2 (M_W^2 - M_Z^2)}, \tag{5.33}$$

where dMf1(3,3) stands for the 1-loop top quark mass renormalization constant coming from diagram 6 in Fig. 27. This renormalization constant contains the α_s factor, it is

also the only one-loop renormalization constant of the order $\mathcal{O}(\alpha_s)$ in the SM. Inserting the values of Passarino-Veltman integrals

$$\begin{aligned} \mathrm{A}_0[M_Z^2] &= 1 + 1/\varepsilon + 1.82246703\varepsilon + 1.42178139\varepsilon^2 + 0.54449888\varepsilon^3, \qquad (5.34) \\ \mathrm{B}_0[M_W^2, 0, M_t^2] &= -0.16666204 + 1/\varepsilon + 1.40016276\varepsilon - 0.26638219\varepsilon^2 \\ &- 0.39697889\varepsilon^3, \qquad (5.35) \end{aligned}$$

the final result is

$$\delta^{(2)}_{CT} M_W^2|_{p^2=M_W^2} = e^2 \mathrm{dMf1}[3,3]\Big(0.26327664 - 0.16188588/\varepsilon - 0.30891168\,\varepsilon\Big). \qquad (5.36)$$

Together, the two parts in (5.31) and (5.33) account for the total two-loop $\mathcal{O}(\alpha\alpha_s)$ contribution to δM_W^2.

As we go into higher orders of perturbative series, i.e. higher loop orders, the complexity and the number of contributions grow rapidly. In general, at the three-loop level, we follow the same principles as at the lower orders. The splitting into different parts is done by our choice and convenience, and can be done arbitrarily. Here, let us begin with the bare three-loop W boson SE diagrams, analogous to contributions discussed in chapter 5.1 for the Z boson. Numerical result of the order $\mathcal{O}(\alpha^2\alpha_s)$ for this contribution is

$$\begin{aligned} \delta^{(3)}_{\mathrm{noCTs}} M_W^2|_{p^2=M_W^2} &= \alpha^2\alpha_s\Big(- 17.9159811373 - 0.2005725404i + \big(5.3959246294 \\ &+0.2201754044i\big)/\varepsilon + \big(1.5546940358 + 0.0i\big)/\varepsilon^2 + 0.1138227954/\varepsilon^3\Big) C_A C_F. \qquad (5.37) \end{aligned}$$

Families for the corresponding diagrams and identified equivalent topologies (see appendix G) are given in a file dMWsq3_3loop_diags.nb in repository [166].

Let us continue with the three-loop diagrams composed of a two-loop diagram with a one-loop counterterm of the $\mathcal{O}(\alpha^2\alpha_s)$ order, see exemplary diagrams in Fig. 28.

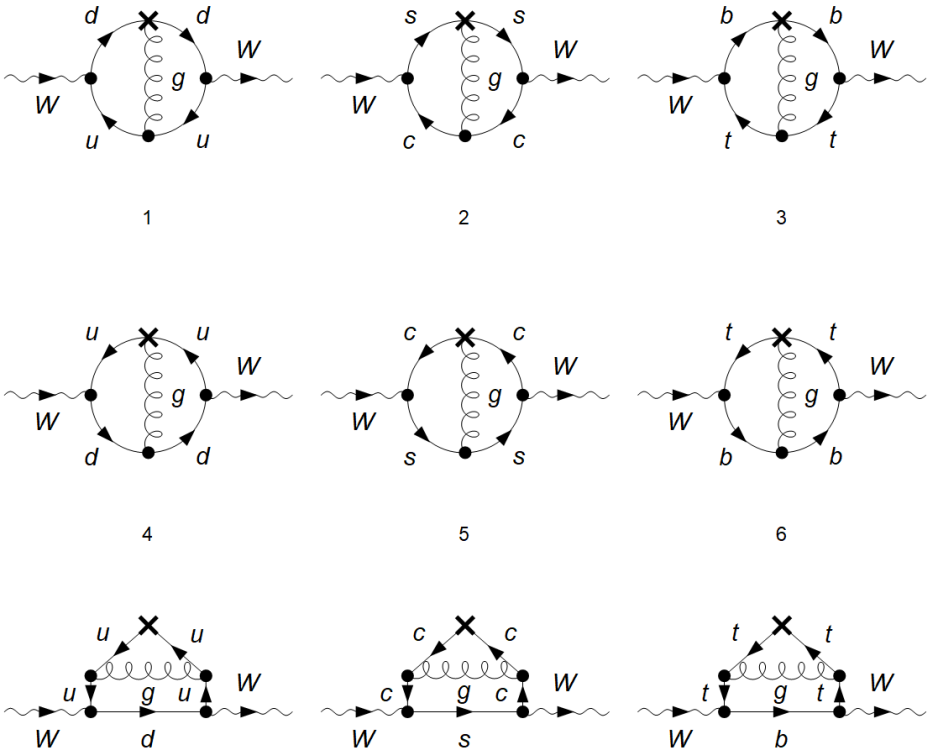

Figure 28: Three-loop diagrams for the δM_W^2 with the one-loop counterterm insertions and internal gluon. The complete set of 81 diagrams can be found in repository [166].

Note that these diagrams contain the internal gluon. The corresponding numerical result is

$$\begin{aligned}
\delta_g^{(3)} M_W^2|_{p^2=M_W^2} &= C_F\,\alpha\alpha_s\Big[\mathrm{dZW1}\left(2.02346 - 0.416155i + 1.21518/\varepsilon - 0.461224/\varepsilon^2\right) \\
&\quad +\mathrm{dZe1}\left(-4.04692 + 0.83231i + 2.43037/\varepsilon - 0.922449/\varepsilon^2\right) \\
&\quad +\mathrm{dSW1}\left(8.5718 - 1.76292i - 5.14778/\varepsilon + 1.95284/\varepsilon^2\right) \\
&\quad +\mathrm{dMf1}[3,3]\left(-4.7895 + 2.31302/\varepsilon + 0.485658/\varepsilon^2\right)\Big]\,, \\
&+ \varepsilon\, C_F\,\alpha\alpha_s\Big[\mathrm{dSW1}(-6.9900 - 0.09621i) + \mathrm{dZe1}(3.30013 + 0.04542i) \\
&+ \mathrm{dZW1}(1.65007 + 0.02271i) + \mathrm{dMf1}[3,3]7.72012\Big] \qquad (5.38)
\end{aligned}$$

where dZW1 is 1-loop W boson wave function renormalization constant, dSW1 denotes the renormalization constant of $\sin\theta_W$ at the 1-loop level and dZe1 is the 1-loop charge

renormalization constant and from dMf1[3,3] we only take part proportional to α, so the final contribution is of the desired $\mathcal{O}(\alpha^2\alpha_s)$ order.

Another contribution of a similar kind is three-loop diagrams with one-loop counterterm, this time without the gluon in loops. In this case, Fig. 29 shows only a part of all 907 contributing diagrams.

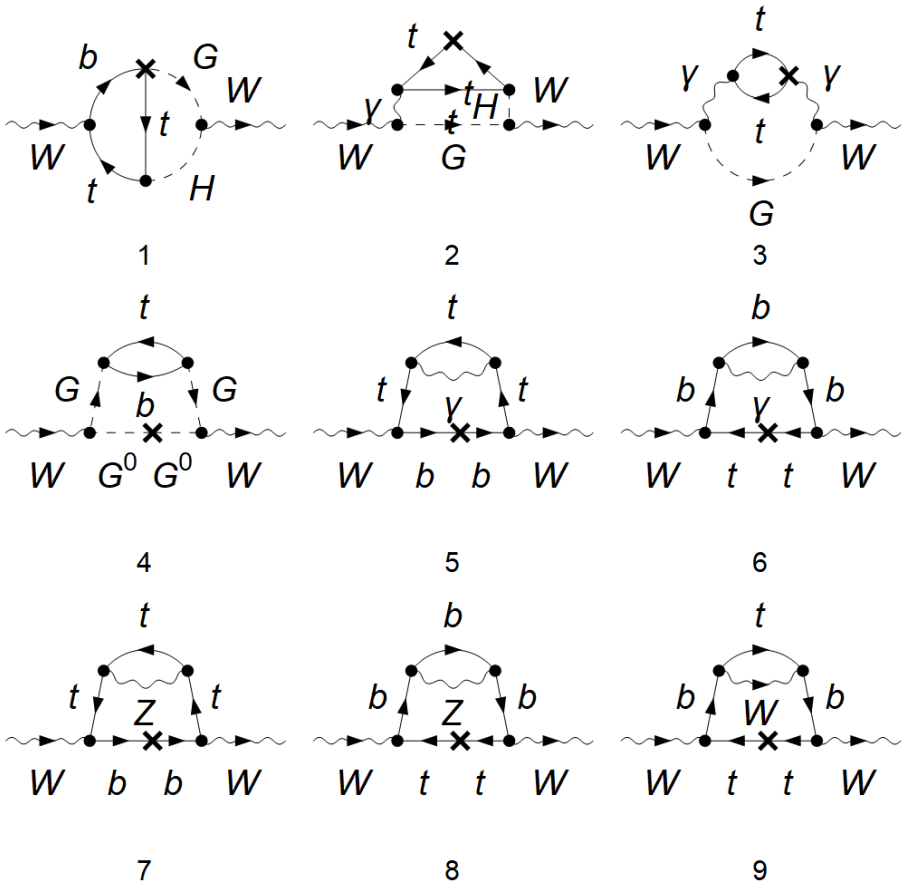

Figure 29: Three-loop diagrams for the δM_W^2 with the one-loop counterterm insertions without the internal gluon. The complete set of 907 diagrams can be found in repository [166].

The corresponding numerical result, obtained with `AMFlow` is:

$$\delta^{(3)}_{ng} M_W^2|_{p^2=M_W^2} = e^4 \text{ dMf1}[3,3]*\Big[0.0103140074/\varepsilon^2 - 0.1191549032/\varepsilon + 0.2515969524 - 0.5383272738\,\varepsilon\Big]. \quad (5.39)$$

The next step is to include the two-loop order counterterms. We split them into two parts, with one two-loop counterterm and two one-loop counterterms inside. These

we further divide into bosonic and fermionic parts, where fermionic means that there is a closed fermionic loop in the diagram, whereas bosonic is the remaining part, see Fig. 30 and Fig. 31 for the bosonic and fermionic diagrams with two-loop counterterms insertions, respectively.

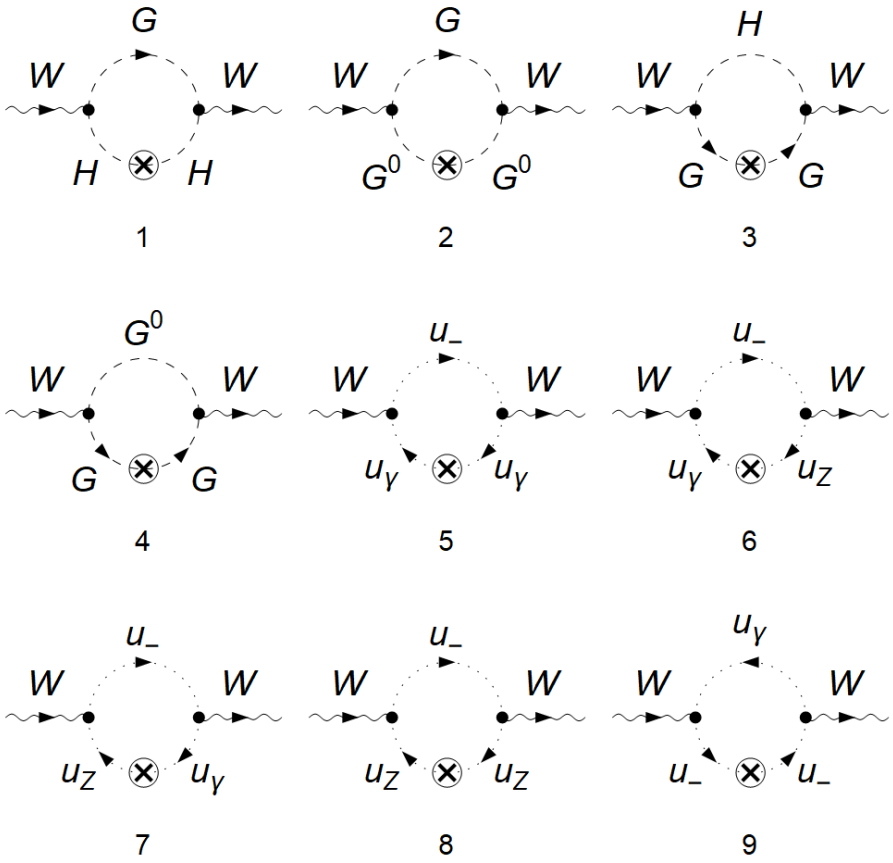

Figure 30: Three-loop bosonic diagrams for the δM_W^2 with the two-loop counterterm insertions. The complete set of 75 diagrams can be found in repository [166].

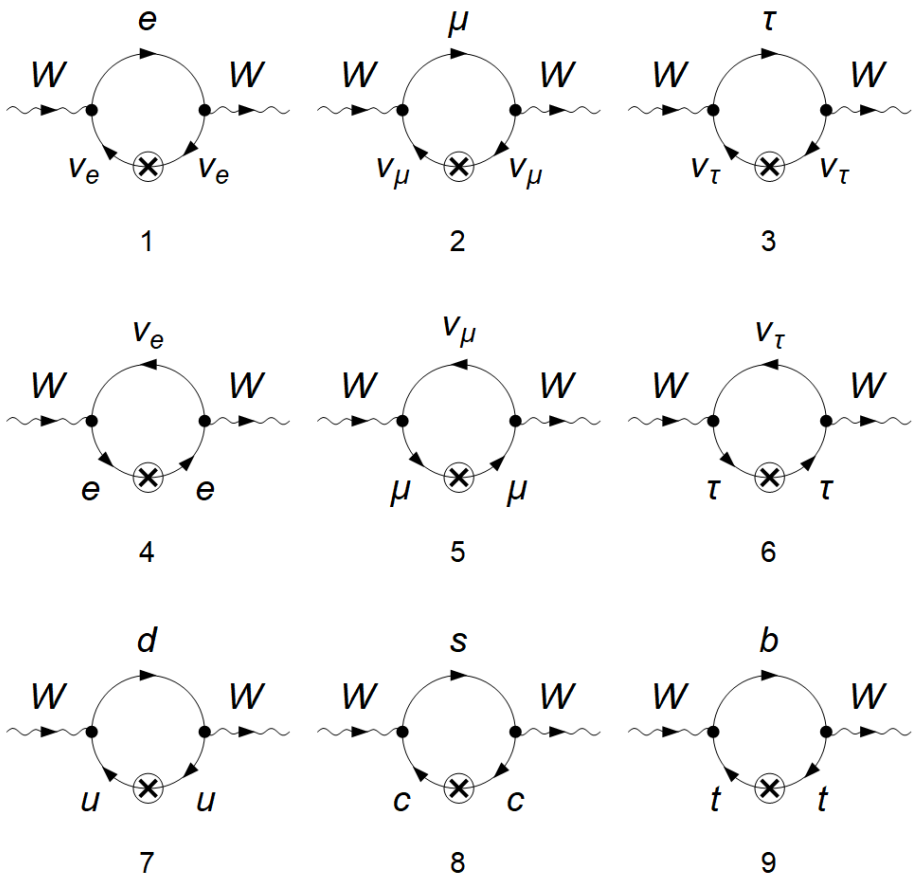

Figure 31: Three-loop fermionic diagrams for the δM_W^2 with the two-loop counterterm insertions. The complete set of 24 diagrams can be found in repository [166].

The corresponding numerical results for bosonic and fermionic three-loop with two-loop counterterms contribution are presented below.

$$\begin{aligned}
\delta_b^{(3)} M_W^2|_{p^2=M_W^2} &= \Big(\mathrm{dMHsq2}\,(-0.0107623) + \mathrm{dMWsq2}\,(0.0312278 - 0.0187213/\varepsilon) \\
&+ \mathrm{dMZsq2}\,(0.0495707 - 0.0291803/\varepsilon) + \mathrm{dSW2}\,(0.2378212 + 0.4242118/\varepsilon) \\
&+ \mathrm{dTH2}\,(0.0007809 - 0.0038039/\varepsilon) + \mathrm{dZe2}\,(-0.1833895 - 0.1713158/\varepsilon) \\
&+ \mathrm{dZG02}\,(-0.0071026/\varepsilon) + \mathrm{dZGp2}\,(-0.0027838 - 0.0110389/\varepsilon) \\
&+ \mathrm{dZW2}\,(-0.0916948 - 0.0856579/\varepsilon)\Big) e^2, \qquad (5.40) \\
\delta_f^{(3)} M_W^2|_{p^2=M_W^2} &= \mathrm{dMf2}(3,3)\Big(0.26327663 + 0.16188588/\varepsilon\Big) e^2. \qquad (5.41)
\end{aligned}$$

The complete results in (5.40) and (5.41) should have terms up to the ε^2 order. They are given in repository [166]. Here one can see the dependence of the result on two-

loop W, Z and H boson mass renormalization constants (dMWsq2, dMZsq2, dMHsq2), electric charge renormalization constant (dZe2), sin of Weinberg angle renormalization constant (dSW2), two loop Higgs boson tadpole (dTH2) and two loop Goldstone field renormalization constants at the two-loop level (dZG02, dZGp2) in bosonic case. For the fermionic contribution, the dependence is only on the top quark mass renormalization constant at the two-loop level (dMf2(3,3)). The last part that has to be included for the $\mathcal{O}(\alpha^2\alpha_s)$ order are the three-loop diagrams with two one-loop counterterm insertions, $\delta_{b2}^{(3)}, \delta_{f2}^{(3)}$. In this case, the bosonic part is zero, there are no contributions to this order of corrections, and we only have fermionic diagrams that we have to take into account. These diagrams are presented in Fig. 32.

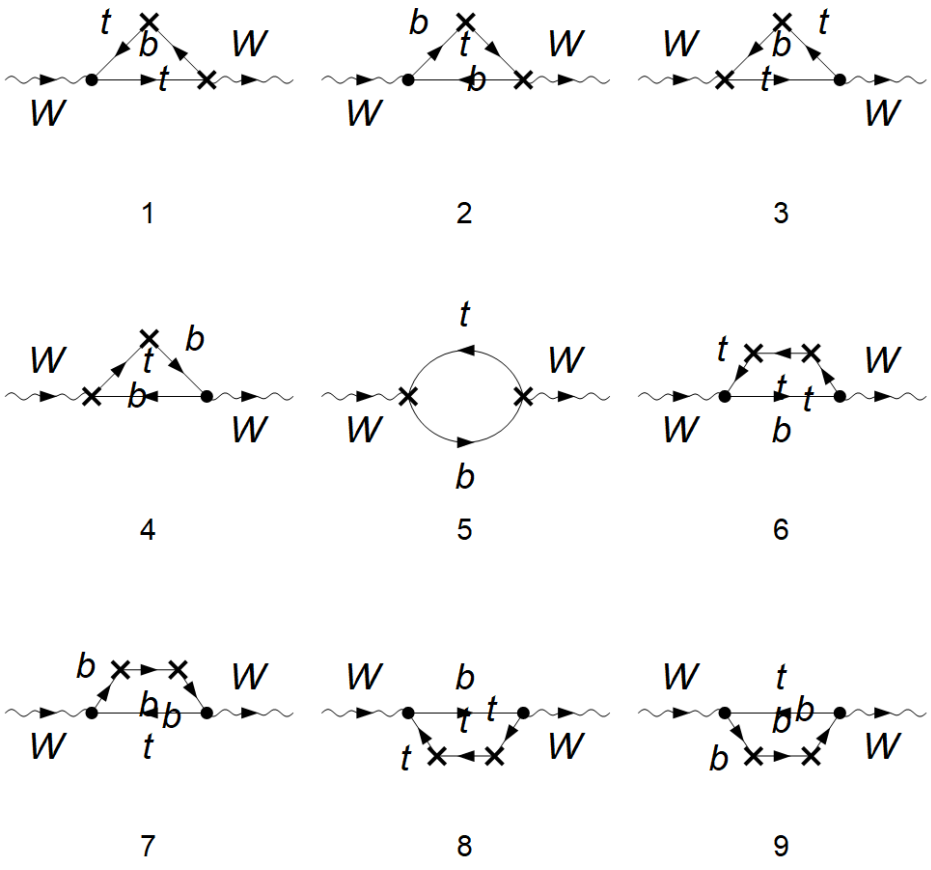

Figure 32: Three-loop fermionic diagrams for the δM_W^2 with the two one-loop counterterm insertions. From many diagrams generated with `FeynArts`, the only non-zero contributions at $\mathcal{O}(\alpha^2\alpha_s)$ come from top-quark diagrams where one contribution includes a gluon, see (3.63). The complete set of diagrams can be found in repository [166].

The corresponding result is again expressed in terms of the Passarino-Veltman

integrals and various one-loop renormalization constants:

$$\delta_{b2}^{(3)} M_W^2 = 0, \tag{5.42}$$

$$\begin{aligned}
&\delta_{f2}^{(3)} M_W^2 = \\
&-\frac{3e^2 M_t^2 \left(M_t^2 - M_W^2\right) \left(M_t^2 + (D-2) M_W^2\right) \mathrm{D_0}[M_W^2, 0, 0, M_W^2, 0, 0, M_t^2, M_t^2, M_t^2] \mathrm{dMf1}[3,3]^2}{8(D-1) M_W^2 \pi^2 s_W^2} \\
&\frac{-3e^2 \mathrm{A_0}[M_t^2]}{128 (D-1) M_t^2 M_W^2 \left(M_t^2 - M_W^2\right) \pi^2 s_w^3} \Big(4\mathrm{dSW1} M_t^2 \left(M_t^2 - M_W^2\right) \left(\mathrm{dZW1} \left(M_t^2 - (D-2) M_W^2\right)\right. \\
&\left. +4 (D-1) M_t \mathrm{dMf1}[3,3]\right) - s_W \Big(\mathrm{dZW1}^2 M_t^2 \left(M_t^2 - M_W^2\right) \left(M_t^2 - (D-2) M_W^2\right) \\
&+8 (D-1) \mathrm{dZW1} M_t^3 \left(M_t^2 - M_W^2\right) \mathrm{dMf1}[3,3] + 2\Big(\left(-18 + 8D + D^2\right) M_t^4 \\
&- \left(-42 + 40D - 11D^2 + D^3\right) M_t^2 M_W^2 + (D-4) (D-2)^2 M_W^4 \Big) \mathrm{dMf1}[3,3]^2 \\
&+4\mathrm{dZe1} M_t^2 \left(M_t^2 - M_W^2\right) \left(\mathrm{dZW1} \left(M_t^2 - (D-2) M_W^2\right) + 4 (D-1) M_t \mathrm{dMf1}[3,3]\right)\Big)\Big) \\
&+\frac{-3e^2 \mathrm{B_0}[M_W^2, 0, M_t^2]}{128 (D-1) M_W^2 \left(M_t^2 - M_W^2\right) \pi^2 s_w^3} \Big(- 4\mathrm{dSW1} \left(M_t^2 - M_W^2\right) \left(\mathrm{dZW1} \left(M_t^2 - M_W^2\right)\right. \\
&\left. * \left(M_t^2 + (D-2) M_W^2\right) + 4 (D-1) M_t \left(M_t^2 + (D-3) M_W^2\right) \mathrm{dMf1}[3,3]\right) \\
&+s_W \Big(\mathrm{dZW1}^2 \left(M_t^2 - M_W^2\right)^2 \left(M_t^2 + (D-2) M_W^2\right) + 8 (D-1) \mathrm{dZW1} M_t \left(M_t^2 - M_W^2\right) \\
&* \left(M_t^2 + (D-3) M_W^2\right) \mathrm{dMf1}[3,3] + 4\Big(3 (3D-7) M_t^4 + \left(36 - 29D + 5D^2\right) M_t^2 M_W^2 \\
&- \left(3 - 4D + D^2\right) M_W^4 \Big) \mathrm{dMf1}[3,3]^2 + 4\mathrm{dZe1} \left(M_t^2 - M_W^2\right) \left(\mathrm{dZW1} \left(M_t^2 - M_W^2\right)\right. \\
&\left. * \left(M_t^2 + (D-2) M_W^2\right) + 4 (D-1) M_t \left(M_t^2 + (D-3) M_W^2\right) \mathrm{dMf1}[3,3]\right)\Big)\Big),
\end{aligned} \tag{5.43}$$

where dZW1 is W boson wave renormalization constant at the one-loop level. The other contributions are connected to renormalization constants of $\sin\theta_w$, electric charge and top quark mass at the one-loop level. Note the presence of the $\mathrm{D_0}$ function in (5.43). However, the appearance of this function in the expression is artificial as a direct transformation of 4 propagators for top quark 1LCT in diagrams 6 and 8 in Fig. 32. This D0 function can be eliminated by IBP relations (for diagrams 6 and 8, Feynman integrals include the top propagator with the same momenta flow to the power 3). IBP reduction gives (we used `FIRE` package)

$$\begin{aligned}
\mathrm{D_0}[\mathrm{M_W^2}, 0, 0, \mathrm{M_W^2}, \mathrm{M_W^2}, 0, 0, \mathrm{M_t^2}, \mathrm{M_t^2}, \mathrm{M_t^2}] &= \frac{(-4+D)(-2+D)(3M_t^2 - M_W^2)}{8M_t^4 (M_t^2 - M_W^2)^2} \mathrm{A_0}[\mathrm{M_t^2}] \\
&+ \frac{(-4+D)(-3+D)}{2(M_t^2 - M_W^2)^2} \mathrm{B_0}[\mathrm{M_W^2}, 0, \mathrm{M_t^2}].
\end{aligned} \tag{5.44}$$

Thus, $\delta^{(3)}_{f2} M^2_W$ is a function of $\mathrm{A}_0[M_t^2]$ and $\mathrm{B}_0[\mathrm{M}^2_\mathrm{W}, 0, \mathrm{M}^2_\mathrm{t}]$ only.

Notice that diagrams 6 and 8 in Fig. 32 are, due to symmetry, identical. At the two-loop level, it is not very important to take it into account. Already at the three-loop level, it becomes relevant, and identifying identical diagrams can speed up calculations significantly. See the Appendix G for details. To show the possible speed up, let us consider a bare 3-loop W boson self-energy. In the initial list with integrals simplifications between numerators and denominators (see example in section 5.1.2) needed for partial analysis and comparisons results using `TVID2` package, there are in total 3064 *individual* integrals that have to be evaluated. Instead, identification of topologically identical diagrams reduces the initial number to 796 diagrams in 155 families. This means, in the end, we need to run `AMFlow` calculation only 155 times, instead of 3064 times. Saving of good shifts of momenta into some variable and starting to search shifts from there, and not from ∼300 000 of all possible shifts (first search we of course start from all possible combinations) speeds generation of target integrals up to seconds. Altogether, the complete calculation for the considered genuine bare 3-loop W boson self-energy takes about one day (using 4 threads of average server CPU, in our case, this number is limited by the number of Wolfram licenses available), about one order of magnitude better than without consideration of topology symmetries To clarify, the final number of diagrams is achieved by finding topologically identical diagrams, the number of families, though, comes from our own script `SEFlow` described in section 5.1.4 and schematically in Appendix F. A diagram family consists of a diagram with the highest propagator count and all diagrams obtained by removing some of its propagators.

Having all the lower-order renormalization constants already calculated and put into the parts described before in this section, we can sum up all the contributions from different parts to finally get the three-loop W boson mass renormalization constant of the order $\mathcal{O}(\alpha^2\alpha_s)$.

The analogous results for the δM_Z^2 can be found in repository [166].

Let us now consider the three-loop $W\bar{\ell}\nu_\ell$ vertex, beginning with the one-loop diagrams with two-loop counterterm insertions as in Fig. 33.

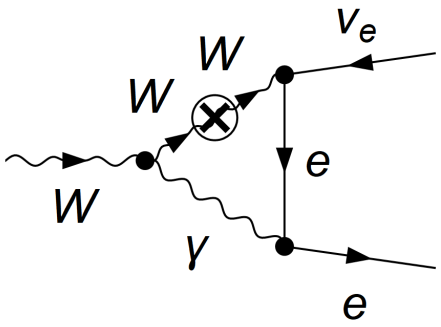

Figure 33: Exemplary three-loop $W\bar{\ell}\nu_\ell$ vertex contribution of one-loop diagram with two-loop counterterm insertions. The complete set of 33 diagrams can be found in repository [166].

Since these diagrams only need one-loop integration, the intermediate result is composed of the products of Passarino-Veltman functions and the two-loop renormalization constants. The numerical result, with the renormalization constants kept symbolically is

$$\begin{aligned} W\bar{\ell}\nu_\ell^{2lCT} &= e^2\Big[-0.0656957\,\mathrm{dMWsq2} - 0.0308292\,\mathrm{dMZsq2} - 0.0423301\,\mathrm{dSW2} \\ &+ 0.00515558\,\mathrm{dZAA2} + 0.00421067\,\mathrm{dZAZ2} + 0.0603508\,\mathrm{dZe2} \\ &- 0.00171594\,\mathrm{dZGp2} + 0.000404491\,\mathrm{dZW2} + 0.00421067\,\mathrm{dZZA2} \\ &- 0.00973314\,\mathrm{dZZZ2} + \frac{1}{\varepsilon}\Big(-0.498292\,\mathrm{dSW2} + 0.00474943\,\mathrm{dZAA2} \\ &- 0.00506416\,\mathrm{dZAZ2} + 0.240497\,\mathrm{dZe2} + 0.0613905\,\mathrm{dZW2} \\ &- 0.00506416\,\mathrm{dZZA2} + 0.011493\,\mathrm{dZZZ2}\Big)\Big] \end{aligned} \tag{5.45}$$

Note that for the result to be of the order $\mathcal{O}(\alpha^2\alpha_s)$ we need the renormalization constants at the $\mathcal{O}(\alpha\alpha_s)$ order. The complete results in (5.45) should have terms up to the ε^2 order. They are given in repository [166].

Next, we consider two-loop diagrams with one-loop counterterms for the three-loop $W\bar{\ell}\nu_\ell$ vertex. An exemplary diagram is shown in Fig. 34.

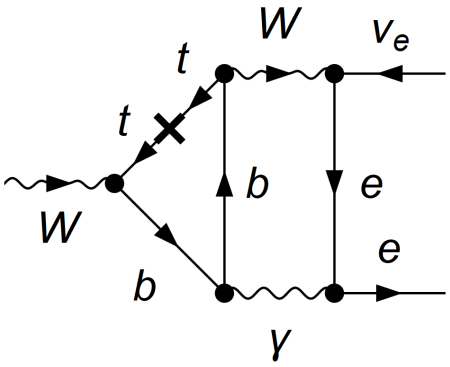

Figure 34: Exemplary three-loop $W\bar{\ell}\nu_\ell$ vertex contribution of two-loop diagram with one-loop counterterm insertions. The complete set of 348 diagrams can be found in repository [166].

The corresponding numerical result at the $\mathcal{O}(\alpha^2\alpha_s)$ is

$$W\bar{\ell}\nu_\ell^{1lCT} = e^4\Big(-0.0558686\,\varepsilon + 0.0292356 - 0.017415/\varepsilon\Big)\mathrm{dMf1}[3,3] \tag{5.46}$$

Note that the result is proportional to the top quark mass renormalization constant, which is the only one-loop renormalization constant of the $\mathcal{O}(\alpha_s)$ order, see (3.63).

For the genuine three-loop vertex $W\bar{\ell}\nu_\ell$ we have 604 diagrams generated by `FeynArts`, exemplary diagrams are presented in Fig. 35 and the corresponding numerical result for the genuine 3-loop vertex at the $\mathcal{O}(\alpha^2\alpha_s)$ order is

$$W\bar{\ell}\nu_\ell \;=\; \Big(-0.0032240421 + 0.0012580235/\varepsilon - 0.0004342680/\varepsilon^2\Big)\,\alpha^2\alpha_s\;. \tag{5.47}$$

The result includes the standard prefactor $e^{3\varepsilon\gamma_E}$, and it normalized by the division of the final result by the tree-level diagram, i.e.

$$W\bar{l}\nu_l{}^{tree} = \frac{e}{\sqrt{2}\sin\theta_W} \tag{5.48}$$

The $W\bar{l}\nu_l$ vertex form-factor result in (5.47) has been obtained within the `NDR` scheme and does not include genuine 3-loop integrals from diagrams with subloop $O(\alpha\alpha_s)$ triangle which should be computed with PV regulator Λ, see appandix B.

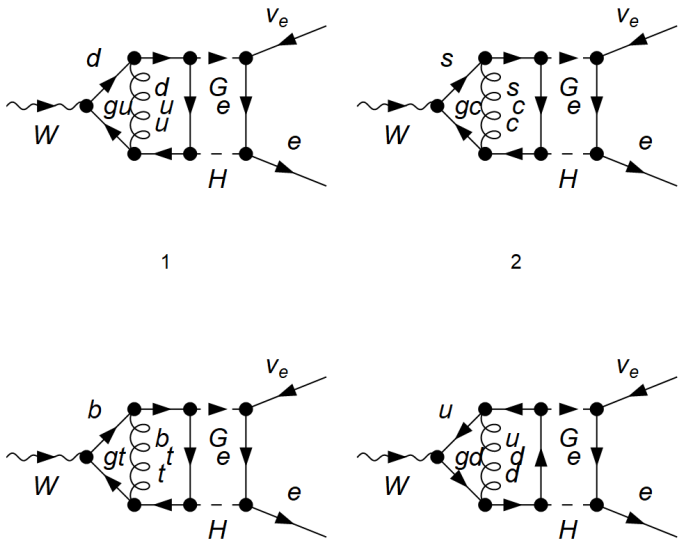

Figure 35: Exemplary three-loop diagrams for the $W\bar{\ell}\nu_\ell$ vertex with the gluon at the $\mathcal{O}(\alpha^2\alpha_s)$ order. The complete set of 604 diagrams can be found in repository [166].

5.4 Remarks on the implementation of higher order SM radiative corrections to the global analysis of the electroweak data

Beyond the SM models include new particles which couple with SM particles weakly. With new 3-loop fermionic and bosonic results for the SM corrections $\delta^{(3)}_{f,b}M_W^2$ and $\delta^{(3)}_{f,b}M_Z^2$ at the $\mathcal{O}(\alpha^2\alpha_s)$ order, more refined analysis and phenomenological studies for models which go beyond the SM are possible. On top of that, as discussed already in the Introduction, the present discrepancy between the foreseen experimental and the actual theoretical capabilities is a serious problem because it is bigger than the accuracy of the planned experimental setups; see Tab. 1. Thus, further calculations are needed, see Tab. 2, justifying our studies and calculations of the $\mathcal{O}(\alpha^2\alpha_s)$ order corrections.

Ultimately, calculated higher-order corrections are encoded in special libraries, which should be merged with Monte Carlo generators [275, 276]. A new EW Griffin library [277] is constructed differently from the Zfitter/Dizet EWPOs library, which has been used widely since the LEP times. For the recent version of Dizet, see [128]. The Griffin library aims at a universal description of the SM higher-order corrections applicable for precision studies at future lepton colliders, with gauge invariant corrections

at the amplitude level, extendable to new corrections and *new physics* contributions.

The ρ parameter introduced in (1.4) includes the discussed in the previous section corrections $\delta^{(3)}_{f,b} M_W^2$ and $\delta^{(3)}_{f,b} M_Z^2$, thus they can be implemented in future studies including fits to the BSM parameters. Such refined investigations go beyond the scope of the thesis. There are dedicated studies for the global analysis of electroweak data in the SM (see e.g. [71]) where a complete set of EWPOs SM corrections up to 2-loop order worked out in [64, 66, 141] are already included.

The ρ-parameter defined as $\rho = \frac{m_W}{\overline{M}_Z \cos^2 \theta_W^0}$ equals to one at the tree level in SM. In general, it depends on the scalar sector and on the scalar multiplets' vacuum expectation values v_i of some neutral scalar fields h_i. The unity at the tree level is due to gauge boson mass relations in the SM (1.9) and the SM spontaneous symmetry breaking mechanism, for which the textbook relation reads [49]

$$\rho = \frac{\sum_i \left[T_i(T_i+1) - (T_{3i})^2\right] v_i^2}{2\sum_i T_{3i}^2 v_i^2}. \tag{5.49}$$

For the SM Higgs doublet with the hypercharge $Y = 1$, weak isospin $T = \frac{1}{2}$ and the third isospin component T_{3i} (as well as for scalar multi-doublets and singlets), the ρ-parameter is naturally equal to 1. In this case, the model has a custodial $SU(2)$ global symmetry [278]. In the SM, this symmetry is broken at the loop level when fermions of the same doublets have different masses [36] and by the hypercharge group.

The SM tree level ρ-parameter discussed in (1.4) and section 2.2 on the muon decay gets modifications due to radiative corrections, which change M_W, M_Z and s_W^2

$$s_W^2 = \left(1 - \frac{M_W^2}{M_Z^2}\right)_{\text{tree}} + \delta s_W^2 \tag{5.50}$$

$$= 1 - \frac{M_W^2}{M_Z^2} + c_W^2 \left(\frac{\Sigma_T^W(M_W^2)}{M_W^2} - \frac{\Sigma_T^Z(M_Z^2)}{M_Z^2}\right) \equiv 1 - \frac{M_W^2}{M_Z^2} + c_W^2 \Delta\rho. \tag{5.51}$$

In the SM, this correction due to the top-quark is substantial (at the percentage level) while the correction due to H^0 is moderate (logarithmic behaviour, screening theorem [279])

$$\Delta\rho = 3\frac{G_\mu M_t^2}{8\sqrt{2}\pi^2}\left[1 + \Delta\rho^{\text{t}} + \Delta\rho^{\text{H}} + \ldots\right], \tag{5.52}$$

$$\Delta\rho^t = \frac{3\sqrt{2} M_t^2 G_\mu}{16\pi^2}, \tag{5.53}$$

$$\Delta\rho^{\text{H}} \sim -\frac{3 G_\mu M_W^2}{8\sqrt{2}\pi^2}\,\frac{s_W^2}{c_W^2}\log\frac{M_H^2}{M_W^2} \quad \text{for } M_H \gg M_W. \tag{5.54}$$

Thus, $\Delta\rho$ is one of the key parameters considered in the precision physics calculations. It is one of the so-called oblique corrections [280] (self-energy corrections) which is also used to parametrize BSM radiative contributions through S, T, U parameters, which are defined as follows [280]

$$\begin{aligned}
\alpha S &= 4s_W^2 c_W^2 \left[\Sigma_T^{ZZ}(0) - (c_W^2 - s_W^2)/(s_W c_W)\Pi^{ZA}(0) - \Pi^{AA}(0)\right], \\
\alpha T &= \Sigma_T^{WW}(0)/M_W^2 - \Sigma_T^{ZZ}(0)/M_Z^2, \\
\alpha U &= 4s_W^2 \left[\Pi^{WW}(0) - c_W^2\Pi^{ZZ}(0) - 2s_W c_W \Pi^{ZA}(0) - s_W^2\Pi^{AA}(0)\right]. \qquad (5.55)
\end{aligned}$$

The Π in the above equations states for the derivative of self-energies over momenta squared, same as in (2.35). Let us note that the definition of the oblique corrections is not unique [281].

Finally, we remark that there are two different approaches to the SM and BSM tests. The bottom-up approach focuses on studying discrepancies between experimental results and the SM predictions without assuming the form of the underlying theory (read: effective theories are considered). However, the SMEFT theories discussed in recent years, based on functional matching for constructing EFTs with heavy fields of UV-complete models, often do not include BSM renormalization and no validation for observables [282]. As discussed recently in [283], decomposition into SMEFT and non-SMEFT operators in a complete renormalization scheme is not unique. Thus, tests of the SM and its extensions are non-trivial and need further efforts in order to tackle the fine details needed for demanding precision of foreseen collider experiments.

The top-down approach is based on the specific Standard Model extensions (see e.g. discussion of specific BSM models in [271,284] and importance of model-dependent $\Delta\rho$ on derived SM and BSM parameters in [284]). In both bottom-up and top-down approaches $\Delta\rho$ parameter and the 3-loop self-energy results derived in the last section will certainly improve the precision of underlying investigations and global analysis, which is an important issue in the context of demanding precision of Tera-Z physics discussed in the Introduction.

6 Summary and outlook

Whether SM based theoretical predictions can be made accurate enough to meet the demands posed by the emerging progress in collider technologies is a key issue for the entire field of high-energy physics research at the high-energy and luminosity frontiers. The piece of calculation addressed in this thesis is an important part of the massive project for improving these predictions. Presently, theory is still much behind the experimental demands [PhD4]. The key technique is the derivation and calculation of a huge number of Feynman integrals with unprecedented precision. Integrals that stand behind the Feynman diagrams are, together with a renormalization procedure, at the core of the technical difficulties, which increase rapidly with the number of legs and loops involved in calculating contemporary QCD and electroweak processes [PhD2, PhD3, PhD4]. Thus, steady progress in particle physics needs new ideas and crafting ever-changing theoretical tools and techniques of calculations with the rapidly growing complexity of the integrals.

In the thesis, I present the considerable progress made in the development of methods and tools for the multi-loop Feynman integrals evaluation, as well as results needed for the three-loop mixed QCD-weak contributions to the muon and Z boson decays.

Concerning the development of methods, in [PhD1] the calculation of the intricated multiscale SM 3-loop self-energy, vertex and box Feynman integrals has been undertaken using differential equations with Euclidean boundary transport. The most important novelty of this method is the construction of an automated framework for the application of the DEqs transport method to the calculation of physical processes. This automation is based on two key features: (a) an algorithmic procedure for finding an integral basis for which the DE system is finite, and (b) a prescription for analytically continuing the series solutions across physical thresholds. With the availability of these automated procedures, the feasibility of any cutting-edge calculation is only limited by the availability of the numerical boundary conditions and the integration-by-parts reductions, but no further analytic studies are needed. This method was developed in parallel and independently of the `AMFlow`. Having several competing methods is crucial, as it allows for cross-checks for these very complex calculations. The method and its usage are described in detail in sections 4.5 and 5.1.3.

In the thesis, I have also tested at the 3-loop level the capabilities of the sector decomposition as well as Mellin-Barnes methods [PhD2,PhD3], see sections 4.3, 5.1.2 and 5.1.3. These methods were used successfully in previous studies for the complete two-loop calculations of the Z boson EWPOs [64, 66, 141] . For the three-loop self-energy

calculations of the W and Z bosons, they turned out not to be sufficient. For numerous integrals, the MB and SD methods could not fulfil the accuracy needs or even get any result at all. There was a need for either an enormous improvement in these methods or a new method capable of solving the three-loop integrals for the Z boson and muon decays. I have been working on improvements that could result in better accuracy and easier computation of encountered Feynman integrals using `pySecDec`, including rescaling and, for a short time, on Taylor expansion of integrands as presented in appendices D and E, respectively. With emergence of the `AMFlow` and the `DEqsEBT` approaches, I became familiar with numerical approaches to differential equations and soon it became evident not only that the gaps, where MB and SD methods failed, could be filled, but also the overall accuracy of the computation was brought easily up to 30 digits for all individual integrals, exceeding the accuracy needs for the calculations. I have also tested that these newly developed methods and tools are sufficient to deal with the three-loop Z boson decay vertices, as this is a natural continuation of our studies, see section 5.1.3.

Despite having the accurate integral evaluation methods available, to efficiently perform the calculations of several thousand Feynman integrals, only for the self-energy, there was a burning need for automation. Even more so, for the calculation of Z boson decay vertices, where there are $\mathcal{O}(10^6)$ diagrams collectively to be evaluated for different decay modes as shown in section 5.2. I have prepared scripts to automate the process from the list of input integrals up to the numerical results with two independent methods, using `pySecDec` and `AMFlow`, as described in sections 5.1.1 and 5.1.4 respectively. The former served for the benchmarking tests of `pySecDec` capabilities as well as cross-checks of the results, while the latter was used for the complete, three-loop W and Z bosons self-energies calculation. The scripts I developed can be used not only for the W and Z bosons' self-energies at the three-loop level, but also for the upcoming calculations of Z boson decay vertices and others.

Besides working on the development and tests of the tools for numerical evaluation of Feynman integrals and their automation for our in-house setups, I also worked on the preparation of an independent setup to generate expressions for counterterms starting at one- and two-loop level, see sections 3.3.1 and 5.3. This setup is made in such a way as to be compatible with the automated numerical methods mentioned before. This was done to make another set of cross-checks in this complex project. With this setup ready, not only can we compare numerical results for the individual integrals, partial contributions from single integral classes or full results, but also we can compare expressions symbolically at intermediate steps of calculations. These cross-

checks are extremely important in such a project, where bookkeeping for each step of calculations is one of the most important issues, especially since the methods and tools can sometimes give a false result that cannot be identified without the method of verification, such as another independent approach.

All of the aforementioned numerical results for the three-loop W and Z bosons self-energy and one- and two- loop renormalization constants used for Z boson and muon decay studies are added into the publicly available repository [166].

The impact of the three-loop $\mathcal{O}(\alpha^2\alpha_s)$ calculations considered in the thesis for the discussed processes is under study. The numerical values obtained for genuine 3-loop corrections in chapter 5.2 were obtained for the central values of M_Z, M_W, M_H, M_t masses as defined in (5.32). To get an estimate of parametric uncertainties, a grid over input values should still be done, repeating results for a wider range of mass parameters, as was worked out for the 2-loop case in [64]. Also, genuine 3-loop integrals from diagrams with subloop $O(\alpha\alpha_s)$ fermionic triangles should be computed with PV regulator Λ, showing convergence of the cut-off parameter Λ with increasing Λ, see appendix B. Then, the discussed corrections will be coded in Dizet [128] and can be used for BSM analysis and global fits, as was the case of NNLO EWPOs corrections and global fits [71]. In addition, IR-finite boxes and QED boxes, with Fermi model contribution subtracted [117] beyond 1-loop level, should be worked out.

Acknowledgments

This work was supported by the Polish National Science Center (NCN) under grants 2017/25/B/ST2/01987 and 2023/50/A/ST2/00224 and by the COST (European Cooperation in Science and Technology) Action CA16201 PARTICLEFACE.

Appendices

A Renormalization examples

A.1 W boson mass renormalization

Let us show how to get the gauge bosons' mass renormalization conditions and their explicit form on the example of the W mass renormalization constant, i.e.

$$\delta M_W^2 = \Re\left(\Sigma_T^W(M_W^2)\right). \tag{A.1}$$

The bare, unrenormalized W boson propagator is defined in the following way

$$D_0^{\mu\nu} = -\frac{1}{p^2 - M_W^2} P_T^{\mu\nu} - \frac{\xi}{p^2 - \xi M_W^2} P_L^{\mu\nu} = \frac{1}{p^2 - M_W^2}\left(-g^{\mu\nu} + (1-\xi)\frac{p^\mu p^\nu}{p^2 - \xi M_W^2}\right), \tag{A.2}$$

where

$$P_T^{\mu\nu} = g^{\mu\nu} - \frac{p^\mu p^\nu}{p^2} \quad \text{and} \quad \mathrm{P_L^{\mu\nu}} = \frac{\mathrm{p^\mu p^\nu}}{\mathrm{p^2}}. \tag{A.3}$$

We find the inverse of the propagator $(D_0^{-1})^{\mu\nu}$ knowing that $D * D^{-1} = 1$

$$D_0^{\mu\nu} = aP_T^{\mu\nu} + bP_L^{\mu\nu}, \tag{A.4}$$

$$\left(-\frac{1}{p^2 - M_W^2} P_T - \frac{\xi}{p^2 - \xi M_W^2} P_L\right)(aP_T + bP_L) = 1.$$

Finally, it results in

$$(D_0^{-1})^{\mu\nu} = -(p^2 - M_W^2) P_T^{\mu\nu} - \frac{p^2 - \xi M_W^2}{\xi} P_L^{\mu\nu}. \tag{A.5}$$

With the following substitution

$$A = -\frac{1}{p^2 - M_W^2} \quad \text{and} \quad \mathrm{B} = -\frac{\xi}{\mathrm{p^2} - \xi \mathrm{M_W^2}},$$

we can write the propagator and its inverse in a compact way

$$(D_0)^{\mu\nu} = AP_T^{\mu\nu} + BP_L^{\mu\nu}, \tag{A.6}$$

$$(D_0^{-1})^{\mu\nu} = \frac{1}{A} P_T^{\mu\nu} + \frac{1}{B} P_L^{\mu\nu}. \tag{A.7}$$

The tree-level propagator has two poles, when $p = M_W^2$ and $p = \xi M_W^2$. Mass of the particle cannot depend on the gauge parameter ξ. Thus, the experimentally measured mass comes from the transverse part of the propagator.

A similar approach can be applied to the renormalized propagator

$$D = D_0 + D_0 \Sigma D_0 + \cdots = D_0 \Sigma D, \tag{A.8}$$

$$D = \frac{1}{D_0^{-1} - D_0 \Sigma D_0^{-1}} = a P_T + b P_L, \tag{A.9}$$

where the self-energy can also be decomposed into transverse and longitudinal parts

$$\Sigma^{\mu\nu} = \Sigma_T P_T^{\mu\nu} + \Sigma_L P_L^{\mu\nu}. \tag{A.10}$$

Using the $D * D^{-1} = 1$ relation again, we find:

$$D^{\mu\nu} = -\frac{1}{p^2 - M_W^2 + \Sigma_T} P_T^{\mu\nu} - \frac{\xi}{p^2 - \xi M_W^2 + \xi \Sigma_L} P_L^{\mu\nu}. \tag{A.11}$$

Following the same reasoning as for the tree level, we see that the observed mass is connected to the transverse part of the propagator, and its longitudinal part cannot contribute to the loop corrections.

The renormalization condition for W boson mass in (3.4), $M_{W,0}^2 = M_W^2 + \delta M_W^2$ becomes

$$\delta M_W^2 = \Sigma_T. \tag{A.12}$$

If we take the real part of the self-energy, we get the renormalization constant form as in (3.18).

Alternatively, as discussed already in section 2.3 for the Z boson case, coming from the propagator pole s_0, the mass and decay width of the W boson, the pole and the on-shell mass and width of the W boson are

$$s_0 \equiv \overline{M}_W^2 - i \overline{M}_W \overline{\Gamma}_W, \tag{A.13}$$

$$\overline{M}_W = \frac{M_W}{\sqrt{1 + \Gamma_W / M_W^2}}, \qquad \overline{\Gamma}_W = \frac{\Gamma_W}{\sqrt{1 + \Gamma_W / M_W^2}}. \tag{A.14}$$

The massive two-point function of the W boson with radiative corrections included becomes

$$D(p^2) = p^2 - s_0 + \Sigma_T(p^2) - \delta\overline{M}^2_W, \tag{A.15}$$

where $\delta\overline{M}^2_W$ is the mass counterterm. As for s_0 being a pole of the propagator, it is required that $D(s_0) = 0$, which leads to the following conditions

$$\begin{aligned} \delta\overline{M}^2_W &= \Re\Sigma_T(\overline{M}^2_W - i\overline{M\Gamma_W}), & \text{(A.16)} \\ \overline{\Gamma}_W &= \frac{1}{\overline{M}_W}\Im\Sigma_T(\overline{M}^2_W - i\overline{M}_W\overline{\Gamma}_W). & \text{(A.17)} \end{aligned}$$

By inserting the (A.17) into (A.16) recursively and expanding in next orders of perturbation, we arrive at the W-mass counterterms at one, two and three-loop level [285]

$$\begin{aligned} \delta\overline{M}^2_{W(1)} &= \Re\,\Sigma_{W(1)}(\overline{M}^2_W), & \text{(A.18)} \\ \delta\overline{M}^2_{W(2)} &= \Re\,\Sigma_{W(2)}(\overline{M}^2_W) + \left[\Im\,\Sigma_{W(1)}(\overline{M}^2_W)\right]\left[\Im\,\Sigma'_{W(1)}(\overline{M}^2_W)\right], & \text{(A.19)} \\ \delta\overline{M}^2_{W(3)} &= \Re\,\Sigma_{W(3)}(\overline{M}^2_W) + \left[\Im\,\Sigma_{W(2)}(\overline{M}^2_W)\right]\left[\Im\,\Sigma'_{W(1)}(\overline{M}^2_W)\right] \\ &\quad + \left[\Im\,\Sigma_{W(1)}(\overline{M}^2_W)\right]\Big\{\Im\,\Sigma'_{W(2)}(\overline{M}^2_W) - \left[\Im\,\Sigma'_{W(1)}(\overline{M}^2_W)\right]\left[\Re\,\Sigma'_{W(1)}(\overline{M}^2_W)\right] \\ &\quad - \frac{1}{2}\left[\Im\,\Sigma_{W(1)}(\overline{M}^2_W)\right]\left[\Re\,\Sigma''_{W(1)}(\overline{M}^2_W)\right]\Big\}. & \text{(A.20)} \end{aligned}$$

The lower index T is dropped for the self-energy Σ to avoid the index cluttering. Similarly, we can approach the Z boson mass counterterm, though the mixing with photon results in extra terms in comparison to (A.16) and (A.17)

A.2 Charge renormalization constant

For the derivation of the charge renormalization constant we will use the Ward identity and (amputated) Green functions.

$G(\phi_i, \dots)$ – complete Green function with boson fields,
$\phi_i \equiv B_\mu, W^3_\mu$ – gauge field,
$D^{-1}_{ij}G(\phi_i, \dots)$ – amputated Green function for gauge field,
$D_{ij} =< \phi_i\phi_j >$ –propagator of the $\phi_i\phi_j$ fields

Transition from gauge fields to renormalized physical fields A_{mu},Z_μ is described by the U matrix:

$$\phi_i = U_{ij}\phi'_j.$$

Then

$$\begin{aligned} D_{ij} &= U_{im}U_{jm}\Delta'_{mn} = (UD'U^T)_{ij}, \\ G(\phi_i, \dots) &= U_{ik}G(\phi'_k, \dots). \end{aligned} \tag{A.21}$$

The amputated diagram is described by the following function

$$\begin{aligned} D^{-1}_{ij}G(\phi_j, \dots) &= (UD'U^T)^{-1}_{ij}U_{jm}G(\phi'_m, \dots), \\ D^{-1}_{ij}G(\phi_j, \dots) &= (U^T)^{-1}_{ij}(\Delta')^{-1}_{jk}G(\phi'_k, \dots), \end{aligned} \tag{A.22}$$

$$\begin{pmatrix} \psi_0\overline{\psi_0}W^3_\mu \\ \psi_0\overline{\psi_0}B_\mu \end{pmatrix}_{amp} = (U^T)^{-1}\begin{pmatrix} \psi_0\overline{\psi_0}Z_\mu \\ \psi_0\overline{\psi_0}A_\mu \end{pmatrix}_{amp}, \tag{A.23}$$

where ψ_0, B_μ, W^3_μ are unrenormalized whereas Z_μ, A_μ are renormalized.

For further simplification, let us consider right-handed fermionic fields only. Then, $\psi_{right}\overline{\psi_{right}}W^a_\mu = 0$ and from the construction of the SM we can assume that bosonic coupling to fermions, both right- and left-handed, depend on the same constant e.

$$\begin{pmatrix} \psi_0\overline{\psi^R_0}Z_\mu \\ \psi_0\overline{\psi^R_0}A_\mu \end{pmatrix}_{amp} = U^T\begin{pmatrix} 0 \\ \psi^R_0\overline{\psi^R_0}B_\mu \end{pmatrix}_{amp}, \tag{A.24}$$

where ψ^R_0 is right-handed unrenormalized amputated fermionic field, and the *amp* subscript indicates that that these are amputated.

We can now use the Ward identity for the zero-momentum boson

$$(\psi^R_0\overline{\psi^R_0}B_\mu)_{amp} = g_1\frac{\partial S^{-1}_F(p)}{\partial p^\mu}, \tag{A.25}$$

where S^{-1}_F is the unrenormalized fermionic propagator, $g_1 = e_0/c_0$. Let

$$\psi_0 = Z^{1/2}_F\psi \text{ - for the unamputated fields,} \tag{A.26}$$

then

$$< \psi_0\overline{\psi_0} > \sim S_F^{-1} = Z_F^{-1} S_{F,R}^{-1} \,,$$
$$(\psi_0\overline{\psi_0})_{amp} = Z_F^{-1}(\psi\overline{\psi})_{amp} \text{ - for the amputated fields.} \tag{A.27}$$

Since on-shell renormalization vertex is $\Sigma^R(p^2) = 0$ and $(\Sigma^R)' = 0$ so

$$\frac{\partial S_{F,R}^{-1}}{\partial p_\mu} = -i\gamma_\mu, \tag{A.28}$$

where $S_F^{-1} = -i(\not{p} - m - \Sigma(p^2))$. Assuming that the photonic vertex is the same as in QED $\psi\overline{\psi}A_\mu = -ie\gamma_\mu$ for all renormalized fields.

$$Z_F^{-1} \begin{pmatrix} \psi\overline{\psi}Z_\mu \\ \psi\overline{\psi}A_\mu \end{pmatrix} = U^T \begin{pmatrix} 0 \\ -ig_1\gamma_\mu Z_F^{-1} \end{pmatrix},$$

$$\begin{pmatrix} \psi\overline{\psi}Z_\mu \\ -ie\gamma_\mu \end{pmatrix} = U^T \begin{pmatrix} 0 \\ -ig_1\gamma_\mu \end{pmatrix}. \tag{A.29}$$

Now we only need to find the U matrix.

$$\begin{pmatrix} W_\mu^3 \\ B_\mu \end{pmatrix} = U \begin{pmatrix} Z_\mu \\ A_\mu \end{pmatrix}, \tag{A.30}$$

$$U = \begin{pmatrix} c_0 & -s_0 \\ s_0 & c_0 \end{pmatrix} \begin{pmatrix} Z_{ZZ}^{1/2} & Z_{ZA}^{1/2} \\ Z_{AZ}^{1/2} & Z_{AA}^{1/2} \end{pmatrix} \equiv U_{cs}U_Z, \tag{A.31}$$

$$U^T = (U_{cs}U_Z)^T = U_Z^T U_{cs}^T = \begin{pmatrix} Z_{ZZ}^{1/2} & Z_{AZ}^{1/2} \\ Z_{ZA}^{1/2} & Z_{AA}^{1/2} \end{pmatrix} \begin{pmatrix} c_0 & s_0 \\ -s_0 & c_0 \end{pmatrix}, \tag{A.32}$$

$$U^T = \begin{pmatrix} Z_{ZZ}^{1/2}c_0 - Z_{AZ}^{1/2}s_0 & Z_{ZZ}^{1/2}s_0 + Z_{AZ}^{1/2}c_0 \\ Z_{ZA}^{1/2}c_0 - Z_{AA}^{1/2}s_0 & Z_{ZA}^{1/2}s_0 + Z_{AA}^{1/2}c_0 \end{pmatrix}, \tag{A.33}$$

where s_0, c_0 are unrenormalized $\sin\theta_W$ and $\cos\theta_W$, respectively. For the charge renormalization constant, we only need the U_{22}^T. From (A.29) we get

$$-ie\gamma_\mu = -ig_1\gamma_\mu \left(s_0 Z_{ZA}^{1/2} + c_0 Z_{AA}^{1/2}\right), \tag{A.34}$$

so

$$1 = \frac{e_0}{e}\left(\frac{s_0}{c_0} Z_{ZA}^{1/2} + Z_{AA}^{1/2}\right). \tag{A.35}$$

Finally, the charge renormalization constant has the following form

$$Z_e\left(Z_{AA}^{1/2} + \frac{s+\delta s}{c+\delta c} Z_{ZA}^{1/2}\right) = 1. \tag{A.36}$$

Expanding at the 1-loop level

$$\left(1+\delta Z_e^{(1)}\right)\left(1+\frac{1}{2}\delta Z_{AA}^{(1)} + \left(s+\delta s^{(1)}\right)\left(\frac{1}{c}\right)\left(1-\frac{\delta c^{(1)}}{c}\right)\frac{1}{2}\delta Z_{ZA}^{(1)}\right) = 1. \tag{A.37}$$

After simplification, neglecting the higher-order terms

$$1 - \delta Z_e^{(1)} = 1 + \frac{1}{2}\delta Z_{AA}^{(1)} + \frac{s}{2c}\delta Z_{ZA}^{(1)}, \tag{A.38}$$

and finally

$$\delta Z_e^{(1)} = -\frac{1}{2}\delta Z_{AA}^{(1)} - \frac{s}{2c}\delta Z_{ZA}^{(1)}. \tag{A.39}$$

Following the same procedure, at the higher orders, we get the following expression of the charge renormalization constant

$$\delta Z_e^{(2)} = \left(\delta Z_e^{(1)}\right)^2 - \frac{1}{2}\delta Z_{AA}^{(2)} + \frac{1}{8}\left(\delta Z_{AA}^{(1)}\right)^2 - \frac{s_W}{2c_W}\delta Z_{ZA}^{(2)} - \frac{1}{2c_W^3}\delta s_W^{(1)}\delta Z_{ZA}^{(1)}, \tag{A.40}$$

$$\begin{aligned}\delta Z_e^{(3)} = & -\frac{1}{2}\delta Z_{AA}^{(3)} - \frac{s_W}{2c_W}\delta Z_{ZA}^{(3)} + 2\delta Z_e^{(2)}\delta Z_e^{(1)} + \frac{1}{4}\delta Z_{AA}^{(2)}\delta Z_{AA}^{(1)} \\ & -\frac{1}{2c_W^3}\left(\delta s_W^{(2)}\delta Z_{ZA}^{(1)} + \delta s_W^{(1)}\delta Z_{ZA}^{(2)}\right) \\ & -\left(\delta Z_e^{(1)}\right)^3 - \frac{1}{16}\left(\delta Z_{AA}^{(1)}\right)^3 - \frac{3s_W}{4c_W^5}\left(\delta s_W^{(1)}\right)^2\delta Z_{ZA}^{(1)}.\end{aligned} \tag{A.41}$$

B Divergences handling and the γ_5 problem

One of the major issues that has to be dealt with, while calculating loop integrals, is the divergences. Consider a simple one-loop scalar integral with zero external momentum.

$$I = \int \frac{d^4k}{(2\pi)^4} \frac{1}{(k^2)^2}, \tag{B.1}$$

where k denotes loop momentum. We can see that the integral is divergent when k^2 approaches either infinity or zero. These are the ultraviolet (UV) and infrared (IR) divergences, respectively. It is clear that any quantity given by a divergent integral is ill-defined and so these integrals have to be regulated. The standard method to achieve it is by the method of dimensional regularization [286–288]. The idea of this scheme is to replace the integral over loop momentum in four dimensions by a $D = 4 - 2\varepsilon$ dimensional integral, where ε is a new parameter that can be non-integer as well as even a complex number. In the end, the result of the integration is a function of ε, and we want to recover the result when $D \to 4$. Original integral divergences appear as poles in $1/\varepsilon$, which can be systematically subtracted or absorbed via renormalization. The integral in $D = 4 - 2\varepsilon$ dimensions keeps all the standard properties of integration such as linearity, translation invariance and scaling behaviour [289,290]. This approach also preserves gauge invariance and Lorentz symmetry. In principle, both UV and IR divergences can be treated with dimensional regularization. See e.g. [291] for a detailed discussion as well as the way to treat integrals with both UV and IR divergences with dimensional regularization.

Besides dimensional regularization, there are other schemes to regularize the infinities appearing in Feynman integrals. One of them is the cut-off method, in which we limit the range of loop momenta integration by a hard cut-off, $k^\mu < \Lambda$ then calculate the integral in $D = 4$ dimensions and expand the result into power-log or Laurent series in a parameter r which is a ratio $r \equiv$ (masses and external momenta)$/\Lambda$. As a result, the terms in the expansion with positive logarithm powers of Λ account for the divergent part. Although this scheme of regularization may be appealing for its conceptual simplicity, it turns out to be quite problematic in practice, as it breaks the Lorentz invariance of the theory and the additional energy scale Λ dependence can be non-trivial.

Another important issue that has to be taken into account when calculating Feynman integrals is the behaviour of γ_5 in $D \neq 4$. The γ_5 in $D = 4$ dimensions has two properties that cannot simultaneously be preserved when going to e.g. $D = 4 - 2\varepsilon$

dimensional space, when working with dimensional regularization. First, the anticommutativity relation

$$\{\gamma_5, \gamma_\mu\} = 0. \tag{B.2}$$

Secondly, the cyclicity of the Dirac trace

$$\mathrm{Tr}(\gamma_{\mu_1} \dots \gamma_{\mu_{2n}} \gamma_5) = \mathrm{Tr}(\gamma_{\mu_2} \dots \gamma_{\mu_{2n}} \gamma_5 \gamma_{\mu_1}) = \mathrm{Tr}(\gamma_{\mu_3} \dots \gamma_{\mu_{2n}} \gamma_5 \gamma_{\mu_1} \gamma_{\mu_2}) = \dots \tag{B.3}$$

For this reason, multiple approaches, aiming to avoid these issues and still obtain correct results, exist. Among the most commonly used schemes are: Naive Dimensional Regularization (NDR) [292], Breitenlohner-Maison (BMHV) scheme [286, 293] and Larin's scheme [294]. Each of them has both good and bad sides, and at the moment, there is no simple solution to the γ_5 problem that can work in any theory at any loop order and in an automated manner.

Throughout the thesis and computation, the NDR scheme for γ_5 was used. In this approach, we assume that the properties of γ_5 naively extend to D dimensions. It is very easy, fast and convenient to use, especially in non-chiral theories, vector-like theories. On the other hand, while using this scheme, any diagrams contributing to closed fermion loops with traces of an odd number of γ_5 as in Fig. 36 are ill-defined and this approach leads to ambiguities for the diagrams related to the Adler-Bell-Jackiw anomaly [295, 296].

In these cases, where NDR scheme fails, we use another approach for the integral regularization i.e. the method by Pauli and Villars (PV) [297]. It works for the UV divergent integrals and follows from the idea behind the origin of UV divergences, i.e. the virtual particles carry enough energy to transform spontaneously into any state, yet the theory is designed in such a way that can only describe effects up to a given energy scale. So, the formalism fails to account for the effects of possible contributions from heavier fields that still do contribute to physical processes. The basic idea of Pauli-Villars regularization is to introduce additional fields that mimic physical fields, but with a very large mass $\Lambda \gg$ (other masses and momenta). The new fields effectively modify the integrals in a way that the divergent parts at high energies drop out. This regularization scheme preserves the Lorentz invariance and Ward-Takahashi identities.

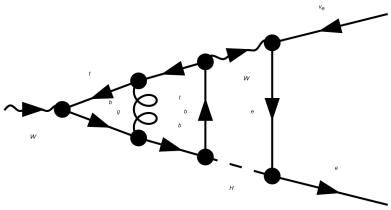

Figure 36: Exemplary three-loop $W\bar{\ell}\nu_\ell$ vertex with a closed fermionic loop that is treated with Pauli-Villars regularization in our calculations.

We apply the PV approach in cases such as in Fig. 36, where NDR leads to the anomaly. We apply the Pauli-Villars regularization with different values of regulator Λ for internal gluon to see if the integral converges for large values of Λ, which is the case.

C Symanzik polynomials

The functions U and F in (4.11) and (4.12) are called graph polynomials. They are polynomials in the Feynman parameters and have the following properties:

- They are homogeneous in the Feynman parameters, U is of degree L, F is of degree $L+1$.
- U is linear in each Feynman parameter. If all internal masses are zero, then also F is linear in each Feynman parameter.
- In expanded form each monomial of U has a coefficient $+1$.

U and F are the first and the second Symanzik polynomials of the graph, respectively. These polynomials can also be derived from the topology of the underlying graph.

To explain the graphical method of graph polynomial construction, one needs to introduce some basic definitions first:

- Spanning tree T of the graph G is a sub-graph with the following properties:
  - T contains all the vertices of G
  - the number of loops in T is zero
  - T is connected

  T can be obtained from G by deleting L edges (L – number of loops in G).

- Spanning k–forest $\mathcal{T}_k$ for the graph G has the same properties as T, but it is not required that a spanning forest be connected. Instead, we require that it should have exactly k connected components.
  F can be obtained from G by deleting $L + k - 1$ edges.

If $\mathcal{T}$ is the set of all spanning forests of G and $\mathcal{T}_k$ is the set of all spanning k-forests of G then

$$\mathcal{T} = \bigcup_{k=1}^{r} \mathcal{T}_k \quad (r - \text{number of vertices}).$$

Each element of $\mathcal{T}_k$ has k connected components $(T_1, \ldots, T_k)$. With P_{T_i} we denote a set of external momenta attached to T_i for a given k–forest. Depending on the "direction" of external momenta (whether they are incoming or outgoing), they enter the P_{T_i} with a different relative sign.

The graph polynomials U and F can be obtained from the spanning trees and the spanning 2–forests of a graph G as follows:

$$U = \sum_{T \in \mathcal{T}_1} \prod_{e_i \notin T} x_i, \tag{C.1}$$

$$F = - \sum_{(T_1,T_2)\in\mathcal{T}_2} \left(\prod_{e_i \notin (T_1,T_2)} x_i \right) \left(\sum_{p_i \in P_{T_1}} p_i \right) \left(\sum_{p_j \in P_{T_2}} p_j \right) + U \sum_{i=1}^{n} x_i m_i^2 \tag{C.2}$$

$$\equiv F_0 + U \sum_{i=1}^{n} x_i m_i^2. \tag{C.3}$$

A simple one-loop example of how to find Symanzik polynomials is given in Fig. 37.

Cuts of internal lines (lines removed in Fig. 37) are made according to Eqs. (C.1) and (C.3) such that:

- U: (i) every vertex is still connected to every other vertex by a sequence of uncut lines; (ii) no further cuts are made without violating (i).

- F: (iii) the cuts divide the graph into two disjointed parts, such that within each part (i) and (ii) are valid, and at least one external momentum line is connected to each part.

Regarding Fig. 37, let us note that the delta function $\delta(1 - \sum_{i=1}^{N} x_i)$ in (4.10) in any 1-loop diagram goes over all variables x_i, so $U = 1$. This feature is used in the so-called loop-by-loop MB representation construction [175].

Let us note that F and U polynomials can be obtained algebraically using `MB.m` or the `Mathematica` module, which can be found in [298].

Basic 1-loop box diagram 

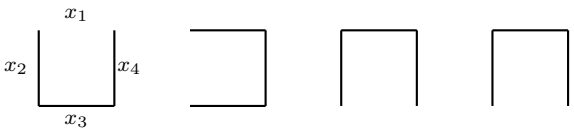

$$U = x_1 + x_2 + x_3 + x_4$$

Trees contributing to the U polynomial for the 1-loop box diagram are drawn above.

$$F = t \cdot x_1 x_3 + s \cdot x_2 x_4$$

2 - trees contributing to the F polynomial for the 1-loop box diagram are drawn above.

Figure 37: Graphical construction of F and U Symanzik polynomials. Kinematic variables t and s are defined as $t = (p_1 - p_3)^2$ and $s = (p_1 + p_2)^2$. External particles are considered massless.

D pySecDec with rescaling

The following theorem (CW) has been considered by Cheng and Wu in a work on proton scattering [299].

Theorem D.1. *For the Feynman parameter representation in (4.10), the Cheng–Wu (CW) theorem states that the same formula holds with the delta function* $\delta(1 - \sum_{i=1}^{N} x_i)$ *replaced by*

$$\delta\left(\sum_{i\in\Omega} x_i - 1\right), \tag{D.1}$$

where Ω *is an arbitrary subset of the lines* $1, \ldots, L$*, when the integration over the rest of the variables, i.e. for* $i \notin \Omega$*, is extended to the integration from zero to infinity.*

This theorem is key to minimizing the number of terms in Symanzik polynomials for Mellin-Barnes representations [165].

In short, Cheng-Wu's theorem states that a Feynman integral remains invariant under the rescaling of the Feynman parameters by an arbitrary number, i.e.

$$\alpha_i \to \lambda \alpha_i, \qquad d\alpha_i \to \lambda d\alpha_i. \tag{D.2}$$

This feature may turn out very handy in the case of pySecDec calculations, if one can find a set of rescaling parameters that make computation more efficient.

We have selected three benchmark integrals to test if we can find any rules or features of the integrals that can help us select a helpful rescaling[4]

$$I_T^{2L} = \frac{1}{k_1^2 * (k_1+p_1+p_2)^2 * (k_1-k_2)^2 * ((k_1-k_2+p_1)^2 - M_Z^2) * (k_2)^2 * (k_2+p_2)^2}, \quad \text{(D.3)}$$

$$I_{7PR}^{3L} = \frac{1}{k_1^2 * (k_1-k_2)^2 * (k_1-k_3)^2 * (k_2-k_3)^2 * (k_3^2-1) * (k_1+p_1)^2 * (k_2+p_1)^2}, \quad \text{(D.4)}$$

$$I_{8PR}^{3L} = \frac{1}{k_1^2 * (k_1-k_2)^2 * k_2^2 * (k_1-k_3)^2 * (k_2-k_3)^2 * (k_3^2-1) * (k_1+p_1)^2 * (k_2+p_1)^2}. \quad \text{(D.5)}$$

First, I_T^{2L} the two-loop, non-planar triangle diagram, with one massive leg, for the Z boson decay, see Fig. 38 and discussion in section 4.3. This particular integral was very problematic for the pySecDec and was computed with the MB method at first. Then pySecDec developers added a 'split' option that can help avoid problems with singularities at Feynman parameters $x_i = 1$. The U polynomial for this integral reads

$$\begin{aligned} U_T^{2L} \quad &= x_3 * x_5 + x_3 * x_4 + x_2 * x_5 + x_2 * x_4 + x_1 * x_5 + x_1 * x_4 + \\ &\quad x_1 * x_3 + x_1 * x_2 + x_0 * x_5 + x_0 * x_4 + x_0 * x_3 + x_0 * x_2. \end{aligned} \quad \text{(D.6)}$$

It creates a lot more sectors and slows down the calculation a lot, so it should only be used if the standard approach fails to converge. For this particular example, it solved the computational problem, but due to the fact that it is so much slower, the accuracy that one could aim at, in a reasonable computational time, leaves a lot of space for improvements, and it serves as a benchmark example for pySecDec from then on.

Second I_{7PR}^{3L} and third I_{8PR}^{3L} integrals are the scalar, self-energy integrals for the Z boson from the lh_merc class, see Fig. 38. Both of them could have been calculated with the standard pySecDec approach (no split needed), but with very poor (1-digit) accuracy, so it leaves a lot of space for possible improvements. The U polynomials for these integrals are

[4]This work has been done together with Stephen Jones from the pySecDec group during my visit to CERN .

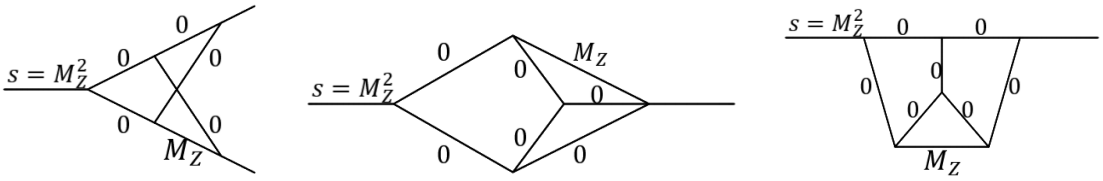

Figure 38: Feynman diagrams corresponding to integrals in equations (D.3), (D.4) and (D.5) respectively.

$$\begin{aligned} U_{7PR}^{3L} \quad &= x_4 * x_5 * x_6 + x_3 * x_5 * x_6 + x_3 * x_4 * x_5 + x_2 * x_5 * x_6 + \\ &x_2 * x_4 * x_6 + x_2 * x_3 * x_6 + x_2 * x_3 * x_5 + x_2 * x_3 * x_4 + x_1 * x_4 * x_6 + \\ &x_1 * x_4 * x_5 + x_1 * x_3 * x_6 + x_1 * x_3 * x_5 + x_1 * x_3 * x_4 + x_1 * x_2 * x_6 + \\ &x_1 * x_2 * x_5 + x_1 * x_2 * x_4 + x_0 * x_4 * x_6 + x_0 * x_3 * x_6 + x_0 * x_3 * x_4 + \\ &x_0 * x_2 * x_6 + x_0 * x_2 * x_3 + x_0 * x_1 * x_4 + x_0 * x_1 * x_3 + x_0 * x_1 * x_2, \end{aligned} \tag{D.7}$$

$$\begin{aligned} U_{8PR}^{3L} \quad &= x_5 * x_6 * x_7 + x_4 * x_6 * x_7 + x_4 * x_5 * x_6 + x_3 * x_6 * x_7 + x_3 * x_5 * x_7 + \\ &x_3 * x_4 * x_7 + x_3 * x_4 * x_6 + x_3 * x_4 * x_5 + x_2 * x_5 * x_6 + x_2 * x_4 * x_6 + \\ &x_2 * x_3 * x_6 + x_2 * x_3 * x_5 + x_2 * x_3 * x_4 + x_1 * x_5 * x_7 + x_1 * x_5 * x_6 + \\ &x_1 * x_4 * x_7 + x_1 * x_4 * x_6 + x_1 * x_4 * x_5 + x_1 * x_3 * x_7 + x_1 * x_3 * x_6 + \\ &x_1 * x_3 * x_5 + x_1 * x_2 * x_5 + x_1 * x_2 * x_4 + x_1 * x_2 * x_3 + x_0 * x_5 * x_7 + \\ &x_0 * x_4 * x_7 + x_0 * x_4 * x_5 + x_0 * x_3 * x_7 + x_0 * x_3 * x_4 + x_0 * x_2 * x_5 + \\ &x_0 * x_2 * x_4 + x_0 * x_2 * x_3 + x_0 * x_1 * x_5 + x_0 * x_1 * x_4 + x_0 * x_1 * x_3. \end{aligned} \tag{D.8}$$

At first, we tried to see if it was possible to increase the efficiency (decrease computation time/increase precision) for the I_T^{2L}, as the one that had the fewest Feynman parameters that could have been rescaled. Starting from trying to multiply each of the Feynman parameters by some random number and then decreasing the number of rescaling parameters from 6 down to 1, we observed better performance when, minimally, two parameters were changed. This was a good starting point for a broader analysis of what particular values of rescaling parameters increase the computation efficiency, and then if we can find out the rules to choose the rescaling parameters in other cases. The scan of the 2-dimensional parameter space was done, resulting in Fig. 39.

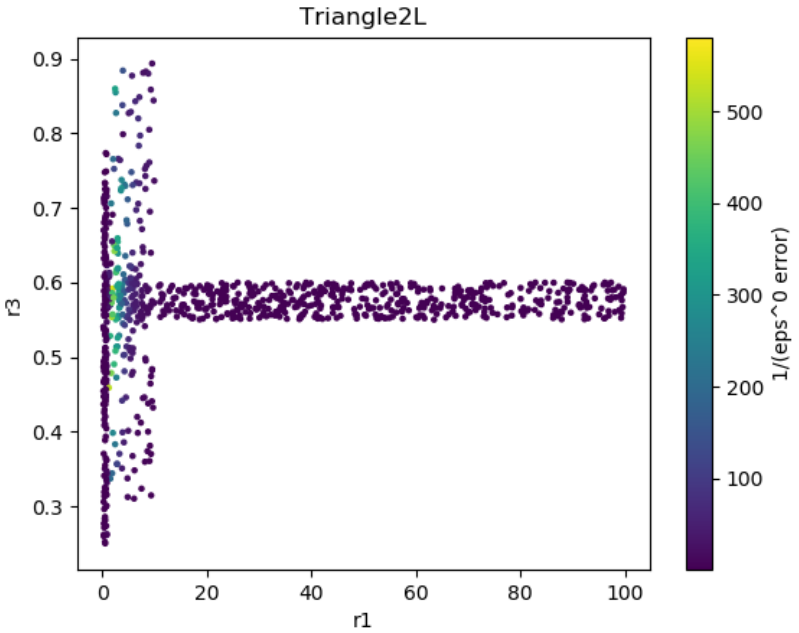

Figure 39: Scan over the two rescaling parameters space to find the point at which we minimize the error with a set number of integration points.

The scan showed that the following values of the rescaling parameters give the best results:

$$r1 = 2.26327557652, \quad r3 = 0.649642611183. \tag{D.9}$$

The tests performed on some representative integrals considered in the thesis helped improve the rescaling method. However, it seems that presently `pySecDec` is more efficient using Symanzik polynomial analysis without contour deformations [212], as discussed in section 4.3.

E Taylor expansion of multi-scale integrals

To reduce the number of scales in the integral, they can be Taylor expanded as described and applied in [300, 301] in more general contexts. We have also tried this approach in [PhD2]. It is beneficial for IBP reduction, `MB` and `SD` methods. To test the approach, we apply it to the integral corresponding to the diagram in Fig. 40. We choose to expand the integrand at $M_W = M_Z$, then the expanded W boson propagator takes the form

$$\frac{1}{k^2 - M_W^2} = \frac{1}{k^2 - M_Z^2} + \frac{(M_W^2 - M_Z^2)}{(k^2 - M_Z^2)^2} + \frac{(M_W^2 - M_Z^2)^2}{(k^2 - M_Z^2)^3} + \frac{(M_W^2 - M_Z^2)^3}{(k^2 - M_Z^2)^4} + \dots \,. \quad \text{(E.1)}$$

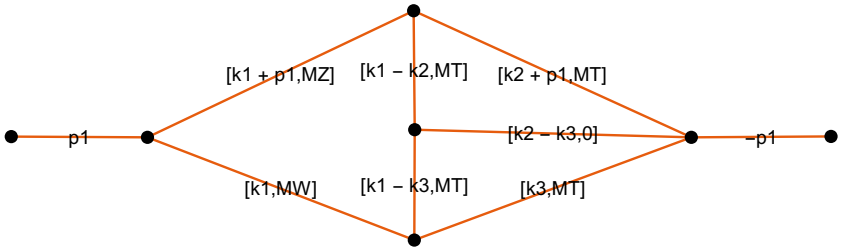

Figure 40: The exemplary integral in which a W boson propagator was expanded as shown in (E.1). An artificial integral was also considered, where the W boson propagator was replaced by the Higgs boson propagator and then expanded in $M_H = M_Z$.

The goal of this approach is to end up with integrals that can be evaluated faster and with better accuracy. Indeed, instead of one difficult integral, we end up with several simpler integrals, and the approach can be applied recursively if necessary. For both considered integrals, with W and Higgs bosons, we studied the convergence of the series. The results are graphically presented in Fig. 41 and Fig. 42 for W and the Higgs boson, respectively. One can see that the result converges when more terms of the expansion are included. These terms were all evaluated in the Minkowskian kinematics, i.e. for $s = 1$. Each point of the plots represents the integral value with another expansion term included.

The integral with the W boson propagator converges faster than the second one, with the Higgs boson. The simple explanation of this fact is that the difference between M_W and M_Z is smaller than for M_H and M_Z. Yet, for both integrals, we can achieve a good convergence of the result. In the case of the integral with the W boson, it is enough to include 9 terms of expansion to achieve $\mathcal{O}(10^{-8})$ accuracy, whereas for the integral with the Higgs boson, including 21 terms of expansion leads to the $\mathcal{O}(10^{-4})$ accuracy. The final result depends strongly on the accuracy achieved for individual integrals in the expansion, which is, in principle, higher than what we can get for the original integral.

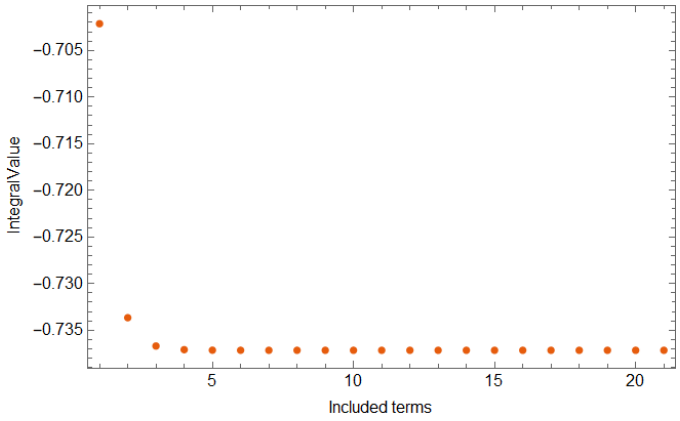

Figure 41: Numerical result for the integral corresponding to the diagram in Fig. 40 expanded at $M_W = M_Z$ including sequential terms of expansion as in (E.1).

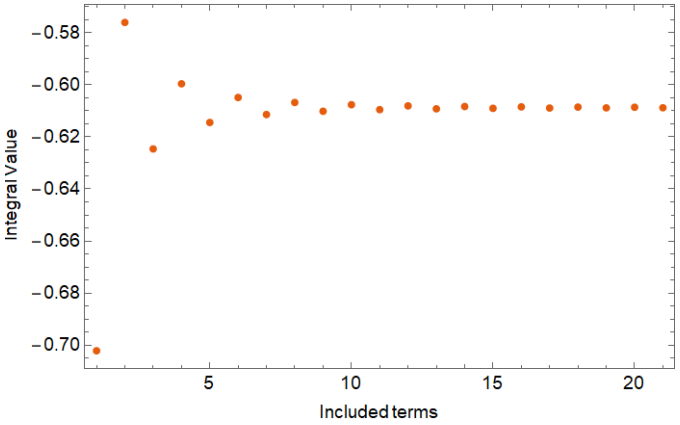

Figure 42: Numerical result for the integral corresponding to the diagram in Fig. 40 with Higgs boson instead of W boson, expanded at $M_H = M_Z$ including sequential terms of expansion analogous to (E.1).

F The scheme used for `AMFlow` automation

To illustrate the workflow of the `AMFlow` automation, two flowcharts are presented below. First, for the general scheme of processing the integrals up to the numerical results, the second depicts how the integrals are matched to the basis, i.e. to find integrals originating from the same Feynman diagram, including all possible momenta shifts in the integral.

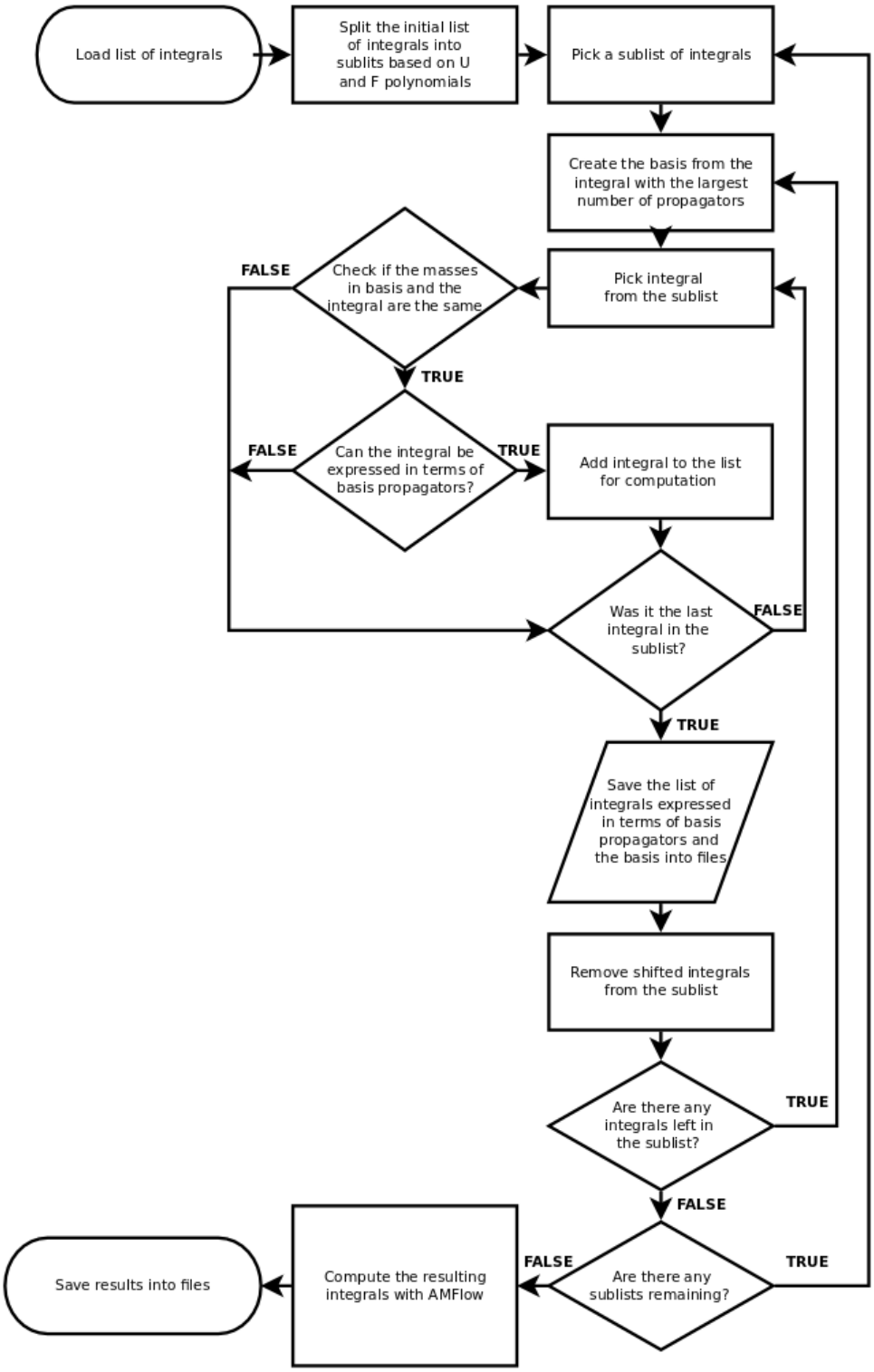

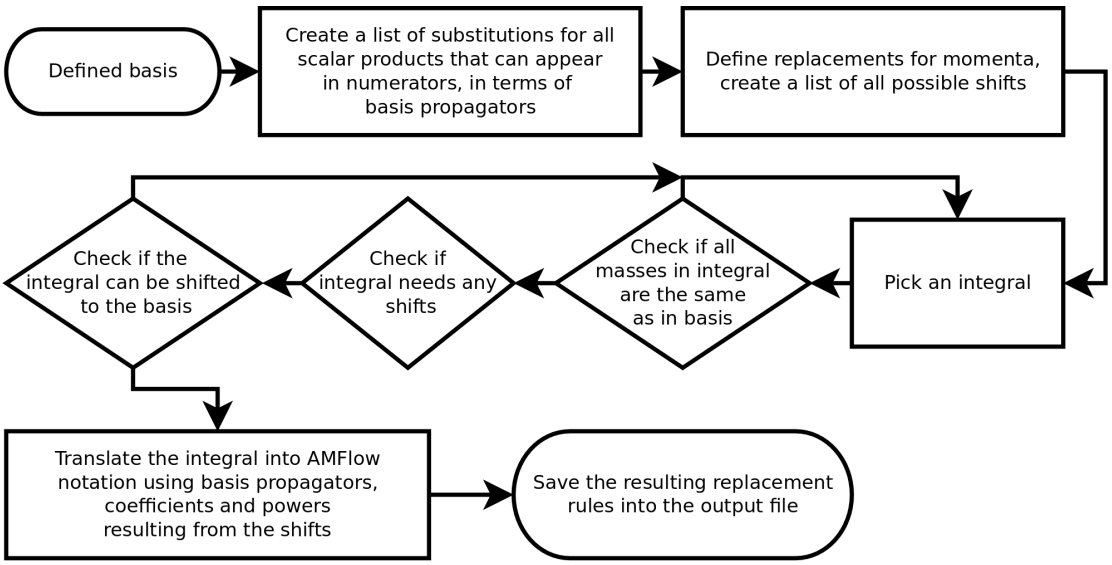

G Identification of equivalent Feynman integrals

As mentioned in section 5.3, generating multiloop amplitudes, for instance, by `FeynArts`, we can get many integrals that look different but are actually mathematically equivalent due to symmetries or redefinitions of loop momenta. The goal of the algorithm is to recognise when two integrals are the same or are so-called topologically equivalent. The algorithm is based on the structure of the U and F graph polynomials. U and F polynomials do not depend on the momenta flow of propagators, and for two equivalent diagrams, the polynomials must be the same up to permutation of the Feynman parameter indices. As a reminder, see section C: The U polynomial (First Symanzik Polynomial) encodes the topology of the graph (i.e., how loops are connected), and the F polynomial (Second Symanzik Polynomial) encodes both the topology and the kinematics (external momenta and masses). The canonical labelling algorithm for polynomials—especially in the context of Feynman integrals—aims to assign a unique, standardized representation to each integral based on its U and F graph polynomials. The algorithm performs a permutation of the Feynman parameter indices and, among all permutations, selects the one that gives the lexicographically smallest polynomial representation. The algorithm can be used for the sum as well as for the product of U and F polynomials. From the package[5] `TopoID` [303, 304], we used only the part which computes the canonical form of a given polynomial. Our approach works in the following way

[5]For the original concept, see [268], also [302].

1. take Feynman propagators corresponding to a diagram from a list of diagrams and mark the diagram as belonging to the n'th diagram family (n = 1, 2, 3, etc.);

2. compute U and F polynomials;

3. find the canonical form of the product $U * F$;

4. take the next diagram and repeat steps 2) and 3);

5. if canonical forms are the same, we put this diagram into the n'th family;

6. repeat procedure to the end of all diagrams;

7. remove from the starting list all diagrams belonging to the n'th family;

8. repeat steps 1)-7) until all diagrams are distributed into different families.

After that, within each diagram family, we perform a shift of loop momenta to have the same momenta flow for all diagrams. An example of such a family's identification is given in a file dMWsq3_3loop_diags.nb in repository [166].

We take these families as input for our `SEflow` script, and we are sure that our shifting procedure is not wasting time trying to fit different topologies. Diagrams in the starting list must be sorted from diagrams with the largest number of propagators to the smallest. Talking about diagram families, it may happen that a diagram with a smaller number of propagators belongs to a family of diagrams with a bigger number of propagators. This becomes possible when we remove one or more propagators in the family with a larger number of propagators (later, to compute individual Feynman integrals, we use IBP's method, and cancellation of propagators is a typical situation). Removing a propagator is equivalent to setting the corresponding Feynman parameter to zero. An example of such a situation is shown in Fig. 43, where the third diagram appears after removing the $W(G)$ propagator from the first (second) diagram. When we meet a diagram with a smaller number of propagators on step 4), we need to modify the $U*F$ function for the starting set of propagators and perform the test several times. For example, if the starting set has N propagators and a new diagram - N-1, we set one of the Feynman parameters to zero for the starting diagram. Repeating this for each parameter, we get N different functions from the function $U*F$, then we compare them with the $U*F$ function for the diagram with N-1 propagators. After getting the match, the new diagram is marked as belonging to the family.

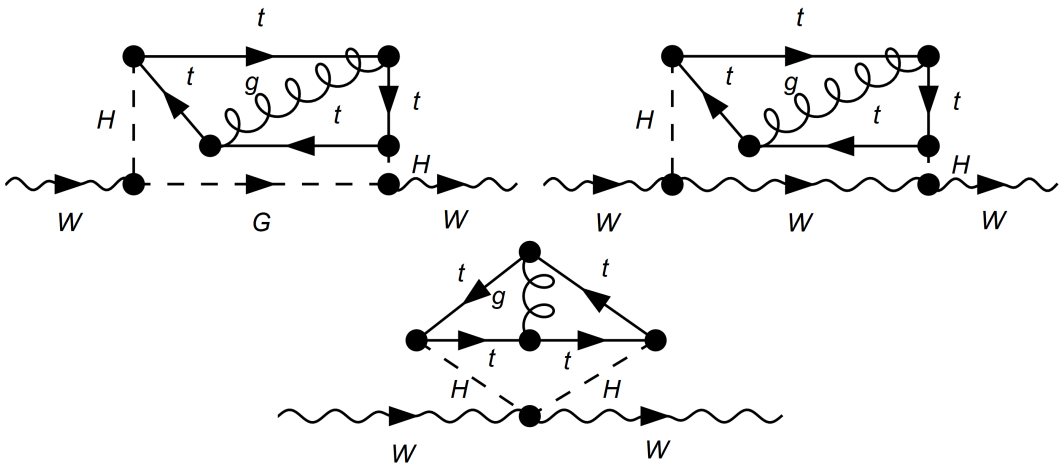

Figure 43: Diagrams from family 46 of the genuine 3-loop W self-energy discussed in the text as defined in dMWsq3_3loop_diags.nb.

In the genuine 3-loop self-energy and vertex cases, described identification of symmetrical topologies speed up complete calculations typically by at least one order of magnitude.

References

[1] Physics at the Precision Frontier: Then, Now, and Tomorrow by Harrison B. Prosper, RADCOR-LoopFest 2021, https://indico.cern.ch/event/958085/.

[2] A. A. Michelson, E. W. Morley, On the Relative Motion of the Earth and the Luminiferous Ether, Am. J. Sci. 34 (1887) 333–345. doi:10.2475/ajs.s3-34.203.333.

[3] J. Rafelski, Modern Special Relativity: A Student's Guide with Discussions and Examples, Springer International Publishing, 2022.
URL https://books.google.pl/books?id=hieXzQEACAAJ

[4] G. Kunstatter, S. Das, A First Course on Symmetry, Special Relativity and Quantum Mechanics: The Foundations of Physics, Undergraduate Lecture Notes in Physics, Springer International Publishing, 2022.
URL https://books.google.pl/books?id=4ZCzzgEACAAJ

[5] Y. Fukuda, et al., Evidence for oscillation of atmospheric neutrinos, Phys. Rev. Lett. 81 (1998) 1562–1567. arXiv:hep-ex/9807003, doi:10.1103/PhysRevLett.81.1562.

[6] Q. R. Ahmad, et al., Direct evidence for neutrino flavor transformation from neutral current interactions in the Sudbury Neutrino Observatory, Phys. Rev. Lett. 89 (2002) 011301. arXiv:nucl-ex/0204008, doi:10.1103/PhysRevLett.89.011301.

[7] G. Aad, et al., Observation of a new particle in the search for the Standard Model Higgs boson with the ATLAS detector at the LHC, Phys. Lett. B716 (2012) 1–29. arXiv:1207.7214, doi:10.1016/j.physletb.2012.08.020.

[8] S. Chatrchyan, et al., Observation of a new boson at a mass of 125 GeV with the CMS experiment at the LHC, Phys. Lett. B716 (2012) 30–61. arXiv:1207.7235, doi:10.1016/j.physletb.2012.08.021.

[9] G. Aad, et al., A Particle Consistent with the Higgs Boson Observed with the ATLAS Detector at the Large Hadron Collider, Science 338 (6114) (2012) 1576–1582. doi:10.1126/science.1232005.

[10] B. P. Abbott, et al., Observation of Gravitational Waves from a Binary Black Hole Merger, Phys. Rev. Lett. 116 (6) (2016) 061102. arXiv:1602.03837, doi:10.1103/PhysRevLett.116.061102.

[11] Precision Alignment of the LIGO 4km Arms Using The Dual-Frequency Differential Global Positioning System (GPS), https://dcc.ligo.org/LIGO-P000006/public.

[12] D. B. Newell, et al., The CODATA 2017 values of h, e, k, and NA for the revision of the SI, Metrologia 55 (1) (2018) L13. doi:10.1088/1681-7575/aa950a.

[13] S. Navas, et al., Review of particle physics, Phys. Rev. D 110 (3) (2024) 030001. doi:10.1103/PhysRevD.110.030001.

[14] L. Morel, Z. Yao, P. Cladé, S. Guellati-Khélifa, Determination of the fine-structure constant with an accuracy of 81 parts per trillion, Nature 588 (7836) (2020) 61–65. doi:10.1038/s41586-020-2964-7.

[15] K. Beloy, et al., Frequency ratio measurements at 18-digit accuracy using an optical clock network, Nature 591, 564–569 (2021), doi:https://doi.org/10.1038/s41586-021-03253-4.

[16] D. Soyuer, L. Zwick, D. J. D'Orazio, P. Saha, Searching for gravitational waves via Doppler tracking by future missions to Uranus and Neptune, Monthly Notices of the Royal Astronomical Society: Letters 503 (1) (2021) L73–L79. doi:10.1093/mnrasl/slab025.

[17] Precision: The Measure of All Things, BBC-Four documentary series, https:/www.bbc.co.uk/programmes/b02xbjmf, https://www.dailymotion.com/video/x612oj6.

[18] M. Florio, S. Forte, E. Sirtori, Forecasting the Socio-Economic Impact of the Large Hadron Collider: a Cost-Benefit Analysis to 2025 and BeyondarXiv:1603.00886, doi:10.1016/j.techfore.2016.03.007.

[19] I. Shipsey, Vision and Outlook: The Future of Particle Physics, in: 38th International Conference on High Energy Physics, 2017. arXiv:1707.03711.

[20] R. Frisch, O. Stern, Über die magnetische Ablenkung von Wasserstoffmolekülen und das magnetische Moment des Protons. I, Z. Phys. 85 (1-2) (1933) 4–16. doi:10.1007/bf01330773.

[21] E. D. Bloom, et al., High-Energy Inelastic e-p Scattering at 6-Degrees and 10-Degrees, Phys. Rev. Lett. 23 (1969) 930–934. doi:10.1103/PhysRevLett.23.930.

[22] M. Breidenbach, et al., Observed behavior of highly inelastic electron-proton scattering, Phys. Rev. Lett. 23 (1969) 935–939. doi:10.1103/PhysRevLett.23.935.

[23] S. S. Schweber, QED and the men who made it: Dyson, Feynman, Schwinger, and Tomonaga, Princeton, USA, Univ. Pr. (1994) 732 p.

[24] H. A. Bethe, The Electromagnetic shift of energy levels, Phys. Rev. 72 (1947) 339–341. doi:10.1103/PhysRev.72.339.

[25] W. E. Lamb, R. C. Retherford, Fine Structure of the Hydrogen Atom by a Microwave Method, Phys. Rev. 72 (1947) 241–243. doi:10.1103/PhysRev.72.241.

[26] F. J. Dyson, The Radiation theories of Tomonaga, Schwinger, and Feynman, Phys. Rev. 75 (1949) 486–502. doi:10.1103/PhysRev.75.486.

[27] F. J. Dyson, The S matrix in quantum electrodynamics, Phys. Rev. 75 (1949) 1736–1755. doi:10.1103/PhysRev.75.1736.

[28] R. P. Feynman, The Theory of positrons, Phys. Rev. 76 (1949) 749–759. doi:10.1103/PhysRev.76.749.

[29] R. P. Feynman, Space-time approach to quantum electrodynamics, Phys. Rev. 76 (1949) 769–789. doi:10.1103/PhysRev.76.769.

[30] D. Kaiser, Drawing theories apart: the dispersion of Feynman diagrams in postwar physics, Chicago Univ. Press, Chicago, IL, 2005.
URL http://cds.cern.ch/record/941915

[31] J. S. Schwinger, On Quantum electrodynamics and the magnetic moment of the electron, Phys. Rev. 73 (1948) 416–417. doi:10.1103/PhysRev.73.416.

[32] D. P. Aguillard, et al., Measurement of the Positive Muon Anomalous Magnetic Moment to 0.20 ppm, Phys. Rev. Lett. 131 (16) (2023) 161802. arXiv:2308.06230, doi:10.1103/PhysRevLett.131.161802.

[33] A. Keshavarzi, The muon mystery deepens, Physics World 38 (3) (2025) 30. doi:10.1088/2058-7058/38/03/28.
URL https://dx.doi.org/10.1088/2058-7058/38/03/28

[34] R. Aliberti, et al., The anomalous magnetic moment of the muon in the Standard Model: an update. arXiv:2505.21476.

[35] T. Aoyama, et al., The anomalous magnetic moment of the muon in the Standard Model, Phys. Rept. 887 (2020) 1–166. arXiv:2006.04822, doi:10.1016/j.physrep.2020.07.006.

[36] M. J. G. Veltman, Limit on Mass Differences in the Weinberg Model, Nucl. Phys. B 123 (1977) 89–99. doi:10.1016/0550-3213(77)90342-X.

[37] F. Abe, et al., Observation of top quark production in $\bar{p}p$ collisions, Phys. Rev. Lett. 74 (1995) 2626–2631. arXiv:hep-ex/9503002, doi:10.1103/PhysRevLett.74.2626.

[38] S. Abachi, et al., Observation of the top quark, Phys. Rev. Lett. 74 (1995) 2632–2637. arXiv:hep-ex/9503003, doi:10.1103/PhysRevLett.74.2632.

[39] M. J. G. Veltman, Second Threshold in Weak Interactions, Acta Phys. Polon. B 8 (1977) 475–492.

[40] A. A. Akhundov, D. Y. Bardin, T. Riemann, Electroweak One Loop Corrections to the Decay of the Neutral Vector Boson, Nucl. Phys. B 276 (1986) 1–13. doi:10.1016/0550-3213(86)90014-3.

[41] W. Beenakker, W. Hollik, The Width of the Z Boson, Z. Phys. C 40 (1988) 141. doi:10.1007/BF01559728.

[42] F. Jegerlehner, Physics of precision experiments with Zs, Prog. Part. Nucl. Phys. 27 (1991) 1–76. doi:10.1016/0146-6410(91)90002-6.

[43] J. Bernabeu, A. Pich, A. Santamaria, Γ (Z —> B anti-B): A Signature of Hard Mass Terms for a Heavy Top, Phys. Lett. B 200 (1988) 569–574. doi:10.1016/0370-2693(88)90173-6.

[44] K. Hikasa, et al., Review of particle properties. Particle Data Group, Phys. Rev. D 45 (1992) S1, [Erratum: Phys.Rev.D 46, 5210 (1992)]. doi:10.1103/PhysRevD.45.S1.

[45] S. Schael, et al., Precision electroweak measurements on the Z resonance, Phys. Rept. 427 (2006) 257–454. arXiv:hep-ex/0509008, doi:10.1016/j.physrep.2005.12.006.

[46] D. Y. Bardin, et al., Electroweak working group report, in: Workshop Group on Precision Calculations for the Z Resonance (2nd meeting held Mar 31, 3rd meeting held Jun 13), 1997. arXiv:hep-ph/9709229.

[47] D. Y. Bardin, A. Leike, T. Riemann, Higgs production in e+ e- —> lepton anti-lepton q anti-q at LEP and NLC, Phys. Lett. B 353 (1995) 513–518. arXiv:hep-ph/9504204, doi:10.1016/0370-2693(95)00587-B.

[48] F. Jegerlehner, $\alpha_{QED,eff}$(s) for precision physics at the FCC-ee/ILC, CERN Yellow Reports: Monographs 3 (2020) 9–37. doi:10.23731/CYRM-2020-003.9.

[49] F. Halzen, A. D. Martin, Quarks and leptons: an introductory course in modern particle physics, Wiley, 1984.

[50] Open Symposium on the European Strategy for Particle Physics, Venice 2025, https://agenda.infn.it/event/44943/overview.

[51] A. Blondel, et al., LEP3: A High Luminosity e^+e^- Collider to Study the Higgs Boson. arXiv:1208.0504.

[52] A. Abada, et al., FCC-ee: The Lepton Collider: Future Circular Collider Conceptual Design Report Volume 2, Eur. Phys. J. ST 228 (2) (2019) 261–623. doi:10.1140/epjst/e2019-900045-4.

[53] CEPC Conceptual Design Report: Volume 1 - Accelerator arXiv:1809.00285.

[54] M. Dong, et al., CEPC Conceptual Design Report: Volume 2 - Physics & Detector arXiv:1811.10545.

[55] Physics and Detectors at CLIC: CLIC Conceptual Design Report. arXiv:1202.5940, doi:10.5170/CERN-2012-003.

[56] The International Linear Collider Technical Design Report - Volume 1: Executive Summary. arXiv:1306.6327.

[57] M. Narain, et al., The Future of US Particle Physics - The Snowmass 2021 Energy Frontier Report. arXiv:2211.11084.

[58] Future Colliders Comparative Evaluation - Working Group Report, https://indico.cern.ch/event/1439855/contributions/6542430/.

[59] N. Alipour Tehrani, et al., FCC-ee: Your Questions Answered, in: A. Blondel, P. Janot (Eds.), CERN Council Open Symposium on the Update of European Strategy for Particle Physics, 2019. arXiv:1906.02693.

[60] A. Freitas, et al., Theoretical uncertainties for electroweak and Higgs-boson precision measurements at FCC-ee, arXiv:1906.05379.

[61] A. Blondel, A. Freitas, J. Gluza, T. Riemann, S. Heinemeyer, S. Jadach, P. Janot, Theory Requirements and Possibilities for the FCC-ee and other Future High Energy and Precision Frontier Lepton Colliders arXiv:1901.02648.

[62] M. Benedikt, et al., Future Circular Collider Feasibility Study Report: Volume 1, Physics, Experiments, Detectors arXiv:2505.00272, doi:10.17181/CERN.9DKX.TDH9.

[63] A. Abada, et al., FCC Physics Opportunities: Future Circular Collider Conceptual Design Report Volume 1, Eur. Phys. J. C 79 (6) (2019) 474. doi:10.1140/epjc/s10052-019-6904-3.

[64] I. Dubovyk, A. Freitas, J. Gluza, T. Riemann, J. Usovitsch, Electroweak pseudo-observables and Z-boson form factors at two-loop accuracy, JHEP 08 (2019) 113. arXiv:1906.08815, doi:10.1007/JHEP08(2019)113.

[65] A. Blondel, et al., Standard model theory for the FCC-ee Tera-Z stage, in: Mini Workshop on Precision EW and QCD Calculations for the FCC Studies : Methods and Techniques, Vol. 3/2019 of CERN Yellow Reports: Monographs, CERN, Geneva, 2018. arXiv:1809.01830, doi:10.23731/CYRM-2019-003.

[66] I. Dubovyk, A. Freitas, J. Gluza, T. Riemann, J. Usovitsch, Complete electroweak two-loop corrections to Z boson production and decay, Phys. Lett. B 783 (2018) 86–94. arXiv:1804.10236, doi:10.1016/j.physletb.2018.06.037.

[67] Workshop on Precision Measurements of alphas. arXiv:1110.0016.

[68] D. D'Enterria, High-precision α_S from W and Z hadronic decays (2019) 145–149doi:10.22323/1.365.0008.

[69] A. Abada, et al., FCC-ee: The Lepton Collider: Future Circular Collider Conceptual Design Report Volume 2, Eur. Phys. J. ST 228 (2) (2019) 261–623. doi:10.1140/epjst/e2019-900045-4.

[70] A. Blondel, P. Janot, FCC-ee overview: new opportunities create new challenges, Eur. Phys. J. Plus 137 (1) (2022) 92. arXiv:2106.13885, doi:10.1140/epjp/s13360-021-02154-9.

[71] J. de Blas, M. Ciuchini, E. Franco, A. Goncalves, S. Mishima, M. Pierini, L. Reina, L. Silvestrini, Global analysis of electroweak data in the Standard Model, Phys. Rev. D 106 (3) (2022) 033003. arXiv:2112.07274, doi:10.1103/PhysRevD.106.033003.

[72] A. Blondel, P. Janot, Circular and Linear e^+e^- Colliders: Another Story of Complementarity, arXiv:1912.11871.

[73] Gamma Factory – New physics opportunities for CERN by D. M. Krasny, Corfu SM and Beyond 2022, https://indico.cern.ch/event/1166991.

[74] E. Adli, Plasma Wakefield Linear Colliders - Opportunities and Challenges. arXiv:1905.01879, doi:10.1098/rsta.2018.0419.

[75] A. Salam, Weak and Electromagnetic Interactions, Conf. Proc. C 680519 (1968) 367–377. doi:10.1142/9789812795915_0034.

[76] S. L. Glashow, Partial Symmetries of Weak Interactions, Nucl. Phys. 22 (1961) 579–588. doi:10.1016/0029-5582(61)90469-2.

[77] S. L. Glashow, J. Iliopoulos, L. Maiani, Weak Interactions with Lepton-Hadron Symmetry, Phys. Rev. D 2 (1970) 1285–1292. doi:10.1103/PhysRevD.2.1285.

[78] S. Weinberg, A Model of Leptons, Phys. Rev. Lett. 19 (1967) 1264–1266. doi:10.1103/PhysRevLett.19.1264.

[79] G. 't Hooft, Renormalizable Lagrangians for Massive Yang-Mills Fields, Nucl. Phys. B 35 (1971) 167–188. doi:10.1016/0550-3213(71)90139-8.

[80] D. J. Gross, F. Wilczek, Ultraviolet Behavior of Nonabelian Gauge Theories, Phys. Rev. Lett. 30 (1973) 1343–1346. doi:10.1103/PhysRevLett.30.1343.

[81] H. D. Politzer, Reliable Perturbative Results for Strong Interactions?, Phys. Rev. Lett. 30 (1973) 1346–1349. doi:10.1103/PhysRevLett.30.1346.

[82] G. Aad, et al., Observation of a new particle in the search for the Standard Model Higgs boson with the ATLAS detector at the LHC, Phys. Lett. B 716 (2012) 1–29. arXiv:1207.7214, doi:10.1016/j.physletb.2012.08.020.

[83] S. Chatrchyan, et al., Observation of a New Boson at a Mass of 125 GeV with the CMS Experiment at the LHC, Phys. Lett. B 716 (2012) 30–61. arXiv:1207.7235, doi:10.1016/j.physletb.2012.08.021.

[84] H. Georgi, Lie algebras in particle physics, 2nd Edition, Vol. 54, Perseus Books, Reading, MA, 1999.

[85] R. E. Behrends, R. J. Finkelstein, A. Sirlin, Radiative corrections to decay processes, Phys. Rev. 101 (1956) 866–873. doi:10.1103/PhysRev.101.866.

[86] T. Kinoshita, A. Sirlin, Radiative corrections to Fermi interactions, Phys. Rev. 113 (1959) 1652–1660. doi:10.1103/PhysRev.113.1652.

[87] W. Greiner, B. Muller, Gauge theory of weak interactions, 1993.

[88] D. Y. Bardin, G. Passarino, The standard model in the making: Precision study of the electroweak interactions, 1999.

[89] (i) Electroweak Theory and LEP Physics and (ii) Physics of precision experiments with Z's by F. Jegerlehner, http://www-com.physik.hu-berlin.de/~fjeger/books.html.

[90] M. Bohm, A. Denner, H. Joos, Gauge theories of the strong and electroweak interaction, 2001. doi:10.1007/978-3-322-80160-9.

[91] A. Sirlin, Radiative Corrections in the SU(2)-L x U(1) Theory: A Simple Renormalization Framework, Phys. Rev. D 22 (1980) 971–981. doi:10.1103/PhysRevD.22.971.

[92] W. J. Marciano, A. Sirlin, Radiative Corrections to Neutrino Induced Neutral Current Phenomena in the SU(2)-L x U(1) Theory, Phys. Rev. D 22 (1980) 2695, [Erratum: Phys.Rev.D 31, 213 (1985)]. doi:10.1103/PhysRevD.22.2695.

[93] A. Sirlin, W. J. Marciano, Radiative Corrections to Muon-neutrino N —> mu- X and their Effect on the Determination of rho**2 and sin**2-Theta(W), Nucl. Phys. B 189 (1981) 442–460. doi:10.1016/0550-3213(81)90574-5.

[94] W. J. Marciano, The Weak Mixing Angle and Grand Unified Gauge Theories, Phys. Rev. D 20 (1979) 274. doi:10.1103/PhysRevD.20.274.

[95] A. Sirlin, On the O(alpha**2) Corrections to tau (mu), m (W), m (Z) in the SU(2)-L x U(1) Theory, Phys. Rev. D 29 (1984) 89. doi:10.1103/PhysRevD.29.89.

[96] M. Consoli, W. Hollik, F. Jegerlehner, The Effect of the Top Quark on the M(W)-M(Z) Interdependence and Possible Decoupling of Heavy Fermions from Low-Energy Physics, Phys. Lett. B 227 (1989) 167–170. doi:10.1016/0370-2693(89)91301-4.

[97] A. Djouadi, C. Verzegnassi, Virtual Very Heavy Top Effects in LEP / SLC Precision Measurements, Phys. Lett. B 195 (1987) 265–271. doi:10.1016/0370-2693(87)91206-8.

[98] L. Avdeev, J. Fleischer, S. Mikhailov, O. Tarasov, $0(\alpha\alpha_s^2)$ correction to the electroweak ρ parameter, Phys. Lett. B 336 (1994) 560–566, [Erratum: Phys.Lett.B 349, 597–598 (1995)]. arXiv:hep-ph/9406363, doi:10.1016/0370-2693(94)90573-8.

[99] K. G. Chetyrkin, J. H. Kuhn, M. Steinhauser, Corrections of order $\mathcal{O}(G_F M_t^2 \alpha_s^2)$ to the ρ parameter, Phys. Lett. B 351 (1995) 331–338. arXiv:hep-ph/9502291, doi:10.1016/0370-2693(95)00380-4.

[100] K. G. Chetyrkin, J. H. Kuhn, M. Steinhauser, QCD corrections from top quark to relations between electroweak parameters to order alpha-s**2, Phys. Rev. Lett. 75 (1995) 3394–3397. arXiv:hep-ph/9504413, doi:10.1103/PhysRevLett.75.3394.

[101] K. G. Chetyrkin, J. H. Kuhn, M. Steinhauser, Three loop polarization function and O (alpha-s**2) corrections to the production of heavy quarks, Nucl. Phys. B 482 (1996) 213–240. arXiv:hep-ph/9606230, doi:10.1016/S0550-3213(96)00534-2.

[102] J. J. van der Bij, F. Hoogeveen, Two Loop Correction to Weak Interaction Parameters Due to a Heavy Fermion Doublet, Nucl. Phys. B 283 (1987) 477–492. doi:10.1016/0550-3213(87)90284-7.

[103] R. Barbieri, M. Beccaria, P. Ciafaloni, G. Curci, A. Vicere, Radiative correction effects of a very heavy top, Phys. Lett. B 288 (1992) 95–98, [Erratum: Phys.Lett.B 312, 511–511 (1993)]. arXiv:hep-ph/9205238, doi:10.1016/0370-2693(92)91960-H.

[104] R. Barbieri, M. Beccaria, P. Ciafaloni, G. Curci, A. Vicere, Two loop heavy top effects in the Standard Model, Nucl. Phys. B 409 (1993) 105–127. doi:10.1016/0550-3213(93)90448-X.

[105] J. Fleischer, O. V. Tarasov, F. Jegerlehner, Two loop heavy top corrections to the rho parameter: A Simple formula valid for arbitrary Higgs mass, Phys. Lett. B 319 (1993) 249–256. doi:10.1016/0370-2693(93)90810-5.

[106] G. Degrassi, P. Gambino, A. Vicini, Two loop heavy top effects on the m(Z) - m(W) interdependence, Phys. Lett. B 383 (1996) 219–226. arXiv:hep-ph/9603374, doi:10.1016/0370-2693(96)00720-4.

[107] G. Degrassi, P. Gambino, A. Sirlin, Precise calculation of M(W), sin**2 theta(W) (M(Z)), and sin**2 theta(eff)(lept), Phys. Lett. B 394 (1997) 188–194. arXiv:hep-ph/9611363, doi:10.1016/S0370-2693(96)01677-2.

[108] A. Djouadi, O(alpha alpha-s) Vacuum Polarization Functions of the Standard Model Gauge Bosons, Nuovo Cim. A 100 (1988) 357. doi:10.1007/BF02812964.

[109] B. A. Kniehl, Two Loop Corrections to the Vacuum Polarizations in Perturbative QCD, Nucl. Phys. B 347 (1990) 86–104. doi:10.1016/0550-3213(90)90552-O.

[110] A. Djouadi, P. Gambino, Electroweak gauge bosons selfenergies: Complete QCD corrections, Phys. Rev. D 49 (1994) 3499–3511, [Erratum: Phys.Rev.D 53, 4111 (1996)]. arXiv:hep-ph/9309298, doi:10.1103/PhysRevD.49.3499.

[111] F. Halzen, B. A. Kniehl, Δ r beyond one loop, Nucl. Phys. B 353 (1991) 567–590. doi:10.1016/0550-3213(91)90319-S.

[112] A. Freitas, W. Hollik, W. Walter, G. Weiglein, Complete fermionic two loop results for the M(W) - M(Z) interdependence, Phys. Lett. B 495 (2000) 338–346, [Erratum: Phys.Lett.B 570, 265 (2003)]. arXiv:hep-ph/0007091, doi:10.1016/S0370-2693(00)01263-6.

[113] A. Freitas, W. Hollik, W. Walter, G. Weiglein, Electroweak two loop corrections to the $M_W - M_Z$ mass correlation in the standard model, Nucl. Phys. B 632 (2002) 189–218, [Erratum: Nucl.Phys.B 666, 305–307 (2003)]. arXiv:hep-ph/0202131, doi:10.1016/S0550-3213(02)00243-2.

[114] M. Awramik, M. Czakon, Complete two loop electroweak contributions to the muon lifetime in the standard model, Phys. Lett. B 568 (2003) 48–54. arXiv:hep-ph/0305248, doi:10.1016/j.physletb.2003.06.007.

[115] M. Awramik, M. Czakon, Complete two loop bosonic contributions to the muon lifetime in the standard model, Phys. Rev. Lett. 89 (2002) 241801. arXiv:hep-ph/0208113, doi:10.1103/PhysRevLett.89.241801.

[116] A. Onishchenko, O. Veretin, Two loop bosonic electroweak corrections to the muon lifetime and M(Z) - M(W) interdependence, Phys. Lett. B 551 (2003) 111–114. arXiv:hep-ph/0209010, doi:10.1016/S0370-2693(02)03004-6.

[117] M. Awramik, M. Czakon, A. Onishchenko, O. Veretin, Bosonic corrections to Delta r at the two loop level, Phys. Rev. D 68 (2003) 053004. arXiv:hep-ph/0209084, doi:10.1103/PhysRevD.68.053004.

[118] J. J. van der Bij, K. G. Chetyrkin, M. Faisst, G. Jikia, T. Seidensticker, Three loop leading top mass contributions to the rho parameter, Phys. Lett. B 498 (2001) 156–162. arXiv:hep-ph/0011373, doi:10.1016/S0370-2693(01)00002-8.

[119] M. Faisst, J. H. Kuhn, T. Seidensticker, O. Veretin, Three loop top quark contributions to the rho parameter, Nucl. Phys. B 665 (2003) 649–662. arXiv:hep-ph/0302275, doi:10.1016/S0550-3213(03)00450-4.

[120] Y. Schroder, M. Steinhauser, Four-loop singlet contribution to the rho parameter, Phys. Lett. B 622 (2005) 124–130. arXiv:hep-ph/0504055, doi:10.1016/j.physletb.2005.06.085.

[121] K. G. Chetyrkin, M. Faisst, J. H. Kuhn, P. Maierhofer, C. Sturm, Four-Loop QCD Corrections to the Rho Parameter, Phys. Rev. Lett. 97 (2006) 102003. arXiv:hep-ph/0605201, doi:10.1103/PhysRevLett.97.102003.

[122] R. Boughezal, M. Czakon, Single scale tadpoles and O(G(F m(t)**2 alpha(s)**3)) corrections to the rho parameter, Nucl. Phys. B 755 (2006) 221–238. arXiv:hep-ph/0606232, doi:10.1016/j.nuclphysb.2006.08.007.

[123] M. Czakon, A. Czarnecki, M. Dowling, Three-loop corrections to the muon and heavy quark decay rates, Phys. Rev. D 103 (2021) L111301. arXiv:2104.05804, doi:10.1103/PhysRevD.103.L111301.

[124] M. Awramik, M. Czakon, A. Freitas, G. Weiglein, Precise Prediction for the W Boson Mass in the Standard Model, Phys. Rev. D 69 (2004) 053006. arXiv:hep-ph/0311148, doi:10.1103/PhysRevD.69.053006.

[125] A. Arbuzov, M. Awramik, M. Czakon, A. Freitas, M. Grünewald, K. Mönig, S. Riemann, T. Riemann, ZFITTER: A Semi-analytical program for fermion pair production in e^+e^- annihilation, from version 6.21 to version 6.42, Comput. Phys. Commun. 174 (2006) 728–758. arXiv:hep-ph/0507146, doi:10.1016/j.cpc.2005.12.009.

[126] D. Bardin, M. Bilenky, P. Christova, M. Jack, L. Kalinovskaya, A. Olchevski, S. Riemann, T. Riemann, ZFITTER 6.21: A semi-analytical program for fermion pair production in e^+e^- annihilation, Comput. Phys. Commun. 133 (2001) 229–395. arXiv:hep-ph/9908433, doi:10.1016/S0010-4655(00)00152-1.

[127] The ZFITTER homepage, http://sanc.jinr.ru/users/zfitter.

[128] A. Arbuzov, J. Gluza, L. Kalinovskaya, S. Riemann, T. Riemann, V. Yermolchyk, Computer package DIZET v. 6.45, Comput. Phys. Commun. 291 (2023) 108846. arXiv:2301.07168, doi:10.1016/j.cpc.2023.108846.

[129] F. Jegerlehner, Variations on Photon Vacuum Polarization, EPJ Web Conf. 218 (2019) 01003. arXiv:1711.06089, doi:10.1051/epjconf/201921801003.

[130] S. Riemann, *Suche nach einem Z'-Boson auf der Z-Resonanz mit dem L3-Detektor am LEP-Beschleuniger*, Dissertation, Technische Hochschule Aachen (1994), 94 S., Internal Report: DESY-Zeuthen 94-01, September 1994.

[131] S. Willenbrock, G. Valencia, On the definition of the Z boson mass, Phys. Lett. B 259 (1991) 373–376. doi:10.1016/0370-2693(91)90843-F.

[132] R. G. Stuart, Gauge invariant perturbation theory near a gauge resonance, in: Workshop on High-energy Phenomenology (CINVESTAV), 1991.
URL https://inspirehep.net/literature/322288

[133] A. Leike, T. Riemann, J. Rose, S matrix approach to the Z line shape, Phys. Lett. B 273 (1991) 513–518. arXiv:hep-ph/9508390, doi:10.1016/0370-2693(91)90307-C.

[134] T. Riemann, Cross-section asymmetries around the Z peak, Phys. Lett. B 293 (1992) 451–456. arXiv:hep-ph/9506382, doi:10.1016/0370-2693(92)90911-M.

[135] M. Passera, A. Sirlin, Radiative corrections to W and quark propagators in the resonance region, Phys. Rev. D 58 (1998) 113010. arXiv:hep-ph/9804309, doi:10.1103/PhysRevD.58.113010.

[136] P. Gambino, P. A. Grassi, The Nielsen identities of the SM and the definition of mass, Phys. Rev. D 62 (2000) 076002. arXiv:hep-ph/9907254, doi:10.1103/PhysRevD.62.076002.

[137] A. R. Bohm, N. L. Harshman, On the mass and width of the Z boson and other relativistic quasistable particles, Nucl. Phys. B 581 (2000) 91–115. arXiv:hep-ph/0001206, doi:10.1016/S0550-3213(00)00249-2.

[138] M. Awramik, M. Czakon, A. Freitas, Electroweak two-loop corrections to the effective weak mixing angle, JHEP 11 (2006) 048. arXiv:hep-ph/0608099, doi:10.1088/1126-6708/2006/11/048.

[139] D. Y. Bardin, A. Leike, T. Riemann, M. Sachwitz, Energy Dependent Width Effects in e+ e- Annihilation Near the Z Boson Pole, Phys. Lett. B 206 (1988) 539–542. doi:10.1016/0370-2693(88)91627-9.

[140] T. Riemann, S-matrix Approach to the Z Resonance, Acta Phys. Polon. B 46 (11) (2015) 2235. arXiv:1610.04501, doi:10.5506/APhysPolB.46.2235.

[141] I. Dubovyk, A. Freitas, J. Gluza, T. Riemann, J. Usovitsch, The two-loop electroweak bosonic corrections to $\sin^2\theta^{\rm b}_{\rm eff}$, Phys. Lett. B 762 (2016) 184–189. arXiv:1607.08375, doi:10.1016/j.physletb.2016.09.012.

[142] D. Y. Bardin, P. K. Khristova, O. M. Fedorenko, On the Lowest Order Electroweak Corrections to Spin 1/2 Fermion Scattering. 1. The One Loop Diagrammar, Nucl. Phys. B 175 (1980) 435–461. doi:10.1016/0550-3213(80)90021-8.

[143] D. Y. Bardin, P. K. Khristova, O. M. Fedorenko, On the Lowest Order Electroweak Corrections to Spin 1/2 Fermion Scattering. 2. The One Loop Amplitudes, Nucl. Phys. B 197 (1982) 1–44. doi:10.1016/0550-3213(82)90152-3.

[144] W. J. Marciano, A. Sirlin, Testing the Standard Model by Precise Determinations of W+- and Z Masses, Phys. Rev. D 29 (1984) 945, [Erratum: Phys.Rev.D 31, 213 (1985)]. doi:10.1103/PhysRevD.29.945.

[145] M. Awramik, M. Czakon, A. Freitas, G. Weiglein, Complete two-loop electroweak fermionic corrections to $\sin^2\theta^{\rm lept}_{\rm eff}$ and indirect determination of the Higgs boson mass, Phys. Rev. Lett. 93 (2004) 201805. arXiv:hep-ph/0407317, doi:10.1103/PhysRevLett.93.201805.

[146] M. Awramik, M. Czakon, A. Freitas, Bosonic corrections to the effective weak mixing angle at O(alpha**2), Phys. Lett. B 642 (2006) 563–566. arXiv:hep-ph/0605339, doi:10.1016/j.physletb.2006.07.035.

[147] W. Hollik, U. Meier, S. Uccirati, The Effective electroweak mixing angle sin**2 theta(eff) with two-loop fermionic contributions, Nucl. Phys. B 731 (2005) 213–224. arXiv:hep-ph/0507158, doi:10.1016/j.nuclphysb.2005.10.015.

[148] W. Hollik, U. Meier, S. Uccirati, The Effective electroweak mixing angle sin**2 theta(eff) with two-loop bosonic contributions, Nucl. Phys. B 765 (2007) 154–165. arXiv:hep-ph/0610312, doi:10.1016/j.nuclphysb.2006.12.001.

[149] M. Awramik, M. Czakon, A. Freitas, B. A. Kniehl, Two-loop electroweak fermionic corrections to sin**2 theta**b anti-b(eff), Nucl. Phys. B 813 (2009) 174–187. arXiv:0811.1364, doi:10.1016/j.nuclphysb.2008.12.031.

[150] A. Freitas, Two-loop fermionic electroweak corrections to the Z-boson width and production rate, Phys. Lett. B 730 (2014) 50–52. arXiv:1310.2256, doi:10.1016/j.physletb.2014.01.017.

[151] A. Freitas, Electroweak precision tests in the LHC era and Z-decay form factors at two-loop level, in: 12th DESY Workshop on Elementary Particle Physics: Loops and Legs in Quantum Field Theory, 2014. arXiv:1406.6980.

[152] A. Freitas, Higher-order electroweak corrections to the partial widths and branching ratios of the Z boson, JHEP 04 (2014) 070. arXiv:1401.2447, doi:10.1007/JHEP04(2014)070.

[153] A. Denner, Techniques for calculation of electroweak radiative corrections at the one loop level and results for W physics at LEP-200, Fortsch. Phys. 41 (1993) 307–420. arXiv:0709.1075, doi:10.1002/prop.2190410402.

[154] A. Denner, S. Dittmaier, Electroweak Radiative Corrections for Collider Physics, Phys. Rept. 864 (2020) 1–163. arXiv:1912.06823, doi:10.1016/j.physrep.2020.04.001.

[155] https://www.aidansean.com/feynman/.

[156] T. Hahn, Generating Feynman diagrams and amplitudes with FeynArts 3, Comput. Phys. Commun. 140 (2001) 418–431. arXiv:hep-ph/0012260, doi:10.1016/S0010-4655(01)00290-9.

[157] V. Shtabovenko, R. Mertig, F. Orellana, FeynCalc 10: Do multiloop integrals dream of computer codes?, Comput. Phys. Commun. 306 (2025) 109357. arXiv:2312.14089, doi:10.1016/j.cpc.2024.109357.

[158] T. Hahn, M. Perez-Victoria, Automatized one loop calculations in four-dimensions and D-dimensions, Comput. Phys. Commun. 118 (1999) 153–165. arXiv:hep-ph/9807565, doi:10.1016/S0010-4655(98)00173-8.

[159] A. Alloul, N. D. Christensen, C. Degrande, C. Duhr, B. Fuks, FeynRules 2.0 - A complete toolbox for tree-level phenomenology, Comput. Phys. Commun. 185 (2014) 2250–2300. arXiv:1310.1921, doi:10.1016/j.cpc.2014.04.012.

[160] D. Fontes, J. C. Romão, FeynMaster Manual, 2025. arXiv:2504.01865.

[161] H. H. Patel, Package-X: A Mathematica package for the analytic calculation of one-loop integrals, Comput. Phys. Commun. 197 (2015) 276–290. arXiv:1503.01469, doi:10.1016/j.cpc.2015.08.017.

[162] H. H. Patel, Package-X 2.0: A Mathematica package for the analytic calculation of one-loop integrals, Comput. Phys. Commun. 218 (2017) 66–70. arXiv:1612.00009, doi:10.1016/j.cpc.2017.04.015.

[163] S. Carrazza, R. K. Ellis, G. Zanderighi, QCDLoop: a comprehensive framework for one-loop scalar integrals, Comput. Phys. Commun. 209 (2016) 134–143. arXiv:1605.03181, doi:10.1016/j.cpc.2016.07.033.

[164] A. van Hameren, OneLOop: For the evaluation of one-loop scalar functions, Comput. Phys. Commun. 182 (2011) 2427–2438. arXiv:1007.4716, doi:10.1016/j.cpc.2011.06.011.

[165] I. Dubovyk, J. Gluza, G. Somogyi, Mellin-Barnes Integrals: A Primer on Particle Physics Applications, Lect. Notes Phys. 1008 (2022) pp. arXiv:2211.13733, doi:10.1007/978-3-031-14272-7.

[166] Github repository with the thesis results https://github.com/k-grzanka/PhD_res.

[167] L. Chen, A. Freitas, Mixed EW-QCD leading fermionic three-loop corrections at $\mathcal{O}(\alpha_s\alpha^2)$ to electroweak precision observables, JHEP 03 (2021) 215. arXiv:2012.08605, doi:10.1007/JHEP03(2021)215.

[168] L. Chen, A. Freitas, Leading fermionic three-loop corrections to electroweak precision observables, JHEP 07 (2020) 210. arXiv:2002.05845, doi:10.1007/JHEP07(2020)210.

[169] G. Heinrich, Collider Physics at the Precision Frontier, Phys. Rept. 922 (2021) 1–69. arXiv:2009.00516, doi:10.1016/j.physrep.2021.03.006.

[170] S. Borowka, G. Heinrich, S. Jahn, S. P. Jones, M. Kerner, J. Schlenk, T. Zirke, pySecDec: a toolbox for the numerical evaluation of multi-scale integrals, Comput. Phys. Commun. 222 (2018) 313–326. arXiv:1703.09692, doi:10.1016/j.cpc.2017.09.015.

[171] G. Heinrich, S. Jahn, S. P. Jones, M. Kerner, F. Langer, V. Magerya, A. Pöldaru, J. Schlenk, E. Villa, Expansion by regions with pySecDec, Comput. Phys. Commun. 273 (2022) 108267. arXiv:2108.10807, doi:10.1016/j.cpc.2021.108267.

[172] A. V. Smirnov, N. D. Shapurov, L. I. Vysotsky, FIESTA5: Numerical high-performance Feynman integral evaluation, Comput. Phys. Commun. 277 (2022) 108386. arXiv:2110.11660, doi:10.1016/j.cpc.2022.108386.

[173] M. Czakon, Automatized analytic continuation of Mellin-Barnes integrals, Comput. Phys. Commun. 175 (2006) 559–571. arXiv:hep-ph/0511200, doi:10.1016/j.cpc.2006.07.002.

[174] J. Usovitsch, Numerical evaluation of mellin-barnes integrals in minkowskian regions and their application to two-loop bosonic electroweak contributions to the weak mixing angle of the zbb(bar)-vertex, Ph.D. thesis, Humboldt-Universitat zu Berlin, Mathematisch-Naturwissenschaftliche Fakultat (2018). doi:http://dx.doi.org/10.18452/19484.

[175] J. Gluza, K. Kajda, T. Riemann, AMBRE: A Mathematica package for the construction of Mellin-Barnes representations for Feynman integrals, Comput. Phys. Commun. 177 (2007) 879–893. arXiv:0704.2423, doi:10.1016/j.cpc.2007.07.001.

[176] I. Dubovyk, J. Gluza, T. Riemann, J. Usovitsch, Numerical integration of massive two-loop Mellin-Barnes integrals in Minkowskian regions, PoS LL2016 (2016) 034. arXiv:1607.07538, doi:10.22323/1.260.0034.

[177] A. V. Belitsky, A. V. Smirnov, V. A. Smirnov, MB tools reloaded, Nucl. Phys. B 986 (2023) 116067. arXiv:2211.00009, doi:10.1016/j.nuclphysb.2022.116067.

[178] M. Prausa, Mellin–Barnes meets Method of Brackets: a novel approach to Mellin–Barnes representations of Feynman integrals, Eur. Phys. J. C 77 (9) (2017) 594. arXiv:1706.09852, doi:10.1140/epjc/s10052-017-5150-9.

[179] M. Hidding, DiffExp, a Mathematica package for computing Feynman integrals in terms of one-dimensional series expansions, Comput. Phys. Commun. 269 (2021) 108125. arXiv:2006.05510, doi:10.1016/j.cpc.2021.108125.

[180] T. Armadillo, R. Bonciani, S. Devoto, N. Rana, A. Vicini, Evaluation of Feynman integrals with arbitrary complex masses via series expansions, Comput. Phys. Commun. 282 (2023) 108545. arXiv:2205.03345, doi:10.1016/j.cpc.2022.108545.

[181] X. Liu, Y.-Q. Ma, AMFlow: A Mathematica package for Feynman integrals computation via auxiliary mass flow, Comput. Phys. Commun. 283 (2023) 108565. arXiv:2201.11669, doi:10.1016/j.cpc.2022.108565.

[182] R. M. Prisco, J. Ronca, F. Tramontano, LINE: Loop Integrals Numerical Evaluation, arXiv:2501.01943.

[183] P. Maierhöfer, J. Usovitsch, P. Uwer, Kira—A Feynman integral reduction program, Comput. Phys. Commun. 230 (2018) 99–112. arXiv:1705.05610, doi:10.1016/j.cpc.2018.04.012.

[184] P. Maierhöfer, J. Usovitsch, Kira 1.2 Release Notes. arXiv:1812.01491.

[185] F. Lange, J. Usovitsch, Z. Wu, Kira 3: integral reduction with efficient seeding and optimized equation selection. arXiv:2505.20197.

[186] A. V. Smirnov, Algorithm FIRE – Feynman Integral REduction, JHEP 10 (2008) 107. arXiv:0807.3243, doi:10.1088/1126-6708/2008/10/107.

[187] A. V. Smirnov, F. S. Chuharev, FIRE6: Feynman Integral REduction with Modular Arithmetic, Comput. Phys. Commun. 247 (2020) 106877. arXiv:1901.07808, doi:10.1016/j.cpc.2019.106877.

[188] A. V. Smirnov, M. Zeng, FIRE 6.5: Feynman integral reduction with new simplification library, Comput. Phys. Commun. 302 (2024) 109261. arXiv:2311.02370, doi:10.1016/j.cpc.2024.109261.

[189] R. N. Lee, LiteRed 1.4: a powerful tool for reduction of multiloop integrals, J. Phys. Conf. Ser. 523 (2014) 012059. arXiv:1310.1145, doi:10.1088/1742-6596/523/1/012059.

[190] C. Studerus, Reduze-Feynman Integral Reduction in C++, Comput. Phys. Commun. 181 (2010) 1293–1300. arXiv:0912.2546, doi:10.1016/j.cpc.2010.03.012.

[191] A. von Manteuffel, C. Studerus, Reduze 2 - Distributed Feynman Integral ReductionarXiv:1201.4330.

[192] Z. Capatti, V. Hirschi, D. Kermanschah, A. Pelloni, B. Ruijl, Manifestly Causal Loop-Tree Duality. arXiv:2009.05509.

[193] W. J. T. Bobadilla, Lotty – The loop-tree duality automation, Eur. Phys. J. C 81 (6) (2021) 514. arXiv:2103.09237, doi:10.1140/epjc/s10052-021-09235-0.

[194] M. Borinsky, H. J. Munch, F. Tellander, Tropical Feynman integration in the Minkowski regime, Comput. Phys. Commun. 292 (2023) 108874. arXiv:2302.08955, doi:10.1016/j.cpc.2023.108874.

[195] S. Borowka, T. Gehrmann, D. Hulme, Systematic approximation of multi-scale Feynman integrals, JHEP 08 (2018) 111. arXiv:1804.06824, doi:10.1007/JHEP08(2018)111.

[196] R. Pittau, B. Webber, Direct numerical evaluation of multi-loop integrals without contour deformation, Eur. Phys. J. C 82 (1) (2022) 55. arXiv:2110.12885, doi:10.1140/epjc/s10052-022-10008-6.

[197] K. Pyretzidis, J. J. M. de Lejarza, G. Rodrigo, Unlocking Multi-Dimensional Integration with Quantum Adaptive Importance Sampling. arXiv:2506.19965.

[198] V. Smirnov, "Evaluating Feynman Integrals" (Springer Verlag, Berlin, 2004).

[199] N. I. Usyukina, On a Representation for Three Point Function, Teor. Mat. Fiz. 22 (1975) 300–306, http://www.mathnet.ru/php/getFT.phtml?jrnid=tmf&paperid=3683&what=fullt&option_lang=eng. doi:10.1007/BF01037795.

[200] E. Boos, A. I. Davydychev, A Method of evaluating massive Feynman integrals, Theor. Math. Phys. 89 (1991) 1052–1063. doi:10.1007/BF01016805.

[201] V. A. Smirnov, Analytical result for dimensionally regularized massless on shell double box, Phys. Lett. B460 (1999) 397–404. arXiv:hep-ph/9905323, doi:10.1016/S0370-2693(99)00777-7.

[202] J. Tausk, Nonplanar massless two loop Feynman diagrams with four on-shell legs, Phys. Lett. B469 (1999) 225–234. arXiv:hep-ph/9909506, doi:10.1016/S0370-2693(99)01277-0.

[203] A. Gehrmann-De Ridder, T. Gehrmann, G. Heinrich, Four particle phase space integrals in massless QCD, Nucl. Phys. B 682 (2004) 265–288. arXiv:hep-ph/0311276, doi:10.1016/j.nuclphysb.2004.01.023.

[204] G. Somogyi, Angular integrals in d dimensions, J. Math. Phys. 52 (2011) 083501. arXiv:1101.3557, doi:10.1063/1.3615515.

[205] J. Berntsen, T. O. Espelid, A. Genz, Algorithm 698: Dcuhre: an adaptive multidemensional integration routine for a vector of integrals, ACM Trans. Math. Softw. 17 (4) (1991) 452–456. doi:10.1145/210232.210234.
URL https://doi.org/10.1145/210232.210234

[206] T. Hahn, CUBA: A Library for multidimensional numerical integration, Comput. Phys. Commun. 168 (2005) 78–95. arXiv:hep-ph/0404043, doi:10.1016/j.cpc.2005.01.010.

[207] J. Usovitsch, Numerical evaluation of Mellin-Barnes integrals in Minowskian regions and their application to two-loop bosonic electroweak contributions to the weak mixing angle of the Z$\bar{b}$b - vertex, Ph.D. thesis, Humboldt U., Berlin, Inst. Math. (2018). doi:10.3204/PUBDB-2017-12744.

[208] J. Usovitsch, I. Dubovyk, T. Riemann, MBnumerics: Numerical integration of Mellin-Barnes integrals in physical regions, PoS LL2018 (2018) 046. arXiv:1810.04580, doi:10.22323/1.303.0046.

[209] I. Dubovyk, J. Gluza, T. Jelinski, T. Riemann, J. Usovitsch, New prospects for the numerical calculation of Mellin-Barnes integrals in Minkowskian kinematics, Acta Phys. Polon. B 48 (2017) 995. arXiv:1704.02288, doi:10.5506/APhysPolB.48.995.

[210] J. Fleischer, A. V. Kotikov, O. L. Veretin, Analytic two loop results for selfenergy type and vertex type diagrams with one nonzero mass, Nucl. Phys. B 547 (1999) 343–374. arXiv:hep-ph/9808242, doi:10.1016/S0550-3213(99)00078-4.

[211] https://github.com/idubovyk/mbspringer, http://jgluza.us.edu.pl/mbspringer.

[212] S. Jones, A. Olsson, T. Stone, Positive Integrands from Feynman Integrals in the Minkowski Regime, arXiv:2506.24073.

[213] F. V. Tkachov, A theorem on analytical calculability of 4-loop renormalization group functions, Phys. Lett. B 100 (1981) 65–68. doi:10.1016/0370-2693(81)90288-4.

[214] K. G. Chetyrkin, F. V. Tkachov, Integration by parts: The algorithm to calculate β-functions in 4 loops, Nucl. Phys. B 192 (1981) 159–204. doi:10.1016/0550-3213(81)90199-1.

[215] A. V. Smirnov, A. V. Petukhov, The Number of Master Integrals is Finite, Lett. Math. Phys. 97 (2011) 37–44. arXiv:1004.4199, doi:10.1007/s11005-010-0450-0.

[216] S. Laporta, High-precision calculation of multiloop Feynman integrals by difference equations, Int. J. Mod. Phys. A 15 (2000) 5087–5159. arXiv:hep-ph/0102033, doi:10.1142/S0217751X00002159.

[217] A. von Manteuffel, R. M. Schabinger, A novel approach to integration by parts reduction, Phys. Lett. B 744 (2015) 101–104. arXiv:1406.4513, doi:10.1016/j.physletb.2015.03.029.

[218] T. Peraro, Scattering amplitudes over finite fields and multivariate functional reconstruction, JHEP 12 (2016) 030. arXiv:1608.01902, doi:10.1007/JHEP12(2016)030.

[219] J. Klappert, F. Lange, Reconstructing rational functions with FireFly, Comput. Phys. Commun. 247 (2020) 106951. arXiv:1904.00009, doi:10.1016/j.cpc.2019.106951.

[220] J. Klappert, S. Y. Klein, F. Lange, Interpolation of dense and sparse rational functions and other improvements in FireFly, Comput. Phys. Commun. 264 (2021) 107968. arXiv:2004.01463, doi:10.1016/j.cpc.2021.107968.

[221] D. A. Kosower, Direct Solution of Integration-by-Parts Systems, Phys. Rev. D 98 (2) (2018) 025008. arXiv:1804.00131, doi:10.1103/PhysRevD.98.025008.

[222] P. Mastrolia, S. Mizera, Feynman Integrals and Intersection Theory, JHEP 02 (2019) 139. arXiv:1810.03818, doi:10.1007/JHEP02(2019)139.

[223] J. Böhm, A. Georgoudis, K. J. Larsen, H. Schönemann, Y. Zhang, Complete integration-by-parts reductions of the non-planar hexagon-box via module intersections, JHEP 09 (2018) 024. arXiv:1805.01873, doi:10.1007/JHEP09(2018)024.

[224] A. V. Smirnov, An Algorithm to construct Grobner bases for solving integration by parts relations, JHEP 04 (2006) 026. arXiv:hep-ph/0602078, doi:10.1088/1126-6708/2006/04/026.

[225] A. V. Smirnov, V. A. Smirnov, S-bases as a tool to solve reduction problems for Feynman integrals, Nucl. Phys. B Proc. Suppl. 160 (2006) 80–84. arXiv:hep-ph/0606247, doi:10.1016/j.nuclphysbps.2006.09.032.

[226] R. N. Lee, Group structure of the integration-by-part identities and its application to the reduction of multiloop integrals, JHEP 07 (2008) 031. arXiv:0804.3008, doi:10.1088/1126-6708/2008/07/031.

[227] X. Liu, Y.-Q. Ma, Determining arbitrary Feynman integrals by vacuum integrals, Phys. Rev. D 99 (7) (2019) 071501. arXiv:1801.10523, doi:10.1103/PhysRevD.99.071501.

[228] A. V. Smirnov, V. A. Smirnov, FIRE4, LiteRed and accompanying tools to solve integration by parts relations, Comput. Phys. Commun. 184 (2013) 2820–2827. arXiv:1302.5885, doi:10.1016/j.cpc.2013.06.016.

[229] A. V. Smirnov, FIRE5: a C++ implementation of Feynman Integral REduction, Comput. Phys. Commun. 189 (2015) 182–191. arXiv:1408.2372, doi:10.1016/j.cpc.2014.11.024.

[230] C. Anastasiou, A. Lazopoulos, Automatic integral reduction for higher order perturbative calculations, JHEP 07 (2004) 046. arXiv:hep-ph/0404258, doi:10.1088/1126-6708/2004/07/046.

[231] A. V. Kotikov, Differential equations method: New technique for massive Feynman diagrams calculation, Phys. Lett. B 254 (1991) 158–164. doi:10.1016/0370-2693(91)90413-K.

[232] A. Kotikov, Differential equations method: The Calculation of vertex type Feynman diagrams, Phys. Lett. B259 (1991) 314–322.

[233] A. V. Kotikov, Differential equation method: The Calculation of N point Feynman diagrams, Phys. Lett. B267 (1991) 123–127.

[234] E. Remiddi, Differential equations for Feynman graph amplitudes, Nuovo Cim. A110 (1997) 1435–1452. arXiv:hep-th/9711188.

[235] J. M. Henn, Multiloop integrals in dimensional regularization made simple, Phys. Rev. Lett. 110 (2013) 251601. arXiv:1304.1806, doi:10.1103/PhysRevLett.110.251601.

[236] M. Czakon, J. Gluza, T. Riemann, Master integrals for massive two-loop bhabha scattering in QED, Phys. Rev. D 71 (2005) 073009. arXiv:hep-ph/0412164, doi:10.1103/PhysRevD.71.073009.

[237] J. M. Henn, V. A. Smirnov, Analytic results for two-loop master integrals for Bhabha scattering I, JHEP 11 (2013) 041. arXiv:1307.4083, doi:10.1007/JHEP11(2013)041.

[238] R. N. Lee, Libra: A package for transformation of differential systems for multiloop integrals, Comput. Phys. Commun. 267 (2021) 108058. arXiv:2012.00279, doi:10.1016/j.cpc.2021.108058.

[239] R. N. Lee, Reducing differential equations for multiloop master integrals, JHEP 04 (2015) 108. arXiv:1411.0911, doi:10.1007/JHEP04(2015)108.

[240] M. Prausa, epsilon: A tool to find a canonical basis of master integrals, Comput. Phys. Commun. 219 (2017) 361–376. arXiv:1701.00725, doi:10.1016/j.cpc.2017.05.026.

[241] O. Gituliar, V. Magerya, Fuchsia: a tool for reducing differential equations for Feynman master integrals to epsilon form, Comput. Phys. Commun. 219 (2017) 329–338. arXiv:1701.04269, doi:10.1016/j.cpc.2017.05.004.

[242] C. Meyer, Algorithmic transformation of multi-loop master integrals to a canonical basis with CANONICA, Comput. Phys. Commun. 222 (2018) 295–312. arXiv:1705.06252, doi:10.1016/j.cpc.2017.09.014.

[243] C. Dlapa, J. Henn, K. Yan, Deriving canonical differential equations for Feynman integrals from a single uniform weight integral, JHEP 05 (2020) 025. arXiv:2002.02340, doi:10.1007/JHEP05(2020)025.

[244] J. Blümlein, C. Schneider, P. Paule (Eds.), Proceedings, KMPB Conference: Elliptic Integrals, Elliptic Functions and Modular Forms in Quantum Field Theory: Zeuthen, Germany, October 23-26, 2017, 2019. doi:10.1007/978-3-030-04480-0.

[245] G. Travaglini, et al., The SAGEX review on scattering amplitudes, J. Phys. A 55 (44) (2022) 443001. arXiv:2203.13011, doi:10.1088/1751-8121/ac8380.

[246] S. Weinzierl, Feynman Integrals. A Comprehensive Treatment for Students and Researchers, UNITEXT for Physics, Springer, 2022. arXiv:2201.03593, doi:10.1007/978-3-030-99558-4.

[247] S. Pozzorini, E. Remiddi, Precise numerical evaluation of the two loop sunrise graph master integrals in the equal mass case, Comput. Phys. Commun. 175 (2006) 381–387. arXiv:hep-ph/0505041, doi:10.1016/j.cpc.2006.05.005.

[248] M. K. Mandal, X. Zhao, Evaluating multi-loop Feynman integrals numerically through differential equations, JHEP 03 (2019) 190. arXiv:1812.03060, doi:10.1007/JHEP03(2019)190.

[249] M. L. Czakon, M. Niggetiedt, Exact quark-mass dependence of the Higgs-gluon form factor at three loops in QCD, JHEP 05 (2020) 149. arXiv:2001.03008, doi:10.1007/JHEP05(2020)149.

[250] X. Liu, Y.-Q. Ma, C.-Y. Wang, A Systematic and Efficient Method to Compute Multi-loop Master Integrals, , Phys. Lett. B 779 (2018) 353–357. arXiv:1711.09572, doi:10.1016/j.physletb.2018.02.026.

[251] C. Brønnum-Hansen, C.-Y. Wang, Contribution of third generation quarks to two-loop helicity amplitudes for W boson pair production in gluon fusion, JHEP 01 (2021) 170. arXiv:2009.03742, doi:10.1007/JHEP01(2021)170.

[252] F. Moriello, Generalised power series expansions for the elliptic planar families of Higgs + jet production at two loops, JHEP 01 (2020) 150. arXiv:1907.13234, doi:10.1007/JHEP01(2020)150.

[253] R. Bonciani, V. Del Duca, H. Frellesvig, J. M. Henn, M. Hidding, L. Maestri, F. Moriello, G. Salvatori, V. A. Smirnov, Evaluating a family of two-loop non-planar master integrals for Higgs + jet production with full heavy-quark mass dependence, JHEP 01 (2020) 132. arXiv:1907.13156, doi:10.1007/JHEP01(2020)132.

[254] P. Banerjee, et al., Theory for muon-electron scattering @ 10 ppm: A report of the MUonE theory initiative, Eur. Phys. J. C 80 (6) (2020) 591. arXiv:2004.13663, doi:10.1140/epjc/s10052-020-8138-9.

[255] R. E. Cutkosky, Singularities and discontinuities of Feynman amplitudes, J. Math. Phys. 1 (1960) 429–433. doi:10.1063/1.1703676.

[256] L. D. Landau, On the Analytic Properties of Vertex Parts in Quantum Field Theory, Zh. Eksp. Teor. Fiz. 37 (1) (1960) 62–70. doi:10.1016/B978-0-08-010586-4.50103-6.

[257] N. Nakanishi, Ordinary and Anomalous Thresholds in Perturbation Theory, Prog. Theor. Phys. 22 (1) (1959) 128–144. doi:10.1143/ptp.22.128.

[258] W. Flieger, W. J. Torres Bobadilla, Landau and leading singularities in arbitrary space-time dimensions, Eur. Phys. J. Plus 139 (11) (2024) 1022. arXiv:2210.09872, doi:10.1140/epjp/s13360-024-05796-7.

[259] S. Borowka, G. Heinrich, S. Jahn, S. P. Jones, M. Kerner, J. Schlenk, A GPU compatible quasi-Monte Carlo integrator interfaced to pySecDec, Comput. Phys. Commun. 240 (2019) 120–137. arXiv:1811.11720, doi:10.1016/j.cpc.2019.02.015.

[260] M. Beneke, V. A. Smirnov, Asymptotic expansion of Feynman integrals near threshold, Nucl. Phys. B 522 (1998) 321–344. arXiv:hep-ph/9711391, doi:10.1016/S0550-3213(98)00138-2.

[261] V. A. Smirnov, Problems of the strategy of regions, Phys. Lett. B 465 (1999) 226–234. arXiv:hep-ph/9907471, doi:10.1016/S0370-2693(99)01061-8.

[262] A. I. Davydychev, J. B. Tausk, Two loop selfenergy diagrams with different masses and the momentum expansion, Nucl. Phys. B 397 (1993) 123–142. doi:10.1016/0550-3213(93)90338-P.

[263] D. J. Broadhurst, Massive three - loop Feynman diagrams reducible to SC* primitives of algebras of the sixth root of unity, Eur. Phys. J. C 8 (1999) 311–333. arXiv:hep-th/9803091, doi:10.1007/s100529900935.

[264] Y. Schroder, A. Vuorinen, High-precision epsilon expansions of single-mass-scale four-loop vacuum bubbles, JHEP 06 (2005) 051. arXiv:hep-ph/0503209, doi:10.1088/1126-6708/2005/06/051.

[265] T. Luthe, Fully massive vacuum integrals at 5 loops, Ph.D. thesis, Bielefeld U. (2015).

[266] T. Luthe, A. Maier, P. Marquard, Y. Schroder, Complete renormalization of QCD at five loops, JHEP 03 (2017) 020. arXiv:1701.07068, doi:10.1007/JHEP03(2017)020.

[267] B. A. Kniehl, A. F. Pikelner, O. L. Veretin, Three-loop massive tadpoles and polylogarithms through weight six, JHEP 08 (2017) 024. arXiv:1705.05136, doi:10.1007/JHEP08(2017)024.

[268] A. Pak, The toolbox of modern multi-loop calculations: novel analytic and semi-analytic techniques, J. Phys. Conf. Ser. 368 (2012) 012049. arXiv:1111.0868, doi:10.1088/1742-6596/368/1/012049.

[269] J. Kuipers, T. Ueda, J. A. M. Vermaseren, J. Vollinga, FORM version 4.0, Comput. Phys. Commun. 184 (2013) 1453–1467. arXiv:1203.6543, doi:10.1016/j.cpc.2012.12.028.

[270] S. Bauberger, A. Freitas, D. Wiegand, TVID 2: Evaluation of planar-type three-loop self-energy integrals with arbitrary masses, JHEP 01 (2020) 024. arXiv:1908.09887, doi:10.1007/JHEP01(2020)024.

[271] M. Czakon, M. Zralek, J. Gluza, Left-right symmetry and heavy particle quantum effects, Nucl. Phys. B 573 (2000) 57–74. arXiv:hep-ph/9906356, doi:10.1016/S0550-3213(99)00717-8.

[272] M. Czakon, J. Gluza, J. Hejczyk, Muon decay to one loop order in the left-right symmetric model, Nucl. Phys. B 642 (2002) 157–172. arXiv:hep-ph/0205303, doi:10.1016/S0550-3213(02)00638-7.

[273] A. Lorca, T. Riemann, An integrated tool for loop calculations: aITALC, Computer Physics Communications 174 (1) (2006) 71–82. doi:10.1016/j.cpc.2005.09.003.

[274] L. Chen, A. Freitas, Leading fermionic three-loop corrections to W-boson mass and Z-pole observables, SciPost Phys. Proc. 7 (2022) 019. arXiv:2111.00066, doi:10.21468/SciPostPhysProc.7.019.

[275] S. Jadach, B. F. L. Ward, Z. Was, The Precision Monte Carlo event generator K K for two fermion final states in e+ e- collisions, Comput. Phys. Commun. 130 (2000) 260–325. arXiv:hep-ph/9912214, doi:10.1016/S0010-4655(00)00048-5.

[276] S. Jadach, B. F. L. Ward, Z. Was, S. A. Yost, A. Siodmok, Multi-photon Monte Carlo event generator KKMCee for lepton and quark pair production in lepton colliders, Comput. Phys. Commun. 283 (2023) 108556. arXiv:2204.11949, doi:10.1016/j.cpc.2022.108556.

[277] L. Chen, A. Freitas, GRIFFIN: A C++ library for electroweak radiative corrections in fermion scattering and decay processes, SciPost Phys. Codeb. 2023 (2023) 18. arXiv:2211.16272, doi:10.21468/SciPostPhysCodeb.18.

[278] M. J. G. Veltman, Reflections on the Higgs system, doi:10.5170/CERN-1997-005.

[279] M. J. G. Veltman, The Screening theorem and the Higgs system, Acta Phys. Polon. B 25 (1994) 1627–1636.

[280] M. E. Peskin, T. Takeuchi, Estimation of oblique electroweak corrections, Phys. Rev. D 46 (1992) 381–409. doi:10.1103/PhysRevD.46.381.

[281] A. Nyffeler, A. Schenk, The Electroweak chiral Lagrangian reanalyzed, Phys. Rev. D 62 (2000) 113006. arXiv:hep-ph/9907294, doi:10.1103/PhysRevD.62.113006.

[282] S. Dittmaier, S. Schuhmacher, M. Stahlhofen, Integrating out heavy fields in the path integral using the background-field method: general formalism, Eur. Phys. J. C 81 (9) (2021) 826. arXiv:2102.12020, doi:10.1140/epjc/s10052-021-09587-7.

[283] S. Dittmaier, *Effective Lagrangians for heavy particles via functional matching*, talk held at the Loop Summit 2 - new perturbative results and methods in precision physics: Quantum Field Theory and Collider Physics, https://indico.desy.de/event/44685/contributions/185322/attachments/98417/136016/Dittmaier1.pdf.

[284] M. Czakon, J. Gluza, F. Jegerlehner, M. Zralek, Confronting electroweak precision measurements with new physics models, Eur. Phys. J. C 13 (2000) 275–281. arXiv:hep-ph/9909242, doi:10.1007/s100520000278.

[285] L. Chen, The Study of The Standard Model Electroweak Precision Physics at Future Electron-Positron Colliders, Ph.D. thesis, U. Pittsburgh (main), https://d-scholarship.pitt.edu/43653/ (2022).

[286] G. 't Hooft, M. J. G. Veltman, Regularization and Renormalization of Gauge Fields, Nucl. Phys. B 44 (1972) 189–213. doi:10.1016/0550-3213(72)90279-9.

[287] C. G. Bollini, J. J. Giambiagi, Dimensional Renormalization: The Number of Dimensions as a Regularizing Parameter, Nuovo Cim. B 12 (1972) 20–26. doi:10.1007/BF02895558.

[288] G. M. Cicuta, E. Montaldi, Analytic renormalization via continuous space dimension, Lett. Nuovo Cim. 4 (1972) 329–332. doi:10.1007/BF02756527.

[289] K. G. Wilson, Quantum field theory models in less than four-dimensions, Phys. Rev. D 7 (1973) 2911–2926. doi:10.1103/PhysRevD.7.2911.

[290] J. C. Collins, Renormalization : An Introduction to Renormalization, the Renormalization Group and the Operator-Product Expansion, Vol. 26 of Cambridge Monographs on Mathematical Physics, Cambridge University Press, Cambridge, 1984. doi:10.1017/9781009401807.

[291] S. Weinzierl, Introduction to Feynman Integrals, in: 6th Summer School on Geometric and Topological Methods for Quantum Field Theory, 2013, pp. 144–187. arXiv:1005.1855, doi:10.1017/CBO9781139208642.005.

[292] M. S. Chanowitz, M. Furman, I. Hinchliffe, The Axial Current in Dimensional Regularization, Nucl. Phys. B 159 (1979) 225–243. doi:10.1016/0550-3213(79)90333-X.

[293] P. Breitenlohner, D. Maison, Dimensional Renormalization and the Action Principle, Commun. Math. Phys. 52 (1977) 11–38. doi:10.1007/BF01609069.

[294] S. A. Larin, The Renormalization of the axial anomaly in dimensional regularization, Phys. Lett. B 303 (1993) 113–118. arXiv:hep-ph/9302240, doi:10.1016/0370-2693(93)90053-K.

[295] S. L. Adler, Axial vector vertex in spinor electrodynamics, Phys. Rev. 177 (1969) 2426–2438. doi:10.1103/PhysRev.177.2426.

[296] J. S. Bell, R. Jackiw, A PCAC puzzle: $\pi^0 \to \gamma\gamma$ in the σ model, Nuovo Cim. A 60 (1969) 47–61. doi:10.1007/BF02823296.

[297] W. Pauli, F. Villars, On the Invariant regularization in relativistic quantum theory, Rev. Mod. Phys. 21 (1949) 434–444. doi:10.1103/RevModPhys.21.434.

[298] A.V. Smirnov, Tools-UF, https://www.ttp.kit.edu/~asmirnov/Tools-UF.htm.

[299] H. Cheng, T. Wu, "Expanding protons: Scattering at High Energies" (MIT Press, Cambridge, Massachusetts, 1987).

[300] V. A. Smirnov, Asymptotic expansions in momenta and masses and calculation of Feynman diagrams, Mod. Phys. Lett. A 10 (1995) 1485–1500. arXiv:hep-th/9412063, doi:10.1142/S0217732395001617.

[301] M. Misiak, M. Steinhauser, Three loop matching of the dipole operators for $b \to s\gamma$ and $b \to sg$, Nucl. Phys. B 683 (2004) 277–305. arXiv:hep-ph/0401041, doi:10.1016/j.nuclphysb.2004.02.006.

[302] M. Gerlach, F. Herren, M. Lang, tapir: A tool for topologies, amplitudes, partial fraction decomposition and input for reductions, Comput. Phys. Commun. 282 (2023) 108544. arXiv:2201.05618, doi:10.1016/j.cpc.2022.108544.

[303] Github repository for the Feynman diagrams identification TopoID https://github.com/thejensemann/TopoID.

[304] J. Grigo, J. Hoff, Mass-corrections to double-Higgs production & TopoID, PoS LL2014 (2014) 030. arXiv:1407.1617, doi:10.22323/1.211.0030.